PHD

Atomistic modelling of perovskite solar cells

Brivio, Federico

Award date:
2016

Awarding institution:
University of Bath

Atomistic modelling of perovskite solar cells

Federico BRIVIO

A thesis submitted for the degree of Doctor of Philosophy

UNIVERSITY OF BATH

Department of Chemistry

August 2016

Declaration of Authorship

This thesis may be made available for consultation within the University Library and may be photocopied or lent to other libraries for the purposes of consultation with effect from June 7th 2016.

Signed on behalf of the Faculty of Science:

"Stat Roma pristina nomine, nomina nuda tenemus."

Bernardus Cluniacensis

Acknowledgements

This thesis and all the results achieved could not have been possible without the precious help and supervision of Prof. Aron Walsh. I must thank also Prof. Alison Walker for the supervision of the Destiny project that provided more than generous funding and formation experiences.

At the end of the day, the credit goes also to the every-day fellows, colleagues, and researcher that makes research worth beyond results.

Special thanks goes to Clovis that moves me out of the DFT-comfort-zone (a concept I think I just created, so please cite this thesis if you use it), and to Jonathan who taught me that there is no such thing as *enough budget*.

Other even more special thanks goes to all the members of the *downstairs office* where the coffee brews and people struggle to survive to my experiments (you made it Jess! You survived!) and to the people of the *upstairs office* who can see the sky.

We live an eternal present, but I am grateful also to the people that are no more in the WMD group and scattered around the world. As well I need to thank the fellowship of the Sun and the lovely/crazy people you meet at conferences.

I would not be here without the support of my Family, and I would be even more insane without all the friends that cross their path with mine during these three years.

At the end I want to thank you who did not find his name written here (I wrote really few names!) and maybe you did not even identified with one of the groups above, I want to thank you because you found the time to read up to this point, and I hope you will enjoy the following pages. Just to be clear the reason why I did not write your name is not personal and lot of people deserved it! But I am running to print this thesis!!

Thanks!

Federico.

UNIVERSITY OF BATH

Abstract

Faculty of Science

Department of Chemistry

Doctor of Philosophy

Atomistic modelling of perovskite solar cells

by Federico BRIVIO

This thesis focuses on the study of hybrid perovskites properties for the purposes of photovoltaic applications. During the almost four years PhD project that has lead to this thesis the record photovoltaic efficiency for this technology has increased from 10.9% to 22.1%. Such a significant pace of development can be compared with few other materials. It is for this reason that hybrid perovsites have attracted impressive research efforts. We approached the study of such unique materials using computational *ab-initio* techniques, and in particular Density Functional Theory. We considered different materials, but most of the attention was concentrated on MAPI ($CH_3NH_3PbI_3$).

The results are divided in three chapters, each exploring a different material property. The first chapter reports the electronic structure of the material bulk, surfaces, and other electronic-related properties such as the rotation barrier for the organic component and the Berry phase polarization.

The second chapter focuses on the vibrational properties primary employing the harmonic approximation but also extends to the quasi-harmonic approximation. The outcome of these calculations permitted us to calculate theoretical IR and Raman spectra which are in good agreement with different experimental measurements. The quasi-harmonic approximation was used to calculate temperature dependent properties, such as the Grüneisen parameter, the thermal dependence of heat capacity and the thermal volumetric expansion.

The third and last chapter reviews the thermodynamic properties of binary halide compounds. The cobination of *ab-initio* calculations with the generalised quasi-chemical approximation has allowed to study the stability of mixed composition perovskites. The results certified a set of stable structures that could stand at the base of observed phenomena of photo-degradation of hybrid perovskite based devices.

All three chapters have been written to understand the chemical and physical behaviour of hybrid perovskites and to extended and contribute to the understanding of experimental work.

Contents

Chapter 1

Introduction

1.1 From fossil fuels to photovoltaics

1.1.1 Energy landscape

Energy is one of the basic requirements of the human society. The technological improvement of production, storage and distribution of energy drives human evolution and influences the environment, politics and the economy.

Energy is not simple to define. From the simplest thermodynamic point of view it is a measure of an object's capability to do work. More generally, it is a property of bodies that can be only transformed or converted to other forms, but not created nor destroyed.[1] In the arena of human activities energy is the medium to power devices, enable transport and produce goods.

Nowadays the main sources of energy are fossil fuels (oil, coal and natural gas): together they sum up to more then 80% of world consumption,[2] while the remaining are nuclear power, hydroelectric power and other renewable sources of energy.

This imbalance leads to political issues and environmental problems. It is therefore clear that a new, more sustainable source of energy is needed. In the next paragraphs we will present a more detailed overview of fossil fuel issues, and propose photovoltaic as a valid alternative.

1.1.2 Fossil fuels

Fossil fuels originate from the organic mass that has accumulated in a particular zone of Earth and has been processed by micro-organisms,[3,4] although some abiotic theories had been presented.[5] At the moment fossil fuels represent the largest source of energy for human activities[2,6] and they can be consumed to produce mechanical work or electricity. Exploiting fossil fuel involves powering a

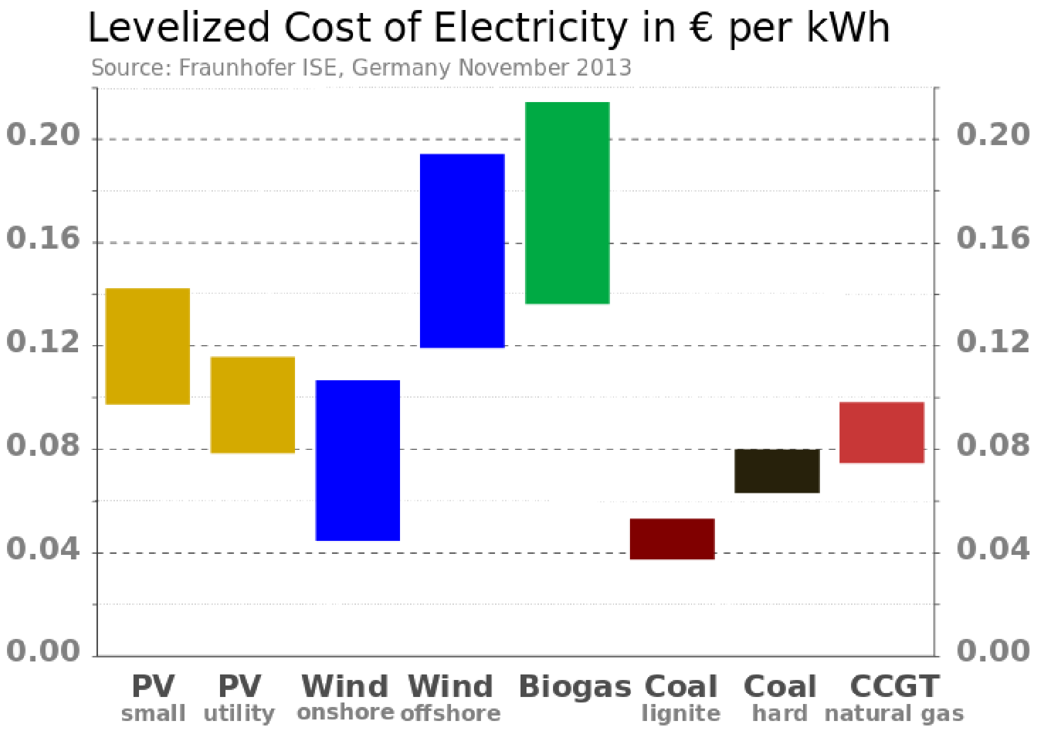

FIGURE 1.1: The chart reports the cost spread per kWh in € for different energy sources in Germany.[11] We can observe that renewable energy are in general more expensive than fossil fuel, but especially wind generated electricity can be competitive. Image taken from reference.[11]

combustion engine or a turbine whose efficiency is:

$$\eta = \frac{\text{work done}}{\text{heat absorbed}} = \frac{Q_{in} - Q_{out}}{Q_{in}} \tag{1.1}$$

where Q_{in} is the heat provided to the system and Q_{out} is the output of the process. In an engine, or in a power plant, this process is far from ideal and lot of heat is dissipated limiting the overall efficiency to about 40%.[7–10] Even if the efficiency is low, fossil fuels have flourished due to their competitive cost. In Figure 1.1 is reported the energy cost for energy production in Germany[11] for the year 2013, as example.

Since the industrial revolution the consumption of fossil fuel has increased steadily but it is not easy to assess when the reserves of different resources are going to be depleted.[12,13] According to different studies the reserves could last for some decades, or at most one century with coal to last the longest,[6] but these predictions can be affected by the discovery of new fossil fuel sites or future economical and political scenarios.[14]

Würfel[15] estimated that the maximum amount of fossil fuel present on earth is about 35 times the actual known reserves, leaving margin for the discovery of new reserves. This figure is based on the coarse assumption that all the oxygen and organic material present nowadays in the atmosphere is the result of photosynthesis.[16] The primordial Earth's atmosphere had a reductive character (i.e. it was rich in CO_2) without any significant presence of gaseous oxygen; O_2 was produced along with carbohydrates accordingly by photosynthesis as:

$$n(H_2O + CO_2) \rightarrow C_nH_{2n}O_n + nO_2 \uparrow \tag{1.2}$$

This type of processes transformed the CO_2 into oxygen, which was released into the atmosphere, and organic material that ultimately contributed to the formation of fossil fuel.

The large discrepancy between the known reserves of fossil fuels and the theoretical limit could support the research of different and new sources of oil, coal or gas. If these resources were available, energy would be produced with the inverse reaction shown in equation 1.2. To obey conservation mass law, the use to completion would consume all atmospheric oxygen with tragic consequences for life. It is clear that in the long term fossil fuels are not, and can not be, a sustainable source of energy regardless of their availability.

1.1.3 Global warming and pollution

The concerns about the use of fossil fuels are not limited to their scarcity, but to the production of Green House Gases (GHG) and CO_2 in particular.[17]

Increasing atmospheric concentration of CO_2 has many environmental impacts, such as raising global temperatures[18] and acidifying the oceans.[19,20] A proof of anthropogenic effects on the atmosphere comes from the atmospheric concentration of CO_2 that surpassed 400 ppm,[21] effectively providing confirmation that the upward trend which started with the industrial revolution is real[22] as pictured in Figure 1.2.

We explained in the previous sections how photosynthetic organisms transformed the initial CO_2-rich atmosphere into an oxygen-rich. Combustion of fossil fuel inverts this process and induces, among other effects, a rise in the average global temperature.

If Earth had no atmosphere, its temperature would be the result of the balance between energy absorbed and the energy reflected by the surface. The atmosphere only partially reflects[24] the radiation with a consequent rise in temperature similar to what happens in a green house. The green house effect is mostly due to the IR-reflectance of CO_2.[25,26] Early estimations[27] forecast an increment in mean surface temperature in a range of 1^o to 5^oC. This trend has been verified on a long timescale, back from data availability.[28] The temperature trends, obtained as averages over different time interval, are reported in Figure 1.3.

Most recent data show a *hiatus* in temperature raising that different authors[29,30] suggest is due to compensating effects and biased estimations.

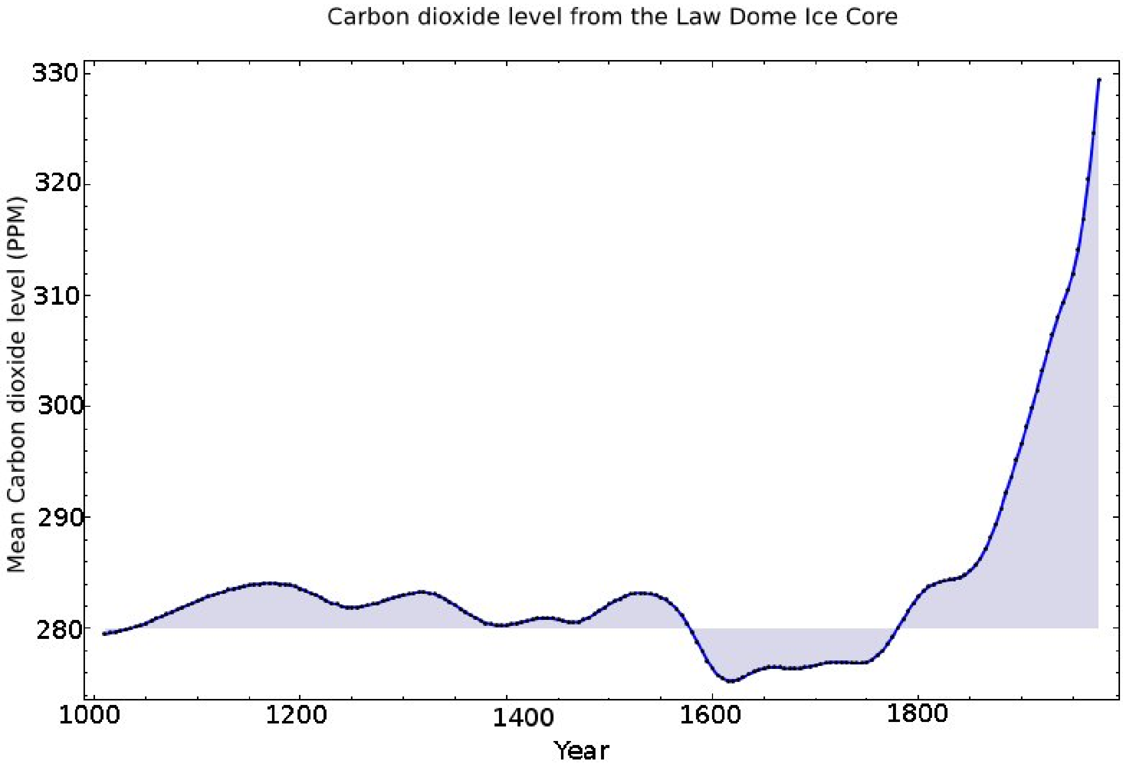

FIGURE 1.2: Historical CO_2 atmospheric concentration as measured from the Law Dome DE08, DE08-2, and DSS Ice Cores. Image taken from reference.[23]

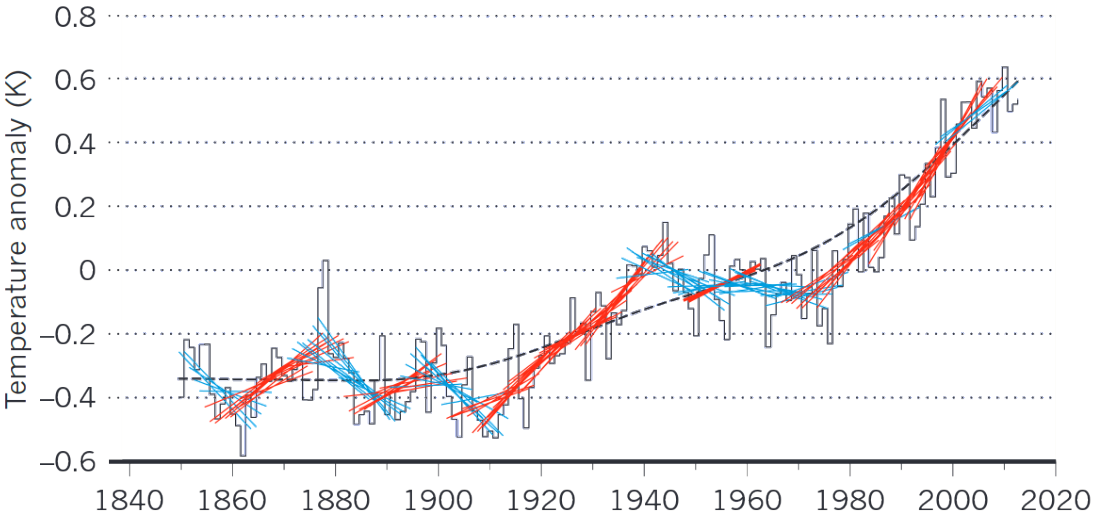

FIGURE 1.3: The continuous line reports the global mean surface temperature variation with respect to 1960-1990 average per year, while the dashed line is a smooth fit to this trend. The graphic also shows the linear tread over periods of 15 years. This trend is reported in blue if the 15 year trend is steeper than the long term average, red otherwise. Image taken from reference.[28]

The rise of mean temperature leads to biological undercompensation and could ultimately melt the west Antarctic ice sheet,[31] which would also result in a average raise of global sea level of 5 meters.[32] Besides, the increase of temperature would also result in effects with positive feedback such as the increase of water vapour concentration.[33]

In terms of environmental impact another important effect regards the acidification of the oceans. Approximately 50%[15] of the atmospheric CO_2 is dissolved in the ocean according to:

$$\mathrm{CO_{2(atm)}} \rightleftharpoons \mathrm{CO_{2(aq)}} + \mathrm{H_2O} \rightleftharpoons \mathrm{H^+} + \mathrm{HCO_3}^- \rightleftharpoons 2\,\mathrm{H^+} + \mathrm{CO_3}^{2-}. \tag{1.3}$$

This acidification has negative effect on the microscopic flora with a reduction of photosynthesis[34–36].

In general fossil fuels are not pure and do not undergo perfect combustion, this lead to the production of other toxic gasses as CO, SO_2, NO_x, etc. .[37–39] These gases contribute to the greenhouse effect and represent a hazard for human health with economic repercussions.[40,41]

1.1.4 Fossil fuel alternatives

The greenhouse effect is highly debated for political reasons, but there is an overwhelming scientific consensus[42–45] that human activity is changing the climate of the globe. As explained in the previous section the main reason of climate change is found to be GHGs. To invert this trend it is necessary to change the energy production paradigm. Historically fossil fuels have dominated the market due to their lower price,[46,47] but in the recent past the gap is closing as pictured in Figure 1.4.

Substitution of fossil fuel is not a simple task but different alternatives are available:

- wind
- photovoltaic
- tidal
- biomass
- hydroelectric
- nuclear

From 1973 to 2013, according to the International Energy Agency,[49] the world's energy supply more than doubled. There has been a significant decrease in oil consumption compensated by the growth of natural gas and coal, which we saw are the most abundant fossil fuels. All the data are collected in Figure 1.5.

Nuclear power plants represent a possible way to reduce the emission of GHG, but nuclear waste disposal is still a technological issue and the general production

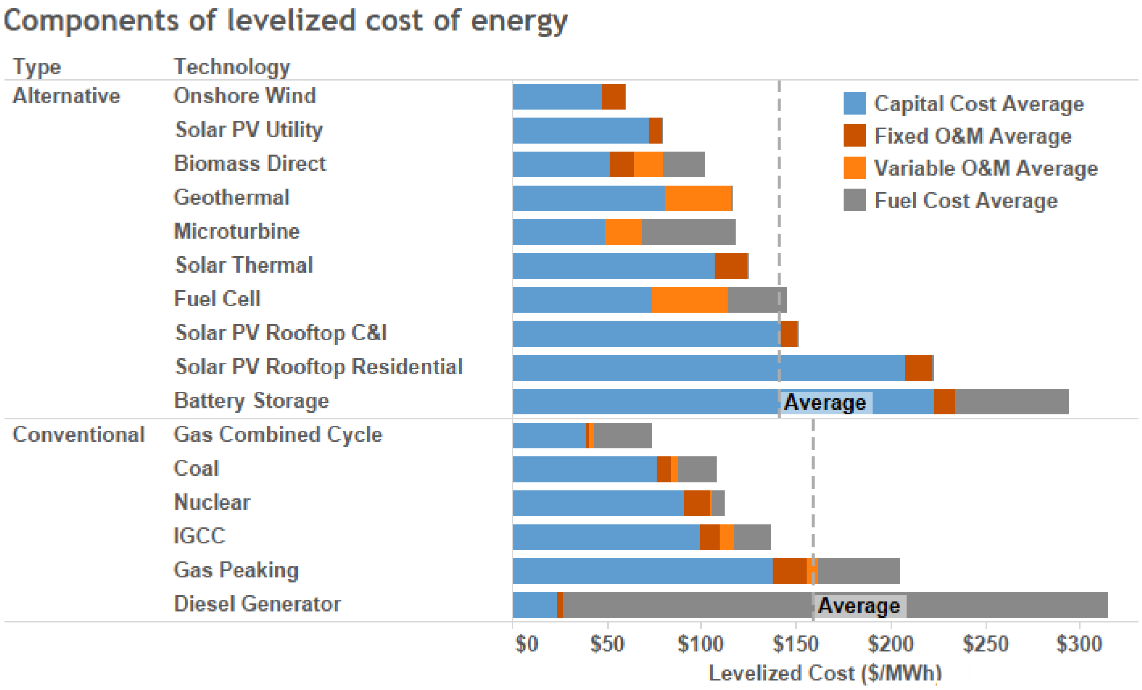

FIGURE 1.4: Summary of the normalised cost of 16 different energy sources, divided per component. The data are taken from Lazard's Levelized Cost of Energy Analysis, Version 8.0, September 2014. Image taken from reference[46,48].

declined in the last two decades at advantage of wind power as reported in Figure 1.6.[50]

Part of the fall of nuclear power started in 2011 after the disaster of Fukushima, Japan[51]. Nonetheless, to reduce the impact of radioactive waste, different cleaner and safer reactors have been proposed,[52,53] in particular based on different fissile materials such as thorium, but even with these technologies various concerns on process safety are still present[54].

Even if nuclear power could be a solution to reduce the production of CO_2, such power plants are based on the exploitation of nuclear fuel whose amount is limited[55] and there is not a clear solution for the waste.

A long term sustainable form of energy has to be based on resources that are almost inexhaustible. Hence, to obtain a virtually endless source of energy, it is necessary to exploit the natural phenomena that spontaneously occur in nature. These phenomena include wind, sea currents, water flows and light.

Actually hydroelectric power plants were the first source of renewable energy, and every year they contribute to the 2.4 % production of world energy supply.[49] Other technology such as wind generators, or tide power plants cover a smaller fraction of world energy production but are growing.[56–58]

One problem of renewable energy sources is the need for large infrastructures that often exploit the landscape and have a negative impact on the environment. For example, hydroelectric plants require the construction of a basin and a dam

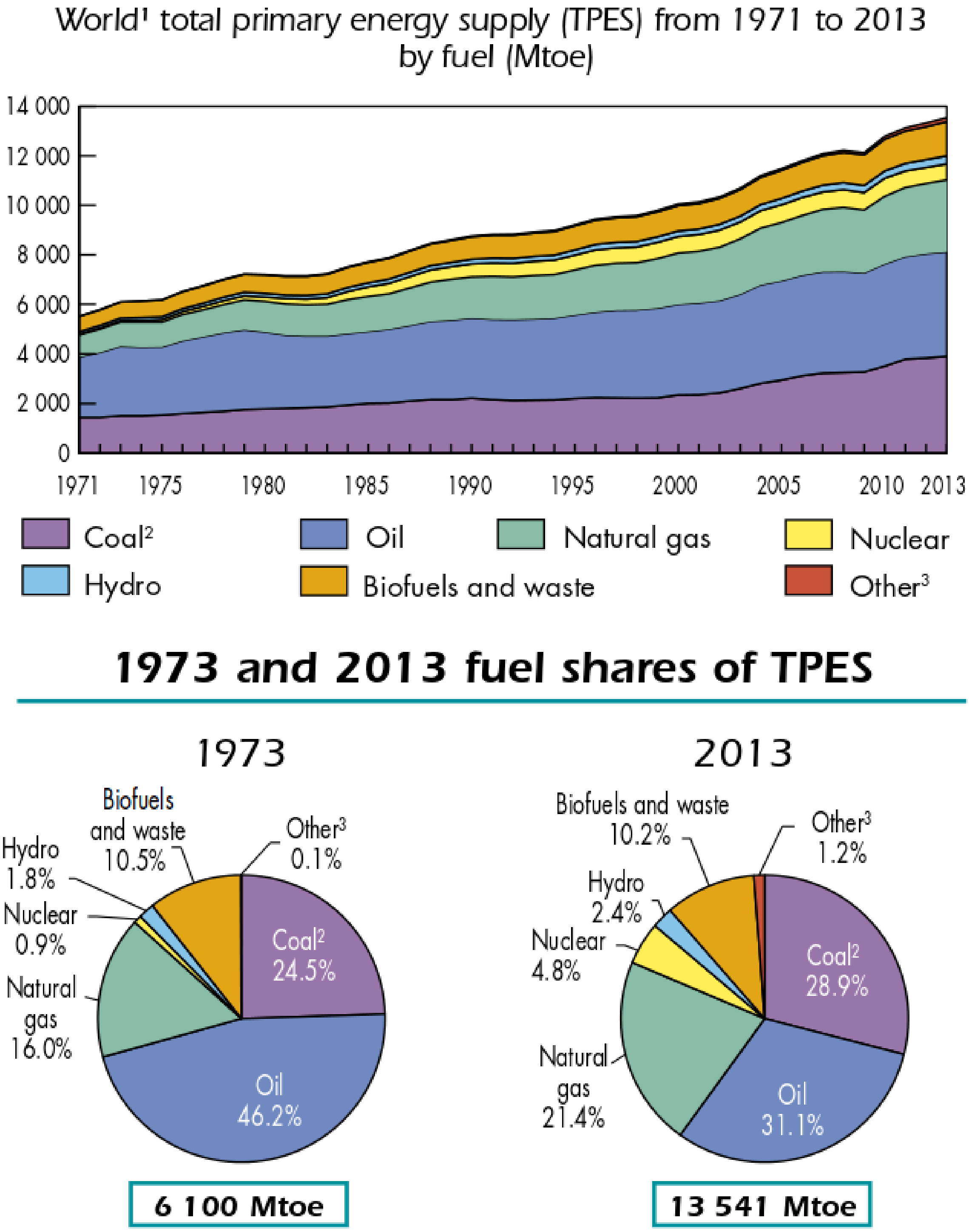

1. *World includes international aviation and international marine bunkers.*
2. *In these graphs, peat and oil shale are aggregated with coal.*
3. *Includes geothermal, solar, wind, heat, etc.*

FIGURE 1.5: Comparison of world total primary energy supply between 1973 and 2013. The data are reported in toe, tonne of oil equivalent. One toe is equivalent to 11.65 MWh. Image taken from reference.[49]

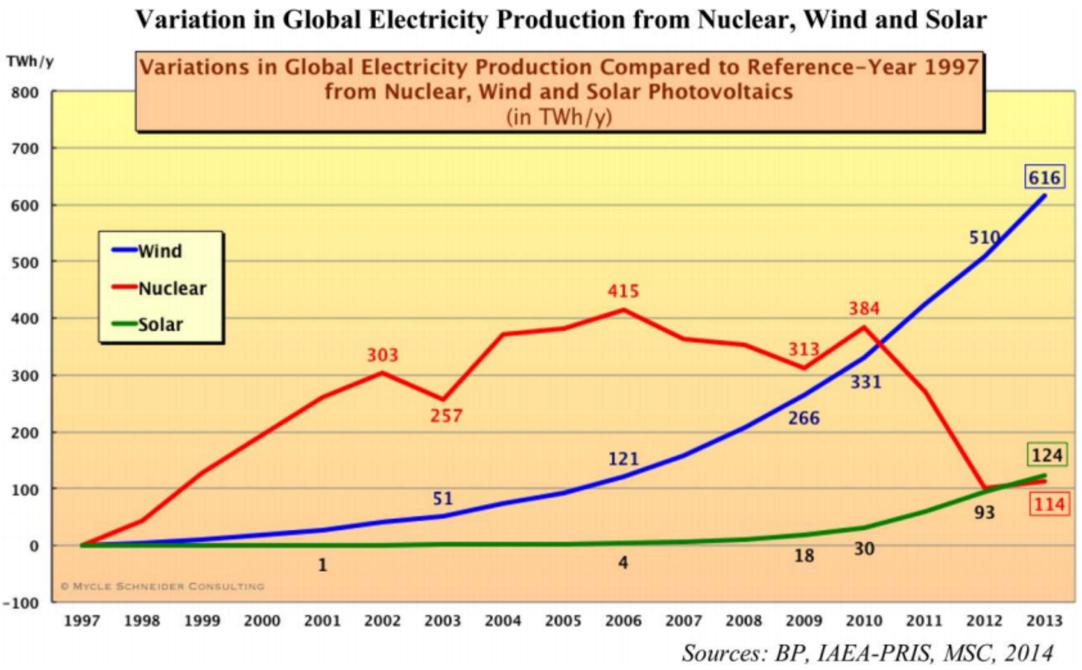

FIGURE 1.6: Evolution of global electricity production from nuclear wind and solar power plants. Image adapted from reference[50].

that significantly impact the environment and the local micro-climate.[59,60] Another example is wind turbines: they are often accused of ruining the natural landscape of large areas, being towers of more than 100m in height.[61]

A general limitation on employing natural phenomena arises from their lack of consistency. This induces a non-constant production of energy that is affected by daily or seasonal regimes. The presence of such time schemes makes management of the overall electricity production difficult and requires a mixture of resources to provide energy in a constant manner.

At this point of discussion it is worth noting that all of the fossil fuels, the movement of huge mass of air and most of the Earth natural phenomena depends on the energy irradiated by the sun. Smill in 2005[62] estimated that the total human mean power consumption per year was 13 TW (18TW in 2015,[49]) while the sun was providing 122 PW dwarfing the human demands. Energy is not equally distributed on Earth's surface and an annual average of sun irradiation is reported in Figure 1.7.

1.2 Photovoltaics

1.2.1 Motivation and background

Among all the alternative sources of energy, in this work we consider the direct exploit of solar energy, through the photovoltaic process, to produce electricity.

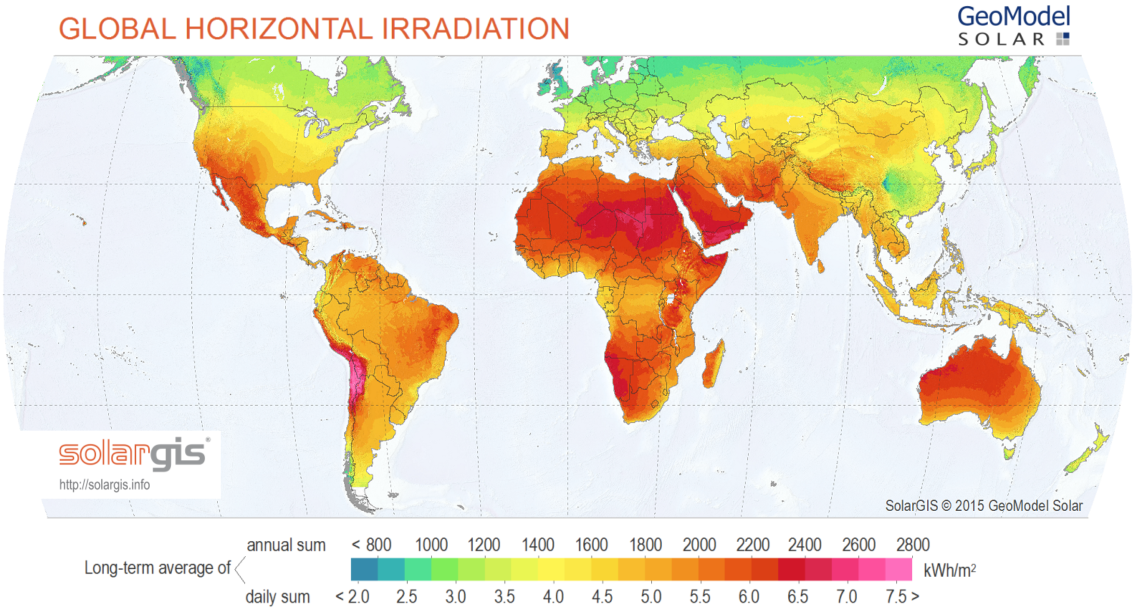

FIGURE 1.7: Annual average of energy irradiated on Earth by the sun. Image taken from reference.[63]

Photovoltaic devices have some critical limitations, but in the last decade they became the fastest growing alternative source of energy.[49] The total annual energy demand by human activity in 2013 equals $157PWh$,[49] equivalent to an annual-mean power usage of 18 TW. The total human supply of energy could be obtained only converting a fraction of the sun's energy that irradiates the Earth's surface. In order for photovoltaics technologies to be competitive economically, some problems must be solved.

The first issue regards the fact that human activity relies mostly on non-electric form of energy, and electricity constitutes of roughly 30% of human energy consumption.[49] A photovoltaic-based energy revolution needs a shift of paradigm toward electrically powered devices to be possible.

The second issue is linked to technical aspects of photovoltaic panels. In particular, due to the daily and seasonal oscillations of solar irradiation, photovoltaics, need to be paired with other sources of energy, or with storage systems.

An indirect consequence of these issues is the need for an electrical infrastructure able to respond to different load of consumption. On this side of the story a positive sign arrived in 2015 when during the total solar eclipse the European production with photovoltaics resisted to the abrupt change in light irradiation without major consequences.[64] The resolution of such problems would make photovoltaic even more competitive, but nowadays photovoltaic is already a valid alternative source of energy. In particular, historically a lack of competitiveness was of economical nature, but the prices have steadily dropped as reported in Figure 1.8.

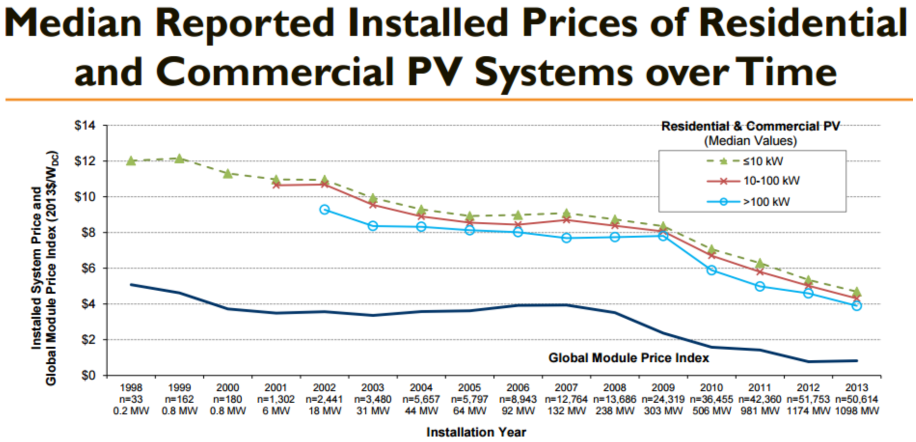

FIGURE 1.8: Electricity price evolution in US for commercial photovoltaic production. Since 1998 every year the price of photovoltaics devices dropped in average of 7 %. In the last year this trend has been dominated by the price of large systems, while the average module price remained constant.Image taken from reference.[65]

1.2.2 Device generations and evolution

The photovoltaic evolution is captured by the National Center for Photovoltaics (NCPV) at the National Renewable Energy Laboratory (NREL). They certified and collect the data for research-cell efficiency that are reported in Figure 1.9.

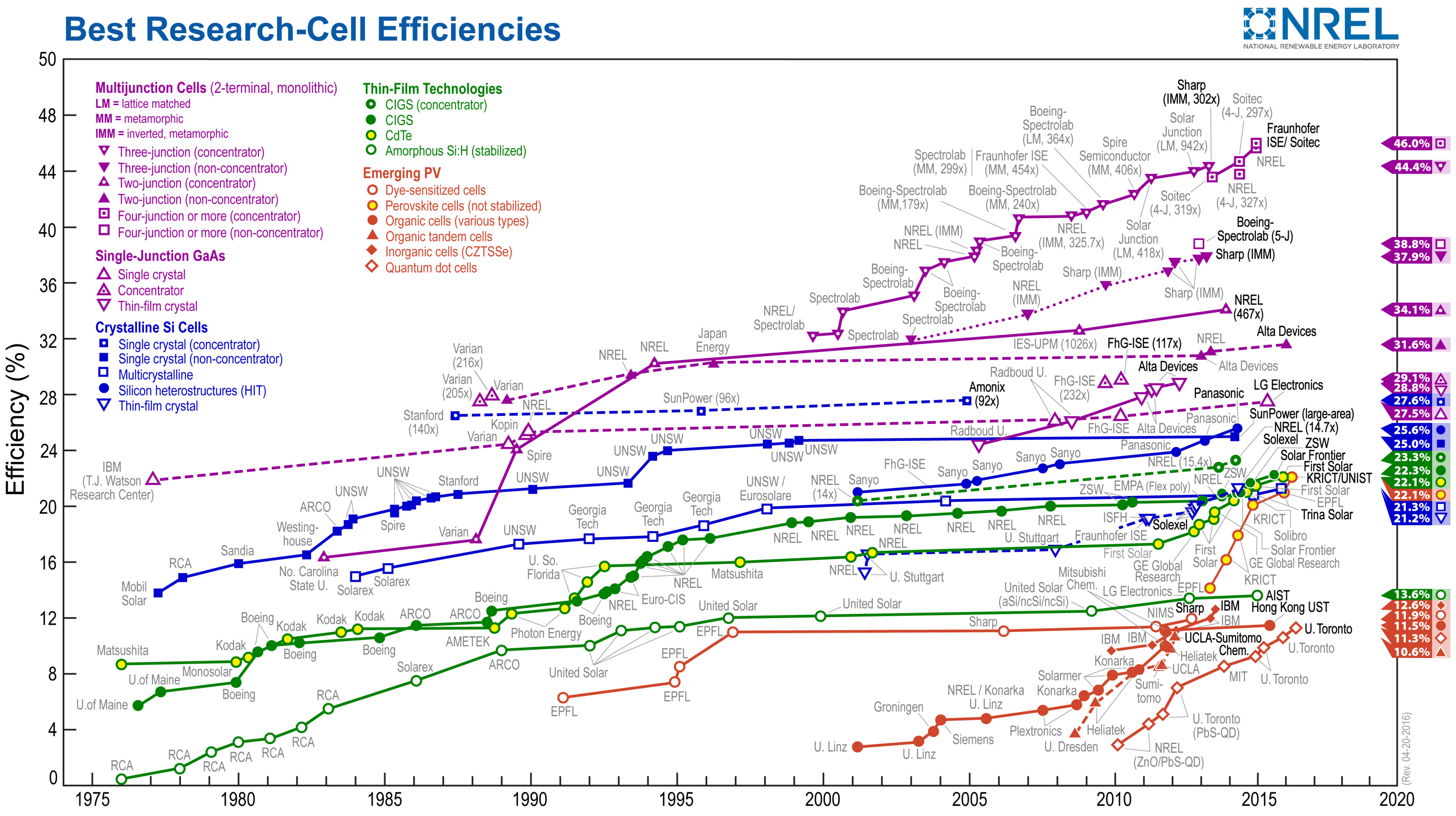

FIGURE 1.9: The figure reports the best research-cell efficiency as June 2016[66]. Perovskite solar cells are indicated on this chart by the red-yellow filled circles with a current record efficiency of 22.1%. Image taken from reference.[66]

Historically the photovoltaic technology are grouped in three main *generations*[67–69] and, in fact, it is possible to divide the cells reported in Figure 1.9 in three main areas. This division reflects the historic evolution of research to develop better technologies and reduce the effective cost of cells.

The term *First-generation* is usually associated with the first solar panels that were based on bulk semiconductors p-n junctions. This class of solar cells occupies the actual high efficiency part of the NREL chart, and are based on silicon or gallium arsenide (GaAs).

Second-generation of photovoltaics panels are based on similar mechanism, but employ thin-film materials. Thin film cells allows easier production, and, in general, a reduction of costs.[70,71] They represent a mature technology, and appear in the contemporary central-upper part of the NREL Chart.

Third-generation solar cells include frontier technologies and exploit molecular or nanostructures properties. The main examples of this cell are the organic bulk-heterojunction solar cell, and the dye sensitized solar cell (DSSC). The former are based on a photoinduced charge transfer between soft materials[72]. The latter are more complex systems where a light harvester is chemiadsorbed on a semiconductor (typically TiO_2).[73] At this interface a charge transfer between the excited state of the molecular light absorber and the conduction band of the semiconductor occurs, which leads to the formation of the photoelectric voltage.

1.3 Physics of solar devices

1.3.1 Electronic levels

Materials can be distinguished according to the shape of their electronic density of states (DOS) that originates from the overlap of electronic orbitals as pictured in Figure 1.10. The main parameter is the energy difference between the conduction band (CB) and the valence band (VB). This band gap represents the minimum energy needed to excite one electron in an excited state, and it determinates the principal optical and electronic properties.

At absolute zero, the electrons occupy only the lowest energy bands and the energy of the highest energy electron is called Fermi energy (E_F). When the temperature is increased some electron are promoted to levels with energy larger than E_F. The probability for an electron to occupy a state with a specific energy at a given temperature is determinate by the Fermi distribution:

$$f_0(E, \mu, T) = \left(e^{\frac{E-\mu}{k_B T}} + 1\right)^{-1} \tag{1.4}$$

The E_F is meaningful only at 0 K, at higher temperature for a system in thermodynamic equilibrium, it is more appropriate to introduce the Fermi Level or

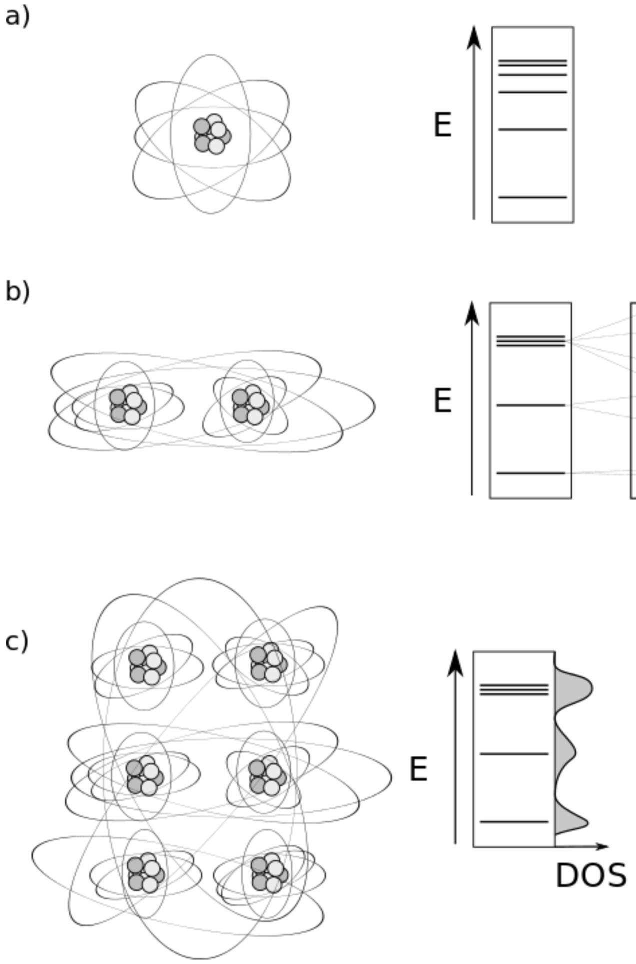

FIGURE 1.10: Panel a) reports an atom with the distribution in energy of the levels, each one can host 2 electrons with different spin. The energy difference is larger for lower energy levels, and decreases going upwards. Panel b) show to atom interacting. Some electronic levels remains on the single atoms, but others interact originating bonding levels. Panel c) show more atom interacting. The level originates from the interaction are very similar in energy, and the system is described through a density of state (DOS) instead of some specific levels.

electrochemical potential, μ. This is an ideal energy level, with occupancy probability of 50%. For an non-doped insulator or a semiconductor at 0 K it lies at the center of the band gap.

In order to move, electrons need to have enough energy to have access to empty states. According to 1.4, if the probability to occupy a state in the CB is negligible at room temperature, the material is an insulator. Otherwise, if the band gap is smaller, electron can be thermally or optical (an optical excitation is due to light absorption) excited and the material is a semiconductor.

Metals do not have a band gap, CB and VB are continuous and form one partially filled band. In this case electrons at higher energy have access to empty state. These electrons are free to move, and their collective motion results in a current when a bias is applied.

1.3.2 Semiconductors

In the previous section when we described the behaviour of an electron promoted from a state to another, we did not consider that the electron leaves behind a vacancy. The presence of an electron in the excited state is connected to the existence of a correspondent vacancy which behaves, by any mean, as virtual particle. This virtual particle is called hole, and it has a behaviour similar to the electron, but with opposite charge. The introduction of holes permits to simplify the description of the collective response of the VB electrons to the promotion of one of them to the CB. This allow to describe the process with the dynamic of a single particle. Because each hole corresponds to an excited electron for an intrinsic semiconductor, their concentration is also determined by equation 1.4.

The concentration of holes and electron controls the behaviour of the material. One method to tune these parameter is the doping, i.e. adding atomic impurities, which results in the introduction of extra states in the band-gap. Doping concentration are of the order of 10^{17} impurities per cm^3, a quantity that interferes enough to change the occupation probability, without significantly alter the electronic structure[74].

Impurities with more electrons than the host material (*n*-doping) introduce filled levels below the CB. The presence of electron with higher energy shifts upwards the Fermi level. This lead to a concentrations of electrons promoted from the impurities levels to the CB larger than the holes in the VB. Upon excitation of electron, in fact, the holes remain trapped in the intra-gap states and can not participate to the conduction.

Analogously when the impurities have less electrons (*p*-doped), they will create empty states in the band gap above the VB, with a resulting lowering of the Fermi level. Electrons are then excited to these levels rather than the CB. The two situations are represented in Figure 1.11.

CB Electrons and VB holes are subject to an attractive Coulombic force, which results in the relaxation of the electron in its starting level with the annihilation of

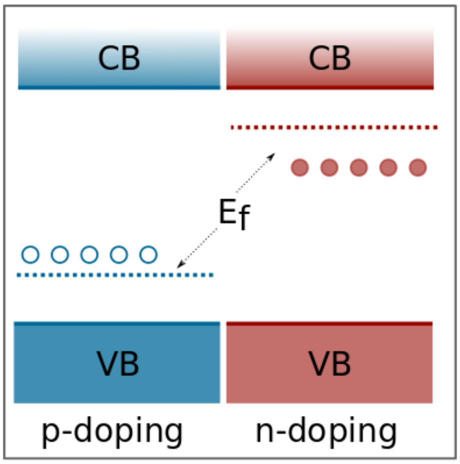

FIGURE 1.11: Schematic of p (left part of the image) and n (right part of the image) doped semiconductors. The p doping induces the inclusion of empty states above the VB with a consequent downshift of the Fermi Level toward the VB. Contrary in the n-doped case the presence of filled stated below the CB shift upwards the Fermi level.

the hole, with a process called recombination. In general, the product of the concentration of holes and electron is constant. This result in a dynamic equilibrium at a certain temperature as regulated by the Fermi distribution.

To generate electricity this equilibrium must be broken with the introduction of a potential that puts the charge in motion, avoiding their recombination. For the scope of photovoltaic this perturbation is achieved by illuminating the material.

1.3.3 p-n junction photovoltaics

We mentioned that the promotion of electron to the CB can be performed by the the thermal excitation, but in most cases this excitation is not enough to promote electrons. For semiconductors with a band gap in the order of 1 eV the electron can also be promoted with visible light whose photons have energy that belongs to the interval 1.5-3 eV corresponding to wavelength of 400-700 nm.

Photons with energy larger than the band gap can scatter with an electron providing enough energy to promote it in the CB.

The promoted electron increases the conductivity of the materials since the CB becomes partially filled similarly to a metal. The same effect happens for holes in the VB. To generate a current it is then necessary to apply a bias. This can be achieved with an external field as in a photodetector, or by an inner driving force. The latter is the case of photovoltaic devices where a driver-force can be created by building an interface between a metal and a semiconductor (Schottky junction) or between two semiconductor with different doping.

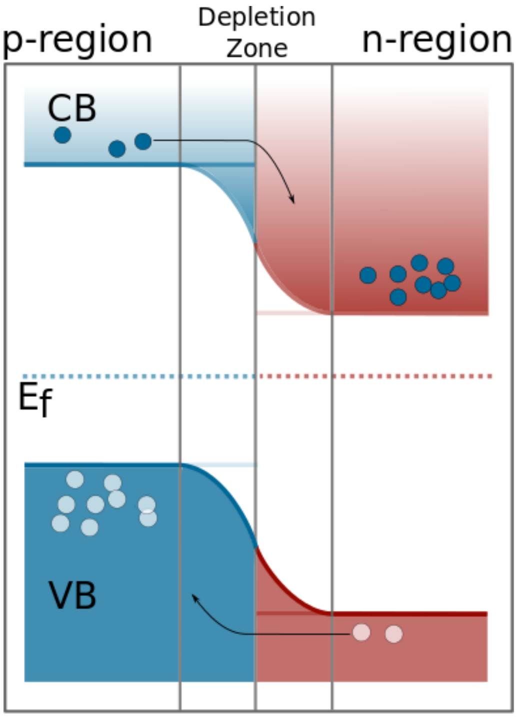

FIGURE 1.12: Schematic of a p-n junction in open circuit condition. At the interface the charges migrate from the n-doped region to the p-doped region. The region where this process happens is called *depletion zone* and the charge diffusion lead to the accumulation of charges on the two sides of the junction that results in the band bending pictured.

If we create a junction between a p-doped and a n-doped semiconductors there will be a mismatch between the Fermi levels of the two materials. Doing so introduces a potential difference that drives the electrons rearrangement with a consequent change in the electrostatic potential.

The presence of a field perturbs the electronic structure. To keep the Fermi level constant through the material a shift of the band energy occurs followed by the bending of the bands in correspondence of the interface in order to remain contiguous. A simplified version of a p-n junction is schemed in Figure 1.12

The bend and the shift of the levels lead to the formation of empty electronic states at a lower energy in the p-type semiconductor and higher energy holes states in the n-type. Therefore it is possible for electrons to diffuse in the p-type part to minimize the energy and analogously the holes diffuse in the opposite direction.

Once the electrons flown in the p-type semiconductor, they recombine with the p-type defect present in the materials, while the opposite process happens in the n-type region. This led to an accumulation of negative and positive charges at the two side of the interface: positive charges in the n-type semiconductor, and negative charges in the p-type. This gives rise to a field that opposes to the charge flow. The equilibrium is reached when the field is large enough to block the flow of the charges. This field extends for few μm across the interface in a zone called *depletion zone* where all the charges are trapped and can not move.

The equilibrium is broken if a photon with energy larger than the band gap will be adsorbed in the depletion zone. In this case one electron is promoted to the CB, leaving an hole behind. In a single semiconductor, after the excitation, the electron and the hole would recombine, but in this case due to the presence of the p-n junction the charges are separated by the interface field and can not recombine.

In an open-circuit condition (the extremes of the cell are not connected) continuous light determinates an accumulation of charges until the interface field is cancelled. This results in a change in the Fermi level at the two sides of the junction. In this case since the system is formally not in equilibrium the level is called quasi-Fermi level rather then Fermi level.

Because the charges accumulated at the two sides have different sign, the levels in the material split. This induces a difference in the potential: the photovoltage, which stands at the base of a working solar cell. Once the two sides of the semiconductor are connected to a circuit (close circuit), the photovoltage set in motion the charges.

This is the general behaviour of a solar cell based on a semiconductor p-n junction. We can highlight three main mechanisms: light absorption, charge separation due to the formation of a photo-bias, and charge conduction.

Most of photovoltaic technologies had been based on semiconductors, until the same mechanisms were mimicked with molecular systems.

1.4 Dye sensitized solar cells

The electronic bands are the result of the overlap of atomic orbitals which extend in the whole crystalline system. This statement does not hold in molecular system: the overlap is localised on a single molecule. Intermolecular conduction is more difficult to achieve and electrons *hop* between molecules rather than diffuse in the material.

Even though the *hopping* process is more difficult than diffusing, it is possible to build a photovoltaic devices exploiting molecular levels. The most representative examples are the Dye Sensitised Solar Cells (DSSC) and the bulk hetero-junction organic solar cells.

1.4.1 Structure of DSSC

We focus here on the DSSC. They have been firstly developed in the ’70s with the work of Fujishima[75] but they became popular in the early ’90s with the work of Grätzel and O’Reagan[73]. The first cell they developed achieved an efficiency of about 7% and started a whole area of research, with thousands of publications as shown in Figure 1.13, making Grätzel one of the most cited living scientist.

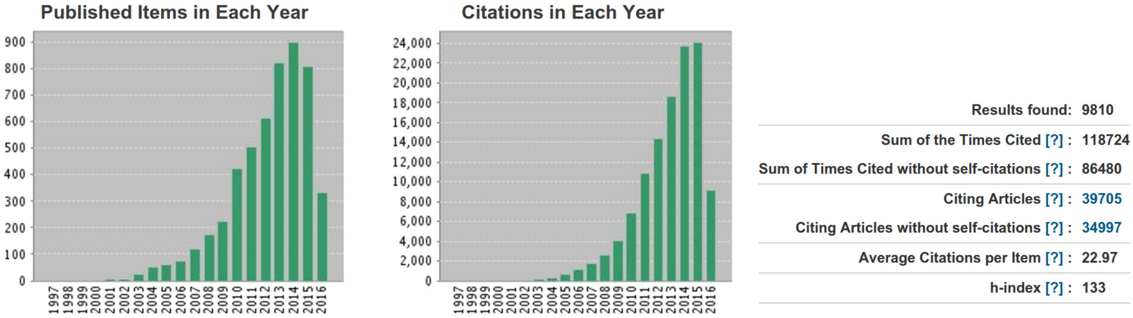

Results found: 9810
Sum of the Times Cited [?] : 118724
Sum of Times Cited without self-citations [?] : 86480
Citing Articles [?] : 39705
Citing Articles without self-citations [?] : 34997
Average Citations per Item [?] : 22.97
h-index [?] : 133

FIGURE 1.13: Citation report for the keyword "DSSC" according to Thomson-Reuters Web of Knowledge. Updated to June 2016.

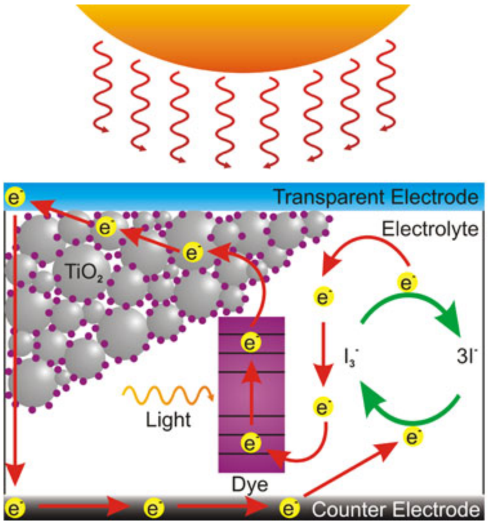

FIGURE 1.14: Working mechanism of DSSC. The light is absorbed by the dye that lead to electron-hole separation. The electron is then injected in the TiO_2 layer and enters the electronic circuit while the hole left in the dye is reduced by the electrolyte. Picture taken from reference.[76]

In DSSC the light collection, the charges separation and transport instead of happening in a semiconductor p-n junction, are performed by three different materials as pictured in Figure 1.14.

The setup and the concept behind DSSC is simple. The main part of the device is composed by molecules (the dyes) chemi-adsorbed on a porous semiconductor. This semiconductor is then immersed in an electrolyte that permit to close the circuit.

The semiconductor is usually a nanostructured mesoporous layer of TiO_2. The morphology of the mesoporous phase has a critical role since its large surface allows to maximise the amount of dye adsorbed. From an electronic point of view titanium dioxide has a large band gap (in the domain of UV spectra) that reduces the recombination between the holes and the electrons leading to a good charge conductivity. Another appealing aspect in the use of titanium dioxide is that it is easy to process and environmentally friendly. On the other side if exposed to UV radiation, it behaves as a catalyst and promotes the photodegradation of the cell.

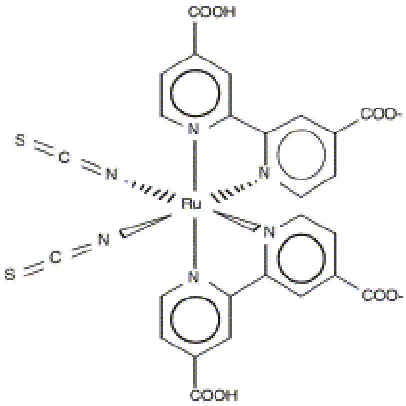

FIGURE 1.15: N3 molecule. This dye is commercially available and known as *black dye*.

For this reason the cells are often coated with anti-UV filter.

The dye is a crucial component of the cell and determinates the amount of light collected by the device. This high absorbance yield is due to the presence of *d*-metals (usually ruthenium[77]) whose levels are responsible for light absorption. Different dyes can be used to control which part of the solar spectra is adsorbed. The most common metallorganic complex are commercially available. Some of these compounds are the N719, Z907 or N3[78,79] whose structure is reported as example in Figure 1.15.

The dyes are very expensive (in the order of thousand pounds per gram)[80], but their impact on the final price is mitigated by the small quantity required. The cell is then completed by an electrolyte that closes the circuit. The most used electrolyte is a ionic liquid that contains the redox couple $I_3^-/_3I^-$. This solution is efficient from an electronic point of view but presented stability issues. The ionic liquid in fact is corrosive, and exposes the cell to the risk of leakage. To improve this aspect new generations of DSSC employ solid state conductor such as spiro-MeOTAD.

1.4.2 Working mechanism

Under operation the light is absorbed by the dye. When a photon is absorbed an electron is promoted from highest occupied molecular level (HOMO) of the molecule to the excited state which is the lowest unoccupied molecular orbital (LUMO). After this excitation the electron is transferred to the conduction band of the semiconductor leaving back an oxidized dye that is reduced by the electrolyte. The semiconductor is connected to the anode. If the circuit is in open condition the electrons generate an electromotive force, once the circuit is closed the electron can reach the cathode generating a current flow.

At the cathode the electrons restore the electrolyte, completing the chain of electrochemical processes. The schematic processes behind DSSC are rather simple, but are difficult to be properly designed. A correct alignment of the electronic levels is not enough if the processes are not kinetically favourable. To explain this requirement we can consider the charge injection in the semiconductor. Because the energy difference between the levels is small, to maximise the probability of injection, thermal excitation is large enough to allow a small probability for the opposite process to happen. If this is the case, the electron can then reduce the dye lowering the over all efficiency of the cell.

To control the kinetic of the processes and the chemical instability it is necessary to introduce blocking layer or to improve the design. This usually improves the stability of the cell, but reduces the total output.

1.4.3 Improving the stability

First DSSCs performed worse than commercial silicon panels in term of efficiency, but they were cheaper, and could be used on flexible and *wearable* substrates. The main limit was their short term stability due to the presence of the liquid electrolyte, which suffered from leakage, and induce corrosion. To overcome this limit most research concentrated on improving solid-state electrolyte beyond the liquid electrolyte. A suitable electrolyte would be a *p*-type semiconductor or a polymer that would behave as an hole transport materials.[78]

Switching from a liquid electrolyte to a solid state conductor requires to solve different problems. Besides being a good charge conductor, the electrolyte has to be transparent and offer a good adhesion with the semiconductor.

The first solid cells appeared few years after the initial cells of Grätzel , but they often did not improve the efficiency of the cells. Most of these devices where base on copper compounds as CuSCN and CuI or organic polymers as OMeTAD. Employing solid state hole transport materials (HTM) had not suddenly improved the efficiency of the materials but allowed to easily replace the organo-metallic dye with quantum dots, or compact films. From this type of approach originates the first hybrid perovskite based solar cells that in a few years substituted the DSSC as the main studied type of third generation solar cell.

1.5 Perovskites

1.5.1 Introduction

Perovskite is the proper name of $CaTiO_3$ mineral identified for the first time by Gustav Rose in 1839,[81,82] who named it after Russian mineralogist Aleksevich von Perovski. Different materials have perovskite or perovskite-related structure and it became an umbrella term to generally indicate crystals with such structure. Perovskites have been intensively studied over time due to the richness of their behaviour. The structure, as we will explain, is favourable to the appearance of different phenomena that go beyond mere scientific interest and have different

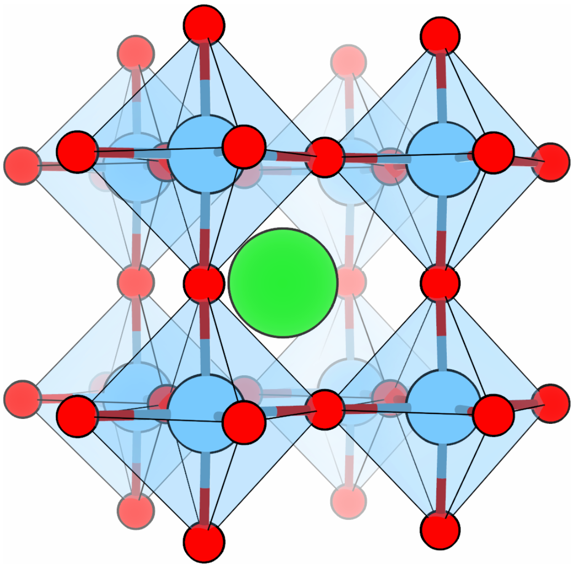

FIGURE 1.16: Structure of archetypical inorganic perovskite. This structure belongs to the space group $Pm\bar{3}m$ (n. 221). In the image is highlighted the octahedra coordination of metallic ions.

technological applications. Piezoelectricity, controllable magnetism, magnetoresistivity, tunable conducibility are, among others, some of the properties found in perovskites that permitted the realisation of different devices.

These properties have been exploited in different cases as the AFTMSTM microscopes where the position and the deformation of the cantilever/tip is controlled with piezoelectric materials[83] or non-volatile memories resistant to radiation.[84] Perovskites as $BaSnO_3$ and $SrTiO_3$ have been employed to build different type of sensors to detect humidity, temperature, gasses, or pressure.[85–88]

The perovskite structure has been found mostly in oxide, but it is possible to find it in different type of ternary compounds, such as halides, or in more complex structures where one or more ions are substituted by molecular cations or ligands. The best example of the first case are the so called hybrid halide perovskites, the main topic of this thesis, the latter are represented by polyanionic perovskites or metallo-organic frameworks with perovskite motif.

1.5.2 Ideal and non-ideal structure

Perovskites crystals have general stoichiometry ABX_3. The atoms are arranged in a cubic lattice with symmetry $Pm\bar{3}m$ (221) and the atomic positions are reported in table 1.1.[1] A picture of an archetypical structure is shown in Figure 1.16.

The crystal is formed by a network of corner sharing BX_6 octahedra that form a cubooctahedra cavity that host the central A cation.

---

[1] The dot indicate oriented site symmetry and it substitutes the symmetry inactive operators[89,90]

TABLE 1.1: Cubic perovskites positions expressed in Wyckoff notation.

Atom	Coordination	Wyckoff notation			Coordinates
		Site	Multiplicity	Site-symmetry	
A	12	a	1	$m\bar{3}m$	(0.0, 0.0, 0.0)
B	6	b	1	$m\bar{3}m$	(1/2, 1/2, 1/2)
X	2	c	3	4/mm.m	(1/2, 1/2, 0.0)

The term perovskite should be used only to name cubic structures, but we can extend the term to denote similar (homotypic)[91] structures which are obtained from the ideal structure via small distortion of bond lengths and angles. Practically this include all ABX_3 structures derived by distortions that keep the topology unaltered: same ion coordination and a corner-sharing octahedra network. These distortion can affect the lattice, hence we can further classify the perovskite according to the lattice shape which can be cubic ($a = b = c$), tetragonal ($a = b \neq c$) or orthorhombic ($a \neq b \neq c$) allowing small deviations ($< 5°$) on the angles.

The stability of a perovskite phase is strictly related to the size of the ions involved. Goldschmidt did the first attempt to rationalize this concept introducing the tolerance factor (*t*-factor) still in use nowadays:

$$t = \frac{R_A + R_X}{\sqrt{2}(R_B + R_X)} \tag{1.5}$$

where R_A and R_B are the radii of the cations and R_X of the anions. He also found that most ternary compound has a stable cubic perovskite structure if *t* falls in the interval ≈[0.9-1.0]. These observations can be extended saying that orthorhombic or tetragonal phases are found for values of t between $\approx [0.7 - 0.9]$. Li *et al.*[92,93] observed that a proper *t-factor* is a necessary, but not sufficient, requirement to obtain a perovskite structure. For this reason they introduced an octahedral factor (μ-factor):

$$\mu = \frac{R_B}{R_X} \tag{1.6}$$

In their work they consider 223 ternary oxides, and 186 halide systems, they showed that oxide perovskite have a stable cubic perovskite structure if the t-factor falls in the interval $[0.74 - 1.0]$ and μ in $[0.414 - 0.732]$ with the only exception of $CaCeO_3$. For halide perovskites they found an analogous trend with 96% of the structure having a *t-parameter* between [0.813-1.107] and μ-factor between [0.442-0.895].

The role of μ-factor reflects the importance of the octahedral environment present in the structure.

One important feature of perovskite regards the tilting of the octahedra on different planes. If a cell is expanded in one direction it is possible to tilt octahedra perpendicular to it. In 1972 and sequentially in 1975 Glazer[94,95] enumerated all

TABLE 1.2: Perovskite classification due to octahedra tilting.[95]

System number	Glazer tilting	Lattice centering	Supercell	Lattice vectors	Space group	Number
3 Tilts						
1	$a^+b^+c^+$	I	222	$a \neq b \neq c$	$Immm$	(71)
2	a^+b^+b+	I	222	$a \neq b = c$	$Immm$	(71)
3	$a^+a^+a^+$	I	222	$a = b = c$	$Im3$	(204)
4	$a^+b^+c^-$	P	222	$a \neq b \neq c$	$Pmmn$	(59)
5	$a^+a^+c^-$	P	222	$a = b \neq c$	$Pmmn$	(59)
6	$a^+b^+b^-$	P	222	$a \neq b = c$	$Pmmn$	(59)
7	$a^+a^+a^-$	P	222	$a = b = c$	$Pmmn$	(59)
8	$a^+b^-c^-$	A	222	$a \neq b \neq c, \alpha \neq 90°$	$A2_1/m11$	(11)
9	$a^+a^-c^-$	A	222	$a = b \neq c, \alpha \neq 90°$	$A2_1/m11$	(11)
10	$a^+b^-b^-$	A	222	$a \neq b = c, \alpha \neq 90°$	$Pmnb$	(62)
11	$a^+a^-a^-$	A	222	$a = b = c, \alpha \neq 90°$	$Pmnb$	(62)
12	$a^-b^-c^-$	F	222	$a \neq b \neq c, \alpha \neq \beta \neq \gamma \neq 90°$	$F\bar{1}$	(2)
13	$a^-b^-b^-$	F	222	$a \neq b = c, \alpha \neq \beta \neq \gamma \neq 90°$	$I2/a$	(15)
14	$a^-a^-a^-$	F	222	$a = b = c, \alpha = \beta = \gamma \neq 90°$	$R\bar{3}c$	(167)
2 Tilts						
15	$a^0b^+c^+$	I	222	$a < b \neq c$	$Immm$	(71)
16	$a^0b^+b^+$	I	222	$a < b = c$	$I4/mmm$	(139)
17	$a^0b^+c^-$	B	222	$a < b \neq c$	$Bmmb$	(63)
18	$a^0b^+b^-$	B	222	$a < b = c$	$Bmmb$	(63)
19	$a^0b^-c^-$	F	222	$a < b \neq c\,, \alpha \neq 90°$	$F2/m11$	(12)
20	$a^0b^-b^-$	F	222	$a < b = c\,, \alpha \neq 90°$	$Imcm$	(74)
1 Tilts						
21	$a^0a^0c^+$	C	221	$a = b < c$	$C4/mmb$	(127)
22	$a^0a^0c^-$	F	222	$a = b < c$	$F4/mmc$	(140)
0 tilt						
23	$a^0a^0a^-$	P	111	$a = b = c$	$Pm\bar{3}m$	(221)

the possible perovskite structures that are obtainable from a perfect ideal cubic structure (aristotype) via a set of rigid tilts of octahedra. To perform this he introduced a nomenclature to distinguish the tilting that can occur along the three different crystallographic axis. For each axis the tilting is represented by a letter (a,b,c) with a superscript (+,-,0). If the tilting in consecutive directions has the same magnitude it is labelled by the same letter. The superscript 0 indicates that no tilting occurs in that direction, while + and - specify if the tilting on consecutive planes proceed in the same direction or not.

The perfect cubic structure has tilting $a^0a^0a^0$, and all the other possibilities are reported in Table 1.2.

The tilting of octahedra are rigid deformations of the structure, and are due to *coordinated* displacements. It is also possible to introduce independent atomic displacement that distort the octahedra or the positions of other ions. This type of displacements further lower the symmetry of the cell and cause most of the interesting electronic and magnetic properties of perovskites. For example in the proper perovskite $CaTiO_3$ two different phase are present: one with a cubic $Pm\bar{3}m$ symmetry, and a distorted one where the Ti at the center of TiO_6^+ octahedra is displaced along a crystallographic direction. This displacement breaks the inversion symmetry of the system and generate an overall neat electronic displacement that gives rise to a polarization moment. The displacement can be induced in different ways, for example applying a pressure as in piezoelectric devices.

1.5.3 Alternative stoichiometry and hybrid perovskite

In the previous paragraph we analysed the behaviour of the perovskite with the variation of the atomic positions. The structure can be influenced by the composition, and stoichiometry is another variable to consider in order to tune and control perovskite chemical-physical properties.

There are different possibilities to achieve charge-neutral perovskite material with general composition ABX_3. The largest and most studied class of perovskite is the oxide. In this case to balance the formal six negative charges of the oxygens the A and B ions could belong to the I and V group ($LiNbO_3$) or the II and the IV ($CaTiO_3$), respectively, or both at the III ($LaAlO_3$).

Another important class of perovskites is the halides, where the anion belongs to the VIIA (17) group of the periodic table. In this case the cation oxidation states have to sum up to -3, which allows only the I-II combination ($CsPbI_3$).

Beyond oxide and halides other perovskitic structure are found in hydrides as CsCaH and RbMgH[96] or in compounds as carbides $MgCNI_3$.[97]

The perovskite or perovskite-derived structure is also found in non-ternary and defective materials. The most famous example is given by the family of superconductor cuprate or borides as Li_2Pd_3B[98] and $LnRh_3B$.[99]

This class of compound are often descried as double perovskites if the material presents ordered structure of alternating cations, or inverted perovskites where the A and X site are swapped, as in the previous cited example of $LnRh_3B$.

In the previously presented examples, the crystal sites have been occupied by single ions, but it is possible to substitute the atomic ions with small molecular species.

Example of these compounds are the polyanionin perovskites where molecular fragments form a hollow structure with cubic symmetry that host a cation. Recently much attention was given to the material subject of this thesis, the so-called hybrid perovskite where the A-site is occupied by small organic molecules.

TABLE 1.3: Ionic radii of different perovskite and relative μ and t-factor parameters for different assumed values of methylammonium (MA) radii. 156 pm refers to half the length of the molecule, while 145 pm is the geometric average of cylinder in which MA could be inscribed.

Element	Radii[100] [pm]		
Cl	181		
Br	196		
I	220		
Pb	119		
Compound	$R_{MA} =$	156 pm	145 pm
	μ	t	t
$MAPbCl_3$	0.66	0.79	0.77
$MAPbBr_3$	0.60	0.79	0.76
$MAPbI_3$	0.54	0.78	0.76

1.6 Hybrid perovskites

1.6.1 Introduction

The term hybrid perovskite has been employed to describe perovskite structure where the octahedral network was composed by an inorganic compound, while the central A cation is a small organic molecule, usually an amine. In literature this class of compounds can be also named metallo-organic perovskite, with the correspondent IUPAC name R-ammonium metal halide. We will stick with the term hybrid perovskite since it is affirmed and it is quite concise and precise at the same time. In general the term hybrid will indicate the presence of organic and inorganic components.

The general chemical formula for these compound is RMX_3. The most studied organic groups R at the center of the cage are methylammonium ($MA{:}CH_3{-}N^{+}H_3$) and formamidinium ($FA{:}H_3N{-}CH{-}N^{+}H_3$). The most common metals in the B-site are Pb and Sn, but other compounds with isovalent metals have been reported. The anion is a halide chosen between Cl, Br, I.

Previously we explained that it is possible to forecast the presence of a perovskite phase observing the value of the t-factor and μ. Those values are derived from a hard spheres model, and it is not directly applicable to the MA cation. We adapted the model assuming two different parameters, one is half the length of the molecule (156 pm) and the other, slightly smaller, is the geometric average of the cylinder dimensions where the molecule can be inscribed (146 pm). The final values of t-factors are not significantly affected. Table 1.3 reports the example values of t and μ parameters for different $MAPbX_3$ materials.

The parameter found, as observed and previously reported,[101] even with some approximation lays in the range for perovskite structure, but are quite far from being ideal. The presence of the molecule breaks the symmetry of the crystal and it induces different distortions. Besides the molecules are not held fixed in some position and orientational disorder increases with temperature.

1.6.2 Development of hybrid perovskite photovoltaic

The history of hybrid perovskite spans over a century, but they became one topic material since employed in photovoltaic from 2012. The last years of development have been intense with counter-intuitive results and contradictory reports. Hereby we report a brief overview of the perovskite development milestones.

The first type of hybrid perovskite has been reported at the beginning of the century and, an initial characterization is reported in literature.[102] The materials have been almost entirely ignored for decades, with some few exceptions.[102–107]

Mitzi et al. investigated hybrid perovskites for their semiconductor properties and employed them in LED and electronic devices. Other consequent studies arrived in 1990s when Onada *et al.*[108,109] performed a thermodynamic analysis of the material suggesting some structural phases for $MAPbX_3$.

Applications in the photovoltaic area emerged from the contribution of the DSSC. One major area of research in this field was the assembly of a full solid state device to eliminate the leakage due to the liquid electrolyte. This involved the development of new hole transport materials and new *dyes* that were compatible to build a solar cell. The first cell substituted the liquid electrolyte with spiro-OMeTAD, but the efficiency was still lower than correspondent standard solid state devices.

Evolution of solid state cells included quantum-dots as sensitizer. Due to quantum confinement effects there is an absorption enhancement of radiation in the visible part of electromagnetic spectra.

The first reported hybrid perovskite based solar cell occurred in 2009[110] when quantum dots of $MAPbI_3$ and $MAPbBr_3$ have been deposited on a mesoporous titanium layer. The efficiency of these cells was as low as below 4%, but the photovoltage of 0.96 V was encouraging. Similar cells have been built with Sb_2S_3 quantum dots, but the efficiency was not significant.

In the following years hybrid perovskites have been the subject for structural and optical studies,[111] interface materials for solar cells,[112] and tunable semiconductors.[113] The second attempt to employ $MAPbI_3$ quantum-dots-sensitized solar cell, lead to an improvement in the photovoltaic conversion up to 6.54%.[114] After this work different research groups employed hybrid perovskite or analogous materials in solar cell with different architectures.[115–122] This large interest was justified for the possibility of developing new all-solid-state solar cells to improve the DSSC whose instability was mainly due to the presence of the liquid electrolyte.

The first wave of research was mostly devices-driven with new record of efficiencies obtained almost at each new use of the material. This great succes was possible because the design of hybrid perovskite solar cells took over the DSSC techniques and expertises developed in the last decades.

The turning point in the field occurred with the work performed in Snaith's group who reached a power conversion efficiency of 10.9%.[119] The particularity of this achievement consisted in the presence of an aluminium dioxide (Al_2O_3) scaffolding on top of which the perovskite had been deposited. This work is particularly significant because until then all the previous devices were based on the assumption that the mechanism behind the cell was similar to the one observed in DSSC: the perovskite was considered responsible of electron-hole couple generation upon light absorption, followed by the injection of the electron in the titanium oxide layer.

If TiO_2 is substituted with Al_2O_3 there is a misalignment of the energy levels between the hybrid material and the semiconductor, and the charge injection would not be possible if based on the DSSC mechanism. This demonstrated that such cells work, or can work, with a mechanism substantially different from a DSSC and the perovskite being able to generate the electron-hole couple and also transport it.

This discovery multiplied the possibilities for the employment of perovskite in solar cells. In particular the research is including other possible architectures, mesoscopic semiconductor solar cells, thin film solar cells and p-n heterojunction cells. A panorama of current technologies and future developments in solar cells covering from DSSC to different architectures employing hybrid perovskites, was presented by Snaith[123] and it is reported in Figure 1.17.

The highest performing solar cells use a mesoscopic the architecture and a mixture of different halide in their composition. Even if efficiency has improved incredibly in the last 3 years, and the field was overpopulated with publications, a clear, comprehensive understand of the behaviour of the material is not present.

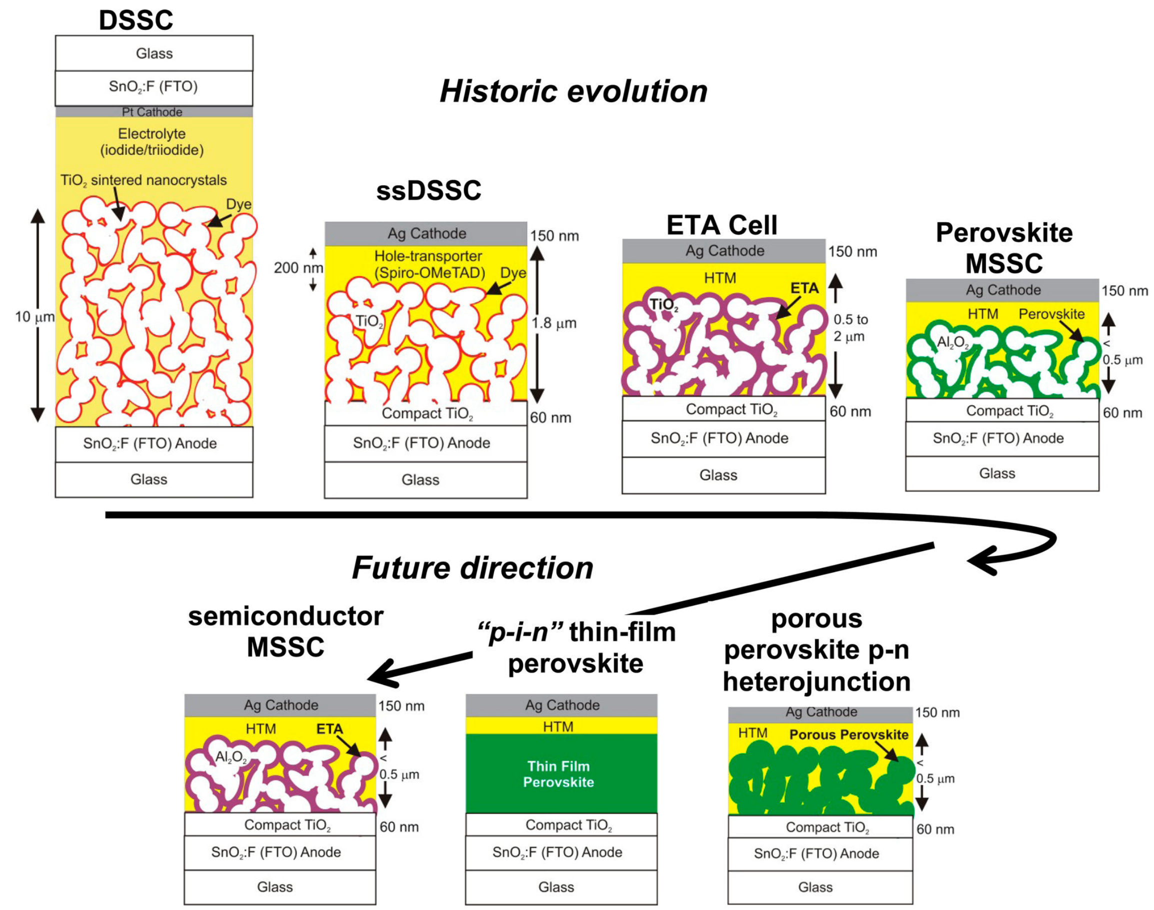

FIGURE 1.17: Schematic of the evolution from DSSC toward different design of hybrid perovskite solar cells. The first row reports in order the evolution from regular DSSC to mesoporous perovskite solar cells. The cartoons reports: DSSC with liquid electrolyte, solid state DSSC, extremely thin adsorber (ETA) solar cell, and mesoporous solar cell, where the perovskite is adsorbed on a alumina scaffolding. The second row reports future development at the time. From left to right: semiconductor mesoporous solar cells, "p-i-n" solar cell (a p-n junction with an insulator layer at the interface, and porous perovskite heterojunction. Image taken from reference.[123]

Chapter 2

Methodology

2.1 Computational materials science

2.1.1 A quick historical overview

The evolution of sciences historically proceeded on two distinct levels: a theoretical and a practical (experimental). Until the 19^{th} century the scientific community focused mainly the description of natural phenomena. Those investigations lead to the development of theories that were able to explain most of the observations. Nonetheless some small exceptions were present and remained unexplained as the ultraviolet catastrophe, or the photoelectric effect[124].

With the aim of solving these and other problems, by the beginning of the 20^{th} century, new theories had been developed to explain such phenomena and, the boundary of the unknown had been pushed forward. Theory predicted phenomena never observed before and the curiosity pushed experimentalist to build new, intriguing experiments, rather than just observe what nature offered. This spirit put the basis for the space exploration or the building of high energies facilities, as the CERN.

The new quantum mechanical theories required intense efforts, from a mathematical point of view, and the application remains constrained to some small simple cases until the second half of the 20^{th} century.

2.1.2 Computational science

The introduction of computers and calculators that arose from the work of Alan Turing quantitatively changed the paradigm of science. The exponential increase of calculation power, reported in Figure 2.1, allowed scientists to actually calculate predictions of different theories, which results could be applied to systems beyond small test-cases. Computers sciences facilitated the development of engineering technique and, more broadly, science. One example of this is the graph represented in Figure 2.2 where the development of computational methods in quantum chemistry are reported. The computational approach to problems grew in popularity to the point to be recognized by the whole community. For example,

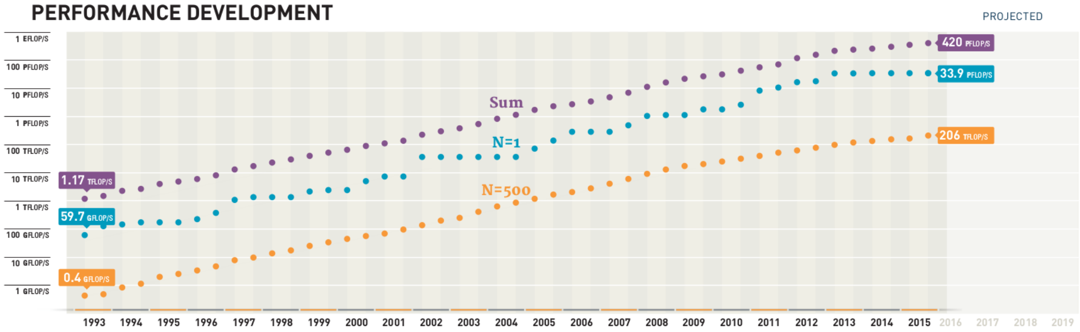

FIGURE 2.1: Time evolution of world top 500 supercomputers updated to November 2015. The purple line report the sum of the calculation power of the top 500 computers; the blue line report the evolution of the most efficient machine; the orange line reports the average of the top 500 computers. We can notice that since 1993 the Moore law has been respected and for all three samples the computational power grew exponentially. Data available at top500.org.[125]

the Nobel Prize in Chemistry of 2013 was assigned to Martin Karplus, Michael Levitt and Arieh Warshel *for the development of multi-scale models for complex chemical systems*[126]. Even if there are times that computational scientists are defined as theoreticians, the possibility to predict experimental results on some theoretical basis is something different that could be described as a *meta-experiment*. In fact, computational sciences are a precious tool that can be used to both test the reliability of a theory or to suggest original experiments, rather than develop a new theoretical framework.

One area where computer science grew intensively and became fundamental was the field of solid state. Science computers allowed the possibility to actually perform calculations for quantum physics predictions and helped the development of methods to investigate the basic electronic and atomic properties of matter.

2.1.3 Schrödinger equation

In 1926 Edwin Schrödinger changed the paradigm behind the behaviour of Nature. He continued the studies about the wave-nature of particles and proposed to describe them with the same methodology used to describe mechanical waves. He defined what it is nowadays called the Schrödinger equation; it allows to follow the temporal evolution of a quantum particle as a wave, and in its more general form, it can be written as:

$$i\hbar\frac{\partial}{\partial t}\Psi = \hat{H}\Psi \tag{2.1}$$

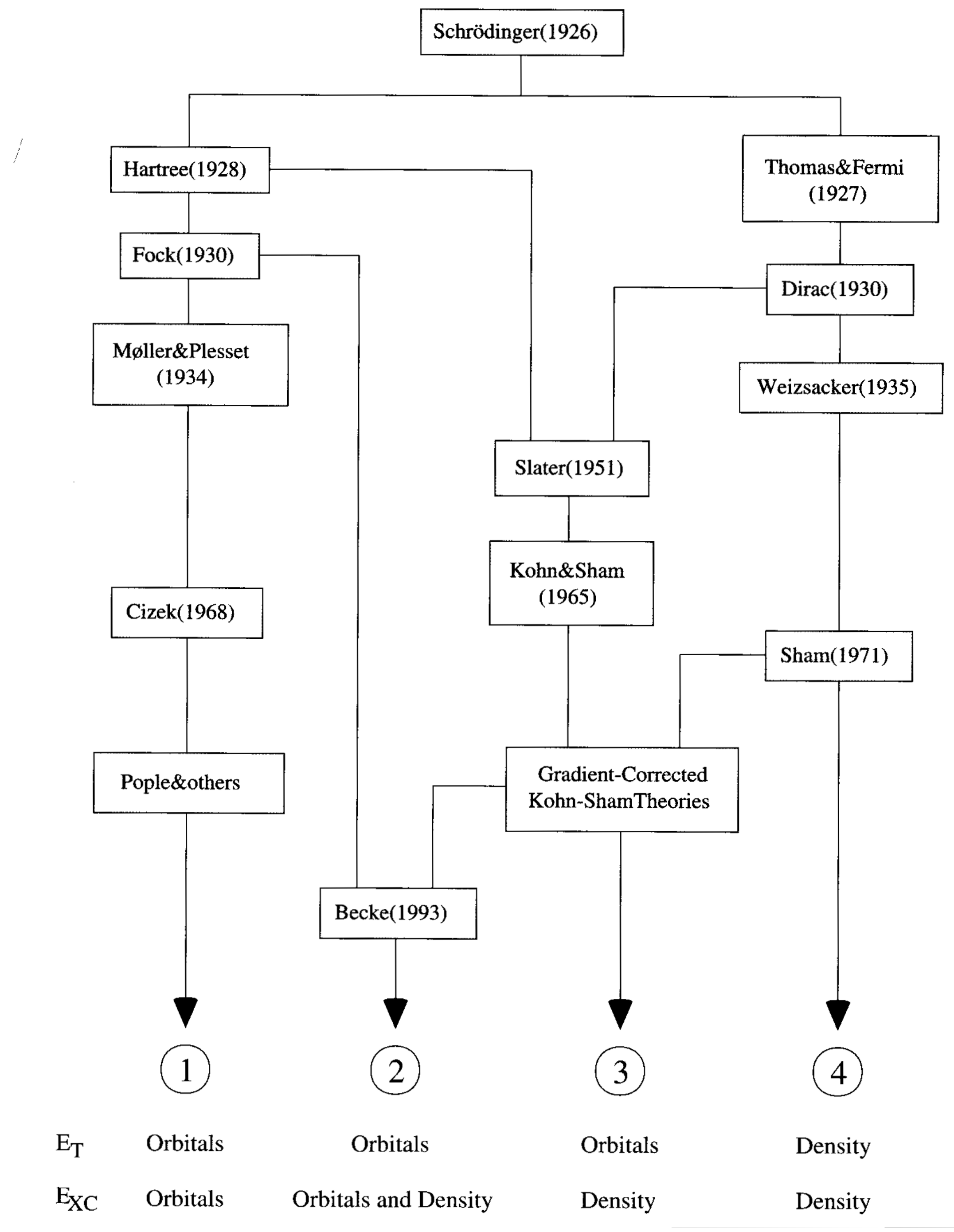

FIGURE 2.2: Graph rappresenting the evolution of method in quantum chemistry. The image is taken form a publication of P. Gill.[127]

where $\hbar$ is the reduced Planck constant, $\Psi(\mathbf{r})$ the system wave-function and $\hat{H}$ the Hamiltonian operator whose spectrum[1] is the set of values that the energy of a system can assume. The solutions of the equations are called *states* since they describe a particular state of the studied system. If the electrons occupy all the lowest energy orbitals, the system is described as being in its ground-state.

It is important to underline that the previous equation describe a very general case and does not impose any constriction on the system studied.

The focus in solid-state physics and quantum chemistry, in general, is the steady-state of atomic (or molecular) systems, then it is more common to refer to the time-independent version of the equation:

$$\hat{H}\Psi = E\Psi \tag{2.2}$$

The Hamiltonian is then written in the form:

$$H = \left[\frac{-\hbar^2}{2m}\nabla^2 + V(\mathbf{r})\right] \tag{2.3}$$

In general a Hamiltonian is composed by two parts: the kinetic energy and the potential energy. If an atomic system of interest is composed of M nuclei and N electrons, the explicit form of the Hamiltonian is the following:

$$\hat{H} = -\frac{\hbar^2}{2m}\sum_{i=1}^{N}\nabla_i^2 - \frac{\hbar^2}{2}\sum_{\alpha=1}^{M}\frac{\nabla_\alpha^2}{M_\alpha} - \sum_{\substack{\alpha=1\\ i=1}}^{M,N}\frac{Z_\alpha e^2}{|\mathbf{r}_{\alpha i}|} + \sum_{\substack{i=1\\ j<i}}^{N,N}\frac{e^2}{|\mathbf{r}_{ij}|} + \sum_{\substack{\alpha=1\\ \beta<\alpha}}^{M,M}\frac{Z_\alpha Z_\beta e^2}{\mathbf{R}_{\alpha\beta}} \tag{2.4}$$

The $\mathbf{R}$ stands for the nuclear coordinates, while $\mathbf{r}$ for electronic. $\mathbf{R}_{\alpha\beta}$ is short notation for $|\mathbf{R}_\alpha - \mathbf{R}_\beta|$ and analogously $\mathbf{R}_{i\alpha}$ stands for $|\mathbf{r}_i - \mathbf{R}_\alpha|$. Each term contributes to the energy and it is possible to simplify the equation as a function of the electronic ($\mathbf{r}$) and atomic positions ($\mathbf{R}$):

$$\hat{H}(\mathbf{r},\mathbf{R}) = \hat{T}_e(\mathbf{r},\mathbf{R}) + \hat{T}_N(\mathbf{r},\mathbf{R}) + \hat{V}_{e-N}(\mathbf{r},\mathbf{R}) + \hat{V}_{e-e}(\mathbf{r},\mathbf{R}) + \hat{V}_{N-N}(\mathbf{r},\mathbf{R}) \tag{2.5}$$

The first two terms represent the kinetic energy of electron and nuclei. The last three terms are the potentials that describe the interactions between the objects considered: electrons and nuclei, electrons and electrons and nuclei with nuclei, respectively. Equation 2.4 can be solved exactly (in the relativistic limit) only for the hydrogen atom. In all other systems, approximations are necessary.

2.1.4 Born-Oppenheimer approximation

The solution of the Schrödinger equation is the set of all possible states of the analysed system. In the discussed case the solution depends on two variables:

---

[1] An operator is a particular linear transformation that acts on functional spaces. The spectrum of an operator is the equivalent concept of eigenvalues of a matrix. For this reason the *solutions* of a problem are often indicated as eigenvectors and the correspondent energy as eigenvalues.

the coordinates of the electrons and the coordinates of the nuclei. It can be observed that electrons are lighter, and *faster*, than nuclei. The coupling of the relative motion between electrons and nuclei, in fact, is proportional to their mass ratio, which is of the order of 0.1%. Due to this, the dynamics of the two components can be decoupled and studied separately for most cases. If a nuclei moves, the solutions change, but the electrons rearrange almost instantly to occupy the new ground-state without affecting the motion of the nuclei. This description reminds the thermodynamic definition of an adiabatic transformation[2], and hence it is also called adiabatic or Born-Oppenheimer approximation. This allows us to simplify the problem assuming that the atomic positions are just parameters for the electronic problem. In this case, it is possible to solve the equations only with respect to the electronic variables. Under the Born-Oppenheimer approximation, the Hamiltonian can be split in two parts, one relative to the electrons where the nuclei positions is only a parameters, and one related to the nuclei:

$$\hat{H}(\mathbf{r},\mathbf{R}) \overset{BO}{=} \hat{H}_e(\mathbf{r};\mathbf{R}) + \hat{H}_N(\mathbf{R}) \tag{2.6}$$

This implies that the solution can be factorized in the product of a purely nuclear part and an electronic part:

$$\Psi(\mathbf{r},\mathbf{R}) = \psi_e(\mathbf{r};\mathbf{R})\phi_N(\mathbf{R}) \tag{2.7}$$

The solution of 2.7 requires two steps. Firstly, one has to find the electronic wave-function using the nuclei coordinates as parameters. Then the electronic eigenvalues, which depend parametrically on $\mathbf{R}$, and are inserted in the equation to find the nuclear wave-function. The total solution is finally given by the product of the two wave-functions. The challenging part that needs to be resolved is the one referring to the electronic wave-function. The next chapters will refer only to the resolution of the electronic problem.

2.1.5 One-electron approximation

The electronic wave-function depends on the position of every single electron:

$$\psi = \psi(\mathbf{x}_1, \mathbf{x}_2, \ldots, \mathbf{x}_N) \tag{2.8}$$

where $\mathbf{x}_i$ represents both the position and the spin of the i-electron. If the interaction between electrons, $\hat{V}_{e-e}(\mathbf{r})$, is assumed constant, the Hamiltonian can be expressed as a sum of independent one-particle Hamiltonians, one for each single electron. Consequently the electronic wave-function can be further factorized:

$$\hat{H}_e = \sum_{i=1}^{N} \hat{h}_{e,i} \tag{2.9}$$

---

[2] A transformation that proceeds between equilibrium states.

$$\psi_e(\mathbf{x}_1, \mathbf{x}_2, \ldots, \mathbf{x}_N) = \prod_{i=1}^{N} \chi_i(\mathbf{x}_i) \tag{2.10}$$

Equation 2.10 is called Hartree function, but it is not enough to describe a multi-electron system. Electrons are Fermions and therefore are described by an anti-symmetric wave-function:

$$\psi_e(\mathbf{x}_1, \mathbf{x}_2, \ldots, \mathbf{x}_i, \mathbf{x}_j, \ldots, \mathbf{x}_N) = -\psi_e(\mathbf{x}_1, \mathbf{x}_2, \ldots, \mathbf{x}_j, \mathbf{x}_i, \ldots, \mathbf{x}_N) \tag{2.11}$$

To avoid this issue it is possible to build a specific function called *Hartree-Fock equation* or *Slater determinant*:

$$\psi_e(\mathbf{x}_1, \mathbf{x}_2, \ldots, \mathbf{x}_i, \mathbf{x}_j, \ldots, \mathbf{x}_N) = \frac{1}{\sqrt{N!}} \begin{vmatrix} \chi_1(\mathbf{x}_1) & \chi_2(\mathbf{x}_1) & \ldots & \chi_N(\mathbf{x}_1) \\ \chi_1(\mathbf{x}_2) & \chi_2(\mathbf{x}_2) & \ldots & \chi_N(\mathbf{x}_2) \\ \vdots & \vdots & \ddots & \vdots \\ \chi_1(\mathbf{x}_N) & \chi_2(\mathbf{x}_N) & \ldots & \chi_N(\mathbf{x}_N) \end{vmatrix} \tag{2.12}$$

Due to matrix determinant properties[3] the Slater determinant will respect prerequisite anti-symmetric property.

The problem is then to reduce the resolution of the single electron wave-functions. When all the solutions are computed, it is then possible to calculate the energy or other properties of the system.

2.1.6 LCAO and Hartree-Fock method

An approach to the resolution of this class of problems is to identify the single-electronic functions with the chemical concept of an orbital. Each function includes also the spin component, and for this reason are also called spin-orbitals.

The orbitals are not known algebraically, and are normally assumed as a linear combination of known functions. One of the first developed method is based on the assumption that any molecular orbital is the superimposition of hydrogen-like orbitals. This method is called Linear Combination of Atomic Orbitals (LCAO) and it is useful in the description of molecular systems. In general, the set used to obtain the linear combination is called *basis set*, and different sets can be chosen to solve a problem. For each single-electronic function one can state that that:

$$\chi_i = \sum_{\mu=1}^{N} c_{\mu i} \phi_\mu \tag{2.13}$$

where $c_{\mu i}$ are the coefficients of the linear combination and ϕ_μ are the elements of the basis set. In this way, the resolution is not focused on the calculation of the wave-function but on the search of an appropriate set of coefficients for a given

---

[3] Any permutation of matrix rows or columns determinates a change in the sign of the matrix determinant.

basis set. This approach was proposed just after the Schrödinger studies and lead to the development of the Hartree-Fock (HF) method.

The HF methods allows the calculation of the ground state of a system in an iterative way. In order to achieve this equations 2.4 and 2.7 have to be rearranged in such a way to define a special operator called Fock operator. This new operator is defined using the function itself and for this reason an iterative approach is needed to solve this equation.

This particular iterative operation is called Self-Consistent Field (SCF) and if the energy is minimized it can be demonstrated that (ideally) it is possible to obtain convergence to the ground-state of a system. Nonetheless, it must be kept in mind that some approximations are present:

- Born-Oppenheimer approximation
- no relativistic effects
- mean and constant electron-electron interaction
- omission f electronic correlation

The HF method describes a single-determinant wave function. For this reason it can not take in account the interaction between electrons with opposite spin, but it fully accounts for the exchange interaction that arises from the antisymmetry of the wavefunction. Correlation and exchange are crucial aspects of related Density Functional Theory (DFT) calculations and we will discussed it in the next sections.

The dimension of the system affects the complexity of the calculation which becomes impracticable for large system. Formally the cost to solve the HF equations scales as the fourth power of the number of elements in the basis set. The complexity for large systems can be reduced by a range of approximations and thus the actual scaling will be close to the square of the number of the basis set.[128] This problem has been the starting point to develop methods that allowed the description of larger systems.

2.1.7 Density Functional Theory

In the HF approach the dimension of the system directly affects the number of variables, *i.e.* electrons coordinates, needed to describe properly the system. Hohenberg and Kohn in 1964 and 1965[129,130] demonstrated two theorems that allowed the replacement of the HF function and its large number of the variables, with a single function that depends only on the three spacial coordinates ($n(x, y, z)$). The two theorems stated that:

- The ground state of a multi electronic system is a functional[4] of the electronic density $n(\mathbf{r})$

---

[4] A functional is a special operator which takes a function as argument and returns a value. An imprecise way to define a functional is to consider it as a function of a function.

- This functional exists and it is unique (universal functional)

It follows then:

$$E_0 = E_0[n(\mathbf{R})] \tag{2.14}$$

It is possible to decompose the total energy in different parts. This operation is similar to what can be done in the HF method and, for this reason, it had been previously omitted. In 1965, in fact, the work of Kohn and Sham proved that the ground-state energy could be rewritten as:

$$E_0 = E_T + E_V[n] + E_j[n] + E_{XC}[n] \tag{2.15}$$

where

$$E_T = 2\sum_i^n \int_{vol} \chi_i^*(j)[-\frac{1}{2}\sum \nabla_j^2]\chi_i(j)d\tau_j \tag{2.16}$$

represents the Kinetic energy of the electrons. $d\tau_j$ is the infinitesimal volume occupied by the j electron for all the considered χ_i orbitals.

$$E_V = -\sum_\alpha^n \int_{vol} \frac{Z_\alpha n(\mathbf{r}_j)}{|\mathbf{R}_\alpha - \mathbf{r}_j|} d\tau_j \tag{2.17}$$

is the electron-nuclei interaction potential,

$$E_J = \frac{1}{2}\sum \iint_{vol} \frac{n(\mathbf{r}_i)n(\mathbf{r}_j)}{|\mathbf{r}_i - \mathbf{r}_j|} d\tau_i d\tau_j \tag{2.18}$$

is the term related to the Coulomb electron-electron interaction. The first three terms are the quantum correspondent to the classic mechanics quantities. The last term, $E_{XC}[n]$, on the other hand, is a peculiar quantity present only in a quantum interpretation of reality and it is impossible to describe it with a classic-physics analogy. This quantity takes into account the interaction between two electrons in the same spacial position with the same spin (*exchange*), and also with opposite spins (*correlation*). This interaction arises from the antisymmetry of the wave-function and is a purely quantum effect. Even if, in principle, the problem is reduced to find a 3-variable function, operatively this is not possible. It is necessary to decompose the whole density in a sum of single-electronic contributions as in the HF theory. Since the density of a function is the square module of the wave-function, this can be written as:

$$n(\mathbf{r}) = |\Psi(x)|^2 = 2\sum_i^n |\chi_i(\mathbf{r})|^2 \tag{2.19}$$

where the factor of 2 takes into account the spin degeneracy and the $\chi_i(\mathbf{r})$ functions, which are known as the Kohn-Sham orbitals and are solutions of the following equation[5]:

$$\mathcal{F}_{KS}(i)\chi_i(i) = \epsilon_{i,KS}\chi_i(i) \tag{2.20}$$

---

[5] again this formalism is analogous to HF theory

where

$$\mathcal{F}_{KS}(i) = -\frac{1}{2}\nabla_i^2 - \sum_{\alpha} \frac{Z_\alpha}{|\mathbf{R}_\alpha - \mathbf{r}_i|} + \int_{vol} \frac{n(\mathbf{r}_i)}{|\mathbf{r}_i - \mathbf{r}_j|} d\tau_i + \mathcal{V}_{XC}(i) \tag{2.21}$$

and it is called the Kohn-Sham operator. It is important to underline how the Kohn-Sham orbitals are a purely mathematical object and they do not have necessarily any physical meaning, if not to reproduce the total charge density.

Differently from HF, DFT includes both the correlation and the exchange effects. They are described in 2.21 by the $\mathcal{V}_{XC}(i)$ term, which is the exchange-correlation potential, and of which the exact form is not explicitly known:

$$\mathcal{V}_{XC} = \frac{\partial E_{XC}[n]}{\partial n} \tag{2.22}$$

Therefore to solve the problem it is necessary to define a $\mathcal{V}_{XC}$ which effectively approximates the real potential. Once the exchange-correlation potential is defined, equation 2.20 is solved using some trial Kohn-Sham orbitals which, accordingly to 2.19, determine the initial electronic density. Since the density appears also in the operator, a SCF approach is needed. However there are some differences with the HF method. In fact, as previously said, the Kohn-Sham orbitals doesn't necessary have a physical meaning and the self-consistent procedure returns only the electronic density and no direct information on the wave-function is provided. Besides it must be pointed out that since the $\mathcal{V}_{XC}$ is not exactly known, the DFT energy can not be considered an upper bound of the true value.[131,132] This implies that contrary to the HF, the SCF procedure can not be improved in a consistent manner.

2.1.8 Pseudopotential

Most of the calculations we performed were completed using the software VASP, which uses a planewave basis set. This basis set is particularly useful to describe systems with free or *nearly*-free electrons, but struggles to reproduce localised feature as bonds and regions where the wavefunction has rapid oscillations, for example near the nuclei.

To solve these problem two different approximations are introduced: the froze-core and the replacement of real potential with pseudopotentials.[133] The frozen-core approximation divides the electrons in two groups: core and valance. Since the properties of materials depends mostly on valence electrons, the electron-electron interaction that appears in equation 2.5 can be rewritten in a core electron contribution, which is precalculated and kept-fixed during the evaluation of a specific system, and a valence electron contribution that is considered in a standard calculation.

As consequence the *real*-potential can be substituted with an effective potential which is easier to treat. This pseudopotential is built in order to match the *real* potential above a certain radius (r_{pp}), and substitute the highly oscillating part,

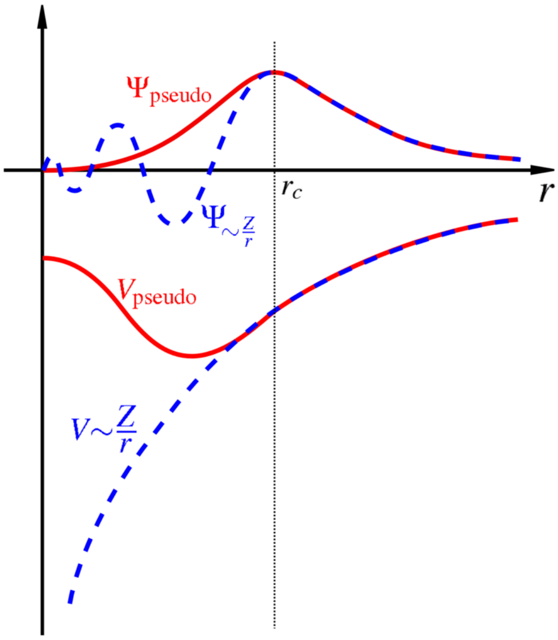

FIGURE 2.3: The dashed blue line reports the *real* potential and the correlated *real* wavefunction. The behaviour in proximity of the nucleus, below a certain radius, is replaced by the pseudopotential and the pseudowave function that are pictured by the solid red line. Image taken from reference[134].

which is poorly described by planewaves, close to the nucleus with a smoother function as represented in Figure 2.3.

As result of this substitution the wavefunction is substituted by a pseudo-wavefunction. The spectra of the pseudo operator is identical to the all-electron one. This approximation also allows us to introduce further corrections to the core-electrons or to the valence electrons[135].

Pseudopotential can be implemented using different methods: norm-conserving,[136] ultrasoft,[137] and projector augmented-wave (PAW).[138,139]

The norm-conserving pseudopotential are built in order to conserve the charge within the pseudopotential radius. Outside this region the pseudo-wavefunction has to match the *real*-wavefunction reproducing the same eigenvalues and the same amplitude resulting in the same charge distribution.[140]

Removing the constraint of norm-conservation leads to the formation of ultrasoft pseudopotential. This type of pseudopotential allows to describe a system using less planewaves simplifying the computational implementation. The PAW is an extention of this method that consists of a linear transformation from the all-electron wavefunction to the pseudo-wavefunction. Doing so, it allows the calculation of the operator expectation value applied of the real-function directly from the pseudo-wavefunction.

2.1.9 Exchange-correlation functional

In the previous section it has been stated that it is necessary to define an approximative exchange-correlation functional. This can be done in many different ways with various results. The energy resulting from the exchange-correlation potential represents only a minor fraction of the total energy, generally less then 10%, but affects many properties of the studied material. For example, it is known how (semi)-local functionals underestimate band gaps because the derivative discontinuity is incorrect.[141]

The choice and the construction of the potential must reflect the properties of the studied material. To simplify this procedure it is possible to decompose the potential in two parts: one of pure exchange and another of pure correlation:

$$E_{XC}[n] = E_X[n] + E_C[n] \tag{2.23}$$

In this way the potential is more flexible and in the case of hybrid functionals experimental data can also be used to fit it. Local Density Approximation (LDA) and the Generalized Gradient Approximation (GGA) are the most common approaches to describe the E_{XC} in DFT.

LDA

The LDA is derived assuming that the density is locally constant and equal to an equivalent homogeneous electrons gas, then:

$$E_{XC}^{LDA}[n(\mathbf{r}')] = E_{XC}[n(\mathbf{r})|_{\mathbf{r}=\mathbf{r}'}] = \int d\mathbf{r}\epsilon_{XC}(n(\mathbf{r}))(n(\mathbf{r})) \tag{2.24}$$

The term $\epsilon_{XC}(n(\mathbf{r}))$ is the single electron exchange-correlation energy in the case of an homogeneous gas of electrons[142] and can be calculated using Monte Carlo simulations. This method was one of the first to be implemented and can describe accurately the behaviour of some metallic materials.

GGA

If the variation of the density is important, such as in molecular systems, the description of the system can be improved considering the gradient of the density, and the same argument can be extended to higher order derivatives:

$$E_{XC}^{GGA}[n(\mathbf{r}')] = E_{XC}[n(\mathbf{r})|_{\mathbf{r}=\mathbf{r}'}\nabla n(\mathbf{r})|_{\mathbf{r}=\mathbf{r}'}; \ldots, \nabla^n n(\mathbf{r})|_{\mathbf{r}=\mathbf{r}'}] \tag{2.25}$$

If equation 2.25 is truncated after the first derivative the functional is defined with the General Gradient Approximation (GGA). If the Laplacian (or further terms) are also considered, the functional is called *meta-GGA*. This type of functional can also be expressed with respect to the kinetic energy of the Kohn-Sham orbital, and hence go under the name of *semi-local* since part of the locality present in LDA and GGA case is lost.[143]

Example of GGA functionals are PBE[144] and PBEsol[145] developed by the Perdew's group. They do not include fitting to experimental data, but the potential is given by different functional expansions of the functional to better describe different aspects of a system. For instance PBEsol is derived from PBE and designed to better reproduce long range interactions. This leads to a better description of equilibrium properties of solid materials, but at the cost of more coarse description of cohesive energies.[146]

Hybrid functional

We observed that most problems of DFT originate from the description of the exchange-correlation functional. We have seen that the LDA and GGA methods are based on a local, or semi-local, description of the electronic interactions. It means that the correction of the energy relies on the density value in a specific point. On the other hand, the exact exchange energy obtained through the HF method is not local, and to calculate it, integrals on the whole space have to be considered. For this reason Hartree-fock is often described as *non-local*. To introduce a non-local correction to the energy within a DFT approach one has to replace the exchange-correlation functional with a linear combination of LDA or GGA functionals with a HF exchange. The obtained functional can be generally expressed as:

$$E_{XC} = (1-\alpha)E_{XC}^{DFT} + \alpha E_X^{HF} \tag{2.26}$$

The linear combination parameter α can be fitted with experimental data or post-HF calculations. Equation 2.26 can be expanded including extra terms to improve the functional.

One particularly successful example of hybrid potential is the B3-LYP[147,148] potential which is defined as a linear combination of different contributions from different previous functionals:

$$E_{XC}^{B3-LYP} = A \cdot E_X^{HF} + (1-A) \cdot E_X^{HF} + B \cdot E_X^{Becke} + E_C^{VdW} + C \cdot \Delta E_C^{non-loc-LYP} \tag{2.27}$$

the parameter A, B and C are fit against set of molecules experimental data. The implementation of experimental data is necessary to recover the poor description of the exchange-correlation effects.

B3-LYP is commonly used in molecular calculations. More recent hybrid functional have been derived from PBE functional, as the PBE0[149,150] and HSE06.[151]

The PBE0 functional is described as:

$$E_{XC} = E_X^{GGA} + 0.25(E_{XC}^{HF} - E_X^{GGA}) \tag{2.28}$$

The HSE06 functional is derived from the PBE0 including long range corrections via the inclusion of a screening parameter that returns the GGA functional response at large distances.

2.2 Many-body interaction

The presence of exchange-correlation functionals within the DFT approach describes, as an average, the electron-electron interaction. The explicit treatment of the interactions between each particle would lead to an impossible or impractical system of equations. As an example, we can consider a system of electrons: the energy of one electron depends on the positions of all the other electrons, but at the same time, the positions and the energy of all the other particles depends on the electron itself. For this reason the fraction of energy of a particle that depends on the system response to the particle itself is called self-energy (Σ).

In the DFT formalism the self-energy contribution is absent. The many-body effects are approximated and contained by the exchange-correlation functional. This approach allows us to calculate properties of extended materials with a good compromise of cost and accuracy.

For specific conditions and materials, for example, if electrons are highly correlated or excited-state energy has to be considered, the proper calculation of the self-energy is crucial to avoid anomalous results.

The self-energy can be calculated using the HF method to obtain the ground-state properties, or with the Configuration Interaction (CI) to include excited-state description, or via a linear response approach that describes the response of a system to a small external perturbation. These methods are usually solved self-consistently and they allows us to reach higher precision and describe accurately different effects, but these require a higher computational cost.

Another alternative is the *GW* approximation that expands the many-body component of the electrons interaction in terms of Green functions (G) considering a screened Coulomb interaction (W). Within the GW approximation it is possible to calculate explicitly the self-energy solving the limitations present in the DFT.

The GW formalism retains a single-particle view of the electronic structure, and it relies on a perturbative approach. If 2-body interactions are a particularly significant, within the Green formalism it is necessary to solve the Bethe-Salpeter equations (BSE), of which the GW method is a specific case[152].

Although computationally cheaper than the resolution of BSE, the GW method is quite demanding and different approximations and methods have been developed to carry out calculations. These efforts have been done because the GW methods allows to introduce a term that describe the electronic screening, not present in HF, preserving at the same time local, non-local and many-body effects.

Since GW is a perturbation theory a starting ground-state wavefunction is needed. Usually starting from a LDA solution is sufficient to improve the description of the electronic bands, a feature particularly useful in the study of semiconductors. Unfortunately this is not a systematic approach with a predictable outcome.

To improve this aspect different GW approaches have been developed. These methods include self-consistent techniques to improve, not only the exchange-correlation part of the ground-state Hamiltonian, but also the screening potential.

The most popular approach is the G_0W_0 method.[153,154] In this approximation the initial wavefunction is assumed to the be same obtained with LDA calculation, and only the first-order perturbations to the self-energy correction are considered. This correction is carried out applying one single calculation, i.e. without applying a self-consistent scheme.[152]

The G_0W_0 can be further improved with the Quasiparticle Self-Consistent GW (QSGW). In this case not only the screening, but the whole Hamiltonian is optimised to obtain bettet results than those provided by the starting point alone. This results in a consistent method that can be applied to most of materials and properties of interest.

2.3 Vibrational properties

The Born-Oppenheimer approximation guarantees that once the ionic position are fixed, the electrons fall almost instantaneously in the ground state configuration. The energy of the system depends, parametrically, also on the atomic positions, so if the atoms are not in an equilibrium position, forces arise. During the geometry optimisation the minimization of these forces lead to the localisation of local, possibly absolute, minima-energy configurations.

The same principle can be exploited also to study the dynamic of a material. In a real crystal atoms are not occupying statically the minima position, but these vibrate to respond to external perturbation and thermal energy. The vibrational effects arise due to an increase of kinetic energy that results in the displacement from the energetic minimum.

2.3.1 Atomic dynamics

The displacements induced by thermal energy are small compared to the size of the cell and inter-atomic distances. The position of an atom can be decomposed in its ideal lattice position, plus a displacement:

$$r_i = R_i + u_i \tag{2.29}$$

The potential that keeps the atoms together can be expressed as a Taylor series of the atomic displacement u_i, expressed as:

$$V_0(R,u_i) = V_0(R) + \sum_i \frac{\partial V}{\delta u_i} u_i + \frac{1}{2}\sum_{ij} \frac{\partial^2 V}{\partial u_i \partial u_j} u_i u_j + \frac{1}{6}\sum_{ijk} \frac{\partial^3 V}{\partial u_i \partial u_j \partial u_k} u_i u_j u_k + \ldots \tag{2.30}$$

The first term is the potential energy of the atom in the frozen position, the second term represents the sum of all the forces acting on an atom, and since the system is in equilibrium it equals to zero according to Newton's law. Higher-order terms express the dependency above the linear-regime.

For our purposes we consider only the second derivatives which correspond to the harmonic approximation. This is equivalent to describing the system as a set of point-masses connected by ideal springs. We can ignore the remaining terms and rewrite 2.30 as:

$$V(R,u_i) = V_0(R) + \frac{1}{2}\sum_{ij} D_{ij} u_i u_j \tag{2.31}$$

$$where\ D_{ij} = \frac{\partial^2 V}{\partial u_i \partial u_j} \tag{2.32}$$

The term D_{ij} is called dynamical matrix and contains the information about the atomic vibrations. It is possible to derive the force that acts on atom i as the sum of all the force resulting by the movement of all the other atoms:

$$F_i = -\sum_j D_{ij} u_j \tag{2.33}$$

The forces acting on each atom must obey Newton's second law of motion:

$$F_i = m a_i = m \ddot{u}_i \tag{2.34}$$

This constrain leads to the definition of a set of differential equations of motion, which solution returns the vibrational frequencies and the displacements allowed in the system:

$$m\ddot{u}_i + \sum_j D_{ij} u_j = 0 \tag{2.35}$$

2.3.2 From the monoatomic chain to 3D crystals

Because the vibration in one direction is decoupled from the movement in the other direction, we can consider a monoatomic chain to better understand the vibrational properties of solids. The chain is formed by N atoms with mass m and lattice a. Applying Equation 2.29, the position of the n^{th} atom is:

$$R_n = na + u_n \tag{2.36}$$

where u_n indicates its displacement with respect to the equilibrium position. To introduce periodicity, the last atom is ideally connected with the first:

$$R_{N+1} = R_1 \tag{2.37}$$

The interaction between each pair of atoms is constant and proportional to the spring constant K:

$$D_{n,n'} = K \; \forall n \neq n' \tag{2.38}$$

$$V = V_0 + \frac{1}{2} K \sum_n u_n^2 \tag{2.39}$$

Applying Newton's law, we can derive the equation of motion of the nth atom:

$$m\ddot{u}_n = K[(u_{n+1} - u_n) - (u_n - u_{n-1})] \tag{2.40}$$

The periodic boundary condition imposes that the force that acts on a specific atom depends only on the next-neighbour displacements. The solution is independent on the choice of the n atom and can be expanded in planewaves. This simplifies extremely the problem and the solutions are formed by a collective motion of atoms called modes. Because the concerted movement leads to properties that resemble one particle, it is possible to identify each solution as a quasiparticle called phonon.

To explicitly build the respective solutions it is possible to consider planewaves of the form:

$$u_t(t) = A_j e^{i(k_j na - \omega_j t)} \tag{2.41}$$

To satisfy the condition of periodicity $u_n(t) = u_{n+N}(t)$, there is a consequent quantization of the states described as:

$$q_j = \frac{2\pi j}{Na} \tag{2.42}$$

Once the solutions are found, the correspondent vibrational energy is:

$$\omega_j = \sqrt{\frac{4K}{m}} \left|\sin(\frac{q_j a}{2})\right| \tag{2.43}$$

As we have specified before, because of the periodic boundary conditions the system is treated as an infinite system where $\lim_{N\to\infty}$, so the frequency (ω_j) dispersion becomes continuous at the Brillouin Zone:

$$\omega(k) = 2\sqrt{\frac{K}{m}} \left|\sin\left(\frac{qa}{2}\right)\right| \tag{2.44}$$

This relationship is reported in figure 2.4.

For small values of q the relationship is linear and the angular coefficient is the speed of sound in that material, i.e. the coherent movement of all the atoms in one

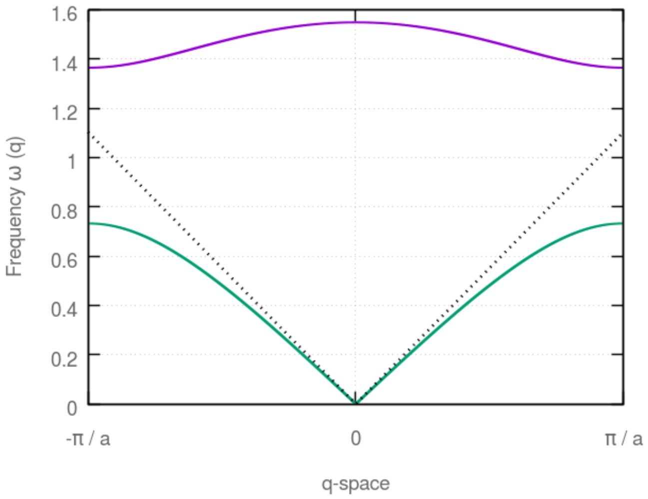

FIGURE 2.4: The diagram reports the phonon dispersion for a diatomic chain. In the mono-atomic chain the only mode present is the acoustic mode (green). For the acoustic branch for small value of q the dispersion is almost linear and the coefficient of such line is the speed of sound in the material. If a second atom with 5 times larger mass is considered, the solution includes a less disperse higher frequency branch (purple) relative to the presence of optical phonons.

direction. The low energy mode that vanishes at the center of the Brillouin-zone ($q \rightarrow 0$) are called acoustic modes. They describe in-phase vibrations associated with sound propagation.

If diatomic mono-dimensional chains are considered the number of degrees of freedom is doubled, thus the dispersion will be described with a new solution with higher frequency, as shown in Figure 2.4. These high energy modes are labelled as optical-modes. In this case, the movement of atoms is out-of-phase, and in ionic materials are induced by the absorption of radiation in the infrared (IR) portion of electromagnetic spectra.

If we consider a finite crystal with N unit-cells and s atoms per cell there will be $3Ns$ degrees of freedom to consider. The introduction of periodic boundary conditions will reduces the number of degrees of freedom to $3s$, so the number of phonon modes. Three of these modes are the acoustic modes associated with the in-phase translations along the three Cartesian directions.

The atomic vibration is not necessary bound to occur in the same direction of the mode propagation. In general, a mode can have a mixture of longitudinal and transversal characters and, usually, the vibrations have a single character only along the high-symmetry lines of the Brillouin-zone.

Similarly to what we described in the electronic section, it is possible to define also a phonon density of states. The phonon density of states is a function that gives the number of vibrational states per unit of energy. Of particular interest in the density of states are the van Hove singularities[155,156] that are physically observable by IR reflectivity measurements and allow to deduce the elastic properties of solids.

2.3.3 Bose-Einstein distribution

In the previous chapter we have considered single atom dynamics to derive the thermal properties of solids. Implicitly, we consider the collective motion of atoms as it is an individual particle with quantised unit of frequency, the phonon. The phonons are in fact quasi-particles and differently than electrons they are not fermions; they have integer spin and are classified as bosons. The expected number of particles with a certain energy (or frequency) is given by the Bose-Einstein distribution:

$$n(\omega, T) = \frac{1}{\exp \frac{\hbar\omega}{k_B T} - 1} \tag{2.45}$$

Because of the Boson spin-statistic, the Pauli exclusion principle does not apply and Bosons can occupy any quantum state accordingly to Equation 2.45 (i.e. each level can host more than two particles).

In the ideal limit of 0 K temperature, this means that all the particles collapse in the level with minimum energy. For an quantum-oscillator even at 0 K the motion of the particle does not freeze, and all the particles keep a small fraction of energy equal to $^{\hbar\omega}/_{2}$, which is called zero-point vibrational energy. This behaviour is characteristic of the quantum nature of a system, and derives from Heisenberg uncertainty principle:

$$\frac{\hbar}{2} \leq \Delta x \Delta p \tag{2.46}$$

where Δx and Δp are the uncertainty of position and momentum, respectively.

2.3.4 Anharmonicity

The results presented to this point were based on the harmonic approximation, i.e. all the atomic interactions have been described as harmonic oscillators. This approximation allows to obtain most of the lattice properties, but lacks to describe anharmonic phenomena such as phase-transitions, melting point, heat transport, or thermal expansion.

The first step towards the understanding of anharmonic properties is to consider the Quasi-Harmonic Approximation (QHA) which allows the description of how the volume affects the harmonic vibrations. This method consists in a set of harmonic calculations performed on systems with different constrained volumes and from this it is possible to obtain temperature-dependent properties.

The QHA retains some limitations of the harmonic approximation. In particular, the life-time of phonons are still infinite, because the scattering events are not considered and the dissipation is zero due to the symmetric nature of the potential. To derive such properties a proper resolution of anharmonic effec is required. This is achieved expanding the potential reported in equation 2.30 beyond the second power term to take in account higher orders.

An alternative to calculate the anharmonic term, i.e. to obtain the heat transport properties is the resolution of Linearized Phonon Boltzman Equation (LPBE).[157]

The LPBE is obtained assuming that, within the crystal periodicity, the dynamic of the phonons will satisfy a hydrodynamic behaviour. The phonons are then treated as constituent of a fluid which particle can diffuse or undergo convection. The fluid properties are due to the phonon-phonon interactions and the solution of the LPBE will allow to the calculation of phonon life time and the lattice thermal conductivity.

2.3.5 Experimental measurement of anharmonic properties

From an experimental point of view, it is important to consider the life-time of phonons, since it affects different experimental results. In particular, it has a role in light-phonons scattering since it defines the line-widths of Raman or IR signals.

The Heisenberg uncertainty principle allows the violation of the conservation of energy for a small period of time. This results in a broadening of signal resulting from spectroscopy measurement. The shape of peak for a signal that occurs at ω_0 is given by the Breit-Wigner line shape:

$$I_i(\omega) = \frac{1}{(\omega - \omega_0)^2 + \frac{\Gamma^2}{4}} \tag{2.47}$$

The parameter Γ is the Full Width Half Maximum (FWHM) and it is directly linked to phonon life time τ through the relationship:

$$\frac{\Gamma}{2} = \frac{\hbar}{2\tau} \tag{2.48}$$

2.4 Computational implementation of vibrational properties

The physical atomic displacement falls within a small percentage points of the absolute position of atoms, i.e. they are small compared to the size of the cell. Exploiting this observation can lead to two main approaches to the problem: perturbational, or relied on the finite difference approximation. Both techniques will be described in the next following sections.

The computational setup required for this type of simulations are reported in Chapter 4.

2.4.1 Density functional perturbation theory

Density functional perturbation theory is based upon the observation that it is possible to probe the variation of the systems's properties in response to small perturbations to the potential The property X of a system subject to a perturbation γ can be expressed as:

$$X(\delta) = X_0 + \frac{\partial X}{\partial \gamma}\gamma + \frac{1}{2}\frac{\partial^2 X}{\partial \gamma^2}\gamma^2 + \ldots \tag{2.49}$$

The previous equation can be truncated to the first-order to obtain the linear response. If different quantities of a system are investigated by applying the linear approximation it is possible to obtain the macroscopic properties of the considered system. For example, it is possible to obtain the phonon modes calculating the variation of the energy under small perturbation of the atomic coordinates, or the polarizability if the dielectric constant is considered.

We used the DFPT method to obtain the phonon modes at the Γ-point of the Brillouin Zone. The frequency of vibrations are calculated by perturbing the energy with small atomic displacements along the normal modes, thus determining the Hessian matrix. Since the standard Raman or IR measurement can not resolve the phonon phase, the Γ-point calculations are enough to simulate the spectra peaks positions. Once the phonon vibrations are calculated it is possible to obtain the associated intensity of IR and Raman spectra. The IR intensity is derived from the Born Effective Charge (BEC) matrix, which is obtained by calculating the linear response of the atomic polarizability to a perturbing electric field along the different Cartesian directions[158,159]. The Raman signal instead originates from the variation of the polarizability that can be obtained calculating the macroscopic dielectric tensor[158].

2.4.2 Finite displacement method

The DFPT method results in quite expensive and difficult calculations, and it is particularly challenging to implement the method for other high-symmetry points of the Brillouin zone, other than the Γ-point. An alternative to this is the Finite Displacement Method[160,161] (FDM) that we have applied, as implemented in the Phonopy package.[162,163] This method relies in the fact that, since the atomic displacements are small, it is possible to calculate the derivative of the energy as a finite ratio:

$$\frac{\partial E}{\partial x} \approx \frac{\Delta E}{\Delta x} \text{ for sufficiently small } \Delta x \tag{2.50}$$

It is possible to calculate ΔE as the difference between the energy of a reference cell with another cell where the atoms have been displaced by a small quantity Δx. Operatively, the FDM consists of a first step to tight optimize the geometry of the studied material. This optimization is required in order to reduce the residual inter-atomic forces below a certain threshold which in our present work was defined as $10^{-3}\ ^{eV}/_{\text{Å}}$ (one order of magnitude smaller than the default one used to calculate the electronic properties).

Once the single cell is optimized for each atom corresponding to the initial unit-cell, supercells are generated where only one of the atomic coordinate is changed of a fixed amount. For a cell that contains N atoms, this results in $6N$ supercells ($x \pm \Delta x$, $y \pm \Delta y$, $z \pm \Delta z$). If the cell belongs to a specific space group, it is possible to reduce this number ignoring the equivalent structures. The use of supercells is needed to avoid self-interaction between an atom and its virtual image. In general a simple $2\times2\times2$ supercell expansion is sufficient to obtain a good description of vibrational properties, but for particularly small cells larger expansions are necessary; instead for particularly large cell the unit-cell is sufficient. To address this aspect a convergence test with different supercell expansions is then appropriate.

Due to the small nature of the energy variance, this method is highly susceptible to the numerical noise present in the calculations. It is then necessary to optimize, not only the size of the cell, and the threshold of the geometric optimization, but all the computational parameters that influence the energy, for example the k-point mesh or the cut-off energy for the planewave basis set.

2.4.3 Soft-modes

The vibrational modes we have have described are considered as perturbations of the ideal ground state of the compounds. According to equation 2.43, since the ground state is the minimum energy state, the vibration results in a positive variation of energy proportional to the square of the frequency:

$$\Delta E = km\omega^2 \textit{ and } \omega = \sqrt{\frac{\Delta E}{km}} \textit{ which is real for } \Delta E > 0 \tag{2.51}$$

from which it follows that the frequency has to be real. However if the energy of a structure is not the global or local minima (in general a transition-states), some vibrations cause the structure to lower its energy. As a consequence, ω will belong to the complex numbers domain. The phonons associated to these frequencies are defined as imaginary (or soft) modes, and they are *fingerprints* to detect that a structure is dynamically unstable, and therefore promote the existence of more stable structures.

If the presence of spurious forces, or noise, is excluded, soft-modes are useful to investigate the different phases of a material, for example to determinate the existence of different phases in experimentally unknown compositions.

2.4.4 Quasi-harmonic approach

As we described in the previous paragraph, it is possible to obtain some properties beyond the harmonic approximation using the quasi harmonic approach (QHA). This method is available through Phonopy sofware which allows to obtain several temperature-dependent properties. Once the different FDM calculations have been performed for different volumes, using different equation of states as the Rose-Vinet,[164] or the Birch-Murnaghan[165,166] to fit the volume-energy curves, it is possible to extrapolate the temperature-dependant thermodynamic quantities such as: bulk modulus, Gibbs free energy, volume and the thermal expansion, Grüneisen parameter, constant pressure specific heat. Besides, it is possible to obtain the heat capacity, and the Helmholtz free energy *versus* the volume. In the case of a material presenting different phases, through the study of Gibbs free energy, it is possible to establish which phase is the thermodynamic stable one, and in principle, predict the phase transition temperature (T_C).

2.4.5 Higher-order anharmonicity

The derivation of the third order anharmonic term can be pursued within the FDM as implemented in the Phono3Py module included in Phonopy. The method is quite intuitive and allows to study the third-order force constants with the FDM. From an unperturbed single cell, a first FDM calculation generates a set of perturbed structures. Then for each of those structure a set of FDM calculations are consequentially performed. This way it is possible to analyse the response of phonon states when they are influenced by other phonons.

This type of calculations allows us to study the third-order force constant to calculate the phonon life-time and by applying the Boltzman Linear Equation the phonons's thermal conductivity can thus be extracted.

2.4.6 Computational note

To calculate vibrational properties requires accurate computational setups are required. In particular the basis-set or the cut-off energy of the planewaves, as well as the k-mesh need tight convergence. The details for each type of calculation that we performed are reported in Chapter 4.

2.5 Mixed halide solid solution

2.5.1 Phase diagrams

This thesis presents some phase diagrams to describe the stability of pseudo-binary alloys. The prefix pseudo, is used to underline the fact that just one component is changed, due to the complex nature of the hybrid perovskites.

Two compounds can be completely immiscible, miscible, or they can form two different phases with partial miscibility. A phase diagram is a synthetic representation of the conditions (in this case the temperature and the composition) that allow the existence of a specific phase. This depends on its free energy, of which the phase diagram is a graphical representation.

In the study of solid alloys it is more appropriate to refer to the Helmholtz free energy, since the volume variation is considered constant. The Helmholtz free

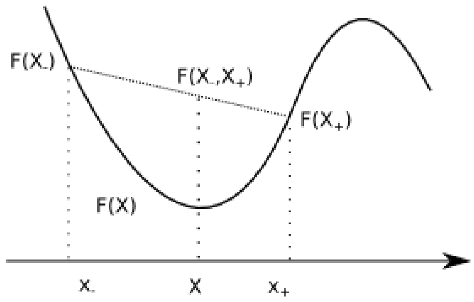

FIGURE 2.5: Example to determinate if a system with composition X undergoes phase separation or not. In this case the free energy of the composition X is lower than the weighted average of two phases with composition X_- and X_+.

energy is obtained as difference between the internal energy of the system and the product of temperature and entropy:

$$F(x,T) = U(x,T) - TS(x,T) \tag{2.52}$$

The stability of a phase is determined, not by the value of the free energy, but by its variation. A process happens spontaneously if it can lower the free energy of a system. In the case of mixing this result in the following equation:

$$\Delta F_{mix}(x,T) = \Delta U_{mix}(x,T) - T\Delta_{mix}S(x,T) \tag{2.53}$$

For a given composition x a binary system can exist in two forms. One single homogeneous phase with compositions x, or it can be divided in two phases with different compositions (one with composition $x_+ > x$, one with composition $x_- < x$) which in average results in the same composition x. The energy of such system is given by the weighted average of the two phases, and is graphically represented by the a straight line that join the two point of the free energy diagram as pictured in Figure 2.5.

If the Helmholtz energy of the single phase is lower than the straight line, then the system can form an homogeneous alloy, otherwise it will phase segregate.

If the free energy has just one minimum the condition is always respected, and the compounds are completely miscible. Mathematically this is verified if the second derivative of the free energy with respect to the composition is positive, $\frac{\partial^2 F}{\partial x^2} \geq 0$ for every composition.

This is not the case we found in the study of the hybrid perovskites alloys. The free energy has a double well shape as showed in the left part of Figure 2.6. In this case there is a set of compositions for which the energy is minimized if the system undergoes a phase separations. The interval where this happens is called miscibility gap and it is defined by the intersections of the free energy curve with the common tangent of the curve itself. Complete miscibility is possible outside this interval. Inside, instead two different situations are possible. As show in the

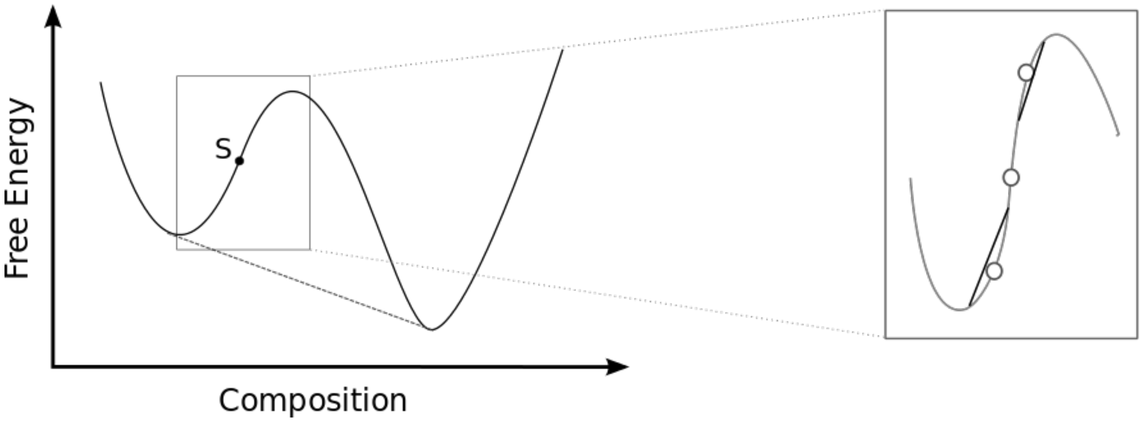

FIGURE 2.6: Representation of spinodal decomposition. The spinodal point is label as "S". The right panel reports the comparison between fluctuations in the free energy curve and the correspondent line related to the phase separation at those compositions.

right part of Figure 2.6, there are points within the miscibility gap where small fluctuations of the composition raise the energy of the system. This occurs for point in the miscibility gap where, in analogy with what said before, the second derivative of the free energy is positive. The flexes (spinodal points) of the free energy divide the miscibility gap in regions with different regimes. Between the boundaries of the miscibility gap and the flex the alloy is a local minimal and the homogeneous phase can be metastable. Inside the flexes instead, the alloys is unstable and undergoes what is called spinodal decomposition.

For metastable compositions the system need to overcome a barrier to minimize the energy: the phase separation happens with a mechanism of nucleation and growth. Instead in the spinodal region, the process is barrier-less and proceed through diffusive mechanism. The analysis of the free energy leads to individuating some critical points that define the behaviour of the alloys.

Until this point we considered a constant temperature. The phase diagram reports the positions of the different critical points in function of the temperature. As the Temperature increases the second term that appears in equation 2.53, becomes more and more prominent, the miscibility gap is reduced and the alloy becomes completely miscible above a critical temperature Tc.

There are different methods to obtain the free energy of mixing of a mixed system, in the next section we present a general overview of the Generalised quasi-chemical approximation that we employed using *ab-initio* calculations.

2.5.2 Generalised quasi-chemical approximation

The study of an alloy is particularly complex because the behaviour of such system depends on multiple different atomic configurations that are determined by long and short range effects. To include all these aspect it is necessary to consider a supercell large enough to provide a good sampling of all the possible local atomic environments, and avoiding self-interaction. DFT methodology is computationally too expensive to treat such large cells and other methods, as classic molecular dynamics or force fields calculations should be considered.

To preserve the DFT accuracy it is necessary to approach the problem from a different prospective. Materials where atoms are disposed with a random pattern can be seen as an ensemble of all the different possible atomic configurations. The alloy properties can then be extrapolated considering each one (or a significant amount) of all these possible configurations to build a partition function.[167]

Different methods have been designed to calculate the partition function of an semiconductor alloy. In this study we considered the Generalised Quasi-Chemical Approximation (GQCA).[168] The GQCA approach has been developed mainly for binary alloys and we applied it to the halide sub-lattice of the perovskite to obtain the entropy and the free energy of mixed halide perovskites.

In its general form the GQCA considers a random system as an ensemble of independent clusters and allows to study a mixed system $A_{1\text{-x}}B_{\text{x}}$ (or a more complex case $CA_{1\text{-x}}B_{\text{x}}$ in this study) as a function of temperature and fractional composition x. Dividing the system in smaller parts, it has the advantage that the results can be systematically improved increasing the clusters size.

To further reduce the number of the calculations, the clusters are considered statistically independent from each others, i.e. the total energy of the system is given as the sum of each of its clusters energy.

Each composition of the system can be represented by a set of M clusters with n atoms each. In a simple system the energy of the cluster could depend directly on its composition (i.e. the number of atom of a specie), but that is not strictly necessary.

Once the clusters are defined, these can be grouped in function of their energy ϵ_j, and there will be a number M_j of clusters with energy ϵ_j so that $\sum M_j = M$. If the atomic positions of a cluster belong to a specific space group such cluster has to be considered with a proper degeneracy factor g_j. The fraction of the clusters with energy ϵ_j is $x_j = \frac{M_j}{M}$.

If different clusters are jointed to form a system with a specific composition x they have to respect an additional constraint:

$$\sum_j n_j(A)x_j = n(1-x) \tag{2.54}$$

where $n_j(A)$ is the number of atoms A for the clusters j. This relation is necessary to ensure that only clusters that concur with a specific composition are taken in account. The size of the cluster, or the number of clusters considered at the same time, also fixed the compositions that are possible to test; only the ones multiple of $\frac{1}{N}$.

Given n sites per cluster, the maximum number of possible clusters is 2^n for a binary system. If some cluster is equivalent or degenerate then:

$$\sum_j g_j = 2^n \tag{2.55}$$

With this set of clusters, it is possible to describe any possible system with a set of clusters that forms it. Once the energies of the clusters are known, the partition function can be built and the interesting properties can be extracted. If we consider the set of clusters $\{M_j\}$ which energy is $E\{M_j\} = \sum_j M_j \epsilon_j$, the partition function will have the general form:

$$Z(\{M_j\}) = \sum_{\{M_j\}} G(\{M_j\}) e^{-\frac{E(\{M_j\})}{k_B T}} \tag{2.56}$$

This definition is possible only if the different clusters are mutually independent. The term $G(\{M_j\})$ takes in to account the degenerate configurations. This number is equal to the combination of N_A and N_B atoms on N sites, multiplied by the fraction of the cluster of such composition. Equation 2.56 can be simplified by defining the quantity:

$$x_j^0 = g_j x^{n_j(B)} (1-x)^{n_j(A)}. \tag{2.57}$$

If we consider $1 - x$ as the probability that an atom A (so, x is the probability relative to atoms B) occupies a random site of the lattice, the quantity x_j^0 is the final probability to obtain a cluster with a specific configuration of $n_j(A)$ and $n_j(B)$ atoms. With this definition it is possible to approximate $G(\{M_j\})$ as:

$$G(\{M_j\}) \approx \frac{N!}{N_A! N_B!} \left(\frac{M!}{\prod_j M_j!} \prod (x_j^0)^{M_j} \right) \tag{2.58}$$

The first factor represents the total number of ways of arranging N_A atoms of type A and N_B atoms B on the N sites, the second takes in to account all the possible arrangement of the clusters and the final term is the probability of finding a specific cluster in the material. It follows that $G(\{M_j\})$ expresses the number of possible combinations to arrange different clusters to obtain a certain energy ϵ_j.

Once the partition function is defined, using the Stirling's approximation, it is possible to calculate the entropy according to the definition of Boltzman that associate the entropy to the number of possible microstates of a system:

$$S = k_b \log G \tag{2.59}$$

$$\begin{aligned} S &= -k_B N \big((1-x)\log(1-x) + x \log x + \sum_j (x_j \log x_j - x_j \log x_j^0) \big) \\ &= k_B N \big([(1-x)\log(1-x) + x\log x] - \sum_j x_j \log(\frac{x_j}{x_j^0}) \big) \end{aligned} \tag{2.60}$$

Analogously the Helmholtz free energy is obtained from the partition function as:

$$F(x,T) = -k_BT\log Z \tag{2.61}$$

The initial form reported in 2.56 can be simplified introducing μ_B to define the maximum number of nearest neighbours ξ for each composition:

$$\frac{x\xi}{1-x} = e^{\frac{\mu_B}{k_BT}} \tag{2.62}$$

Therefore it follows that the number of B atoms is fixed to:

$$nx = \frac{kT}{q}\frac{\partial q}{\partial \mu_B} \tag{2.63}$$

being q, the single cluster grand partition function:

$$q = \sum_j g_j e^{\frac{n_j(b)/mu_B-\epsilon_j}{k_BT}} \tag{2.64}$$

The final partition function is then:

$$Z = \frac{N!}{N_A!N_B!}[q(1-x)^{n(1-x)}x^{nx}e^{\frac{-nx\mu_b}{k_BT}}]^M \tag{2.65}$$

From this it follows that the Helmohltz free energy is:

$$F(x,T) = Mnx\mu_B + k_BT(N-Mn)[x\log x-(1-x)ln(1-x)] - M\log q \tag{2.66}$$

The problem can be simplified in the case of a random distribution:

$$F = Nk_BT[x\log x + (1-x)\log(1-x)] + \epsilon_0 + nx\Delta\epsilon]. \tag{2.67}$$

The introduction of $\Delta\epsilon$ is necessary since the distribution depends not on the absolute values of energy, but on the difference between each one of them.

Chapter 3

Perovskites electronic structure

3.1 Introduction

DFT calculations return the total energy of an electronic system. The energy is obtained from the electron density of the system, $n(r)$, derived from a fictitious wave function as explained in section 3.3.3. In the following chapters we employ different DFT techniques to extract materials electronic and structural properties.

For example, the energy minimisation with respect to the atomic coordinates allows to explore the configuration landscape of the structure and localize to the minima structure. DFT allows us to calculate the electronic structure from which it is possible to extract electronic parameters that are crucial to understand the behaviour of solar cells. DFT fails to catch some properties of materials, and we used many-body calculation to describe more accurately specific effects as the relativistic Rashba splitting.

The first part of this chapter covers the properties of inorganic halide perovskites. At the early stage of research the experimental data on hybrid perovskites were not abundant and straightforward. We considered three compounds: $CH_3NH_3PbI_3$ (MAPI), $CH(NH_2)_2PbI_3$ (FAPI) and NH_4PbI_3 (API). We arbitrary choose these systems, rather than other similar ones such as perovskite with lower dimensionality, to produce test-cases for future developments in the field. A three-dimensional perovskite structure of API, for example has never been reported and the research focused mostly on MAPI. Nonetheless we will discuss the results, because of their insight about the size role of the central cation.

During the development of the research we moved our attention to focus mostly on MAPI following the technological development of the solar cells employing different software and methodology as we will explain.

3.2 Computational setup

3.2.1 Inorganic halide perovskites

The calculations for this first part have been performed with the FHI-AIMS software using DFT.[129,130] FHI-AIMS is an all-electron electronic structure code based on numerical atom-centred orbitals. To describe the electronic wave function different basis set are available, but in all calculations we employed the preconstricted *tight basis set*. This basis set contains a range of diffuse and polarization functions that allow the description of partially localized or diffuse charges. It is intended to provide meV-level accuracy.

Since the materials studied are represented by their crystal structure, periodic boundary conditions (PBC) have been employed. PBC allows modelling of a perfect crystal from the single crystal unit cell. They consist in an infinite replica of the single cell structure in the direct space. This is achieved imposing continuity between the opposite ends of the cell vectors. In practice if we consider a 2D square cell with an atom moving from left to right, once it crosses the right border, it re-enters in the same cell from the left side.

This approach is ideal to study an infinite perfect system, but it relies on choice of a crystallographic cell of proper size. Small cells can lead to the introduction of self-interactions of local environments (e.g. defects), or misrepresentation of long range effect (e.g. dispersion cell); oversized cell increase the computational cost of the calculation oversampling the electronic structures. The study of specific cases, such as point defects or localised charges requires different methods, or the inclusion of correcting potentials.

We considered perovskites with general formula $CsMX_3$ (X= Cl, Br,I and M= Sn, Pb), with a cubic perovskite lattice belonging to the space group $Pm\bar{3}m$ (n. 221). The Cs atom occupies the Wyckoff *a*-site $(0.0, 0.0, 0.0)$, the halogen atoms adopt the *c*-site $(0.5, 0.5, 0.0)$ and the divalent metallic ion sits at the center of the cell ($\frac{1}{2}$, $\frac{1}{2}$, $\frac{1}{2}$), which is the Wyckoff *b*-site.

The cubic phase is the high-temperature stable phase, and for these materials it occurs in a range of temperatures from 320 K for $CsPbCl_3$,[169] to 563 K for $CsPbI_3$.[170]

The first step of this work was the optimisation of the lattices parameters. This operation was performed using the Broyden-Fletcher-Goldfarb-Shanno (BFGS) algorithm.[171] Due to the simple high symmetric structure the initial structure can be deduced empirically, but when possible we used experimental data taken from experimentally-solved x-ray diffraction measurements.[170,172–175]

The energy calculations to achieve the geometry optimization was performed using the semi-local GGA exchange-correlation functional PBEsol[145] with a *k*-point $12\times12\ \times12$ grid, and constraining the cell geometry to cubic.

The presence of heavy element such as lead or tin as in this case, requires the consider the presence of relativistic effect, that are usually negligible if only light elements are presents. These effects were taken into account using the scalar atomic ZORA[176] relativistic correction included in FHI-AIMS.

To calculate the enthalpy of formation, we used a set of calculations that included all the component elements in their standard states. The calculations for those systems have been performed in a consistent manner to the system they have been used to calculate the enthalpy of formation for.

To improve the quality of the band structure we used the hybrid PBE0[144] functional. This functional is derived from PBEsol, with 25 % of the electron exchange energy replaced by exact Hartree-Fock exchange. Since calculations with hybrid functionals are computationally expensive, we reduced the k-point mesh from $12 \times 12 \times 12$ to $4 \times 4 \times 4$. In some cases the calculation with a $4 \times 4 \times 4$ mesh grid gave anomalies in the band structure. Those errors were a sign that the chosen grid was too sparse. Thus additional calculations with a more dense $8 \times 8 \times 8$ mesh were necessary for studying $CsPbCl_3$, $CsSnCl_3$ and $CsSnBr_3$.

3.2.2 Hybrid halide perovskites

Once the inorganic perovskite study was completed we considered the hybrid perovskites systems. To perform these calculation we employed the commercial software VASP.[177] We switched to VASP because it is well tested and the geometry optimization with FHI-AIMS gave some convergence issues for the lower symmetry organic-inorganic materials. VASP is an *ab-initio* simulation package that is based on pseudopotentials (which include relativistic core corrections) and a plane-wave basis set. This type of basis set has the advantage of being defined by a simple energy threshold (cut-off), which sets the number of functions included. The calculations were performed with the PBEsol functional, and are consistent with calculations done with FHI-AIMS. We used a k-point mesh with $6 \times 6 \times 6$ subdivisions generated with the Monkhorst-Pack algorithm.[178] This set of point was a good compromise between cost and accuracy to describe the organic molecule inside the cage.

The geometry optimisation algorithm included in VASP allows for different types of relaxation; for example, it is possible to relax only the cell shape, keeping the volume fixed, or to optimize just the volume, scaling the structure accordingly.

The starting structures for the hybrid perovskite in the cubic phase were generated with a custom Fortran program. This code generates a cubic perovskites lattice with an organic cation at the center of the cage. The software was designed to create structures with different lattice parameters, composition, and orientation of the organic cation. When available, for example for the low temperature phases of MAPI we used crystallographic data to improve the starting point, or to derive the geometry of the system.

TABLE 3.1: Experimental, optimized and ionic radii lattice parameters of $CsMX_3$ perovskites.

Compound	Exp.(Å)	DFT (Å)	Ionic (Å)
$CsPbCl_3$	5.605	5.605	6.000
$CsPbBr_3$	5.874	5.860	6.300
$CsPbI_3$	6.289	6.226	6.780
$CsSnCl_3$	5.504	5.504	5.000
$CsSnBr_3$	5.795	5.754	5.300
$CsSnI_3$	6.219	6.115	5.780

3.3 Inorganic perovskites results

3.3.1 Lattice optimization and bulk modulus

The first step of the calculation is the optimisation of the structure of the material. The energy of the materials depends on the atomic position and cell size. This set of variables determinates an energy hyper-surface called potential energy surface (PES). If the coordinates do not correspond to a minimum, the system is not in equilibrium and the atoms are subjects to forces. Naturally at 0 K the atoms tend to occupy the minimum thermodynamic if possible. To calculate where the absolute is locate in principle it is necessary to explore the whole PES. This is not practical, but there are algorithms design to find local minima and sample the PES to ensure that, within reasonable constrain such minima is also an absolute one.

Hence the first step of any calculation is the geometric optimization of a structure which is aimed to find the equilibrium positions of the atoms in the cell which minimizes the forces on the atoms. In our case, we decided to constrain the geometry of the inorganic perovskites to a perfect cubic symmetry. The optimization then adjusted the volume (lattice parameter) of the cell, keeping the atomic positions fixed. The results are reported in Table 3.1.

There is a small difference, around $\approx 1\%$, between the experimental and optimized results. This discrepancy increases with the atomic weight of the halogen, and it is due to the fact that the accuracy of the calculation decreases as the atomic number increases due to relativistic effects. Furthermore, cubic perovskites are high-temperature stable phases and some errors may arise from the fact that the DFT calculations do not take in account any thermal effects.

Table 3.1 also reports theoretical lattice constants obtained from tabulated ionic radii.[100] For cubic perovskite, the cell size is determined by the distance between the halogen and the divalent metal. The length is given by twice the sum of the metal and the halogen radii. In this case, the bonding also has partial covalent character, and for this reason there is a significant error between the DFT results and the value obtained from the tabulated ionic radii.

Another source of error in this method is the fact that the halide coordination in perovskites is 2, while usually the radii for a negatively charged iodine is fitted for 6-coordinate environment. The ionic radii are thus not particularly helpful to forecast the lattice parameters for future study about materials with experimentally not solved structures.

During the geometry optimisation the introduction of constrains, as the volume, permits to derived the energy dependence on them and fit data to equations of states to obtain thermodynamic quantities.

Thermodynamics relates macroscopic properties of a material with equations which describe a particular state of a system with comparison with an arbitrary *standard state*. The values of an equation of state are particularly useful because they depend only on the state taken in consideration and not on the process followed to obtain that state from the standard one. Since an equation of state relates different quantities it is possible to derive unknown quantities from known ones. For example, if the system is an ideal gas the following equation applies:

$$PV = nRT \tag{3.1}$$

where R is the *gas constant*, *n* the number of moles taken in consideration and *P*, V and T are pressure, volume and temperature. This allows one to obtain the temperature if the pressure and the volume of the system are known.

In solids the equation 3.1 is too simple and another formalism is needed. In our case we used the Birch-Murnaghan equation of state[166] in an isothermic condition to obtain the bulk modulus. The bulk modulus expresses the resistance to an isotropic compression of a substance. It gives information on the elastic properties of a material and it can be obtained solving the following equation:

$$P(V) = \frac{3B_0}{2}\left[\left(\frac{V_0}{V}\right)^{\frac{7}{3}} - \left(\frac{V_0}{V}\right)^{\frac{5}{3}}\right]\left\{1 + \frac{3}{4}\left(B_0' - 4\right)\left[\left(\frac{V_0}{V}\right)^{\frac{2}{3}} - 1\right]\right\}. \tag{3.2}$$

In this expression B_0 refers to the bulk modulus, B_0' is the first derivative of the bulk modulus with respect to pressure and V_0 is a standard reference value for the volume. From equation 3.2 is possible to derive a relation between the internal energy of the system and the cell volume:

$$E(V) = E_0 + \frac{9V_0B_0}{16}\left\{\left[\left(\frac{V_0}{V}\right)^{\frac{2}{3}} - 1\right]^3 B_0' + \left[\left(\frac{V_0}{V}\right)^{\frac{2}{3}} - 1\right]^2\left[6 - 4\left(\frac{V_0}{V}\right)^{\frac{2}{3}}\right]\right\}. \tag{3.3}$$

Finally we obtain the relationship between the bulk modulus and the quantities that we can calculate: the energy and the volume of a solid system. In order to obtain the bulk modulus one single calculation of the equilibrium structure is not sufficient because some derivatives are present in Equation 3.3. To obtain the derivatives we performed a set of calculations with different volumes, and the data obtained have been fitted to the Equation 3.3.

TABLE 3.2: Comparison between bulk modulus calculated in this study and values reported in literature.

Compound	DFT B_0 (GPa)	B_0 (GPa)	B_0 (GPa)
$CsPbCl_3$	22.4	25.8[180]	-
$CsPbBr_3$	19.1	23.5[180]	21.0[179]
$CsPbI_3$	15.3	19.5[180]	16.5[179]
$CsSnCl_3$	23.3	-	-
$CsSnBr_3$	20.0	17.5[181]	-
$CsSnI_3$	15.9	-	-

The calculated values are reported in Table 3.2. The trends agree well with published studies.[179–181]

The trends of the bulk modulus reflect the lattice parameter behaviour. In fact the smaller the lattice parameter the higher is the bulk modulus. Because the DFT-calculated lattice parameters are slightly larger than the experimentally observed values, it follows that there is a small underestimation of bulk modulus with respect to the experimental data.

3.3.2 Thermochemistry

We computed the enthalpy of formation to further characterize the material. In general, the enthalpy of formation is defined as:

$$H = U + PV \tag{3.4}$$

Usually, rather than considering the absolute value of thermodynamic quantities, it is more useful to refer to the variations of the quantities associated with a specific process (formation, crystallisation, ...). For solids the variation of enthalpy could be simplified because the variation of volumes is negligible with standard pressure and then the enthalpy could be substituted with the internal energy:

$$\Delta H_{sol} \approx \Delta U_{sol} \tag{3.5}$$

The perovskites enthalpy of formation then could be expressed as the difference from the DFT-calculated total energy of the perovskites and the sum of total energies of constituent elements in their standard state.

$$\Delta_f H = U_{comp} - \sum_{elements} U^{\ominus}_{el.} \tag{3.6}$$

To have the $U^{\ominus}_{el.}$, it is necessary to calculate, with DFT, the internal energy of the standard states of the elements that form the perovskites.

A problem arises in the case of Br. Since it is liquid in his standard state, it is not possible to compute it with a static simulation. Because of that the calculation

TABLE 3.3: Enthalpy of formation for the studied perovskites.

Compound	ΔH_f (kJ/mol)
$CsPbCl_3$	-752
$CsPbBr_3$	-636
$CsPbI_3$	-488
$CsSnCl_3$	-721
$CsSnBr_3$	-607
$CsSnI_3$	-462

for this element has been split in two steps. The first one was the calculation of the total energy of the gas phase, namely Br_2. The second one regarded the correction of the resulting energy adding the correspondingly standard enthalpy of liquefaction.

As it can be observed by the data showed in Table 3.3 the enthalpies of formation are negative and the compounds are more stable than the elements which form them. They can be formed if no other more stable competitive compounds are present.

3.3.3 Electronic structure

The solution of the Schrödinger equation formally permits us to calculate only the energy and the wavefunction of a system. DFT energy relies on the charge density and in principle it is independent from the wavefunctions. Nonetheless the charge density is obtained from a wavefunction introduced as a linear combination of Kohn-Sham orbitals. The Kohn-Sham orbitals are not necessarly the *real* orbitals, but for most cases can be used as a reasonable approximation.

The wavefunction contains all the properties of the system and they can be extrapolated in different forms such as: the band structure, the density of states (DOS) and the crystalline orbitals.

The band structure contains the information about all the states (energies) that electrons can or can not occupy in a periodic system. Because of the periodic nature of the compounds, the band structure is resolved in reciprocal space (the energy is then plotted against the momentum of the electrons). In particular the whole structure is not reported, but only the projection along the high symmetry lines, usually in the first Brillouin zone (BZ).

The band structure allows to visualize the value and the nature (direct or indirect) of the band gap, the presence of localized or de-localized states, the magnitude of the effective mass and other properties. A parameter that characterizes the band structure of a material is the band gap. It is defined as the minimum difference between the top of the valence band (VB) and the bottom of the conduction band (CB). A band gap is direct when the two extrema occur at the same point in reciprocal space, indirect otherwise. The importance of the band gap is due to the fact

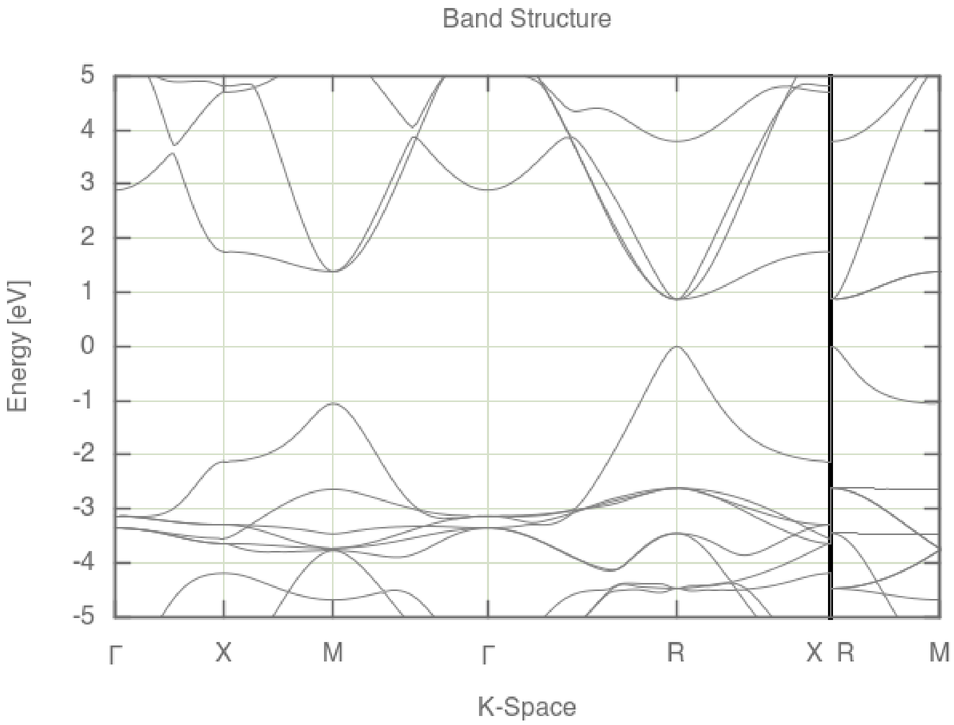

FIGURE 3.1: Band structure for the compound $CsSnI_3$ calculated with PBEsol0 exchange-correlation functional. The bands have been aligned in order to have the zero corresponding to the top of the conduction band.

that it determinates the energy needed to promote an electron from the VB to the CB. In case of a direct band gap the promotion can occur via the absorption of a photon. In order to promote an electron the photon must have an energy equal or larger than the band gap.

Instead, if an indirect gap is present, the bottom of the CB has a momentum value different from the top of VB. For this reason, beside the absorption of a photon, it is needed the annihilation/creation of a phonon in order to conserve the crystalline momentum.

The information of the band structure can be summarized by the density of states (DOS), which is obtained integrating the band structure along the momentum space as a function of the energy. Physically it represents the number of state, which can be occupied or empty for an electron, per unit of energy.

In Figure 3.1 is reported the band structure for $CsSnI_3$. The plotting directions have been chosen according to the space group of the compounds ($Pm\overline{3}m$, n. 221) as reported in the literature.[182]

The band structures of all materials show a direct band gap at the R point of the first BZ ($\frac{1}{2}$,$\frac{1}{2}$, $\frac{1}{2}$). Another direct gap is present at the M point (0.0 ,$\frac{1}{2}$, $\frac{1}{2}$), but it is significantly larger. In order to have a transition at that point it is needed the absorption of a photon with higher energy, but the transition is less probable. The shape of the band structure is similar through the different compositions.

TABLE 3.4: Data from PBEsol0 calculations for Energy band gap, HOCO and LUCO levels, and band gap deformation potentials for the inorganic perovskites.

Compound	E_G (eV)	HOCO (eV)	LUCO (eV)	α_v	α_p
$CsPbCl_3$	3.139	-6.174	-3.035	2.971	-21.242
$CsPbBr_3$	2.628	-5.965	-3.336	4.339	-36.451
$CsPbI_3$	2.218	-5.807	-3.588	3.518	-36.922
$CsSnCl_3$	1.600	-4.922	-3.322	5.905	-40.573
$CsSnBr_3$	1.139	-4.748	-3.610	5.738	-45.867
$CsSnI_3$	0.869	-4.705	-3.837	4.817	-48.562

The main difference is the position of the band, and hence the value of the band gap which always occurs in R.

The calculated band gaps are reported in Table 3.4. The compound containing Pb are significantly larger due to the spin-orbital coupling and relativistic effects. Halogens also play a role defining the band gap which decreases with the size of the halogen.

Because the band-gap depends on the shape of the cell and the inner coordinates of the atoms it is possible to relate it to the volume of the cell. This relationship lead to the definition of the band-gap deformation potentials, α_V, α_P[183]:

$$\alpha_V = \frac{\partial E_g}{\partial lnV} \tag{3.7}$$

$$\alpha_P = -\frac{1}{B}\alpha_V \tag{3.8}$$

These quantities describe the change of band gap with respect to hydrostatic volume and pressure changes, which can be important for electronic applications. Working devices can be subject of thermal or mechanical strain which affect the electronic properties. Deformation potential are useful to take in consideration the magnitude of those effects. The results are reported in Table 3.4.

The results are reported in Table 3.4 which also reports the energy values of the highest occupied crystal orbital (HOCO) and lowest unoccupied crystal orbital (LUCO). These particular orbitals are the projection in the real space of the valence and conduction bands. They are useful to understand which atoms participate to the formation of the band structure. The reference point for the energy is set by the software with respect to the average electrostatic potential of the free atom electron density. Substituting Cl with a heavier halogen, influence more the position of the LUCO rather than the HOCO. For example, the difference between the HOCO levels of $CsSnCl_3$ and $CsSnI_3$, is 0.217 eV against a difference of 0.515 eV for the LUCO levels. An opposite trend is observed substituting Sn with Pb. In fact, the shift is larger for the HOCO and it depends marginally on the halogen. This suggests that the VB is mainly formed by the halogen atom while the CB by the divalent metal.

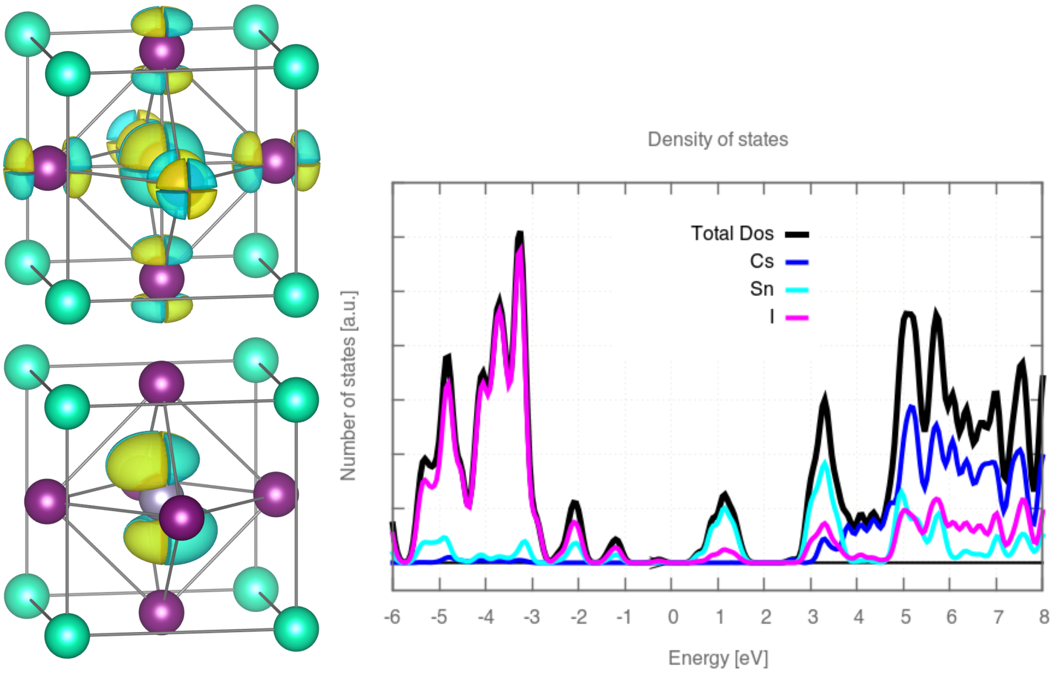

FIGURE 3.2: In the right panel is reported the plot of LUCO (top) and HOCO (bottom) orbitals for $CsSnI_3$ in correspondence of the band gap. The orbitals different phases are reported in yellow and blue. The left panel illustrates the DOS (black), resolved by atomic species(Cs = blue, Sn=light blue, I=violet) for $CsSnI_3$. The other compounds have similar properties.

We can observe this aspect analysing the crystalline orbitals plot. The crystalline orbitals are the portion of space where the probability to find an electron is maximum, or above a certain threshold. The probability of finding an electron in a portion of space is given by the integral over the space of the squared modulus of the wave-function. The charge density is obtained simply multiplying the probability by a unit charge. The nominal electronic charge of an atom is given restricting the integration on a portion of the volume surrounding such atom. Observing the plot of the charge density it could be understood the role of the element in the determination of the energy levels. The plot of charge density of the frontier orbitals for $CsSnI_3$ is illustrated in the left panel of Figure 3.2[1]. We calculate these orbitals using *PBEsol0* exchange correlation functional in correspondence of the R point. From the plotting of the orbitals is possible to extract more precise information than just observing the HOCO and LUCO energy values.

The HOCO is formed by *p-orbital*-like states of the Sn ion and this justify the fact that the HOCO is mainly influence by Sn and Pb. The LUCO is formed by a *p-orbital*-like states of the halogen and *s-orbital*-like states of Sn and confirms the importance of the halogen in defining the LUCO levels.

A further confirmation of this can be obtained also observing the element-solved

---

[1] The plot of the charge density coincides with the concept of orbital and the second term will be used in this discussion.

TABLE 3.5: Element of the reduced mass tensor for specific three directions along the minimum of the CB and the maximum of VB.

Compound	$m^*_{e^-,\Lambda}$	$m^*_{e^-,S}$	$m^*_{e^-,T}$	$m^*_{h^+,\Lambda}$	$m^*_{h^+,S}$	$m^*_{h^+,T}$
$CsPbCl_3$	0.300	0.791	0.777	-0.174	-0.179	-0.174
$CsPbBr_3$	0.236	0.715	0.721	-0.139	-0.139	-0.139
$CsPbI_3$	0.191	0.670	0.671	-0.127	-0.127	-0.127
$CsSnCl_3$	0.294	0.759	0.764	-0.087	-0.086	-0.085
$CsSnBr_3$	0.230	0.666	0.653	-0.055	-0.054	-0.054
$CsSnI_3$	0.190	0.656	0.653	-0.049	-0.049	-0.046

DOS reported in right panel of Figure 3.2. The VB is mainly formed by the halide levels and divalent metal states. On the other hand the CB is formed mainly by the to the divalent metal. This imply that the Cs atom does not play any fundamental role in the determination of the electronic properties of the material.

The electronic structure contains the necessary information to derive the properties of matter. For example, with respect to conductivity, what is defined as effective electron mass tensor is a direct consequence of the band structure. Because in DFT calculations, we deal with ideal infinite system it is possible to appeal to Bloch formalism for the definition of the effective electron mass tensor. In particular, from the band curvatures the effective electron mass tensor is defined as:

$$\left[\frac{1}{m^*}\right]_{ij} = \frac{1}{\hbar^2}\frac{\partial^2 \varepsilon(\mathbf{k})}{\partial k_i \partial k_j} \tag{3.9}$$

where $\varepsilon(\mathbf{k})$ indicates the energy of the band with wave vector $\mathbf{k}$, while i, j are the directions in the k-space.

In a semiconductor the conduction is associated to the promotion of an electron in the CB, and/or the generation of an hole in the VB. For this reason the carriers that are able to move are the one close to the frontier level, i.e. to the maximum of the VB for the holes, and to the minimum of the CB for electrons. In this case the band gap occurs at the R point. Hence the effective masses had been calculated in three different directions starting from the R point, as show in Table 3.5.

The three chosen direction are the following: Λ, from point $\Gamma(0,0,0)$ to $R(\frac{1}{2},\frac{1}{2},\frac{1}{2})$, S from R to $X(0,\frac{1}{2},0)$, T from R to $M(\frac{1}{2},\frac{1}{2},0)$.

From this data we can observe that the electronic reduced masses are higher than the holes masses. Nonetheless the values are comparable. This confirm the nature of this class of perovskites as ambipolar conduction materials with a preferable applications as HTM.

For the electronic carriers Λ is a preferred direction of transport and the reduced mass in that direction decrease as the halogen increases in mass. The values for the other two directions don't change significantly with the composition and are similar in the studied perovskites.

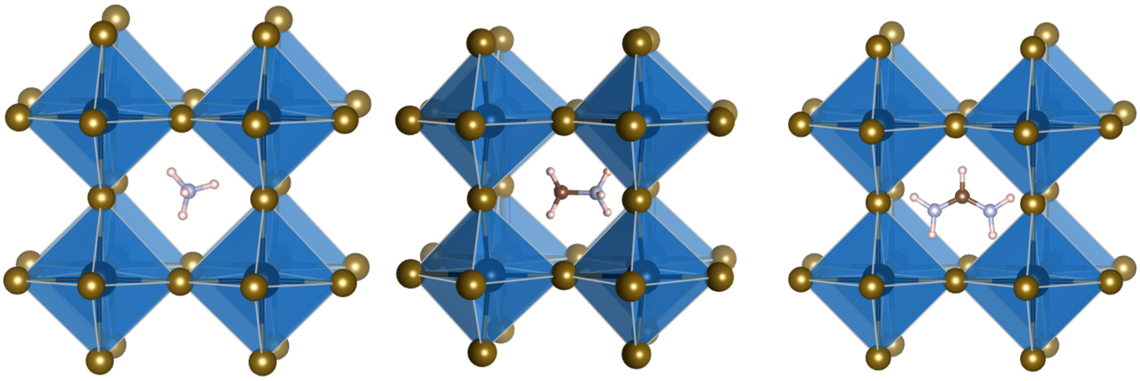

FIGURE 3.3: The figure reports the three hybrid perovskites: API, MAPI and FAPI. The organic cations occupy the center of the cell, while the halides form an octahedra coordination environment around the metallic ion.

The hole reduced masses, on the other side, are almost perfectly anisotropic along all the three chosen directions.

The electronic cloud for heavier halogen is more diffused and this lead to a larger mobility for the electron, and, in fact, a reduction of electronic mass is observed. At the same time hole masses for Sn compounds are smaller than the corresponding Pb compound, suggesting a lower hole mobility for the latter.

3.4 Hybrid perovskite results

3.4.1 Structure optimization

The structure of hybrid perovskite is analogous to inorganic perovskites, discussed previously. The main difference is that the Wyckoff a-site $(0.0, 0.0, 0.0)$ is occupied by an organic cation. The most common and widely investigated hybrid perovskite is methylammonium lead iodide, $CH_3NH_3PbI_3$ (MAPI), shown in the central panel of Figure 3.3. Nonetheless we consider other hybrid materials: formamidinium lead iodide, $CH(NH_2)_2PbI_3$ (FAPI), and ammonium lead iodide NH_4PbI_3 (API) also reported in the other panels of Figure 3.3.

The presence of an organic cation in the cell breaks the symmetry of the structure and affects the optimization. This aspect is particularly problematic because at the time of the first calculation the structures were not completely solved in literature.

The experimental measurement are complex to the presence of different phases, partial occupation and orientation of the organic cations. As much in the laboratory as in the simulations, the main complications consist in finding the position of the molecules inside the cage.

With consistency to the initial space group reported, the organic cations could have occupied different positions with different orientations. This situation generates a very large configuration space that is unlikely to be completely explored

TABLE 3.6: Results of the geometric optimization obtained with PBEsol functional. As parameter of the pseudo-cubic cell has been reported the average of the three different lattice parameters.

Compound	Cubic cell (Å)	Pseudo-cubic cell
$APbI_3$	6.26	6.21
MAPI $< 100 >$	6.21	6.29
MAPI $< 110 >$	-	6.26
MAPI $< 111 >$	-	6.28
$FAPbI_3$	6.46	6.47

by optimization algorithms. To proceed, we applied different approximations in order to get a reasonable starting structure.

Firstly, we considered only the high-temperature cubic phases, the isotropic lattice is easier to model and worked as a general test case for the study of the other perovskite phases. Regarding the molecule we ignored the different conformations that arise from the hydrogen atoms. We assumed the hydrogens to be in eclipsed conformation which is generally more stable in the order of fractions of eV. The position of the molecule in the cell was decided with respect to geometric considerations. The ammonium ion was put with the nitrogen atom in the exact center of the molecule, analogously for FA the carbon was put in the center of the cell. MA instead was positioned in order to have the middle point of the C−N bond at the center of the cell.

If the H positions are ignored there is only one possible orientation for ammonium (NH_4^+). MA ion has a cylindrical shape, so we decided to consider three different orientations of the molecule aligning the C−N bond to the three directions: $< 100 >$, $< 110 >$, $< 111 >$, within the cubic perovskite cage.

In the case of FA we took in consideration only one position for simplicity, even if it can be positioned in different orientation. In our case the molecule was oriented in order to belong to a plane parallel to the cell face, and with the bisecting line of the angle N−C−N aligned to one edge of the cell. We picked only this configuration because it fits the inorganic cage in a reasonable way.

We performed an initial optimization of the cell volume performing energy-volume curves. During the calculation we modify only the lattice parameters and we keep constant the bond-length of the organic molecule. From this initial set of structures we used VASP quasi-Newton (QN) and conjugated-gradient (CG) algorithms to perform a second volume optimization and finally a global optimization of all the parameters.

The lack of symmetry lead to a break of the cubic lattice configuration, but this distortion is in general small, about 2% in terms of lattice parameters, so we decided to use the word *pseudo-cubic* to describe the structure. This term is useful to identify the perovskite nature of the compound without ignoring the critical role of the organic ions. Table 3.6 report the lattice length of the cells obtained.

TABLE 3.7: Enthalpy of formation for the studied perovskites in the pseudo-cube cells.

Compound	ΔH_f ($^{\text{kJ}}/_{\text{mol}}$)
A	-439
MA	-571
FA	-591

The energetics for MAPI does not strongly depend on the organic molecule orientation. Nonetheless we considered for further calculation the minimum energy configuration where the MA cation lays along the $< 100 >$ direction.

3.4.2 Thermodynamic stability

We also calculated the enthalpy of formation and the electronic properties of the hybrid perovskites, similarly to what we did with inorganic ones computing the standard states of the elements involved. Table 3.7 reports the values obtained for the enthalpy of formation. The values are similar to the inorganic iodide perovskite and the presence of the molecules does not change significantly the enthalpy of formation.

MAPI has been experimentally reported with structures similar to the one we consider. On the other hand API has never been reported in a three-dimensional crystal phase, but only in a structure with lowered dimensionality.[184] This effect is due to the small size A^+ that allows it to form a discontinuous lattice. Nonetheless, in principle, the pseudo-cubic phase of API is stable against its constituent and we used it to investigate the role of cation size in hybrid perovskites.

3.4.3 Electronic structure

We consider here the analysis of the electronic and structural properties of hybrid perovskites, with a particular focus on MAPI and API. Formally the structures have symmetry (P1) and no high symmetry directions are present. As an example, in Figure 3.4 is shown the dispersion along eight different lines from Gamma to points (± 0.5,± 0.5,± 0.5). The dispersion is similar in the different direction, so we decided to plot the bands structure following the high symmetry directions belonging to the $Pm\overline{3}m$ (n. 221) space group. In this way the band structure are consistent with the ones reported for the inorganic perovskites.

Substituting the central Cs ion does not affect significantly the shape of the electronic structure. The two band structures are reported in Figure 3.6.

The band gap occurs at the R point, and a second larger gap is present at the M point. At the Γ point the VB is quite flat. The value of the band gaps are reported in Table 3.8. For MAPI we also considered different cases where the central cation has different orientation, but it does not effect significantly the band gap value.

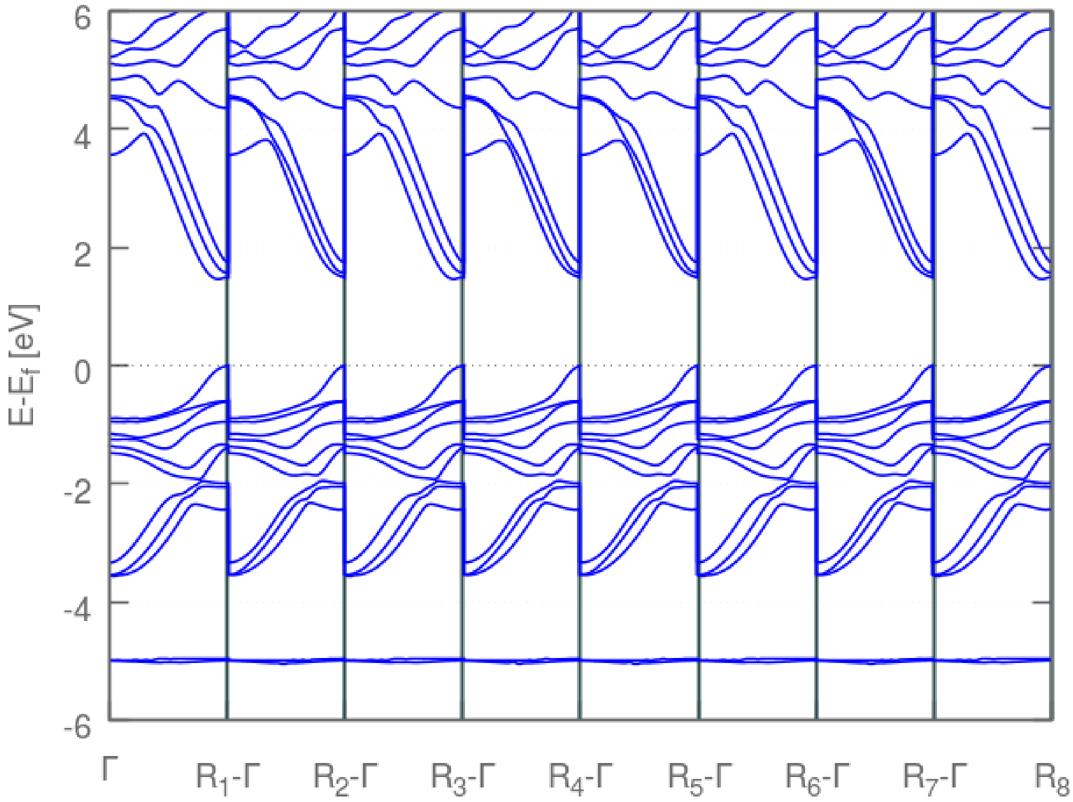

FIGURE 3.4: Dispersion from Gamma to the eight possible R (±0.5,±0.5,±0.5) points for MAPI in the pseudo-cubic perovskite cell. The profile of the band structure is quite similar with small deviations if different directions are compared.

TABLE 3.8: Band gap for API and MAPI in function of the cation position. The value has been calculated using the GGA PBEsol functional.

Material	Band Gap [eV]	ϵ_0 (ϵ_0^{xx},ϵ_0^{yy},ϵ_0^{zz})	ϵ_∞ (ϵ_∞^{xx},ϵ_∞^{yy},ϵ_∞^{zz})
APbI	1.20	(18.62,18.47,18.14)	(6.49, 6.49, 6.47)
MAPbI - <100>	1.38	(22.39,27.65,17.97)	(6.29, 5.89, 5.75)
MAPbI - <110>	1.37	(17.95, 23.56, 22.67)	(5.62, 6.54, 6.26)
MAPbI - <111>	1.37	(36.52, 37.28, 24.94)	(6.10, 6.10, 5.92)

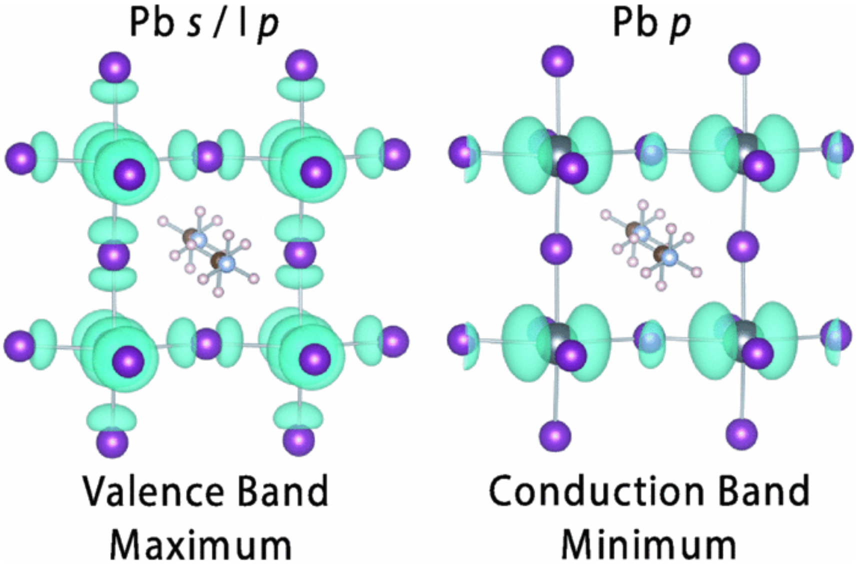

FIGURE 3.5: Band structure for MAPI valence band maximum (right) and conduction band minimum. The structure have been obtained with PBEsol functional. Image taken from reference.[185]

Analogously with Cs cation, also the organic does not affect the the band gap, because, as we can observe, its levels lie deep in the valence band around 5 eV below the Fermi energy, and they do not take part to the bands edges. Those levels are flat and denote the localized nature of those states.

Nonetheless the central cation plays an indirect role on the band gap because it affects the size of the cage. Smaller cation result in a smaller cage, facilitating the overlap of atomic species with a consequent reduction of the band-gap. In Figure 3.5 are shown the orbitals corresponding to the top of VB and the bottom of CB for MAPI.

From the plot, it can be seen that the top of VB is formed by the Pb s states and the I p orbitals, while the bottom of CB is mainly formed by the Pb p orbitals.

3.4.4 Band gap and spin-orbit coupling

The calculation of electronic levels for heavy atoms needs the introduction of an usually neglected correction due to relativistic effects. The most significant one is the spin-orbital coupling (SOC) and it is responsible for the split of degenerate atomic or crystalline levels due to the coupling between the angular momentum ($\boldsymbol{L}$) and the spin ($\boldsymbol{S}$) of electrons. This results in a split proportional to the product $\boldsymbol{L} \cdot \boldsymbol{S}$. In the solid state the SOC interests mostly the states across the Fermi energy hence the band gap of material. Such impact is significant in hybrid perovskites due to the presence of Pb. The inclusion of SOC closes the band gap, reducing it by $\approx 1\,\text{eV}$.

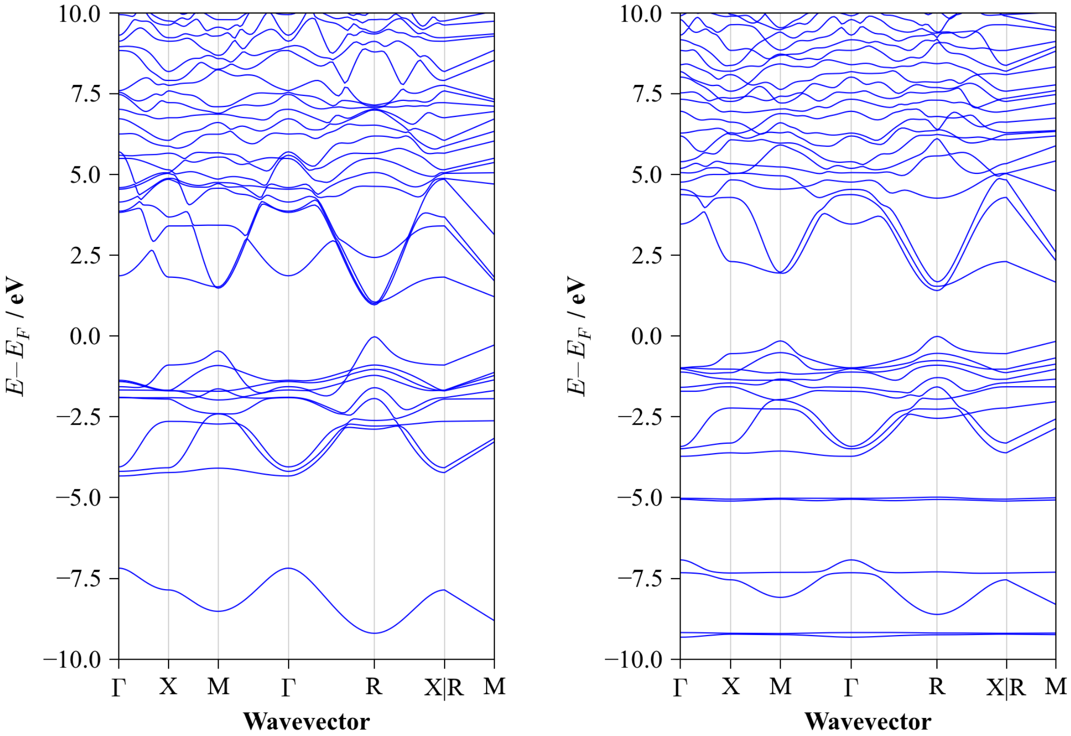

FIGURE 3.6: Band structure for $APbI_3$ (left) and MAPI(right). The structure have been obtained with PBEsol functional.

Nonetheless the MAPI calculations performed without including SOC are in good agreement with the experimentally reported band gap (1.61 eV)[186]. This agreement is due to errors compensation at the GGA-PBEsol level where the absence of SOC is cancelled out by the lack of many-body interactions.

The many-body effects can not be caught by DFT approach and will be explained further in following sections.

3.4.5 Dielectric permittivity

The dielectric permittivity (ϵ) measures the response of a material to an electric field with frequency ω accordingly to the dynamic of the atoms involved.

The dielectric response is a rank 2 tensor, and each component is not necessary parallel to the applied field. Nonetheless the main contributions lie on the diagonal (ϵ_{ii}) of the tensor and we can focus on those values. The dielectric permittivity is crucial to determinate the screening of the charges in a material, and then controls key aspects of the physics of a material as the electron-hole interaction and the formation of exciton or polarons.

Using the density functional perturbation theory (DFPT) we calculated the diagonal components of dielectric permittivity in the limit of a static field (ϵ_0) and of a field with infinite (faster than any atomic response) frequency (ϵ_{inf}). The results are shown in Table 3.8.

The responses are anisotropic for API due to the high symmetry of the ammonium cation, while there are small deviation in the values for MAPI that depends on the molecule orientation. The high frequency component are comparable to the value of other semiconductors ($\epsilon^{300k}_{\text{inf},GaAs} = 10.90^{187}$) and in the case of MAPI the orientation of the molecule determinates the presence of a component with higher value. The response to a static field behaves similarly, but the value is higher, in particular for MAPI. These value are higher than the one observed for other semiconductors ($\epsilon^{300k}_{\text{inf},GaAs} = 12.85^{187}$).

This anomaly can be explained considering the softness of the structure and the easiness of rearrangement to an external stimuli of the central molecule. This high value can screen the electron-hole interaction leading to a longer life time of the charge carriers in photovoltaic devices.

3.5 Beyond the ideal crystal

3.5.1 Molecular rotation

DFT is an athermal theory that does not take into consideration any thermal effect and it is often considered as a 0 K system. As a consequence the geometry optimization returns the most stable structure, and all the properties are derived for this structure in a static fashion. However at a finite temperature the structure could be different with different properties.

In the case of MAPI the thermal energy could be enough to put in motion the molecule at the center of the cage. To understand this aspect we calculated the rotational barrier of the molecule.

To simulate the rotation we calculated a set of single point structures where the molecule is positioned in different directions keeping the inorganic cell frozen. This assumption was made assuming that the movement of the molecule would be faster than the rearrangement of the cell. This is justified by the fact that Pb and I have greater mass, hence higher inertia compared to organic cations.

Instead of considering the optimized quasi-cubic lattice we relied on an ideal perfect cubic cell with higher symmetry. This choice permits us to assign a simple orientation of the molecule inside the cage. We rotate the molecules around the cell center spanning planes (100) and (110) in just one octant of the space. The result was a set of energy-curves like the one reported in Figure 3.7 from which we extracted the rotation barrier. Table 3.9 reports the energy-barrier for the rotation of the molecules.

As expected the barrier depends on the size of the molecule. The rotation barrier for ammonium in the cage is very shallow, indicating the absence of a strong interaction between iodine and the hydrogens. Implicitly these results validate

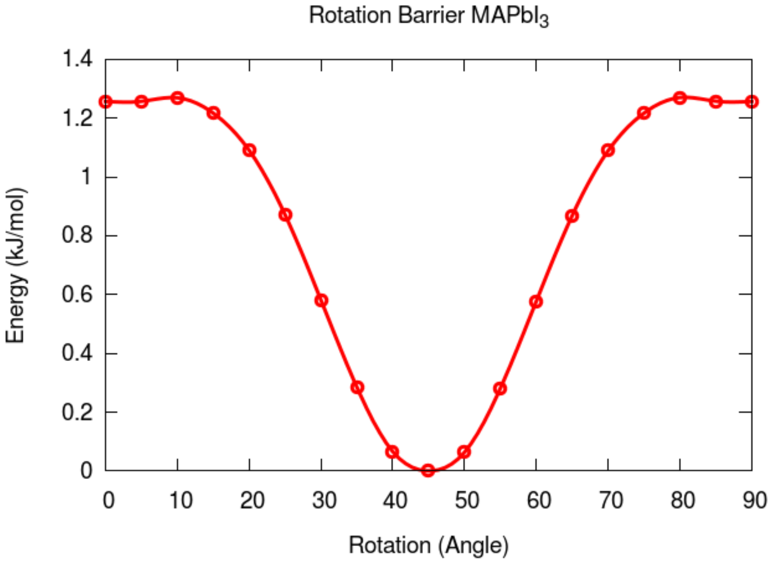

FIGURE 3.7: Rotation barrier of a molecule of MA inside the inorganic cage from the $< 100 >$ direction to $< 010 >$. The minimum energy is found for the molecule tilted of 45^o along the $< 110 >$ direction even if the most stable structure we found was aligned with the starting configuration. This behaviour is due to the fact that the rotation has been performed without the optimization of the structure and in an ideal cubic cage.

TABLE 3.9: Rotation barrier for different organic cations in the lead iodide perovskite cage.

	A	MA	FA
Rotation barrier (kJ/mol)	0.3	1.3	13.9

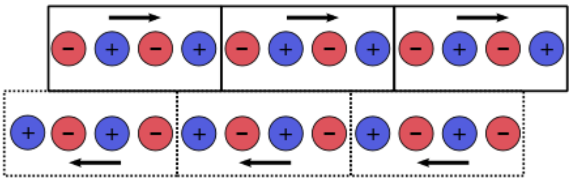

FIGURE 3.8: In a crystal the direction of the polarization vector depends on the choice of the crystallographic cell. In this example, the shift of the cell invert the direction of the vector.

the initial decision of ignoring the hydrogen atoms to determinate the different position of the molecule. The value for MA is larger but it is compatible with room temperature rotation. It is possible to assume that, in standard conditions, the molecules are not frozen in a specific position, but they rotate. This also highlights the difficulties to experimentally solve the atomic structure.

3.5.2 Berry phase analysis

DFT methodology gives access also to macroscopic properties than depends on local configuration. In the case of perovskite an interesting property regards the polarization. Coherent displacements in materials without an inversion center can lead to an asymmetric charge distribution, than gives rise to a spontaneous polarization.

In a molecular system defined in a volume V with charge density ρ the dipole moment in a point $\mathbf{r}_0$ is:

$$\mathbf{p}(\mathbf{r}_0) = \int_V \rho(\mathbf{r})\,(\mathbf{r} - \mathbf{r}_0)\,d^3\mathbf{r} \tag{3.10}$$

The same definition does not hold for an ideal crystal because the polarization value depends on the choice of the crystallographic unit, an example is reported in the cartoon of Figure 3.8.

To solve this limitation, the polarization in a crystalline material can be calculated using the Berry Phase analysis. This method does not give an absolute value of polarization to a system, but instead gives a polarization relative to a reference center. The polarization of a particular structure is obtained from a structural parameter λ that continuously transforms the reference structure in the one of interest. The results are independent of the choice of λ and of the reference. A useful approach is to identify a non polar structure (i.e. with an inversion center) and gradually distort it in the wanted structure.

We discussed how perovskites show different properties related to the presence of possible distortions that change the charge distribution. In inorganic perovskite the distortion usually considers the displacement of the cations with octahedral coordination away from the high symmetry site.

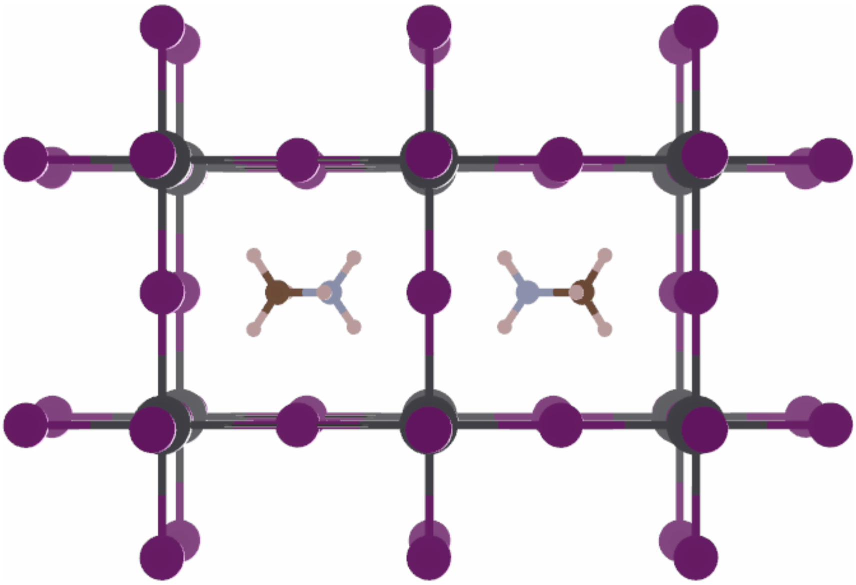

FIGURE 3.9: Centrosymmetric 2×1×1 MAPI supercell used to calculate the Berry phase. As it is observable the molecules are anti-aligned with a zero dipole

In the case of MAPI instead, the MA^+ cation can not occupy the center of the cage for steric effect, so it is naturally displaced. We wanted to explore how the polarization changes as the molecule rotates inside the cage. In order to do so, we consider an apolar cell with a center of inversion. Because it is impossible to build a single MAPI cell with such property we consider a $2\times1\times1$ supercell reported in Figure 3.9. We fully optimized the cell keeping the symmetry space group in order to maintain the inversion center.

As the λ parameter we consider the rotational angle of one molecule around one of the axis and we generated a set of structures that describe the molecule rotation. We rotate the molecules with a 15° step as pictured in Figure 3.10, where only some structures are reported for clearness.

For each one of these it is possible to calculate the polarization components due to the electron and to the ionic positions. The results are reported in Figure 3.10.

The total polarization has a maximum value of $5.74\,{}^{\mu C}/_{cm^2}$ when the two organic molecules are anti-aligned. This value is smaller compared to other perovskites, for example $KNbO_3$ has a polarization value of $30\,{}^{\mu C}/_{cm^2}$. The presence of a strong polarization could lead to the formation of micro-domains that could enhance the photovoltaic effect.

3.5.3 Surfaces

To understand the behaviour of real devices it is necessary to move away from ideal crystals. One feature to be introduced in perfect crystal is the breaking of PBC to form a surface. Surfaces play a crucial role in any PV device because they set the position of the energy levels at the interfaces. For example, if different

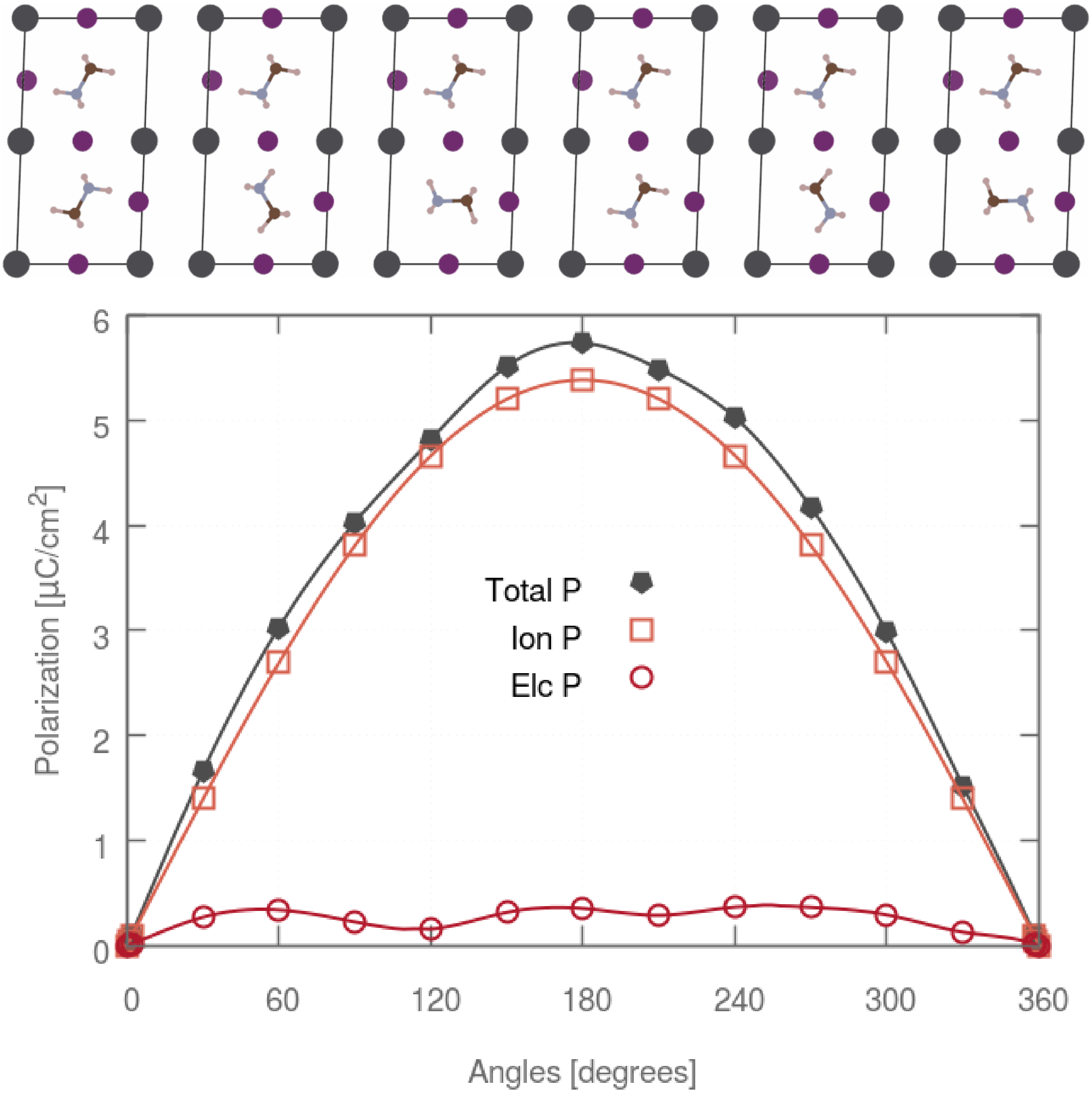

FIGURE 3.10: The top row reports the structures obtained rotating one the MA molecules with incremental steps of 60° in MAPI. Below is plotted the total, ionic and electronic polarization in function of MA$^+$ rotation in a 2×1×1 supercell. The maximum total polarization occurs for anti aligned molecules, 180 ° is 5.74 $^{\mu C}/_{cm^2}$, with a 5.39 $^{\mu C}/_{cm^2}$ ionic component.

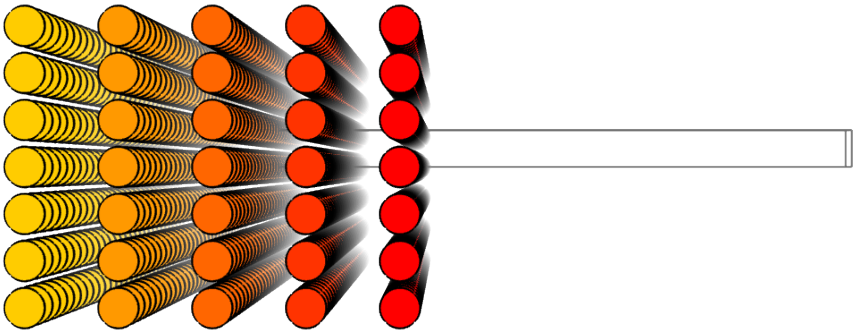

FIGURE 3.11: Scheme of a surface slab, the black lines indicate the surface cell which include also the vacuum layer.

materials are put in contact the reciprocal position of the energy levels can determinate if it is possible to inject a charge from one material to another, or if a specific material works as a blocking layer.

An ideal surface is the interruption of the periodic boundary conditions along a lattice plane. In reality, not every possible surface is observed and other phenomena occur. Generally, only the surface generated by planes with low Miller index are observed. Atoms at the surfaces can rearrange breaking the bulk symmetry at the surface to minimize the energy. For these reasons, the modelling of surfaces represents a computational challenge.

Firstly, it is necessary to select which surfaces are interesting for the desired study. Secondly, to perform the calculations one needs to consider the presence of surface dipoles, and non-stoichiometric structures or other surface behaviour that have to be included.

VASP and other all planewave codes have been written with the intention of studying crystals and PBC can not selectivity chosen. In order to simulate the interruption of PBC perpendicular to the surface, a workaround is necessary. The crystal cell must be enlarged, introducing an empty space above the surface. In this way, the software will then reproduce slabs of material separated by vacuum. An example of a cell used to simulate a surface is reported in Figure 3.11. The size of this empty space must be set in a way that the replica slabs are distant enough to not interact each other. If the unit cell is small, it is also necessary to build a supercell before introducing the vacuum. In fact, the slab must be thick enough to approximate the bulk properties of the material at its core.

Since no experimental data about surface morphology of hybrid perovskites has been reported, we used the software METADISE[188] to generate the possible different structures. METADISE takes into account the geometry and the basic electrostatic properties of the surfaces in order to remove any equivalent or polarized surfaces, but does not exclude slabs with different surface moieties. These types of slab are called anti-symmetrical and should be manually excluded for our purposes. In the case of hybrid perovskites the presence of the organic ions makes the structure too complex to enumerate the significant surfaces. For this reason, we computed the surfaces for an equivalent supercell $(2 \times 1 \times 1)$ of $CsPbI_3$ with METADISE, and afterwards substituted the Cs atom with the organic molecules.

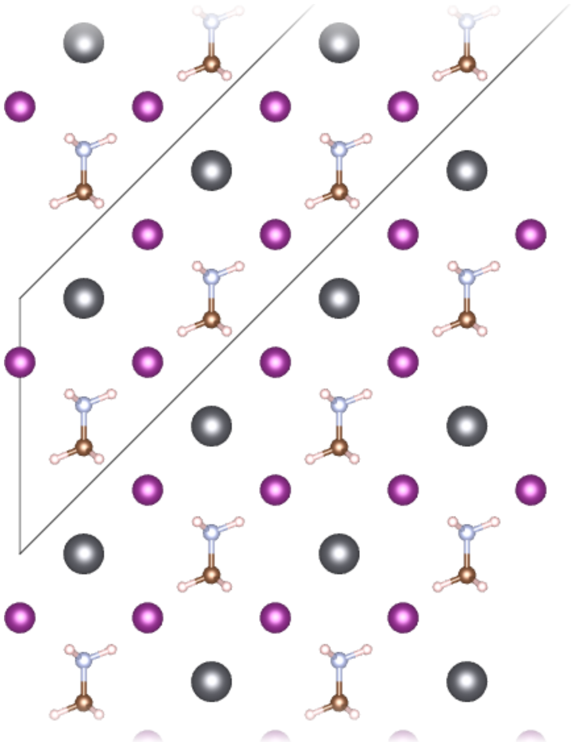

FIGURE 3.12: Representation of $< 110 >$ surface slab for MAPI. The MA is aligned to the surface. The black line delimit the cell, the vacuum part of the cell is not reported for simplicity.

MA and FA had been positioned lying parallel to the surface. One of the surfaces studied is pictured in Figure 3.12

With this procedure only two different surfaces along the $< 110 >$ plane were found, but because one of the two was anti-symmetrical we excluded it.

The work function is the minimum energy required to extract one electron from a surface. It can be described as the energy difference between the top of the VB and the vacuum level. If the work function is known, it is an absolute reference that can be used to align on an absolute scale band structures of different materials.

In our calculation we defined the work function as the energy difference between the top of the VB in the bulk and the potential in the vacuum level. To provide an absolute alignment of the energy levels, we used the Pb 1s level as a reference state between the surface and the bulk calculation. The work function could then be defined as:

$$w = U_{vac} - \epsilon_{VB,bulk} - \Delta_{\epsilon_{1s}}. \tag{3.11}$$

Where U_{vac} is the potential energy of the vacuum, $\epsilon_{VB,bulk}$ is the energy of the bulk VB and $\Delta_{\epsilon_{1s}}$ is the energy difference between the 1 s core levels. The results are reported in Table 3.10, while Figure 3.13 reports an example of the electrostatic potential for a slab of API.

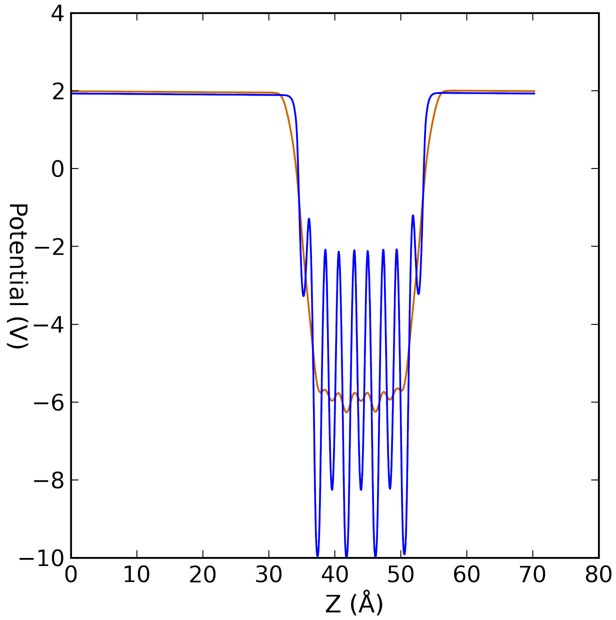

FIGURE 3.13: Planar averaged electrostatic potential for a $APbI_3$ slab. The potential oscillates in correspondence of the slab and plateaus to a vacuum level outside it.

TABLE 3.10: Calculated values of the work function of hybrid perovskites, namely ammonium lead iodide (API, formamidinium lead iodide (FAPI) and methylammonium lead iodide (MAPI). For MAPI we computed four different configurations. In *a*, the molecules are aligned to form a striped pattern, while in *b* they are anti-aligned in a head-tail motif. Configurations *c* and *d* are analogous, but the molecules are rotated of 90 ° with respect to *a* and *b*.

	API	FAPI	MAPI - *a*	- *b*	- *c*	- *d*
DFT Work Function (eV)	5.78	5.17	5.75	5.77	5.76	5.78
	TiO_2	MAPI	spiro-MeOTAD			
Exp. Work Function (eV)	7.0[189]	5.4[190,191]	5.1[189]			

In the case of MAPI, since the molecule has a dipole moment (2.29 Debye[192]), we considered different surfaces which differ in the mutual orientation of the MA molecules. In order to do this, we calculated the polarization of different orientation of the MA molecules using the Berry Phase analysis provided in VASP. We defined four different motifs labelled a, b, c, d. In the a structure the molecules form a striped pattern, while in b they are anti-aligned in a head-tail motif. c and d are equivalent structures to a and b, but with the molecules rotated $90\,^o$. From the data reported in Table 3.10 we can conclude that the orientation of the molecule does not play an important role in the work function. Our results are in accordance with the experimental values for MAPI[110] and are compatible with an ideal device where the perovskites acts just and active material, while the charges are transported by TiO_2 and spiro-MeOTAD.

3.6 Publications

The first publication regards the initial calculation of electronic structure of MAPI and API using DFT and DFPT was published in APL Materials (2013). Comparing different methods the paper outlines the key properties of the material that stands behind the high photovoltaic efficiencies of perovskites based solar cells.

The results on electronic structure were extended in collaboration with Prof. Mark van Schilfgaarde in King's College London. This results in a second paper published in Physical Review B (2014) that included many-body GW calculations on the same system. GW methods permits to recover the many-body effects neglected in DFT. This leads to a better description of the behaviour of hybrid perovskites. In particular it emerges a similarity with typical inorganic semiconductors (i.e. GaAs) in the adsorption spectra, and the presence of the Rashba splitting, both effects that could better explain the surprising performance of hybrid perovskites as light harvester.

Both publication are reproduced under Creative Commons license.

APL MATERIALS **1**, 042111 (2013)

Structural and electronic properties of hybrid perovskites for high-efficiency thin-film photovoltaics from first-principles

Federico Brivio,[1] Alison B. Walker,[2] and Aron Walsh[1,a]
[1]*Centre for Sustainable Chemical Technologies and Department of Chemistry, University of Bath, Claverton Down, Bath BA2 7AY, United Kingdom*
[2]*Department of Physics, University of Bath, Claverton Down, Bath BA2 7AY, United Kingdom*

(Received 14 August 2013; accepted 20 September 2013; published online 10 October 2013)

The performance of perovskite solar cells recently exceeded 15% solar-to-electricity conversion efficiency for small-area devices. The fundamental properties of the active absorber layers, hybrid organic-inorganic perovskites formed from mixing metal and organic halides [e.g., $(NH_4)PbI_3$ and $(CH_3NH_3)PbI_3$], are largely unknown. The materials are semiconductors with direct band gaps at the boundary of the first Brillouin zone. The calculated dielectric constants and band gaps show an orientation dependence, with a low barrier for rotation of the organic cations. Due to the electric dipole of the methylammonium cation, a photoferroic effect may be accessible, which could enhance carrier collection. © *2013 Author(s). All article content, except where otherwise noted, is licensed under a Creative Commons Attribution 3.0 Unported License.* [http://dx.doi.org/10.1063/1.4824147]

Progress in the performance of hybrid pervoskite solar cells has rapidly advanced over the last five years.[1–6] They represent the convergence of inorganic thin-film and dye-sensitised solar cells.[7] The conversion efficiencies have quickly surpassed both those of conventional dye-cells, as well as next-generation thin-film absorbers such as Cu_2ZnSnS_4.[8,9] Despite their high-performance for small area (∼0.2 cm^2) cells, the underlying material properties are largely unknown, which could help with producing more robust large-area devices.

Perovskite refers to the crystal structure of the mineral $CaTiO_3$, which is adopted by a large family of ABX_3 materials, with two notable examples being $SrTiO_3$ and $BaTiO_3$ (Figure 1). They are well known for their phase complexity, with accessible cubic, tetragonal, orthorhombic, trigonal, and monoclinic polymorphs depending on the tilting and rotation of the BX_6 polyhedra in the lattice.[10] Phase transitions are frequently observed under the influence of temperature, pressure, and/or applied electric field.

While oxide perovskites (ABO_3) are formed from divalent A^{II} (1*b* site – cuboctahedral) and tetravalent B^{IV} (1*a* site – octahedral) metals, halide perovskites (e.g., ABI_3) can be formed from monovalent A^{I} and divalent B^{II} metals. For example, the application of $CsSnI_3$ in solar cells has recently been demonstrated.[11] Hybrid organic-inorganic perovskites are produced by replacing one of the inorganic cations by an isovalent molecule, e.g., $CsSnI_3 \rightarrow (NH_4)SnI_3$, where NH_4^+ (A) is the ammonium cation. Recently, the methylammonium (MA) cation (i.e., $CH_3NH_3{}^+$) has been widely applied, resulting in the highest-performance perovskite-structured photovoltaic absorbers.[2,3] More generally, a large series of hybrid perovskites have been reported, which vary in their dimensionality and the orientation of the underlying perovskite lattice.[12–15]

In this letter, we assess the properties of the two archetypal hybrid perovskites $(NH_4)PbI_3$ and $(CH_3NH_3)PbI_3$ using density functional theory (DFT) for the ground-state properties and density functional perturbation theory (DFPT) for the dielectric and optical response functions. We provide

---

[a]Electronic mail: a.walsh@bath.ac.uk

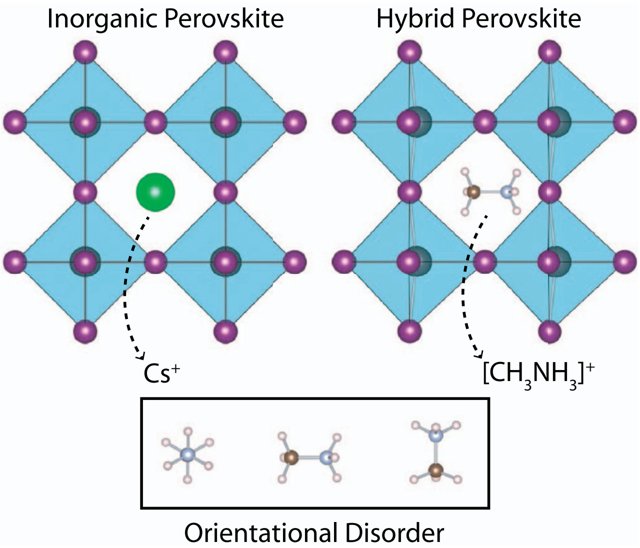

FIG. 1. Illustration of the perovskite structure based on corner sharing octahedra of BX_6 with either a monovalent metal (inorganic) or charged molecule (hybrid) at the centre of the unit cell. For hybrids, there is an orientation dependence on the central cation.

insights into the key properties required for device models and screening procedures and that underpin their utility in photovoltaic cells.

Characterisation of the crystal structures of inorganic perovskites is difficult, and hybrid perovskites are even more challenging. Recent analysis of high-quality $(MA)PbI_3$ crystals identified cubic ($Pm\bar{3}m$), tetragonal ($I4/mcm$), and orthorhombic ($Pnam$) phases from X-ray diffraction, while transmission electron microscopy suggested a pseudo-cubic behaviour that is consistent with variability in the octahedral titling and/or rotations.[16] For our investigation, we take a cubic basis, starting from the $Pm\bar{3}m$ lattice, and investigate the potential energy landscape associated with the molecular orientation.

The crystal structures (internal forces and external pressure) were optimised at the level of DFT, with the exchange-correlation functional of Perdew, Burke, and Ernzerhof revised for solids (PBEsol).[17] The Pb $5d$ orbitals were treated as valence and scalar-relativistic effects are included. Further calculations were made using a non-local hybrid exchange-correlation functional (HSE06).[18] Calculations were performed using the VASP code,[19] a 500 eV plane-wave cut-off, and reciprocal space sampling of $6 \times 6 \times 6$ k-point density. Internal structural parameters were converged to within 5 meV/Å, and the phonon frequencies were checked at the zone-centre to ensure that no imaginary modes were present. The high-frequency (ϵ_∞) and static (ϵ_0) dielectric constants were computed using DFPT[20] based upon a tightly converged electronic wavefunction (within 10^{-9} eV) and a denser grid of $10 \times 10 \times 10$ k-points.

For $(A)PbI_3$ there is no strong orientation dependence of the ammonium ion owing to its approximately spherical topology. A local minimum structure is found where the four hydrogens are directed towards interstitial positions. For $(MA)PbI_3$ the behaviour is more subtle owing to a molecular dipole (of strength 2D) associated with the methylammonium ion (i.e., $[CH_3]^{\delta+} - [NH_3]^{\delta-}$). We identified three local minima, where the dipole is aligned along of the $\langle 100\rangle$, $\langle 110\rangle$, and $\langle 111\rangle$ directions, relative to the origin of the cubic lattice (Figure 1). The total energy difference is within 15 meV per atom, with the $\langle 100\rangle$ orientation being most stable. The absence of a significant barrier to rotation (<40 meV) is consistent with labile movement under standard conditions. Indeed, ^{2}H and ^{14}N spectra have confirmed that MA cation rotation is a rapid process at room temperature.[21]

The predicted lattice constants for $(MA)PbI_3$ vary from 6.26 to 6.29 Å (Table I) depending on the molecular orientation. These compare well to the value of 6.26 Å obtained from powder diffraction measurements[16] and 6.33 Å from computations.[22] Distortions of the PbI_6 octahedra are observed for

TABLE I. Predicted materials properties of hybrid perovskites, from density functional theory (PBEsol functional), where (MA) refers to the CH_3NH_3 cation. The diagonal of the dielectric tensors is given as ϵ^{xx}, ϵ^{yy}, and ϵ^{zz}.

Material	a (Å)	E_g (eV)	ϵ_0	ϵ_∞
$(NH_4)PbI_3$	6.21	1.20	18.62, 18.47, 18.14	6.49, 6.49, 6.47
$(MA)PbI_3 - \langle 100\rangle$	6.29	1.38	22.39, 27.65, 17.97	6.29, 5.89, 5.75
$(MA)PbI_3 - \langle 110\rangle$	6.26	1.37	17.95, 23.56, 22.67	5.62, 6.54, 6.26
$(MA)PbI_3 - \langle 111\rangle$	6.28	1.37	36.52, 37.28, 24.94	6.10, 6.10, 5.92

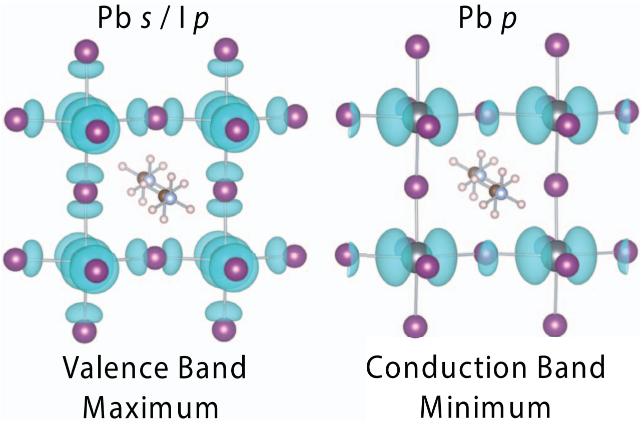

FIG. 2. Isosurface plot of the self-consistent electron density associated with the PBEsol Kohn-Sham wavefunctions of the upper valence and lower conduction bands of $(MA)PbI_3$.

both materials, even within the cubic basis. The presence of the molecule lowers the internal lattice symmetry of the parent perovskite structure and allows octahedral tilting to take place. The inherent structural "softness" of Pb(II) is well documented, arising from the stereochemical activity of the $6s^2$ lone pair electrons.[23]

The electronic band gap is determined by the states at the valence band maximum (VBM) and conduction band minimum (CBM). For both materials, the VBM is formed of an anti-bonding Pb s/I p combination, while the CBM is formed of empty Pb p orbitals, consistent with the formal electronic configuration of $5d^{10}6s^2 6p^0$. From the topology of the band-edge wave functions (Figure 2) isotropic hole and electron band conduction is expected. The strong dispersion of the bands in reciprocal space, confirmed from E(k) plots with m_n^* and $m_p^* < 0.3\ m_e$, is consistent with the reports of effective bipolar electrical conductivity.[24] A dedicated study of the defect physics is required to fully assess the origin of intrinsic conductivity, but partial occupancy of the organic cation sites is likely, which would correspond to p-type doping.

The magnitude of the band gap determines the onset of optical absorption and is closely related to the maximum voltage achievable in a photovoltaic device. The gap increases from 1.20 eV for $(A)PbI_3$ to 1.38 eV for $(MA)PbI_3$ (Table I). In all cases, the band gap is strongly direct and determined at the boundary of the first Brillouin zone ($R : \frac{2\pi}{a}[\frac{1}{2}, \frac{1}{2}, \frac{1}{2}]$). The increase is related to the significant expansion of the cell due to the larger cation: there is no evidence of M or MA contributing electronically to the frontier orbitals. In agreement with our results, a previous investigation of Sn-based hybrids showed that while the organic cations maintain overall charge neutrality, implying electronic mixing with the framework, they do not contribute the upper valence or lower conduction band states responsible for conductivity.[15] Indeed, the $\sigma/\sigma*$ bonds of A and MA are found at least 5 eV below the highest occupied state and 2.5 eV above the lowest empty state, respectively.

Although the application of hybrid perovskites in solar cells has predominately focused on $(MA)PbI_3$, our results suggest that $(A)PbI_3$ would also be effective for sensitisation towards longer wavelengths, and an $(A)_x(MA)_{1-x}PbI_3$ alloy could be used to tune the absorption onset. It should be noted that the same trends calculated with PBEsol are observed using the hybrid HSE06 functional; however, the predicted band gaps are larger. Optical absorption measurements place the band gap of (MA)PbI_3 at 1.5 eV,[16] while PBEsol and HSE06 predict values close to 1.4 eV and 2.0 eV, respectively. The calculated band gaps for materials formed by ns^2 cations such as Pb(II) are reasonably described without non-local electron exchange.[25,26] This originates here from a cancellation of errors with the neglect of spin-orbit splitting in the I 5*p* valence and Pb 6*p* conduction bands.[27]

Due to the pseudo-cubic lattice symmetry, the dielectric response of the hybrid materials is anisotropic (Table I). The high-frequency optical constants (5.6–6.5) are close to those of other absorber materials, e.g., $\epsilon_\infty^{CdTe} = 7.1$;[28] however, the static dielectric response is much larger. The large dielectric constants of pervoskite materials are associated with the structural flexibility that can support ferro-, anti-, and para-electric ordering of dipoles associated with the organic and/or inorganic sublattices. (A)PbI_3 is predicted to have low-frequency constants from 18.1 to 18.6, while (MA)PbI_3 exhibits a stronger screening of 18.0–37.3, which can be understood through the additional response from the molecular dipole in (MA)PbI_3. An isotropic average of the tensor across each orientation results in an effective dielectric constant of 25.7 for (MA)PbI_3, which is significantly larger than most tetrahedral semiconductors (e.g., $\epsilon_0^{CdTe} = 10.4$)[28] and will affect electron transport in a photovoltaic device, with stronger screening of any macroscopic electric fields across the absorber layer.

An order-disorder transition associated with the molecular dipole of MA, in a perovskite analogue, has recently been reported to give rise to reversible switching in the dielectric response.[29] While no evidence has been reported of this effect in hybrid halide perovskites, it is expected that they will also display some degree of amphidynamic behaviour arising from the collective motion of the constituent polar molecules. Tuning of the molecular dipoles represents a potential route for further improving the performance of this class of materials.

In summary, we have reported key properties of the hybrid perovskite layers used in thin-film solar cells. These materials combine low-energy direct band gaps with static dielectric constants larger than 18. Due to the low barrier for rotation of the organic cations, no long-range ordering of the molecular dipoles associated with CH_3NH_3 is expected; however, this could change in the presence of an external electric field. A transition from para- to ferroelectric order would enhance electron-hole separation. If the electric field was light induced, e.g., in a photovoltaic device, this could give rise to a novel photoferroic effect.

We thank L. M. Peter, K. T. Butler, and P. J. Cameron for useful discussions, and acknowledge membership of the UK's HPC Materials Chemistry Consortium, which is funded by EPSRC Grant No. EP/F067496. F.B. is funded through the EU DESTINY Network (Grant No. 316494). A.B.W. has received funding from EPSRC Grant No. EP/J017361/1, and A.W. acknowledges support from the Royal Society and the ERC (Grant No. 277757).

[1] A. Kojima, K. Teshima, Y. Shirai, and T. Miyasaka, J. Am. Chem. Soc. **131**, 6050 (2009).

[2] M. M. Lee, J. Teuscher, T. Miyasaka, T. N. Murakami, and H. J. Snaith, Science **338**, 643 (2012).

[3] J. Burschka, N. Pellet, S.-J. Moon, R. Humphry-Baker, P. Gao, M. K. Nazeeruddin, and M. Grätzel, Nature (London) **499**, 316 (2013).

[4] H.-S. Kim, C.-R. Lee, J.-H. Im, K.-B. Lee, T. Moehl, A. Marchioro, S.-J. Moon, R. Humphry-Baker, J.-H. Yum, J. E. Moser *et al.*, Sci. Rep. **2**, 591 (2012).

[5] J. H. Heo, S. H. Im, J. H. Noh, T. N. Mandal, C.-S. Lim, J. A. Chang, Y. H. Lee, H.-J. Kim, A. Sarkar, M. K. Nazeeruddin *et al.*, Nat. Photonics **7**, 486 (2013).

[6] M. J. Carnie, C. Charbonnaeu, M. L. Davies, J. Troughton, T. M. Watson, K. Wojciechowski, H. Snaith, and D. A. Worsley, Chem. Commun. **49**, 7893 (2013).

[7] N.-G. Park, J. Phys. Chem. Lett. **4**, 2423 (2013).

[8] T. K. Todorov, K. B. Reuter, and D. B. Mitzi, Adv. Mater. **22**, E156 (2010).

[9] A. Walsh, S. Chen, S.-H. Wei, and X.-G. Gong, Adv. Energy Mater. **2**, 400 (2012).

[10] A. M. Glazer, Acta. Cryst. **B28**, 3384 (1972).

[11] I. Chung, B. Lee, J. He, R. P. Chang, and M. G. Kanatzidis, Nature (London) **485**, 486 (2012).

[12] J. Calabrese, N. Jones, R. Harlow, N. Herron, D. Thorn, and Y. Wang, J. Am. Chem. Soc. **113**, 2328 (1991).

[13] D. B. Mitzi, S. Wang, C. A. Feild, C. A. Chess, and A. M. Guloy, Science **267**, 1473 (1995).

[14] K. Liang, D. B. Mitzi, and M. T. Prikas, Chem. Mater. **10**, 403 (1998).

[15] I. Borriello, G. Cantele, and D. Ninno, Phys. Rev. B **77**, 235214 (2008).

[16] T. Baikie, Y. Fang, J. M. Kadro, M. Schreyer, F. Wei, S. G. Mhaisalkar, M. Grätzel, and T. J. White, J. Mater. Chem. A **1**, 5628 (2013).
[17] J. P. Perdew, A. Ruzsinszky, G. I. Csonka, O. A. Vydrov, G. E. Scuseria, L. A. Constantin, X. Zhou, and K. Burke, Phys. Rev. Lett. **100**, 136406 (2008).
[18] A. V. Krukau, O. A. Vydrov, A. F. Izmaylov, and G. E. Scuseria, J. Chem. Phys. **125**, 224106 (2006).
[19] G. Kresse and J. Furthmüller, Phys. Rev. B **54**, 11169 (1996).
[20] S. Baroni, S. de Gironcoli, A. Dal Corso, and P. Giannozzi, Rev. Mod. Phys. **73**, 515 (2001).
[21] R. Wasylishen, O. Knop, and J. Macdonald, Solid State Commun. **56**, 581 (1985).
[22] E. Mosconi, A. Amat, M. K. Nazeeruddin, M. Grätzel, and F. De Angelis, J. Phys. Chem. C **117**, 13902 (2013).
[23] A. Walsh, D. J. Payne, R. G. Egdell, and G. W. Watson, Chem. Soc. Rev. **40**, 4455 (2011).
[24] C. C. Stoumpos, C. D. Malliakas, and M. G. Kanatzidis, Inorg. Chem. **52**, 9019 (2013).
[25] S.-H. Wei and A. Zunger, Phys. Rev. B **55**, 13605 (1997).
[26] A. Walsh, J. Phys. Chem. Lett. **1**, 1284 (2010).
[27] A more accurate treatment than PBEsol would be HSE06+SOC; however, this was not possible due to the high computational cost and the absence of DFPT for this level of theory.
[28] O. M. Madelung, *Semiconductors: Data Handbook*, 3rd ed. (Springer, Berlin, 2004).
[29] W. Zhang, H.-Y. Ye, R. Graf, H. W. Spiess, Y.-F. Yao, R.-Q. Zhu, and R.-G. Xiong, J. Am. Chem. Soc. **135**, 5230 (2013).

PHYSICAL REVIEW B **89**, 155204 (2014)

Relativistic quasiparticle self-consistent electronic structure of hybrid halide perovskite photovoltaic absorbers

Federico Brivio, Keith T. Butler, and Aron Walsh[*]
Centre for Sustainable Chemical Technologies and Department of Chemistry, University of Bath,
Claverton Down, Bath BA2 7AY, United Kingdom

Mark van Schilfgaarde[†]
Department of Physics, Kings College London, London WC2R 2LS, United Kingdom

(Received 14 January 2014; revised manuscript received 1 April 2014; published 21 April 2014)

Solar cells based on a light absorbing layer of the organometal halide perovskite $CH_3NH_3PbI_3$ have recently surpassed 15% conversion efficiency, though how these materials work remains largely unknown. We analyze the electronic structure and optical properties within the quasiparticle self-consistent *GW* approximation. While this compound bears some similarity to conventional *sp* semiconductors, it also displays unique features. Quasiparticle self-consistency is essential for an accurate description of the band structure: Band gaps are much larger than what is predicted by the local-density approximation (LDA) or *GW* based on the LDA. Valence band dispersions are modified in a very unusual manner. In addition, spin-orbit coupling strongly modifies the band structure and gives rise to unconventional dispersion relations and a Dresselhaus splitting at the band edges. The average hole mass is small, which partially accounts for the long diffusion lengths observed. The surface ionization potential (work function) is calculated to be 5.7 eV with respect to the vacuum level, explaining efficient carrier transfer to TiO_2 and Au electrical contacts.

DOI: 10.1103/PhysRevB.89.155204 PACS number(s): 88.40.−j, 61.66.Fn, 71.20.Nr, 72.40.+w

I. INTRODUCTION

One of the most promising third-generation photovoltaic technologies is based on metal-organic halide perovskites [1–10]. The materials physics of inorganic (ABX_3) perovskites is well developed; however, the replacement of the inorganic cation by an isoelectronic organic moiety provides an opportunity for tuning the chemical bonding and optical response. We apply a range of electronic structure techniques to calculate and predict the band structure of hybrid perovskites, demonstrating how the rich and unusual physics of these materials accounts for their widely reported success as absorber layers in solar cells.

It has been established that similar to traditional dielectric perovskites, these hybrid analogs have a range of accessible polymorphs with variations in the tilting and rotation of the BX_6 polyhedra in the lattice [11]. A large family of hybrid perovskites have been reported with inorganic networks ranging from one to three dimensions [12–15]. However, the methylammonium (MA) cation (i.e., $CH_3NH_3{}^+$) has been widely applied, resulting in the highest-performance perovskite-structured solar absorbers [2,3]. The polar MA cation can also be replaced by ammonium ($NH_4{}^+$) as a smaller nonpolar analog.

A large number of density-functional theory (DFT) studies have been reported that examine the electronic properties of hybrid perovskites [15–22]. The majority neglect spin-orbit coupling [15–20], while a relativistic treatment based on local or semilocal exchange-correlation functionals results in severe band gap underestimations [21,22]. Both approaches are insufficient to describe the complexity of the electronic structure of these hybrid semiconductors, with large errors expected in predicted properties such as carrier effective mass and dielectric function.

An alternative approach is the *GW* formalism, which can be used to correct errors in the one-electron Kohn-Sham eigenvalues within a many-body quasiparticle framework. Here we employ quasiparticle self-consistent *GW* theory [23] (QS*GW*) to study the electronic structure of $CH_3NH_3PbI_3$ and NH_4PbI_3, including the effect of spin-orbit coupling (SOC) $\lambda\mathbf{L}\cdot\mathbf{S}$, on the both the kinetic energy and electron self-energy Σ (see the Appendix). As Pb and I are heavy elements, SOC is large and has a major effect on spectral properties. SOC predominantly modifies the kinetic energy; however, in this case relativistic effects are large enough to induce a modest reduction in Σ as well, in contrast to the vast majority of semiconductors, e.g., elemental Sn. As a consequence of large relativistic effects, the conduction and valence bands near the band extrema deviate strongly from parabolic behavior. Effective masses are no longer constant, but depend on doping, temperature, and the property being measured. Average effective masses are nevertheless light, and the dielectric constants large, accounting for the long diffusion lengths that have been recently reported [7,9].

In many respects these perovskites are similar to conventional *sp* semiconductors: Conduction and valence bands near the Fermi level have *sp* character, and local- (and semilocal-) density approximation (LDA) to DFT systematically underestimate the band gap E_G because they do not include spatial nonlocality in the exchange-correlation potential. There are other significant points of departure: In sharp contrast to tetrahedral semiconductors, DFT also poorly describes valence band dispersions. This surprising result, which we discuss further below, indicates that the usual explanations invoked to account for deficiencies in DFT's description of semiconductors are not sufficient here.

---

[*] a.walsh@bath.ac.uk
[†] mark.van_schilfgaarde@kcl.ac.uk

We show that there is a strong feedback between dielectric response and quasiparticle levels, as occurs for $CuInSe_2$ [24]. Thus self-consistency in GW is essential: E_G calculated from $G^{\mathrm{LDA}}W^{\mathrm{LDA}}$, i.e., LDA as the starting Hamiltonian, picks up only a little better than half the gap correction to the LDA. Moreover, the QSGW and LDA valence bands, which the LDA describes reasonably well in tetrahedral semiconductors, are significantly different. These differences underscore the limitations of density-functional-based approaches (LDA, hybrid functionals, or $G^{\mathrm{LDA}}W^{\mathrm{LDA}}$) in describing the properties of these materials. QSGW does not depend on the LDA: Self-consistency renders it more reliable and universally applicable than other forms of GW, which will be important for *in silico* design of hybrid systems. Moreover, QSGW can determine some ground-state properties, e.g., the charge density and electric field gradient. Errors in QSGW tend to be small and highly systematic; most notably there is a tendency to slightly overestimate semiconductor band gaps. Limited data is available for organic-inorganic halide perovskites, but at least for $CH_3NH_3PbI_3$ the universal tendency found in other materials is consistent with recent measurements.

Finally, based on the work function calculated for $CH_3NH_3PbI_3$ within DFT (including an estimate for quasiparticle corrections) we show that band alignments are consistent with efficient electron transfer to TiO_2 and Au electrical contacts.

II. RESULTS

Optimization of the crystal structures of NH_4PbI_3 and $CH_3NH_3PbI_3$ have recently been reported [18] in DFT using the PBEsol [25] exchange-correlation functional. Atomic forces were converged to within 5 meV/Å, and the bond lengths are in good agreement with experiment. The representative $\langle 100\rangle$ configuration of MA is considered here. Lattice vectors of these perovskites are approximately cubic ($a = 6.29$ and 6.21 Å for the MA and NH_4 perovskites, respectively), with small distortions of the simple cubic ones. The valence band maximum and conduction band minimum falls close to a zone boundary point, the analog of the R point $(\frac{1}{2},\frac{1}{2},\frac{1}{2})$ in cubic symmetry. We denote this point as R in the remainder of the paper.

A. Band structure

The quasiparticle (QP) band structures for $CH_3NH_3PbI_3$ and NH_4PbI_3, with colors denoting the orbital character of the states, are shown in Fig. 1. The ions within the inorganic $(PbI_3)^-$ cage have formal electronic configurations of Pb: $5d^{10}6s^26p^0$ and I: $5p^6$. As can be seen from the color coding, the valence band maximum consists of approximately 70% I $5p$ and 25% Pb $6s$ (the Pb $6s$ forms a band centered around -8 eV), while the conduction band consists of a mixture of Pb $6p$ and other orbitals. The molecular units CH_3NH_3 and NH_4 form σ bonds deep in the valence band. They are essentially dispersionless: They do not hybridize with the cage until energies exceed $E_F + 5$ eV. Thus their interaction with the host is largely electrostatic and structural; they provide charge compensation to the ${PbI_3}^-$ cage.

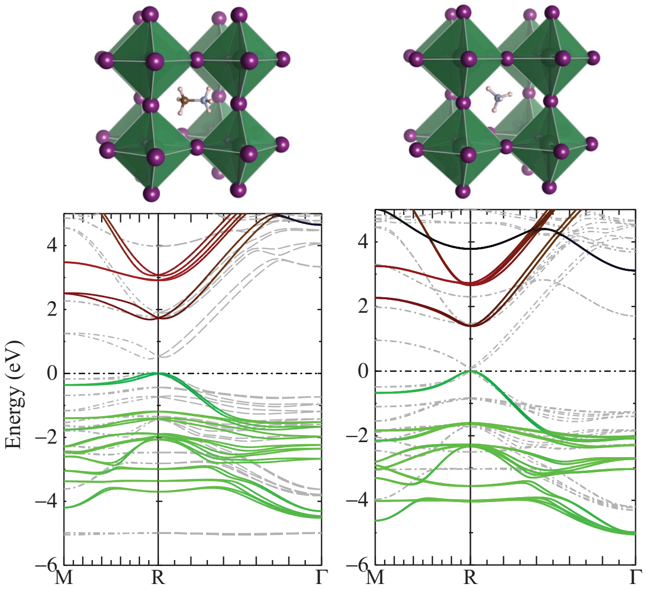

FIG. 1. (Color online) QSGW band structure for $CH_3NH_3PbI_3$ (left) and NH_4PbI_3 (right). Zero denotes valence band maximum. Bands are colored according to their orbital character: green depicts I $5p$, red depicts Pb $6p$, and blue depicts Pb $6s$. Points denoted M and R are zone-boundary points close to $(\frac{1}{2},\frac{1}{2},0)$ and $(\frac{1}{2},\frac{1}{2},\frac{1}{2})$, respectively. The valence band maximum and conduction band minimum are shifted slightly from R as a consequence of the $\mathbf{L}\cdot\mathbf{S}$ coupling. Valence bands near -2 eV (conduction bands near $+3$ eV) are almost purely green (red) showing that they consist largely of I $5p$ (Pb $6p$) character. Bands nearer the gap are darker as a result of intermixing with other states. Light-gray dashed lines show corresponding bands in the LDA. The dispersionless state near -5 eV corresponds to a molecular level of methylammonium. In QSGW this state is pushed down to -7.7 eV. The dispersion of the highest valence bands is very poorly described by the LDA, as described in the text.

The results presented in Table I demonstrate the various contributions to the band energies around the fundamental gap. The contribution from SOC ($\sim$1 eV), is extraordinarily large, of the order of the gap itself; so large that screening is enhanced. As a result there is a smaller, but nonetheless non-negligible contribution of SOC to the electron self-energy ($\Sigma = iGW$), apparent from the difference between "SO(T)" and "SO(Σ)." Furthermore, Table I emphasizes the importance of the feedback between W and QP when calculating the band structure of these systems. The "GW^0" gap is based on a perturbation of the LDA gap; and it is significantly smaller. Because the LDA gap is too small, W is overscreened, and GW understimated. The role of feedback is important in other semiconductors: It is particularly strong in InN [26] and Cu(In,Ga)Se_2. In the latter case the interplay between W and E_G was shown explicitly by comparing functionals that did or did not include the dependence of W on band structure [24]. W and the gap correction is not a function of the fundamental gap alone: All the bands (including valence band dispersions) shift in a nontrivial manner. To reliably determine the electronic structure including the fundamental gap, self-consistency is essential.

TABLE I. Fundamental band gaps (in eV) of $CH_3NH_3PbI_3$ and NH_4PbI_3 calculated at varying levels of approximation. Top rows show DFT results using PBEsol (reported in Ref. [18]) and the Barth-Hedin LDA functional. First columns show that semilocal and local functionals generate similar gaps. $\lambda\mathbf{L}\cdot\mathbf{S}$ (column "LDA+SO") strongly reduces the gap. *GW* gaps are shown without spin-orbit coupling (SO = 0), with $\lambda\mathbf{L}\cdot\mathbf{S}$ added to a fixed potential, modifying the kinetic energy only [SO(T)], and included in the QS*GW* self-consistency cycle [SO(Σ)]. Column "GW^0" is similar to SO(Σ) but G and W are generated from the LDA. (In this calculation the full Σ matrix was generated, not just the diagonal part as is customary. A Z factor of 1 was used to take partial account of self-consistency, which brings the gap in better agreement with the QS*GW* result; see Appendix A in Ref. [30]). An error of order 0.1 eV might be associated with the treatment of SOC (see the Appendix). Room temperature (RT) band gap data is only available for $NH_3CH_3PbI_3$ [27].

	DFT				
	PBEsol	LDA	LDA+SO		Expt. [27]
$NH_3CH_3PbI_3$	1.38	1.46	0.53		1.61 (RT)
NH_4PbI_3	1.20	1.13	0.09		
	QS*GW*				
	SO = 0	SO(T)	SO(Σ)	GW^0	Expt.
$NH_3CH_3PbI_3$	2.73	1.78	1.67	1.27	1.61 (RT)
NH_4PbI_3	2.30	1.36	1.38	0.76	

Recent measurements place the room temperature band gap of $NH_3CH_3PbI_3$ at 1.61 eV [27], which falls slightly below the QS*GW* result. Some tendency for QS*GW* to overestimate gaps is expected. In any case theory and experiment cannot be compared to better than 0.1 eV resolution for several reasons. There are small issues with k-point convergence [28], and with the shape of local wave functions determined by solving a scalar relativistic equation rather than the Dirac equation (see the Appendix). On the experimental side there may be some temperature dependence of the gap given the structural flexibility of the material [29]; this has yet to be explored.

Figure 1 also shows the LDA energy bands. Remarkably, the LDA badly underestimates not only the gap but poorly describes the dispersion in the valence bands. The tendency for LDA to underestimate band gaps is traditionally associated with the energy cost for an excited electron-hole pair. The exchange-correlation potential should distinguish between a neutral excitation (e.g., a hole shifting from one k point in the valence band to another) and one where charge is separated (excitation of an electron-hole pair). Such a distinction is problematic for a local potential, which is by necessity the same for all electrons. Such an error is seen in the present case, as the LDA gap is too small. As Fig. 1 clearly shows, LDA and QS*GW* valence bands also deviate strongly from one another. Note, in particular, the states at R between 0 and -2 eV. This behavior allows us to deduce that the hopping matrix elements between I $5p$ (and to some extent Pb $6s$) states are poorly described by the LDA.

B. Carrier effective mass

Typically light hole masses are too small in the LDA because, according to $k\cdot p$ theory, $m_v^* \propto E_G/V^2$; V is a matrix element of the gradient operator between the conduction and valence bands. m_v^* is expected to be too small because E_G is underestimated; indeed for traditional narrow gap tetrahedral semiconductors, the proportionality between m_v^* and E_G is reasonably well obeyed. The LDA predicts the light hole mass to be too small, while other masses (which do not couple to the nearest conduction band) are reasonably described. For example, GaAs has a gap similar to $CH_3NH_3PbI_3$, and LDA underestimates it by a comparable amount (~ 1 eV). Following expectations, the LDA underestimates the light hole mass in GaAs by a factor of ~3. But for $CH_3NH_3PbI_3$ the situation is reversed: the LDA *overestimates* m_v^* even while it severely underestimates E_G. For NH_4PbI_3 the LDA and QS*GW* masses are comparable, but only because the LDA gap is very small.

Spin-orbit coupling greatly complicates both valence and conduction bands within k_BT of the band edges. We focus on the two valence bands of $NH_3CH_3PbI_3$, as these are the ones that govern transport in hole-based devices. As these two bands approach the R point, they must merge to the same value by symmetry. However, they approach the R point with a linear dispersion in some directions; as a consequence the dispersions in the upper and lower bands are nonanalytic. The upper band is maximum in some directions but increases with a linear slope in the $\pm[11\bar{2}]$ direction. Two maxima form near $R \pm 0.005 \times [11\bar{2}]$ [Fig. 2(a)], arising from Dresselhaus spin-orbit coupling,

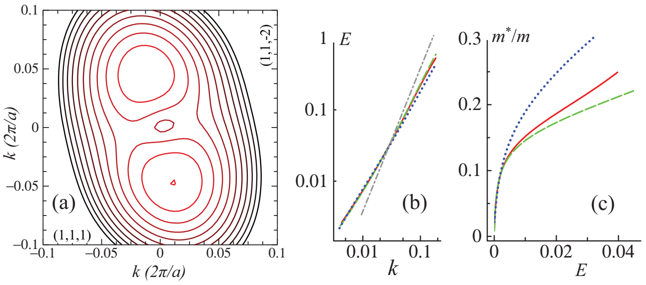

FIG. 2. (Color online) Left: constant energy contours in the $(1\bar{1}0)$ plane for the upper valence band of $CH_3NH_3PbI_3$. The origin corresponds to the R point and [111] and $[11\bar{2}]$ are the horizontal and vertical axes of k. Energy contours are in increments of 2.5 meV, so that the outermost contour corresponds approximately to RT. Corresponding contours in the (111) plane (not shown) appear similar. Valence bands have two maximal points near $R \pm 0.005\,[11\bar{2}]$. At low temperature and low doping, ($E_F < 5$ meV) the two extrema act as independent centers with approximately spherical effective masses. At high doping ($E_F > 20$ meV) or high temperature, holes effectively see a single band maximum with roughly elliptical constant energy surfaces. Panels (b) and (c) show energy $E_v(k) \equiv E(R) - E(k)$ for the lower valence band. This band has a single maximum at R, with approximately spherical dispersion. Panel (b) shows $E_v(k)$, on a log-log scale in the $[1\bar{1}0]$, [111], and $[11\bar{2}]$ directions as red solid, green dashed, and blue dotted lines, respectively. For comparison a parabolic band with effective mass $0.1m$ is shown as a gray dot-dashed line. Panel (c) plots $\hbar^2k^2/(2m\,E_v)$ against E_v, which may be taken as a definition of the effective mass (see text). E_v is in eV; k is in units $2\pi/a$.

which is even more pronounced in the lower conduction band. The lower band has a single maximum at R, and its constant energy surfaces deviate only modestly from spheres for k near R [Fig. 2(b)]. Yet, the right panels of Fig. 2 show $E_v(k) \equiv E(R) - E(k)$ deviates markedly from a parabolic dispersion. This has important consequences for the device behavior of this material. Figure 2(c) shows that, provided $E_v > 10$ meV, the band dispersion can be expressed approximately as a k-dependent mass:

$$\frac{h^2k^2}{2m} = m^*(k)E_v(k), \qquad \frac{m^*(k)}{m} = m_0[1+\alpha E_v(k)] \quad (1)$$

with $m_0^* \sim 0.12$ and α independent of $|\mathbf{k}|$ but dependent on orientation. For E_v large enough, the upper valence band can also be described by an effective mass of roughly the same size. The lower conduction band exhibits a similar behavior, with $m_0^* \sim 0.15$. The small masses explain how these materials can exhibit high mobility and long diffusion lengths. Bands of NH_4PbI_3 differ in important details from $NH_3CH_3PbI_3$ (the influence of SOC is less pronounced), but the basic structure is similar. Both the band gap and effective masses are reduced relative to $NH_3CH_3PbI_3$, as can be seen directly by inspecting Fig. 1.

C. Optical and dielectric response

It is known that these compounds strongly absorb visible light. We confirm this through a random phase approximation (RPA) calculation of $\alpha(\omega)$ from the imaginary part of the macroscopic dielectric function $\epsilon_M(\omega) = [\epsilon^{-1}_{\mathbf{G},\mathbf{G}'=0}(\mathbf{q} \rightarrow 0,\omega)]^{-1}$. As Fig. 3 shows, α is somewhat smaller than—but comparable to—that of GaAs. This explains why very thin layers of the hybrid perovskites have been found to give high photovoltaic efficiencies. Indeed combined with the low carrier effective masses, the resulting electron-hole diffusion lengths exceed the typical film thickness.

Some static (ϵ_0) and high-frequency (ϵ_∞) dielectric constants are shown in Table II. These values are unusually sensitive to the k-point sampling density and require dense meshes for convergence. Those calculated by density-functional perturbation theory (e.g., PBEsol) leave out SOC and thus get fortuitously good band gaps. As a result ϵ_∞ is not so different from the QS*GW* case (which includes SOC). Contributions to ϵ_0 from lattice polarization are significantly larger than seen in typical tetrahedral semiconductors (compare ϵ_0 to ϵ_∞). For $NH_3CH_3PbI_3$, the average value of the static dielectric constant, including QP corrections from Table II, of 24.1, is in very good agreement with permittivity measurements of 23.3 [32]. These values exclude contributions from orientational disorder of the methylammonium ions, which is the subject of further study [33].

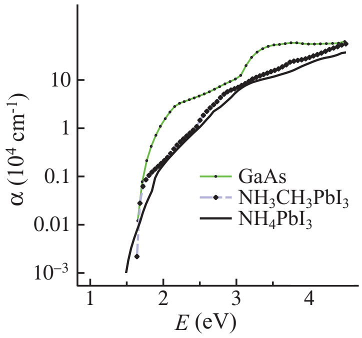

FIG. 3. (Color online) Optical absorption spectrum calculated within the RPA from the QS*GW* potential, for $CH_3NH_3PbI_3$ and NH_4PbI_3. The absorption is smaller than, but comparable to that of GaAs, shown for comparison. Note that similar measurements have been reported in Ref. [31].

TABLE II. Dielectric constants (isotropic average of the tensor) and band gaps (eV), calculated in density-functional perturbation theory without SOC (from Ref. [18]), and in the RPA with SOC.

	PBEsol			QS*GW*	
	E_G	ϵ_0	ϵ_∞	E_G	ϵ_∞
$NH_3CH_3PbI_3$	1.38	25.7	6.1	1.67	4.5
NH_4PbI_3	1.20	18.4	6.5	1.38	5.0

D. Surface ionization potential

In order to place the electronic bands on an absolute energy scale, we have aligned the quasiparticle energies with respect to the vacuum level of a nonpolar (110) termination of the perovskite, generated using METADISE [34]. We take the Pb 1*s* core level as an energy reference and use a planar average of the electrostatic potential following the standard procedure [35,36]. The slab model consisted of four perovskite layers with the dipole of the methylammonium cations aligned parallel to the surface termination, which ensure no macroscopic electric field. The resulting ionization potential is 5.7 eV (5.9 eV from LDA, which is corrected by the GW^0 self-energy), with a corresponding electron affinity of 4.0 eV. These values are in good agreement with initial photoemission measurements of thin films (5.4 eV) and explain the success of TiO_2 (electron) and Au (hole) contacts [37].

III. CONCLUSION

We have explored the electronic structure of two key hybrid halide perovskites. Relativistic and many-body corrections are shown to be essential for a quantitative description of the bulk properties important for photovoltaics: band gap, band dispersion, effective mass and dielectric response. These organic-inorganic materials display quantum-mechanical behavior atypical of traditional semiconductors, which begins to explain their remarkable performance in mesoporous and thin-film solar cells.

ACKNOWLEDGMENTS

We thank L. M. Peter and H. J. Snaith for useful discussions, and acknowledge membership of the UK's HPC Materials Chemistry Consortium, which is funded by EPSRC Grant No. EP/F067496. F.B., K.T.B, and A.W. are funded by the DESTINY ITN (Grant Agreement No. 316494), EPSRC (Grant No. EP/J017361/1), and the ERC (Grant No. 277757), respectively.

APPENDIX: SIMPLIFIED TREATMENT OF SPIN-ORBIT COUPLING IN QS*GW*

Aryasetiwan and Biermann [38] developed a formalism for *GW* with spin-dependent interactions. Rather than proceed with a completely noncollinear treatment, we take advantage of the fact that $\lambda\mathbf{L}\cdot\mathbf{S}$ is relatively small, and moreover that the noncollinear part of the eigenfunctions is unimportant for these semiconductors. We present a simplified treatment that generates results essentially as good as adding $\lambda\mathbf{L}\cdot\mathbf{S}$ nonperturbatively to the scalar Dirac Hamiltonian for M-PbI$_3$ compounds.

Partitioning $\mathbf{L}\cdot\mathbf{S}$ into components, the noninteracting QS*GW* Hamiltonian reads

$$H_0 = H_0(\lambda = 0) + \lambda L^z S^z + \lambda(\mathbf{L}^+ \cdot \mathbf{S}^- + \mathbf{L}^- \cdot \mathbf{S}^+).$$

The first two terms are spin diagonal and can be diagonalized nonperturbatively in the same manner as $H_0(\lambda = 0)$. The eigenvalues ϵ_i and eigenfunctions ψ_i contain the $L^z S^z$ portion of $\mathbf{L}\cdot\mathbf{S}$, keeping ψ_i spin diagonal. The latter two terms, when treated exactly, further shift the ϵ_i and also introduce spin off-diagonal parts to the ψ_i. We allow the former but omit the latter.

The lowest order of correction to the eigenvalues is second order and we follow the spirit of second-order perturbation theory. Let δ_{ij} be the initial splitting in ϵ_i and ϵ_j, $\Delta_{ij} = |\epsilon_i - \epsilon_j|/2$. If H_{ij}^{+-} couples i and j, Δ_{ij} increases by $\delta\Delta_{ij} = |H_{ij}^{+-}|^2/|\epsilon_i - \epsilon_j|$, in lowest order.

Second-order perturbation theory can be problematic when $\epsilon_i \to \epsilon_j$. We instead obtain $\delta\Delta_{ij}$ from

$$\delta\Delta_{ij} = \sqrt{\Delta_{ij}^2 + |H_{ij}^{+-}|^2} - |\Delta_{ij}|.$$

This expression is exact if i and j are isolated from the rest of the system. The final expression (the net shift for each ϵ_i is obtained by summing over each ij pair) is nevertheless correct only to second order because terms involving three or more states are not included.

We carefully tested our quasiperturbative approach in the LDA or LDA + U context for a wide range of materials, e.g., Fe, Sn, Au, GdN, Pu, and the perovskites addressed in this paper. In all cases except Pu ($Z = 94$) the difference between the perturbation expression resulted in ϵ_i very close to $\mathbf{L}\cdot\mathbf{S}$ treated nonperturbatively. For CH$_3$NH$_3$PbI$_3$, for example, E_G changed by less than 0.01 eV. Self-consistency carried through with both approaches generate a slight difference in density, but no significant difference in the ϵ_i.

Tests of the adequacy of the quasiperturbative $\mathbf{L}\cdot\mathbf{S}$ in the QS*GW* were performed as follows: Self-consistency was reached with $\mathbf{L}\cdot\mathbf{S}$ included quasiperturbatively, and for a given Σ, the quasiparticle levels with $\mathbf{L}\cdot\mathbf{S}$ calculated nonperturbatively were compared to the perturbative treatment. As in the LDA case, negligible differences were found for all compounds studied except for Pu, where modest differences were found. As in the LDA case, the nonperturbative treatment generated a slight change in density. Since the ϵ_i are reliably determined, it is unlikely that a better treatment of $\mathbf{L}\cdot\mathbf{S}$ (noncollinear eigenfunctions) will further affect Σ appreciably in these compounds. On the other hand, fully relativistic treatment might affect H_0 a little, since the relativistic radial functions vary as r^γ for small r, where $\gamma^2 = \kappa^2 - (2Z/c)^2$, κ playing the role of the l quantum number. γ reduces the scalar relativistic case only when $c \to \infty$. A better treatment of the small-r behavior of the partial waves modifies spin-orbit splitting of the p levels for Pb by about 10%, which is not included here. An appreciable effect of $\mathbf{L}\cdot\mathbf{S}$ on Σ is observed only for compounds with large-Z constituents. For semiconductors as heavy as Sn ($Z = 50$), and for metals as heavy as Au ($Z = 79$), the effect of $\mathbf{L}\cdot\mathbf{S}$ on Σ appears to be very small. But for the iodide perovskites studied here, $\mathbf{L}\cdot\mathbf{S}$ has a noticeable effect on Σ (Table I) because of the interplay between E_G and ϵ present in semiconductors but not in metals.

[1] A. Kojima, K. Teshima, Y. Shirai, and T. Miyasaka, J. Am. Chem. Soc. **131**, 6050 (2009).

[2] M. M. Lee, J. Teuscher, T. Miyasaka, T. N. Murakami, and H. J. Snaith, Science **338**, 643 (2012).

[3] J. Burschka, N. Pellet, S.-J. Moon, R. Humphry-Baker, P. Gao, M. K. Nazeeruddin, and M. Grätzel, Nature (London) **499**, 316 (2013).

[4] H.-S. Kim, C.-R. Lee, J.-H. Im, K.-B. Lee, T. Moehl, A. Marchioro, S.-J. Moon, R. Humphry-Baker, J.-H. Yum, J. E. Moser, M. Grätzel, and N.-G. Park, Sci. Rep. **2**, 591 (2012).

[5] J. H. Heo, S. H. Im, J. H. Noh, T. N. Mandal, C.-S. Lim, J. A. Chang, Y. H. Lee, H.-j. Kim, A. Sarkar, and M. K. Nazeeruddin, Nat. Photonics **7**, 486 (2013).

[6] M. J. Carnie, C. Charbonnaeu, M. L. Davies, J. Troughton, T. M. Watson, K. Wojciechowski, H. Snaith, and D. A. Worsley, Chem. Commun. **49**, 7893 (2013).

[7] S. D. Stranks, G. E. Eperon, G. Grancini, C. Menelaou, M. J. Alcocer, T. Leijtens, L. M. Herz, A. Petrozza, and H. J. Snaith, Science **342**, 341 (2013).

[8] M. Liu, M. B. Johnston, and H. J. Snaith, Nature (London) **501**, 395 (2013).

[9] G. Xing, N. Mathews, S. Sun, S. S. Lim, Y. M. Lam, M. Grätzel, S. Mhaisalkar, and T. C. Sum, Science **342**, 344 (2013).

[10] H.-S. Kim, I. Mora-Sero, V. Gonzalez-Pedro, F. Fabregat-Santiago, E. J. Juarez-Perez, N.-G. Park, and J. Bisquert, Nat. Commun. **4**, 2242 (2013).

[11] T. Baikie, Y. Fang, J. M. Kadro, M. Schreyer, F. Wei, S. G. Mhaisalkar, M. Graetzel, and T. J. White, J. Mater. Chem. A **1**, 5628 (2013).

[12] J. Calabrese, N. Jones, R. Harlow, N. Herron, D. Thorn, and Y. Wang, J. Am. Chem. Soc. **113**, 2328 (1991).

[13] D. B. Mitzi, S. Wang, C. A. Feild, C. A. Chess, and A. M. Guloy, Science **267**, 1473 (1995).

[14] K. Liang, D. B. Mitzi, and M. T. Prikas, Chem. Mater. **10**, 403 (1998).

[15] I. Borriello, G. Cantele, and D. Ninno, Phys. Rev. B **77**, 235214 (2008).

[16] E. Mosconi, A. Amat, M. K. Nazeeruddin, M. Grätzel, and F. De Angelis, J. Phys. Chem. C **117**, 13902 (2013).

[17] C. Quarti, G. Grancini, E. Mosconi, P. Bruno, J. M. Ball, M. M. Lee, H. J. Snaith, A. Petrozza, and F. De Angelis, J. Phys. Chem. Lett. **5**, 279 (2014).

[18] F. Brivio, A. B. Walker, and A. Walsh, APL Mater. **1**, 042111 (2013).

[19] W.-J. Yin, T. Shi, and Y. Yan, Appl. Phys. Lett. **104**, 063903 (2014).

[20] A. Filippetti and A. Mattoni, Phys. Rev. B **89**, 125203 (2014).

[21] J. Even, L. Pedesseau, J.-M. Jancu, and C. Katan, J. Phys. Chem. Lett. **4**, 2999 (2013).

[22] G. Giorgi, J.-I. Fujisawa, H. Segawa, and K. Yamashita, J. Phys. Chem. Lett. **4**, 4213 (2013).

[23] M. van Schilfgaarde, T. Kotani, and S. Faleev, Phys. Rev. Lett. **96**, 226402 (2006).

[24] J. Vidal, S. Botti, P. Olsson, J.-F. Guillemoles, and L. Reining, Phys. Rev. Lett. **104**, 056401 (2010).

[25] J. P. Perdew, A. Ruzsinszky, G. I. Csonka, O. A. Vydrov, G. E. Scuseria, L. A. Constantin, X. Zhou, and K. Burke, Phys. Rev. Lett. **100**, 136406 (2008).

[26] M. Usuda, H. Hamada, K. Siraishi, and A. Oshiyama, Jpn. J. Appl. Phys., Part 2 **43**, L407 (2004).

[27] Y. Yamada, T. Nakamura, M. Endo, A. Wakamiya, and Y. Kanemitsu, Appl. Phys. Express **7**, 032302 (2014).

[28] Careful convergence checks were made of the eigenfunction and product basis. A $4 \times 4 \times 4$ k mesh was used for the M-PbI_3 compounds. A one-shot calculation with a $6 \times 6 \times 6$ mesh as perturbation to the QSGW result showed that the k-converged gap is about 0.1 eV larger than what is reported in Table I.

[29] A. Poglitsch and D. Weber, J. Chem. Phys. **87**, 6373 (1987).

[30] M. van Schilfgaarde, T. Kotani, and S. V. Faleev, Phys. Rev. B **74**, 245125 (2006).

[31] S. De Wolf, J. Holovsky, S.-J. Moon, P. Löper, B. Niesen, M. Ledinsky, F.-J. Haug, J.-H. Yum, and C. Ballif, J. Phys. Chem. Lett. **5**, 1035 (2014).

[32] N. Onoda-Yamamuro, T. Matsuo, and H. Suga, J. Phys. Chem. Solids **53**, 935 (1992).

[33] J. M. Frost, K. T. Butler, F. Brivio, C. H. Hendon, M. van Schilfgaarde, and A. Walsh, Nano Lett. (2014), doi:10.1021/nl500390f.

[34] G. W. Watson, P. M. Oliver, and S. C. Parker, Phys. Chem. Miner. **25**, 70 (1997).

[35] K. T. Butler, J. Buckeridge, C. R. A. Catlow, and A. Walsh, Phys. Rev. B. **89**, 115320 (2014).

[36] A. Walsh and K. T. Butler, Acc. Chem. Res. **47**, 364 (2014).

[37] N.-G. Park, J. Phys. Chem. Lett. **4**, 2423 (2013).

[38] F. Aryasetiawan and S. Biermann, Phys. Rev. Lett. **100**, 116402 (2008).

3.7 Conclusions

Our study investigated the electronic and mechanical properties of $CsSnI_3$ and analogous materials with general structure $CsMX_3$, where M = Sn, Pb and X = Cl, Br, I.

We calculated the bulk modulus of this compounds after a fit of the Birch-Murnaghan equation of state to the energy-volume curve. The results are comparable with previously pubblished results. The highes values is 23.32 GPa for the compound $CsSnCl_3$ and the lowest is 15.27 GPa for $CsPbI_3$. The value of the bulk modulus depends on the halogen more than the presence of Sn or Pb.

In order to determine the stability of the compounds compared to the elements which form them, we have calculated the enthalpy of formation of the compounds from the elemental standard states. All the enthalpies of formation were negative and hence the compound could be formed if competitive materials are not present.

In terms of electronic structure we calculated the band structure using the hybrid PBEsol0 functional. All the compounds showed a direct band gap in correspondence of the R point of the first BZ. The value of the band gap depends mainly by the halogen and Pb or Sn rather than the central ion. This two component, in fact, contribute in larger part to the definition of the frontier orbitals at the R point, on which the band gap depends.

There was no evidence of any influence of Cs in the band structure.

In the limit of the parabolic approximation, we calculated from the band structure, according to equation 3.9, the values for the effective electrons and holes masses. The values found were compatible with a ambipolar conductor with smaller values for holes masses.

The extension of the calculations to post DFT methods, as the QSGW allowed us to consider more accurately the electronic properties of hybrid perovskites. In particular we observed how the SOC has a role in inducing Rashba splitting with a possible enhancement of the carriers lifetimes. It also shone a light on the nature of the band gap nature in hybrid perovskites helping the understanding of the mechanism behind high efficiency.

Chapter 4

Vibrational properties

4.1 Introduction

Atoms can change their equilibrium position if enough energy is provided. This displacement results in vibrations that reflect the structure and the composition of a material. The investigation of vibrational properties can be done with absorption spectra or analysing the inelastic scattering of light. The energy involved in the processes is in the order of the thermal kinetic energy that correspond to the IR portion of light spectra, just below the visible light. This covers an energy interval that usually goes from few meV with respect to molecular rotation and acoustic modes to 1 eV for the vibrations of particularly strong bonds.

The vibrational properties can be investigated analysing the absorption of photons of materials in this part of the spectra. Similar information is also provided by Raman measurements that allows to observe the inelastic scattering of photons with energy smaller, but comparable to the band gap. The analysis of IR and Raman spectra requires us to assign to every signal the corresponding vibration. The vibrations depends strongly on the symmetry of the system, so if the structure is particularly complex, or not completely resolved, it is quite difficult to interpret the data. In these cases simulations are of fundamental help to assign every peak to proper vibrational mode.

In the case of hybrid perovskites[193] the structures often do not contain any symmetry operations which complicates analysis. Besides the measurements are often complicated by secondary effects, as degradation or impurities.[194] This is particularly evident for the cubic phase, that results as a dynamic average of multiple local displacements.

The correct interpretation of experimental results stands as a motivation to employ different simulation techniques to investigate the vibrational properties of different classes of hybrid perovskites. We calculated the general vibrational spectra resolved over the Brillouin zone (phonon band dispersion) using the Finite Displacement Method (FDM). We also simulated the IR and Raman spectra with the Density functional perturbation theory (DFPT) and an initial analysis of the anharmonicity of these systems using the quasi-harmonic approximation (QHA).

TABLE 4.1: Calculation threshold used to optimize the calculation for the vibrational properties.

System	Cut-off [eV]	k-mesh	Force Threshold [$^{meV}/_{\text{Å}}$]
MAPbX_3- cubic	700	$6 \times 6 \times 6$	1
MAPbI_3- tetra	800	$5 \times 5 \times 3$	1
MAPbI_3- orthorhombic	700	$5 \times 4 \times 5$	1

The next section reports the computational details employed to perform the calculations and the publications where they have been used.

4.1.1 Computational details

Finite Displacement Method

The calculation of the vibrational properties of the structures has been completed using the codes VASP and Phonopy. VASP has been used to perform the quantum-mechanical calculation to optimise the cells and to calculate the forces present in the systems. Phonopy was used to generate the input files for VASP calculations and to analyse the results. The quantum mechanical part was carried out similarly as described in Chapter three. We used the PBEsol exchange-correlation functional, but we considered more tight settings.

This precaution is necessary because the lowest vibrational energies lay in the range of few meV, so in order to be significant, the results must have fluctuations (*noise*) below this threshold. With this consideration in mind we converged the planewave cut-off and the k-mesh density to reduce the fluctuation below 0.5 meV per atom. Besides the electronic convergence threshold for the eigenvalues and the total energy convergence, usually set to 10^{-6} eV, in this case has been reduced to 10^{-8} eV. As an example of the requited set of convergence calculations in Figure 4.1 are reported the preliminary results to decide the cut-off for the cubic structure of MAPbCl.

As well as the electronic parameters, also the structure optimization had to be taken out more tightly than usual. In our case we minimised the forces acting on each single atom below 1 $^{meV}/_{\text{Å}}$. The optimisation of the structure at this level is particularly time consuming, but it is necessary to avoid the presence of imaginary mode and reduce the noise of the calculation. Specifically for VASP it is also necessary to disable the *real-space projector* (LREAL = .FALSE.). This setting makes the calculations more expensive, but reduces the introduction of noise in the calculations. The final parameters used for the simulations are reported in Table 4.1.

Phonopy generated the symmetry-unique atomic displacements for the structures. The displaced structure were created using the default step of of 0.001 Å. To further reduce the noise in the results phonopy was set to symmetrize the

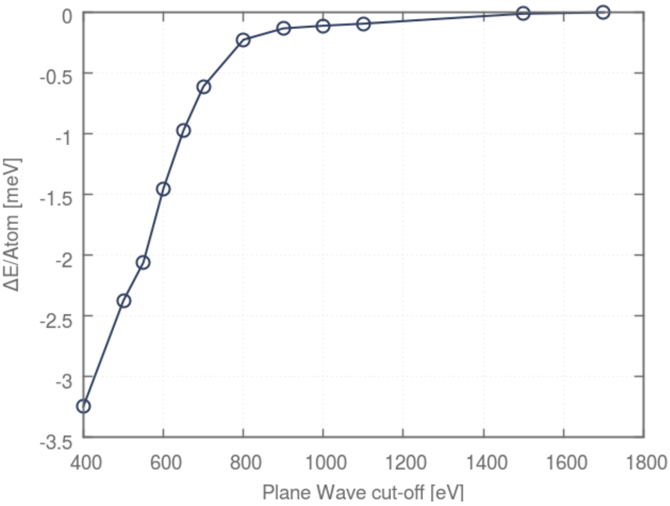

FIGURE 4.1: Preliminary calculation to determinate the energy cut-off for the simulations.

force constants. Because of numerical noise the sum of the forces could be significantly different from zero, so within Phonopy we impose a symmetrization of the force constants. This is a common procedure in most phonon calculations, and it can be performed also in structures with $P1$ symmetry, enforcing the sum rule, i.e. ensuring the acoustic modes have zero frequency at the Γ point.

With respect to the size of the supercell expansion, the cost of the calculation acted as a limiting factor, and we restricted the study to the best applicable case. For the cubic phase of $MAPbX_3$, the orthorhombic phase of MAPI we considered a 2×2×2 supercell expansion while a simple cell was employed for the tetragonal phase. This choice was necessary since the tetragonal phase is 4 times larger than the cubic phase, and the total absence of symmetry would have lead to calculate 288 structures ($6N$) each one with 196 atoms. The effects of this choice are mitigated by the large size of the single cell that reduce the probability of eventual coupling between the displacements. The same argument could be applied to the orthorhombic phase, but due to the fact that in this case the molecules is not breaking the symmetry the actual number of independent structure necessary to describe the system vibration is reduced to only 41 independent calculations.

Density Functional Perturbation Theory

To simulate the IR and Raman spectra we used two different public-available codes.[195,196] The codes have been modified to be used in our study and they act similarly to Phonopy: they rely on VASP to perform quantum-mechanic calculations of which analyse the results. The codes do not requires particular setting to be run, and the DFT related part has been performed consistently with the calculation carried for the FDM. Differently from the FDM the DFPT has the advantage that can be performed without a supercell expansion.

4.2 Related publications

The results of the vibrational studies are contained in three publications. The first paper was published in Physical Review B (2015). Our computations were performed in collaboration with the crystallography group of Prof. Mark Weller at University of Bath. The spectroscopy measurements have been performed by group of Dr. Piers Barnes in Imperial College London, and Dr. Alejandro Goñi at the ICREA center in Barcelona, Spain.

The second paper was published in the Journal of Physical Chemistry C (2016) contains an experimental investigation of Raman properties of hybrid perovskites. I contributed to the analysis of Raman measurement that have been performed in the groups of Dr. Petra Cameron at University of Bath and Prof. Polycarpos Falaras in the NCSR Demokritos center in Athens, Greece, both part of the Destiny project.

The third paper, accepted for publications in Physical Chemistry Chemical Physics (2016) extends and complete the studies presented in the first paper hereby presented, and includes more experimental contributions performed by the groups of Prof. Barnes and Dr. Goñi.

The publication are reproduced under Creative Commons license.

PHYSICAL REVIEW B **92**, 144308 (2015)

Lattice dynamics and vibrational spectra of the orthorhombic, tetragonal, and cubic phases of methylammonium lead iodide

Federico Brivio,[1] Jarvist M. Frost,[1] Jonathan M. Skelton,[1] Adam J. Jackson,[1] Oliver J. Weber,[1] Mark T. Weller,[1]
Alejandro R. Goñi,[2] Aurélien M. A. Leguy,[3] Piers R. F. Barnes,[3] and Aron Walsh[1,4,*]
[1] *Centre for Sustainable Chemical Technologies and Department of Chemistry, University of Bath, Claverton Down, Bath BA2 7AY, United Kingdom*
[2] *ICREA, Passeig Lluís Companys 23, E-08010 Barcelona, Spain*
and Institut de Ciència de Materials de Barcelona (ICMAB-CSIC), Campus UAB, E-08193 Bellaterra, Spain
[3] *Department of Physics, Imperial College London, London SW7 2AZ, United Kingdom*
[4] *Global E^3 Institute and Department of Materials Science and Engineering, Yonsei University, Seoul 120-749, Korea*

(Received 30 May 2015; revised manuscript received 21 September 2015; published 16 October 2015)

The hybrid halide perovskite $CH_3NH_3PbI_3$ exhibits a complex structural behavior, with successive transitions between orthorhombic, tetragonal, and cubic polymorphs around 165 and 327 K. Herein we report first-principles lattice dynamics (phonon spectrum) for each phase of $CH_3NH_3PbI_3$. The equilibrium structures compare well to solutions of temperature-dependent powder neutron diffraction. By following the normal modes, we calculate infrared and Raman intensities of the vibrations, and compare them to the measurement of a single crystal where the Raman laser is controlled to avoid degradation of the sample. Despite a clear separation in energy between low-frequency modes associated with the inorganic $(PbI_3{}^-)_n$ network and high-frequency modes of the organic $CH_3NH_3{}^+$ cation, significant coupling between them is found, which emphasizes the interplay between molecular orientation and the corner-sharing octahedral networks in the structural transformations. Soft modes are found at the boundary of the Brillouin zone of the cubic phase, consistent with displacive instabilities and anharmonicity involving tilting of the PbI_6 octahedra around room temperature.

DOI: 10.1103/PhysRevB.92.144308 PACS number(s): 78.30.−j, 63.20.D−, 63.20.Ry

I. INTRODUCTION

Materials that adopt the perovskite crystal structure are known for their complex structural landscapes, with a large number of accessible polymorphs depending on the temperature, pressure, and/or applied electric field. For ternary ABX_3 perovskites, the A site cation is at the center of a cube formed of corner-sharing BX_6 octahedra. Displacement of the A cation is usually associated with a ferroelectric (Brillouin-zone center) instability, while tilting of the BX_6 octahedral network is usually linked to antiferroelectric (Brillouin-zone boundary) transitions [1,2].

Hybrid organic-inorganic perovskites are formed when one of the elemental perovskite building blocks is replaced by a molecular anion or cation [3,4]. There exists a large family of such compounds, including the widely studied formate perovskites, which contains both molecular anions and cations [5–7]. Hybrid *halide* perovskites are of current intense research effort due to their high-efficiency photovoltaic action [8–16].

Methylammonium lead iodide ($MAPbI_3$, where MA represents the $CH_3NH_3{}^+$ cation) was first reported by Weber in 1978 [17]. It is the most relevant hybrid halide perovskite for photovoltaic application. The transition from orthorhombic to tetragonal to cubic perovskite structures as a function of temperature has been studied by techniques including calorimetry and infrared spectroscopy [18], single-crystal x-ray diffraction [19], and dielectric spectroscopy [20]. Recently analysis of powder neutron-diffraction (PND) measurements has provided more quantitative insight into the temperature-dependent behavior of the MA cation within the anionic $(PbI_3{}^-)_n$ network [21]. There is now direct evidence for the degree of order of the MA cation in the different phases, and the average lattice parameters (and thus extent of octahedral tilting) as a function of temperature through the first- and second-order phase transitions. Quasielastic neutron scattering has provided further insight into the rotational dynamics of the MA cation with a room-temperature residence time of ~14 ps [22], while time-resolved vibrational spectroscopy has identified fast librations (300 fs) and slow rotations (3 ps) of the molecule [23].

In this study, we calculate the phonon dispersion in each phase of $MAPbI_3$ within the harmonic approximation, computing the force constants with density functional theory (DFT). We use the PBEsol functional, which is a generalized-gradient approximation (GGA) to the exchange-correlation functional, numerically evaluated with Perdew's method, adjusted to give more accurate lattice constants and forces for solids [24]. The lattice dynamic calculations allow the atomic origin of each phonon mode to be identified. Changes in lattice polarization and polarizability for each eigenvector provide the infrared and Raman activity of each mode. Spectral features related to the inorganic and organic components (from 0 to 3000 cm^{-1}) are well reproduced in comparison to the Raman spectra of a single crystal of $MAPbI_3$. Overlap is found between the vibrations of the $CH_3NH_3{}^+$ and $PbI_3{}^-$ components up to 130 cm^{-1}, with the modes from 300 to 3000 cm^{-1} being associated with pure molecular vibrations. The phonon dispersion has implications for developing quantitative models for the generation,

---

[*] a.walsh@bath.ac.uk

transport, and recombination of photogenerated electrons and holes in hybrid perovskite solar cells.

Structure models

The normal modes of a system are defined for an equilibrium configuration. Calculating the vibrations for a nonequilibrium structure will result in imaginary frequencies upon diagonalizing the dynamical matrix. Therefore, we have generated well-optimized structures of $\mathrm{MAPbI_3}$. One challenge in calculating the phonons of hybrid perovskites is the soft nature and complicated potential-energy landscape of some of the restoring potentials, particularly those involving the organic cation.

The models for the crystal structures used in this study are discussed in detail below and a comparison with the measured diffraction patterns is provided as Supplemental Material [25].

1. *Orthorhombic phase*

The orthorhombic perovskite structure is the low-temperature ground state of $\mathrm{MAPbI_3}$ and maintains its stability up to around 165 K [21,26,27]. A comparison of the enthalpy from DFT calculations confirms this ordering in stability. The difference in enthalpy is small, i.e., just 2 meV per $\mathrm{MAPbI_3}$ unit, compared to the lowest energy tetragonal phase, yet 90 meV compared to the high-temperature cubic phase.

Initial diffraction pattern solutions are assigned to the $Pna2_1$ space group [18,26]. Recent analysis of higher-quality powder neutron-diffraction data reassigns it to $Pnma$ (a D_{2h} point group) [21]. The structure is a $\sqrt{2}a \times \sqrt{2}a \times 2a$ supercell expansion of the simple cubic perovskite lattice, i.e., following the lattice transformation matrix

$$\begin{pmatrix} 1 & -1 & 0 \\ 1 & 1 & 0 \\ 0 & 0 & 2 \end{pmatrix}. \tag{1}$$

In the $Pna2_1$ phase, the $\mathrm{PbI_6}$ octahedra are distorted and tilt as $a^+b^-b^-$ in Glazer notation [1] with respect to the orientation of the conventional cubic cell. In this low-temperature phase, the four molecular cations in the unit cell are static on the diagonals of the ab planes pointing towards the undistorted facets of the cuboctahedral cavity. Correspondingly, molecules belonging to different planes are antialigned with a head-tail motif. Such an antiferroelectric alignment is expected from consideration of the molecular dipole-dipole interaction [28].

In the low-temperature orthorhombic phase, the $\mathrm{CH_3NH_3}^+$ sublattice is fully ordered (a low-entropy state). The ordering may be sensitive to the material preparation and/or cooling rate into this phase, i.e., the degree of quasithermal equilibrium. It is possible that different ordering might be frozen into the low-temperature phase by epitaxy or application of external force or electric fields.

2. *Tetragonal phase*

At 165 K, $\mathrm{MAPbI_3}$ goes through a first-order phase transition from the orthorhombic to the tetragonal space group $I4/mcm$ (D_{4h} point group), which continuously undergoes a second-order phase transition to the cubic phase around 327 K [21,26,27]. As with the orthorhombic phase, this can be considered a $\sqrt{2}a \times \sqrt{2}a \times 2a$ expansion of the cubic perovskite unit cell.

The molecular cations are no longer in a fixed position as in the orthorhombic phase. The molecules are disordered between two nonequivalent positions in each cage [27,30]. The tetragonal distortion parameter in the cubic basis is greater than unity ($\frac{c}{2a} \sim 1.01$ at 300 K), corresponding to an elongation of the $\mathrm{PbI_6}$ octahedra along the c axis. The associated octahedral tilting pattern is $a^0a^0c^-$ in Glazer notation.

Atomistic simulations within periodic boundary conditions require an ordered configuration. The solved crystal structure shows that there are several possible configurations for the organic cations within the tetragonal unit cell. These configurations have similar enthalpies within DFT [31], which is consistent with the observed disorder. We choose to use the most energetically stable structure, which is also consistent with a previous DFT investigation [32].

In the model of the tetragonal structure, the MA cations are aligned as in the orthorhombic phase, towards the face of the perovskite cage, i.e., $\langle 100 \rangle$ in the cubic basis. The MA in different (001) planes are approximately orthogonal to one another. The orientational dynamics of the methylammonium ions, which exists above 165 K, is not taken into account in this equilibrium configuration study.

3. *Cubic phase*

With increasing temperature, the tetragonal lattice parameters become more isotropic (i.e., $\frac{c}{2a}$ moves closer to 1) and the molecular disorder increases, to the point where a transition to a cubic phase occurs around 327 K. The transition can be seen clearly from changes in the heat capacity [18] as well as in temperature-dependent neutron diffraction [21].

The cubic space group $Pm\bar{3}m$ (O_h symmetry) has been assigned to this high-temperature phase. Although the methylammonium ions possesses C_{3v} symmetry, the orientational disorder gives rise to the effective higher symmetry on average. The local structure will necessarily have a lower symmetry. Indeed, for the bromide and chloride analogues of $\mathrm{MAPbI_3}$, pair-distribution function analysis of x-ray scattering data indicates a local structure with significant distortion of the lead halide framework at room temperature [33].

We previously considered alignment of the molecules along the principal $\langle 100 \rangle$ (face), $\langle 110 \rangle$ (edge), and $\langle 111 \rangle$ (diagonal) directions of the cubic unit cell, and showed that they are of similar DFT enthalpy, with a small barrier for rotation [34]. Further *ab initio* molecular dynamics showed an average preference for the $\langle 100 \rangle$ facial configuration at 300 K [28]. Therefore, we chose the $\langle 100 \rangle$ configuration as our reference structure for the lattice vibrations.

Representations of the crystal structure of each phase are shown in Fig. 1, the equilibrium structure parameters are listed in Table I, and the structures themselves are available in an online repository [29].

II. METHODS

A. Computations

The total energy and atomic forces were computed from first principles within density functional theory as implemented

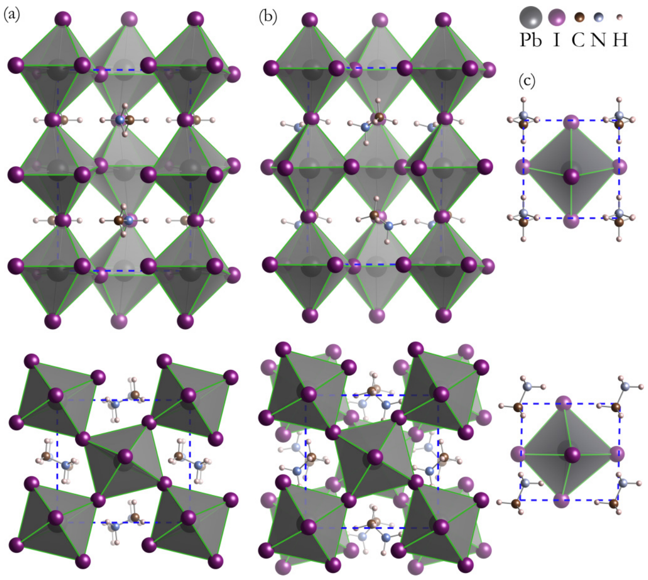

FIG. 1. (Color online) The crystal structures of the (a) orthorhombic, (b) tetragonal, and (c) cubic phases of $CH_3NH_3PbI_3$. The upper and lower panels are oriented through ⟨100⟩ and ⟨001⟩, respectively. Lattice parameters and coordinates obtained from powder neutron diffraction were optimized using density functional theory (PBEsol). The PbI_6 octahedra are shaded gray. All structures are available in an online repository [29].

in the code VASP [36,37]. Noise in the lattice vibrations was minimized by rigorous convergence of total Kohn-Sham energy with respect to the basis set (kinetic-energy cutoff for plane waves) and sampling of reciprocal space (density of the k-point mesh). The final computational setup is summarized in Table I.

We performed complete optimization of the cell volume, shape, and atomic positions, with the PBEsol [24] semilocal exchange-correlation functional. The scalar-relativistic projector-augmented wave method [38] was employed, with a pseudopotential treating the Pb 5d orbitals as valence. Spin-orbit coupling was not considered as it mainly affects the Pb 6p conduction band, which does not influence the interatomic interactions at equilibrium. All atomic forces were reduced to below a threshold of 1 meV/Å. Due to the presence of the organic cations, which break the ideal lattice symmetry, deviations in the expected parameters can occur, e.g., in the high-temperature pseudocubic phase, the three equilibrium lattice parameters are not equal. The equilibrium structure parameters (at 0 K and excluding zero-point contributions) are reported in Table I.

The normal modes are calculated within the harmonic approximation, using the PHONOPY [39–41] package to construct and evaluate the dynamical matrix composed of DFT force constants. Both the finite displacement method (FDM or supercell approach) [42] and density functional perturbation theory (DFPT) [43] approaches to construct the force constants were tested. The results of both approaches produced similar vibrational spectra, with a variance in the mode energies of 6 cm^{-1}.

Within a primitive cell of N atoms, there are 6N possible displacements ($\pm x, \pm y, \pm z$), which can be reduced by the crystal symmetry. For the orthorhombic phase, the 288 possible displacements are reduced to 41, while the tetragonal and cubic phases required 288 and 72 displacements, respectively. The phonon dispersion (for $\mathbf{q}$ points away from the Brillouin-zone center, the Γ point) in the cubic phase was probed in a $2 \times 2 \times 2$ supercell. Due to computational expense, we did not calculate this for the other (larger unit cell) phases, where the phonons are considered at the Γ point only.

Once the normal eigenmodes and eigenvalues are calculated, it is possible to model their associated Raman and infrared (IR) activity by mode following. The two spectroscopic techniques probe different physical responses of the material: the change in polarization for IR and the change in polarizability for Raman. The IR spectra are simulated with the analytic formula of Gianozzi and Baroni (using the Born effective charge tensor) [43]. Prediction of the Raman spectra required computing the change in macroscopic dielectric tensor with respect to each normal mode of the system, a significant DFT calculation in terms of computational expense [44].

B. Experiment

Methylammonium lead iodide single crystals were grown according to the method of Poglitsch and Weber [26]. 12.5 g of lead acetate trihydrate [$Pb(CH_3CO_2)_2 \cdot 3\,H_2O$, Sigma] was

TABLE I. Equilibrium cell parameters from DFT/PBEsol energy minimization, including the converged plane-wave cutoff, k-point mesh, and force threshold. Z represents the number of formula units of $CH_3NH_3PbI_3$ per cell. The calculated difference in enthalpy (ΔH) of each phase is given with respect to the ground-state orthorhombic configuration and per $CH_3NH_3PbI_3$ unit. Shown for comparison are the cell parameters and average Pb-I interatomic separations (d) from powder neutron diffraction (PND) [21].

Phase	a (Å)	b (Å)	c (Å)	d(Pb-I) (Å)	Z	Cutoff (eV)	k points	Forces (meV/Å)	ΔH (meV)
Orthorhombic									
DFT/PBEsol	9.04	12.66	8.35	3.18	4	700	5 × 4 × 5	1	0
PND (100 K)	8.87	12.63	8.58	3.19					
Tetragonal									
DFT/PBEsol	8.70	8.72	12.83	3.19	4	800	5 × 5 × 3	1	2
PND (180 K)	8.81	8.81	12.71	3.17					
Cubic									
DFT/PBEsol	6.29	6.23	6.37	3.17	1	700	6 × 6 × 6	1	90
PND (352 K)	6.32	6.32	6.32	3.16					

dissolved in 10 mL hydroiodic acid (HI_{aq}, 57 wt%, Sigma) in a 50 mL round bottom flask and heated to 100 °C in an oil bath. Separately, 0.597 g of CH_3NH_2 (aq, 40 wt%, Sigma) was added dropwise to a further 2 mL of HI_{aq} kept at 0 °C in an ice bath under stirring. The methylammonium iodide solution was then added to the lead acetate solution and the mixture was cooled over five days to a temperature of 46 °C, resulting in the formation of black crystals with largest face length around 8 mm. The content of the flasks was subsequently filtered and dried for 12 hours at 100 °C.

Raman spectra were collected in backscattering geometry with a high-resolution LabRam HR800 spectrometer using a grating with 600 lines per millimeter and equipped with a liquid-nitrogen-cooled charge coupled device (CCD) detector. The 785 nm line of a diode-pumped solid-state laser was used as excitation beam and focused onto the sample using a long-distance 20× microscope objective. Raman measurements were carried out at 100 K using a gas-flow-type cryostat with optical access that fits under the microscope of the Raman setup. The high spectral resolution and stray-light rejection of the LabRam spectrometer, particularly in combination with the 785 nm line, allowed us to measure the Raman spectrum of MAPI at very low Raman shifts down to 20 to 30 cm^{-1}. In this way, we were able to spectrally resolve several low-frequency modes associated with vibrations of the inorganic cage of the hybrid perovskite.

Heating by laser light directly absorbed by $CH_3NH_3PbI_3$ has been shown to lead to rapid degradation of the material, resulting in PbI_2 Raman signatures [45]. Since 785 nm light is only weakly absorbed, the heating effect of the laser was low enough to ensure the crystal structure was preserved. The power density incident on the sample was kept at 80 W/cm^2. At such power level, it was checked that no appreciable spectral changes in peak width and/or position occurred, while still providing a good signal-to-noise ratio. Further, samples were kept under vacuum inside the cryostat during the measurements.

III. RESULTS

A. Harmonic phonons

The full phonon density of states (DOS) is shown for the three phases of $CH_3NH_3PbI_3$ in Fig. 2. Also plotted is the partial DOS, where assignment to $CH_3NH_3^+$ or PbI_3^- is performed based on the atomic contribution to each eigenvector. An animation of all 36 eigenmodes of the cubic phase is provided as Supplemental Material [25].

Qualitatively, each $MAPbI_3$ phase shows similar vibrational properties with three energetic regions of phonons: (i) a low-frequency band from 0–150 cm^{-1}, (ii) a midfrequency band from 280–1600 cm^{-1}, and (iii) a high-frequency band from 2900–3300 cm^{-1}. These ranges are consistent with previous computational reports [46,47].

Due to the large difference in atomic mass of the organic and inorganic components, and to the difference in bonding between the inorganic cage and the covalently bonded molecule, we anticipated that the low-frequency modes would be comprised entirely of motion by the PbI_6 octahedra, while the high-frequency modes would involve the $CH_3NH_3^+$ cation. This is qualitatively the case, but there is also significant coupling between the two. Taking the example of the cubic phase with 36 modes, the highest-energy 18 modes [forming bands (ii) and (iii)] correspond to molecular vibrations, i.e., the 3N-6 modes of the methylammonium ion. For an isolated nonlinear molecule, the 6 translational and rotational degrees of freedom do not contribute to the pure vibrational spectrum, but this is not the case for a molecule inside a cuboctahedral cavity.

The 6 additional molecular modes are strongly coupled to the 9 modes (i.e., 3N-3 for PbI_3^-) associated with stretching of the Pb-I bonds and breathing of the PbI_6 octahedra, which results in the spectral overlap observed in the partial DOS of band (i). Particularly striking is the low-frequency pivoting motion associated with the libration of the molecular dipole, coupled with a breathing of the octahedral framework (e.g., modes 10 and 15 in the SI). The final three zero-frequency modes correspond to acoustic translations of the lattice.

B. Vibrational spectra

For $MAPbI_3$, it is not possible for the relaxed (nonidealized) crystal structures to assign the spectral activity directly with group theoretic irreducible representation analysis of the phonon modes. The molecule breaks the average crystal symmetry. This symmetry lowering allows for simultaneous Raman and IR activity, even in the pseudocubic phase. The predicted spectra (the Γ-point phonon modes weighted by the computed spectral intensity, convolved with a Lorentzian for experimental comparison) are reported in Fig. 2 for each phase.

Raman and IR activity is observed across each of the three phonon bands previously discussed. A notable exception is the lowest-energy purely molecular vibration near 300 cm^{-1}, which is neither Raman nor IR active.

To understand the effect of embedding the methylammonium in $MAPbI_3$, we calculate the normal-mode vibrations of an isolated methylammonium ion in vacuum with a similar density functional theory method to our periodic calculations Perdew-Burke-Ernzerhof (PBE) with an atom-centered augmented cc-pVQZ basis set. Thereby, we calculate the 18 molecular modes, directly accessing their symmetries and nature. The C_{3v} symmetry of the molecule separates the vibrational bands into one A symmetric mode and blueshifted twofold degenerate asymmetric E modes. The six bands we find are in ascending energy: twist around the C-N axis (282, 886 cm^{-1}), vibration along the C-N axis (923, 1239 cm^{-1}), bending of the C-H bonds (1418, 1451 cm^{-1}), bending of the N-H bonds (1478, 1622 cm^{-1}), stretching of the C-H bonds (3018, 3119 cm^{-1}), and stretching of the N-H bonds (3321, 3395 cm^{-1}).

As the cation charge density is centered towards the N, the motion of the protons associated with N have the strongest affect on the dipole moment and therefore strongest IR activity. Due to the stronger bonds, their frequencies are consistently blueshifted relative to the C end. Owing to the molecular dipole moment (2.2 D [28], which is rotation and position invariant, and corresponds to a polarization contribution of ~3 $\mu C/cm^2$), the two high-frequency asymmetric stretching modes of NH_3^+ [band (iii)] results in the strongest absolute IR intensity. The hydrogen stretching modes [band (iii)] are responsible for

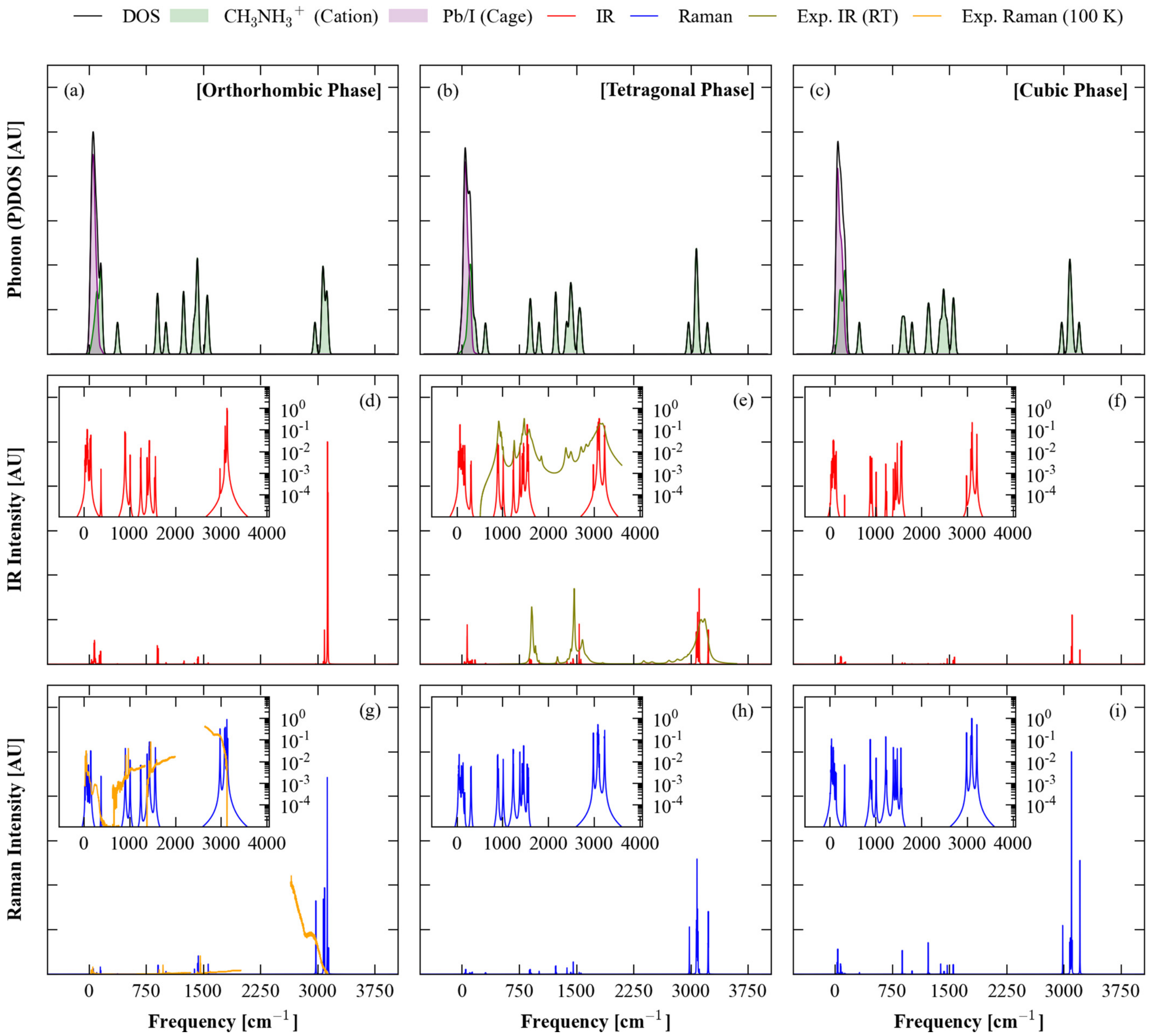

FIG. 2. (Color online) (a)–(c) Projected phonon density of states (PDOS) for the three phases of $CH_3NH_3PbI_3$ as calculated from DFT/PBEsol, generated by convolution with a 16 cm^{-1} Lorentzian. Note that no imaginary (negative) modes are found in the orthorhombic or tetragonal phases. (d)–(f) Simulated infrared (IR) spectra. (e) The measured IR spectrum at 300 K from Ref. [35] is coplotted in green (light gray). (g)–(i) Simulated Raman spectrum. (g) The measured Raman spectrum of a single crystal in the orthorhombic phase at 100 K is coplotted in orange (light gray). Simulated spectra were broadened by convolution with a 2 cm^{-1} Lorentzian. Insets in the simulated spectra are the same data on a logarithmic scale to show the structure in the low-intensity modes.

significant Raman activity. The only mode involving C or N motion is the weakly IR and Raman active vibration at 923 cm^{-1} (vacuum), 1007 cm^{-1} (cubic perovskite).

The rotation of the CH_3 against the NH_3 unit, while being strongly populated in molecular dynamic simulations, and which forms the main source of quasi-inelastic neutron scattering, is entirely IR and Raman inactive in vacuum. This is the mode responsible for the 282 cm^{-1} (vacuum), 318 cm^{-1} (cubic), 300–310 cm^{-1} (tetragonal), 370–372 cm^{-1} (orthorhombic) vibration. Progressive confinement of MA from vacuum to the orthorhombic phase blueshifts the energy of the vibration.

In the solid state, the degeneracies in the molecular modes are typically split by local environment effects, peaks are both redshifted and blueshifted, and the IR and Raman activity varies. As such, it is evident that analysis of the Raman and IR spectra in the experimentally easily accessible molecular frequency range can enable statements to be made about the local structure and configuration of the hybrid perovskite. Our data is collected for a particular representation of the cubic and tetragonal phase; in reality, the location of the MA in these phases will be disordered. As such, a detailed comparison of theory to experiment will require sampling the thermodynamic ensemble of structures.

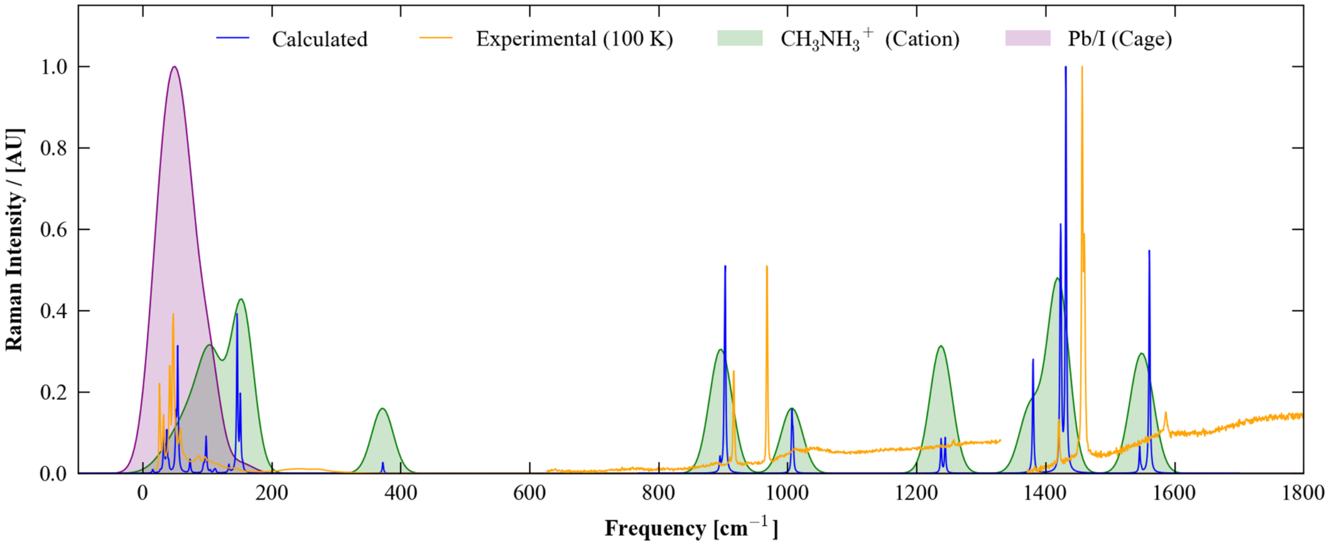

FIG. 3. (Color online) Comparison of the calculated and measured (100 K) Raman spectrum for the orthorhombic perovskite phase of $CH_3NH_3PbI_3$ in the range 0–1800 cm^{-1}, which includes phonon modes centered on the inorganic cage (lowest frequency), organic cage (highest frequency), and coupled modes (intermediate frequency). The simulated spectrum was broadened by convolution of a 2 cm^{-1} Lorentzian, while the underlying phonon density of states is shown for comparison with a broadening of 32 cm^{-1}.

Here, Raman spectra for the three phases is reported across the full frequency range. The spectrum up to 450 cm^{-1} was reported in Ref. [46]. Reliable measurements are a challenge due to chemical instability of the material. $MAPbI_3$ is strongly affected by environmental conditions, such as the presence of ambient moisture [27,48]. Isolated in vacuum, the material can still decompose and bleach due to heating, including by that imposed by the (typically high) Raman laser fluence [45]. Such degradation leads to the formation of PbI_2, which overlaps in Raman spectra with $MAPbI_3$, and so easily leads to misinterpretation.

The Raman spectra of a high-quality single crystal of $MAPbI_3$ is shown in Fig. 2, and compared in detail with the calculations in Fig. 3. Across the full spectral range, the agreement between the predicted and measured spectra is good, with the response across bands (i)–(iii) well reproduced. On closer inspection of Fig. 3, there are noticeable shifts in peak positions, which can be attributed to three potential sources of error: (a) the harmonic approximation (anharmonic renormalization may be large), (b) the limits of the exchange-correlation treatment (nonlocal interactions may be important), and (c) the assumption of a fully ordered structure (local inhomogeneity may be prevalent). There is also a notable case of an absence of measured Raman activity around 150 cm^{-1}, which we can tentatively attribute to a lifetime broadening effect. The same level of theory applied to the lead-based semiconductors PbS and PbTe results in quantitative agreement with measured phonon frequencies and dispersion [49], which highlights the complex nature of $CH_3NH_3PbI_3$.

We have also included in Fig. 2 a room-temperature IR spectrum reported by Glaser *et al.* [35], which again shows excellent agreement across the spectrum. A number of very weak absorption peaks below 3000 cm^{-1} are evident, which could be related to molecular disorder and/or partial decomposition. The temperature-resolved (between 140 and 299 K) IR spectra for tetragonal and orthorhombic phases have been previously reported by Yamamuro [50]. We reproduce the position and the intensity of the peak observed at 900 cm^{-1}, reliably assigning it to the (also Raman-active) C-N bond stretch. High-quality IR measurements, in particular looking at the very low-energy transitions, would provide considerable information on the nature of the domains and local structure in a $MAPbI_3$ film.

C. Anharmonic effects

The lattice dynamic simulations discussed above were performed within the harmonic approximation. All eigenmodes at the center of the Brillouin zone were real (positive frequencies) for each phase, i.e., the structures are locally stable.

The phonon dispersion across the first Brillouin zone is shown for the cubic perovskite structure in Fig. 4. Here imaginary (negative frequency or "soft") modes are found at the zone boundaries. Such instabilities are a common feature of the perovskite structure and represent antiferroelectric distortions linked to to rotations and tiling of the octahedra in neighboring unit cells [2]. The soft modes are centered around the *R* and *M* points, which correspond to the $\langle 111 \rangle$ and $\langle 110 \rangle$ directions in the cubic lattice. This behavior is similar to the inorganic perovskite $CsPbCl_3$, where neutron scattering was used to probe condensation of these modes, which leads to successive transitions from the cubic to tetragonal to orthorhombic phases [51]. The effect of these modes in $MAPbI_3$, and the associated high levels of anharmonicity at room temperature, can be observed directly in molecular dynamics simulations, where temporal rotations of the $CH_3NH_3^+$ ions and distortions of the PbI_6 octahedra have been found in several studies [22,28,52].

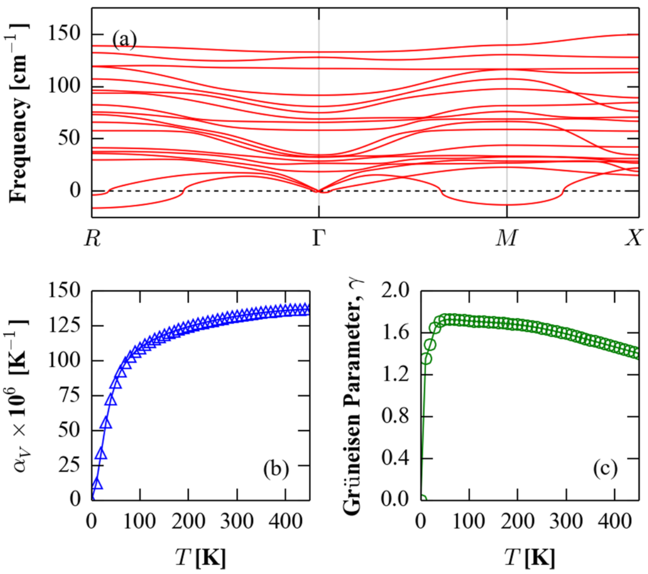

FIG. 4. (Color online) Vibrational properties of the cubic phase of MAPbI$_3$: (a) Phonon dispersion of the low-frequency (inorganic cage) modes within the harmonic approximation. Negative frequency (imaginary or "soft") modes are found at the Brillouin-zone boundary points $M[\frac{2\pi}{a}(\frac{1}{2},\frac{1}{2},0)]$ and $R[\frac{2\pi}{a}(\frac{1}{2},\frac{1}{2},\frac{1}{2})]$. (b) Volumetric thermal expansion within the quasiharmonic approximation. (c) Average Grüneisen parameter within the quasiharmonic approximation.

An approach to include the effects of temperature (thermal expansion) and first-order anharmonicity in lattice dynamic calculations is the quasiharmonic approximation (QHA) [53,54]. The computational cost is one order of magnitude higher than the harmonic approximation and thus was considered for the cubic phase only. The volumetric thermal-expansion coefficient extracted from the PND data at 300 K is 1.32×10^{-4}/K, which compares very well to the value of 1.25×10^{-4}/K computed within the QHA. The predicted thermal expansion for MAPbI$_3$ is similar to inorganic semiconductors (e.g., for PbTe, the value is 0.7×10^{-4}/K at 300 K [40]) and positive over the full temperature range.

The temperature dependence of the phonon modes can be described by the Grüneisen parameter, which has an average of around 1.6 (see Fig. 4), slightly below the value of 1.7 found in PbI$_2$ [55]. The imaginary modes at R and M remain at all temperatures, consistent with the cubic lattice being a dynamic average of a locally distorted structure; the same phenomenon is observed in CsSnI$_3$ [56]. The high level of anharmonicity associated with the soft tilting modes is consistent with the "ultralow" (<1 Wm^{-1} K^{-1} at 300 K) lattice thermal conductivity reported for single crystals and polycrystalline MAPbI$_3$ [57]. Hybrid halide perovskites are thus also promising for application in thermoelectric devices if thermal-stability issues can be overcome [58].

IV. CONCLUSIONS

The vibrational frequencies of three crystallographic phases of the hybrid perovskite CH$_3$NH$_3$PbI$_3$ have been investigated. We identified three main phonon branches present in the three phases. Two high-frequency branches are associated with the vibration and bond stretching of the molecular cation with frequencies in the range 300 to 3300 cm^{-1}. The lowest-energy branch, below 150 cm^{-1}, arises predominately from the inorganic cage, but with half of the modes coupled to the motion of the molecule. The simulated Raman spectrum of the orthorhombic phase is in good agreement with measurements on a single crystal of MAPbI$_3$. Dynamic instabilities occur at the zone boundaries of the cubic phase, which requires methods beyond the harmonic approximation, such as self-consistent phonon theory, for an accurate treatment. These results suggest that the room-temperature structure of MAPbI$_3$ is fluctional, owing to the persistent tilting and distortion of the octahedral networks and rotations of the molecular cations.

These factors may be important for developing a quantitative understanding and model of how hybrid perovskite solar cells operate. Upon excitation, the relative stability of free carriers and excitons depends intimately on the dielectric screening of the material, which includes vibrational and rotational components. The transport and recombination of photogenerated charge carriers will also be influenced by electron-phonon coupling, which can significantly reduce the effective size and distribution of electrons and holes within the perovskite layer.

Note added in proof. A neutron scattering investigation of MAPbBr$_3$ has very recently been reported [59], which identifies strong coupling between the vibrations of the molecule and the inorganic cage, analogous to the overlap identified in our study of the iodide material. A soft mode associated with octahedral titling is also measured that is in support of our observations.

ACKNOWLEDGMENTS

The authors are grateful for helpful discussions with Mariano Campoy-Quiles. The research at the University of Bath has been supported by the EPSRC (Grants No. EP/K016288/1, No. EP/K004956/1, and No. EP/M009580/1), ERC (Grant No. 277757), EU-FP7 (Grant No. 316494), and the Royal Society. A.J.J. and O.J.W. were funded through the CDT in Sustainable Chemical Technologies (EPSRC Grant No. EP/ G03768X/1). P.R.F.B. and A.M.A.L. are grateful to the EPSRC (Grants No. EP/J002305/1, No. EP/M014797/1, and No. EP/M023532/1). A.R.G. acknowledges the Spanish Ministerio de Economa y Competitividad (MINECO) through Projects No. MAT2012-37776 and No. CSD2010-00044 (Consolider NANOTHERM). This work benefited from access to both the University of Bath's High Performance Computing Facility and ARCHER, the United Kingdom's national high-performance computing service, which is funded by the Office of Science and Technology through EPSRC's High End Computing Programme (Grant No. EP/L000202).

[1] A. M. Glazer, Acta Crystallogr. Sect. B **28**, 3384 (1972).

[2] N. A. Benedek and C. J. Fennie, J. Phys. Chem. C **117**, 13339 (2013).

[3] D. B. Mitzi, J. Chem. Soc. Dalt. Trans. **2001**, 1 (2001).

[4] J. M. Frost, K. T. Butler, F. Brivio, C. H. Hendon, M. Van Schilfgaarde, and A. Walsh, Nano Lett. **14**, 2584 (2014).

[5] A. B. Cairns and A. L. Goodwin, Chem. Soc. Rev. **42**, 4881 (2013).

[6] W. Li, Z. Zhang, E. G. Bithell, A. S. Batsanov, P. T. Barton, P. J. Saines, P. Jain, C. J. Howard, M. A. Carpenter, and A. K. Cheetham, Acta Mater. **61**, 4928 (2013).

[7] G. Kieslich, S. Kumagai, K. T. Butler, T. Okamura, C. H. Hendon, S. Sun, M. Yamashita, A. Walsh, and A. K. Cheetham, Chem. Commun. **51**, 15538 (2015).

[8] A. Kojima, K. Teshima, Y. Shirai, and T. Miyasaka, J. Am. Chem. Soc. **131**, 6050 (2009).

[9] J.-H. Im, C.-R. Lee, J.-W. Lee, S.-W. Park, and N.-G. Park, Nanoscale **3**, 4088 (2011).

[10] M. M. Lee, J. Teuscher, T. Miyasaka, T. N. Murakami, and H. J. Snaith, Science **338**, 643 (2012).

[11] M. Liu, M. B. Johnston, and H. J. Snaith, Nature (London) **501**, 395 (2013).

[12] F. De Angelis, Acc. Chem. Res. **47**, 3349 (2014).

[13] J. Even, L. Pedesseau, C. Katan, M. Kepenekian, J.-S. Lauret, D. Sapori, and E. Deleporte, J. Phys. Chem. C **119**, 10161 (2015).

[14] A. Walsh, D. O. Scanlon, S. Chen, X. G. Gong, and S.-H. Wei, Angew. Chemie Int. Ed. **54**, 1791 (2015).

[15] A. Walsh, J. Phys. Chem. C **119**, 5755 (2015).

[16] N. J. Jeon, J. H. Noh, W. S. Yang, Y. C. Kim, S. Ryu, J. Seo, and S. I. Seok, Nature (London) **517**, 476 (2015).

[17] D. Weber, Z. Naturforsch. B **33b**, 1443 (1978).

[18] N. Onoda-Yamamuro, T. Matsuo, and H. Suga, J. Phys. Chem. Solids **51**, 1383 (1990).

[19] Y. Kawamura, H. Mashiyama, and K. Hasebe, J. Phys. Soc. Japan **71**, 1694 (2002).

[20] N. Onoda-Yamamuro, T. Matsuo, and H. Suga, J. Phys. Chem. Solids **53**, 935 (1992).

[21] M. T. Weller, O. J. Weber, P. F. Henry, A. M. Di Pumpo, and T. C. Hansen, Chem. Commun. **51**, 4180 (2015).

[22] A. M. A. Leguy, J. M. Frost, A. P. McMahon, V. G. Sakai, W. Kochelmann, C. Law, X. Li, F. Foglia, A. Walsh, B. C. O'Regan, J. Nelson, J. T. Cabral, and P. R. F. Barnes, Nat. Commun. **6**, 7124 (2015).

[23] A. A. Bakulin, O. Selig, H. J. Bakker, Y. L. A. Rezus, C. Müller, T. Glaser, R. Lovrincic, Z. Sun, Z. Chen, A. Walsh, J. M. Frost, and T. L. C. Jansen, J. Phys. Chem. Lett. **6**, 3663 (2015).

[24] J. P. Perdew, A. Ruzsinszky, G. I. Csonka, O. A. Vydrov, G. E. Scuseria, L. A. Constantin, X. Zhou, and K. Burke, Phys. Rev. Lett. **100**, 136406 (2008).

[25] See Supplemental Material at http://link.aps.org/supplemental/10.1103/PhysRevB.92.144308 for an animation of the zone-center vibrational modes of the cubic perovskite phase and a comparison of the simulated and measured diffraction patterns.

[26] A. Poglitsch and D. Weber, J. Chem. Phys. **87**, 6373 (1987).

[27] T. Baikie, Y. Fang, J. M. Kadro, M. Schreyer, F. Wei, S. G. Mhaisalkar, M. Gratzel, and T. J. White, J. Mater. Chem. A **1**, 5628 (2013).

[28] J. M. Frost, K. T. Butler, and A. Walsh, APL Mater. **2**, 081506 (2014).

[29] https://github.com/WMD-Bath/Hybrid-perovskites.

[30] R. Wasylishen, O. Knop, and J. Macdonald, Solid State Commun. **56**, 581 (1985).

[31] Z. Fan, J. Xiao, K. Sun, L. Chen, Y. Hu, J. Ouyang, K. P. Ong, K. Zeng, and J. Wang, J. Phys. Chem. Lett. **6**, 1155 (2015).

[32] C. Quarti, E. Mosconi, and F. De Angelis, Chem. Mater. **26**, 6557 (2014).

[33] R. J. Worhatch, H. J. Kim, I. P. Swainson, a. L. Yonkeu, and S. J. L. Billinge, Chem. Mater. **20**, 1272 (2008).

[34] F. Brivio, A. B. Walker, and A. Walsh, APL Mater. **1**, 042111 (2013).

[35] T. Glaser, C. Müller, M. Sendner, C. Krekeler, O. E. Semonin, T. D. Hull, O. Yaffe, J. S. Owen, W. Kowalsky, A. Pucci, and R. Lovrinčić, J. Phys. Chem. Lett. **6**, 2913 (2015).

[36] G. Kresse and J. Furthmüller, Comput. Mater. Sci. **6**, 15 (1996).

[37] G. Kresse and D. Joubert, Phys. Rev. B **59**, 1758 (1999).

[38] P. E. Blöchl, Phys. Rev. B **50**, 17953 (1994).

[39] A. Togo, L. Chaput, I. Tanaka, and G. Hug, Phys. Rev. B **81**, 174301 (2010).

[40] J. M. Skelton, S. C. Parker, A. Togo, I. Tanaka, and A. Walsh, Phys. Rev. B **89**, 205203 (2014).

[41] A. Togo, L. Chaput, and I. Tanaka, Phys. Rev. B **91**, 094306 (2015).

[42] R. P. Stoffel, C. Wessel, M.-W. Lumey, and R. Dronskowski, Angew. Chem. Int. Ed. England **49**, 5242 (2010).

[43] S. Baroni and S. D. Gironcoli, Rev. Mod. Phys. **73**, 515 (2001).

[44] J. M. Skelton, E. L. da Silva, R. Crespo-Otero, L. E. Hatcher, P. R. Raithby, S. C. Parker, and A. Walsh, Faraday Discuss. **177**, 181 (2015).

[45] M. Ledinský, P. Löper, B. Niesen, J. Holovský, S.-J. Moon, J.-H. Yum, S. De Wolf, A. Fejfar, and C. Ballif, J. Phys. Chem. Lett. **6**, 401 (2015).

[46] C. Quarti, G. Grancini, E. Mosconi, P. Bruno, J. M. Ball, M. M. Lee, H. J. Snaith, A. Petrozza, and F. D. Angelis, J. Phys. Chem. Lett. **5**, 279 (2014).

[47] T. Ahmed, C. La-o vorakiat, T. Salim, Y. M. Lam, E. E. M. Chia, and J.-X. Zhu, Europhys. Lett. **108**, 67015 (2014).

[48] J. H. Noh, S. H. Im, J. H. Heo, T. N. Mandal, and S. I. Seok, Nano Lett. **13**, 1764 (2013).

[49] J. M. Skelton, D. Tiana, S. C. Parker, A. Togo, I. Tanaka, and A. Walsh, J. Chem. Phys. **143**, 064710 (2015).

[50] N. Onoda-yamamuro, Ph.D. thesis, Osaka University, 1992.

[51] Y. Fujii, S. Hoshino, Y. Yamada, and G. Shirane, Phys. Rev. B **9**, 4549 (1974).

[52] C. Quarti, E. Mosconi, and F. De Angelis, Phys. Chem. Chem. Phys. **17**, 9394 (2015).

[53] M. T. Dove, Am. Mineral. **82**, 213 (1997).

[54] J. Buckeridge, D. O. Scanlon, A. Walsh, C. R. A. Catlow, and A. A. Sokol, Phys. Rev. B **87**, 214304 (2013).

[55] W. M. Sears, M. L. Klein, and J. A. Morrison, Phys. Rev. B **19**, 2305 (1979).

[56] E. L. da Silva, J. M. Skelton, S. C. Parker, and A. Walsh, Phys. Rev. B **91**, 144107 (2015).

[57] A. Pisoni, J. Jaćimović, O. S. Barišić, M. Spina, R. Gaál, L. Forró, and E. Horváth, J. Phys. Chem. Lett. **5**, 2488 (2014).

[58] Y. He and G. Galli, Chem. Mater. **26**, 5394 (2014).

[59] I. P. Swainson, C. Stock, S. F. Parker, L. Van Eijck, M. Russina, and J. W. Taylor, Phys. Rev. B **92**, 100303(R) (2015).

THE JOURNAL OF
PHYSICAL CHEMISTRY C

Article

pubs.acs.org/JPCC

Halogen Effects on Ordering and Bonding of $CH_3NH_3^+$ in $CH_3NH_3PbX_3$ (X = Cl, Br, I) Hybrid Perovskites: A Vibrational Spectroscopic Study

Ralf G. Niemann,[†,⊥] Athanassios G. Kontos,[*,‡,⊥] Dimitrios Palles,[§] Efstratios I. Kamitsos,[§] Andreas Kaltzoglou,[‡] Federico Brivio,[†] Polycarpos Falaras,[‡] and Petra J. Cameron[†]

[†]Department of Chemistry, University of Bath, Bath BA2 7AY, United Kingdom

[‡]Institute of Nanoscience and Nanotechnology, NCSR Demokritos, 15310 Athens, Greece

[§]Theoretical and Physical Chemistry Institute, National Hellenic Research Foundation, 11635 Athens, Greece

S Supporting Information

ABSTRACT: This study reports Raman and infrared spectra of hybrid organic−inorganic $MAPbX_3$ perovskites (MA = CH_3NH_3, X = Cl, Br, I) and their mixed-halide derivatives. Raman spectra were recorded at three laser wavelengths (514, 785, and 1064 nm) under on- and off-resonance conditions, as well as at room temperature and 100 K. The use of different excitation wavelengths allowed the unambiguous acquisition of "true" Raman spectra from the perovskites, without degradation or photoinduced structural changes. Low-frequency PbX vibrational modes were thoroughly identified by comparison of Raman and far-IR results. Red Raman frequency shifts for almost all MA vibrations from 200 to 3200 cm^{-1}, and particularly intense for the torsional mode, were observed toward heavy halide derivatives, indicative of strengthening the interaction between halides and the organic cation inside the inorganic cage. Different MA−X bonding schemes are evidenced by torsional mode pairs emerging in the orthorhombic phase. $MAPbBr_3$ was further characterized by variable temperature Raman measurements (100−295 K). Broadening of the MA rocking mode slightly above the tetragonal I to II phase transition is connected with disorder of the MA cation. Our results advance the understanding of perovksite materials properties (ferroelectric domain formation, anomalous hysteresis) and their use as efficient light absorbers in solar cells.

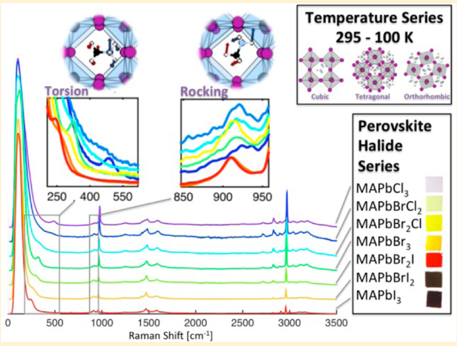

1. INTRODUCTION

Recently, there has been an increase in research on perovskite materials[1−6] leading to a steep rise in cell performances to a certified value of 21%[7] within a few years. Similar developments took decades for other photovoltaic technologies to achieve. Even though perovskites are a large family of compounds which all share the common stoichiometry ABX_3, most of the recent attention has been given to the hybrid organic−inorganic methylammonium lead halide perovskites ($MAPbX_3$, MA = methylammonium, Pb = lead, X = halide) and in particular the iodide derivative $MAPbI_3$. Structure and band gap in ABX_3 perovskites can be easily modified by changing the cation, the metal, or the halide. Partial substitution of the iodide in $MAPbI_3$ results in the isostructural $MAPbI_{3-x}Br_x$ with a blue-shifted band gap, which is favorable for multijunction devices and increases chemical stability.[8−11] However, the photo-instability of the excited state of $MAPbI_{3-x}Br_x$ results in segregation of the material into microdomains for $x > 0.6$.[12] Addition of chloride during perovskite crystallization has been shown to improve charge transport[13,14] even though its exact role remains unclear.[15,16] Besides the influences of chemical composition on optoelectronic performance and stability, temperature-dependent structural changes play a pivotal role as well. The low-temperature orthorhombic phase of $MAPbI_3$ is thermodynamically more stable compared to the tetragonal phase obtained at room temperature[10] and charge-carrier dynamics become more confined and show excitonic behavior in the orthorhombic phase.[17] This indicates that temperature-induced structural changes can tip the scales from an exothermic toward endothermic dissociation enthalpy and from free charge-carrier movement to excitonic confinement. Thus, tuning of the perovskite composition or structure can be used in order to enhance stability and performance of perovskite solar cells, both of which are investigated in this study.

X-ray diffraction has been widely used to determine the crystal structure of $MAPbX_3$ perovskite materials since their discovery in 1978.[18,19] However, it can be difficult to resolve the positions of lighter atoms like nitrogen and carbon in the presence of the heavier lead and iodine. The structural orientation of the MA cation within the inorganic framework has therefore been studied in more detail with NMR spectroscopy[20] and neutron scattering.[21,22] These studies were able to resolve the orientation of MA cations and show

Received: November 17, 2015
Revised: January 4, 2016
Published: January 7, 2016

DOI: 10.1021/acs.jpcc.5b11256

an increasing disorder when moving from the orthorhombic phase toward higher temperature phases alongside a weakening of the bonding between the NH_3 in the MA and the halides.[21,22] Alignment of the MA cations can yield a net dipole that is energetically favorable in the tetragonal phase and is further stabilized in the orthorhombic perovskite phase. It has been suggested that this MA alignment can induce polar-ferroelectric characteristics in the material in low-symmetry phases.[23] Structural dynamics within the perovskite structure have important implications on the operation mechanism of perovskite solar cells. They are thought to assist charge separation,[24] tune the band gap,[25,26] improve open-circuit voltage,[27] and affect hysteresis during current−voltage measurements.[28] These versatile implications show the importance of a detailed study of MA dynamics with Raman and IR spectroscopies.

Perovskite halides have been examined before with mid-IR absorption experiments[29−32] which give valuable information about MA dynamics, hydrogen bonding, and water infiltration inside the perovskites, but they do not cover the important low-frequency range where vibrations of the inorganic lead halide network of corner sharing PbX_6 octahedra are mainly active. Despite the suitability of the infrared absorption technique for obtaining the vibrational modes in light sensitive systems, only limited far-IR data for single halide perovskite compounds have been reported up to now.[33,34] Besides, reports of Raman measurements on $MAPbI_3$ perovskites[23,35−40] have so far been limited to resonant or near resonant conditions with typical excitation wavelengths of 514, 532, or 785 nm. However, this may be problematic because of the high absorbance and photosensitivity of the material. Moreover, the Raman spectrum of $MAPbI_3$ at low frequencies resembles the PbI_2 precursor spectrum, which makes it difficult to distinguish between pristine and (partially) decomposed samples, as we pointed out recently.[41] Ledinsky et al. reported on photo-induced decomposition during resonant Raman measurements and emphasized the use of laser intensities far below the values that would usually be employed.[36] Apart from the photo-induced decomposition,[42] $MAPbI_3$ photoexcitation induces a range of other effects that can alter its structure and therefore the experimental outcome.[12,37,43] As mentioned earlier, mixed-halide perovskites have been shown to segregate into microdomains under illumination, presumably caused by an instability of the photoexcited state.[12] A recent study by Gottesman et al. showed reversible structural modifications of $MAPbI_3$ in the Raman spectrum by excitation under resonant conditions.[39] Experimental results are often backed by computational studies,[23,37,38] which give valuable information. Nevertheless, these calculations are based on several assumptions and produce complex spectra with many superimposed bands especially in the low-frequency range. Also, small uncertainties involved in calculations can result in very large offsets in the spectrum, making peak assignment ambiguous.[37]

The current work investigates $MAPbX_3$ structural dynamics for all halide derivatives by combining far-IR absorption and Raman scattering and addresses most of the critical issues raised in the literature up to now. For the first time we perform off-resonance Raman experiments and manage to obtain unambiguous Raman spectra avoiding decomposition or structural changes in the material. Measurements have also been carried out on the low-frequency Raman and IR active modes of the inorganic PbX_6 octahedra. Variable temperature Raman measurements show characteristic spectroscopic changes of the MA torsion and rocking vibrations which have implications on the ordering and bonding of MA inside the inorganic framework. Understanding the fundamental material properties is the key to the construction of perovskite solar cells with improved efficiency and stability.

2. EXPERIMENTAL METHODS

2.1. Materials and Depostion of Films. The methylammonium halide salts (MAI, MABr, and MACl) were synthesized by dropwise neutralization of an ice-bath cooled solution of 24 mL methylamine (Sigma-Aldrich) in 100 mL of ethanol with the corresponding hydrogen-halide (10 mL of 57 wt % HI in water; 14.6 mL of 48 wt % HBr in water; 15 mL of 37 wt % HCl in water; all Sigma-Aldrich). The solvent was removed in a rotary evaporator, and the powder was recrystallized from ethanol. Upon slow cooling of the ethanol solution white crystals were formed. Washing with diethyl ether and drying at 70 °C for 6 h was performed afterwards. The single halide perovskite ($MAPbI_3$, $MAPbBr_3$, and $MAPbCl_3$) precursor solutions were prepared by mixing a 1:1 stoichiometric ratio of lead(II) halide (PbI_2, 99%; $PbBr_2$, 99.99%; $PbCl_2$, 99.99%; all Sigma-Aldrich) with the corresponding methylammonium halide at a 1 mol/L concentration in DMSO (≥99.9%; Sigma-Aldrich) for 1 h at 60 °C. For the mixed halide perovskite precursor solutions, the respective ratios of single halide solutions were mixed and stirred for 1 h. Synthesis of the precursor salts was performed in the fume hood, while the mixing of the perovskite precursor solutions, films deposition, as well as annealing were done in an argon-filled glovebox (H_2O and O_2 concentration <1 ppm).

For the preparation of planar films the precursor solution was deposited on a microscope glass slide. For mesoporous films, a dispersion of Al_2O_3 nanoparticles (20 wt % in 2-propanol; Sigma-Aldrich) was spin-coated onto glass slides (2000 rpm for 60 s) and annealed at 500 °C for 30 min. All perovskite solutions were spin-coated onto the flat or mesostructured substrates at 2000 rpm for 60 s and then annealed on a hot plate at 100 °C for 30 min. Samples for far-IR characterization were prepared by depositing mesoporous perovskite films on a 0.8 mm thick high-density polyethylene (HDPE) to improve surface wettability. In order to enhance the perovskite Raman scattering volume, measurements were performed on powder samples taken by scratching the films.

2.2. Characterization. The perovskite films were structurally characterized using a Siemens D-500 diffractometer that operates in Bragg−Brentano geometry with Cu $K_{\alpha1}$ radiation ($\lambda = 1.5406$ Å) and Cu $K_{\alpha2}$ radiation ($\lambda = 1.5444$ Å). Data were collected over the angular range $5° \leq 2\theta \leq 100°$ counting for 1 s at each step of 0.05° in detector position. Unit-cell refinements were performed with the GSAS package.[44]

UV−vis diffuse reflectance (R) spectra were acquired on a Hitachi 3010 spectrophotometer using an integrating sphere with 60 mm diameter and $BaSO_4$ as a reference. The data were transformed into Kubelka−Munk absorbance $F(R) = (1 - R)^2/2R$.

The IR transmittance measurements were run at normal incidence on a Bruker Vertex 80v vacuum spectrometer using HDPE-alumina films as a reference. Each spectrum was averaged over 200 scans with a 4 cm^{-1} resolution. The far-infrared (FIR) beam splitter and detector offered a working range of ca. 60−680 cm^{-1}. The transmittance spectra were converted to absorbance and normalized to 1.

DOI: 10.1021/acs.jpcc.5b11256
J. Phys. Chem. C 2016, 120, 2509−2519

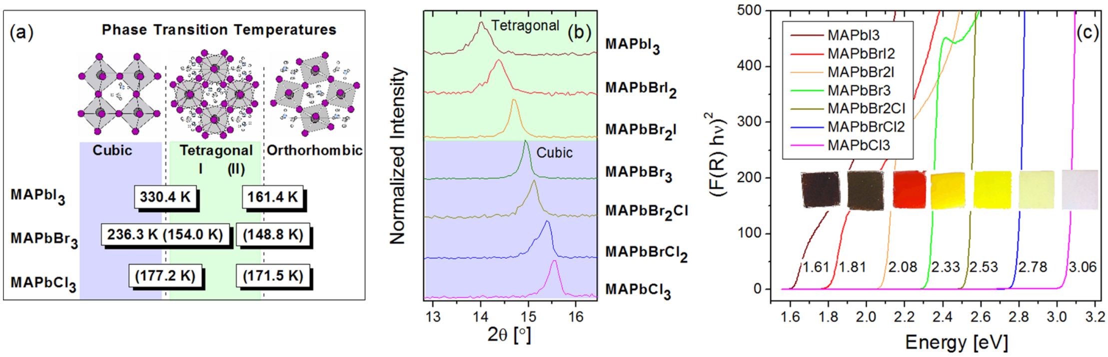

Figure 1. (a) Different phases of the $MAPbX_3$ perovskite, which transform upon changing temperature or halide composition: halides, large purple spheres, Pb, large gray spheres; MA, interstitial. Transition temperatures into tetragonal II $MAPbBr_3$ are in brackets. (b) Powder XRD patterns of the range of interest from all halide perovskites examined in this study. (c) UV−vis spectra (where $F(R)$ is the Kubelka−Munk function) of perovskite films which change in color (from dark brown to white) and show a shift in band gap energy (from 1.61 to 3.06 eV) as lighter halogens are introduced into the structure.

Raman measurements with excitation at 514 and 785 nm were performed with a Renishaw In-Via Reflex dispersive micro-Raman spectrometer with <2 cm^{-1} resolution. The laser beam was focused on a spot of 1 μm in diameter with a ×100 magnification lens. Rayleigh scattering was rejected with 50 or 110 cm^{-1} cutoff dielectric edge filters, and analysis of the scattered beam was performed on a 250 mm focal length spectrometer along with suitable diffraction gratings (1800 lines/mm for visible and 1200 lines/mm for NIR) and a high-sensitivity CCD detector. Cryostatic Raman measurements at low temperature (LT) were done under inert atmosphere in a THMS600PS Linkam cell by focusing the laser beam with a ×50 long focal distance lens. Raman spectra under off-resonance conditions for all samples were acquired with a Bruker RFS100 FT-Raman spectrometer equipped with a Nd:YAG laser emitting at 1064 nm. Each spectrum was averaged over 100 scans or 200 scans with 4 cm^{-1} resolution, while the effective working range was ca. 100−3500 cm^{-1}. All RT Raman measurements were performed in air and at different laser powers to ensure that the intensities used did not induce changes in the spectra. The measured Raman spectra present a strong elastic scattering background in the low-frequency (LF) spectral range. In order to enhance the Raman features at this LF range where very informative PbX and MA vibrations are active, and correctly determine spectral characteristics (frequency, line width, and line shape), the spectra were temperature-reduced using the expression of eq 1[45]

$$I_{\mathrm{red}}(\omega) = I(\omega)\frac{1}{n(\omega,\, \mathrm{T}) + 1}, \quad \text{with}$$
$$n(\omega,\, T) = (\exp^{\frac{hc\omega}{k_B T}} - 1)^{-1} \approx (\exp^{\frac{1.44\omega}{T}} - 1)^{-1} \tag{1}$$

where $I(\omega)$ and $I_{\mathrm{red}}(\omega)$ are the measured and reduced Raman intensity, respectively. $n(\omega, T)$ is the Bose−Einstein statistic factor, h and k_B are the Planck and Boltzmann constants, respectively, c is the speed of light, ω is the Raman shift in cm^{-1}, and T is the temperature in K. The analysis of the reduced spectra was done by fitting them with mixed Lorenzian−Gaussian functions using the Wire software from Renishaw. Line widths were corrected for instrumental broadening.

3. RESULTS AND DISCUSSION

3.1. Structural and Optical Characterization.

Schemes of the perovskites structure at the three different structural modifications (cubic, tetragonal, and orthorhombic) together with transition temperatures[46] are shown in Figure 1a. Powder-XRD patterns of the area of interest for the whole set of $MAPbX_{3-x}Y_x$ materials, shown in Figure 1b, confirm the presence of the perovskites as the main phase. In addition, certain amounts of admixtures were present, in particular PbI_2 for the I-containing samples (for the full patterns see Figure S1 in the Supporting Information). $MAPbCl_3$, $MAPbBrCl_2$, $MAPbBr_2Cl$, and $MAPbBr_3$ were indexed as cubic systems, whereas $MAPbBr_2I$, $MAPbBrI_2$, and $MAPbI_3$ were indexed as tetragonal systems, in accordance to ref 8. A regular trend in the unit-cell expansion with substitution of Cl by Br and I was observed. The determined lattice parameters of the tetragonal $MAPbI_3$ (a = b = 8.861(2) Å, c = 12.653(4) Å) are in agreement with the literature values of a = b = 8.849(2) Å, c = 12.642(2) Å,[47] within the 3σ estimated standard deviation. The lattice parameters are given in Table S1 of Supporting Information.

Substitution of heavy halogen atoms with lighter ones in $MAPbX_{3-x}Y_x$ results in films with tunable color from dark brown to white, as shown in the photographs of the prepared films inserted in Figure 1c. In order to analyze the light harvesting of the films over the solar spectrum, diffuse reflectance measurements were carried out. In Figure 1c, the absorption $F(R)$ data are plotted in terms of $(F(R)h\nu)^2$ vs $h\nu$, which is the standard analysis for materials having a direct band gap. Band gap values (E_g) were found by the intersections of the slope with the energy axis and are shown in the graphs, and further listed in Table S2 where they are compared with the Raman excitation energies. The values are slightly blue-shifted compared to literature values.[8] Blue-shifted absorption onsets were reported recently.[48,49] The shift can be caused by a ferroelectric domain wall-induced band gap reduction and has been observed for mesoporous scaffold architectures.[26,48] The influence of annealing temperature on band gap is another possible explanation for this observation.[49] In general, the reported band gaps for MA lead perovskites can vary significantly.[50] The excitonic peaks appearing in the spectra for lighter halide derivatives are presumably caused by an increase in the exciton binding energies.[51]

3.2. Low-Frequency Pb–X Vibrational Modes: Far-IR and Micro-Raman Results at Room Temperature. The PbX_6 octahedra of the perovskite halides belong to the O_h point group symmetry and have two IR active modes, ν_3 and ν_4, with T_{1u} symmetry and three Raman active modes ν_1, ν_2 and ν_5, with A_{1g}, E_g and T_{2g} symmetry, respectively.[37,52] Splitting of the doubly and triply degenerate modes is expected due to distortion of the octahedra, (a) by interaction between the methylammonium and certain halogen atoms and (b) by the occupation of the octahedral corners with different halide atoms in the complex halide derivatives. According to theoretical calculations,[37] the splitting is considerably larger for the Cl-based perovskites (Cl has the strongest electronegativity). In the present study, and for the first time in the literature, both the IR and Raman low-frequency Pb–X vibrational modes have been observed for all members of the $MAPbX_3$ family.

Far-IR spectra obtained for all $MAPbX_3$ derivatives are shown in the range of 50–300 cm^{-1} in Figure 2a, and analysis of spectral components is shown in Figure S2. HDPE-alumina substrate, taken as a reference, is also included in Figure S2 and has only minor influence in the results. Wide bands are observed in all far-IR spectra, which blue shift towards the lighter halides derivatives and present extensive broadening justified by the polycrystalline character of the materials. According to recent density functional perturbation theory calculations,[34] low-frequency IR-activity (below 120 cm^{-1} for $MAPbI_3$) is mainly due to internal PbI_3 vibrations. The spectra of the $MAPbI_{3-x}Br_x$ series are analyzed with two component bands, which thus are straightforwardly attributed to the ν_3 asymmetric stretching (103–125 cm^{-1}) and ν_4 asymmetric bending (66–76 cm^{-1}) vibrations of PbX_6 octahedra. For the Cl-containing samples, the higher frequency band is split into two component bands, which are well described by mixed Lorenzian–Gaussian character. For the pure Cl perovskite, a very broad band is observed which includes both the ν_4 band, as a low-frequency shoulder, as well as the split ν_3 band at higher frequencies. The peak positions of the deconvoluted ν_3 and ν_4 modes (two peaks for the Cl-containing perovskites) are marked in Figure 2a. In Figure 2b we plot the frequency of the two modes versus the halogen order. For the estimation of the ν_3 frequency for the mixed halides, a weight average of the two ν_3-related component bands was taken into account. First of all we should note that the ratio ν_4/ν_3 remains almost constant in the 0.60–0.64 range. The only exception is $MAPbCl_3$ for which it is slightly larger and equal to 0.67, presumably due to uncertainties in the fitting of the corresponding broad far-IR band. The fixed ν_4/ν_3 ratio verifies self-consistency of the analysis, and the ratio values match the corresponding ratios for several other compounds quite well (e.g., the ratio for the $[PbCl_6]^{2-}$ anion from ref 52 is 0.54).

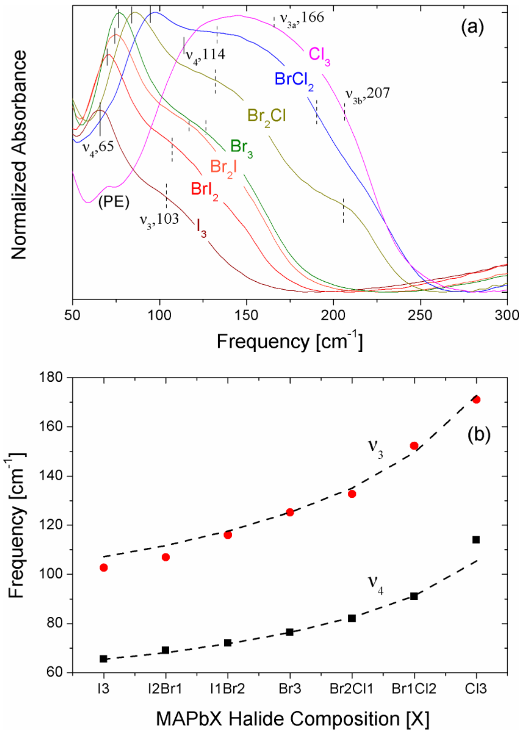

Figure 2. (a) Far-IR spectra for the various perovskite derivatives measured at RT. The band marked by PE is due to the polyethylene substrate. Peak frequencies of the ν_3 and ν_4 bands obtained by fitting the spectra (see Figure S2) are marked with dashed and solid lines, respectively. The values are noted for the end perovskite members, $MAPbI_3$ and $MAPbCl_3$. For Cl-based perovskites the ν_3 band is split into two component bands, ν_{3a} and ν_{3b}. (b) Frequency of ν_3 (average) and ν_4 modes vs halide composition. Dashed lines show predictions based on the harmonic oscillator model.

Both ν_3 and ν_4 modes shift to higher frequencies upon introduction of lighter halogen atoms in the structure. The ν_3 and ν_4 frequencies depend strongly on the reduced mass μ of the Pb–X bond and follow the model for a harmonic oscillator $\nu = \left(\frac{1}{2\pi}\right)\sqrt{k/\mu}$, with the crude assumption of the same bond strength k for all halides. The reduced mass is $\mu^{-1} = m_{Pb}^{-1} + m_X^{-1}$ where m_X for the mixed halides was calculated by the weight average of the halogen atomic masses in their chemical formula. The model calculations have been done by weighting the ν_3 and ν_4 frequencies against those observed for $MAPbBr_3$ and are shown with dashed lines in Figure 2b. These results verify that the low-frequency IR active vibrations are of the inorganic Pb–X type and lack noticeable influence from the MA cation. A similar behavior which consolidates our argument is observed by analyzing the frequency shifts of the Sn–X modes in the analogous $[SnX_6]^{2-}$ octahedral system, irrespective of the vibration mode.[52]

Complementary to the far-IR spectra, low-frequency Raman spectra were obtained above 50 cm^{-1} with 785 nm laser line excitation. The spectra are presented in Figure 3a for all the perovskite compounds apart from the pure $MAPbI_3$ which showed only a strong photoluminescence (PL) response. The vibrational modes of the PbX_6 octahedra were observed below 250 cm^{-1}. At 270 cm^{-1} for $MAPbBrI_2$ and at higher frequencies for the rest of the compounds, a broad and well-formed band was observed. This band is due to the torsion of MA units and will be discussed in detail in the next section.

The Raman spectra below 230 cm^{-1} involve vibrations of Pb–X bonds consisting of heteropolar ionic/covalent interactions in the inorganic framework and show very broad multibands which are not easily resolved into components. The general trend is that all these measured bands increase in frequency by moving toward light halides following the corresponding behavior shown in the far-IR spectra. The multiband character of the Raman features is clearer for the mixed perovskite derivatives and is justified considering the lifting in degeneracy of modes. As already discussed, three

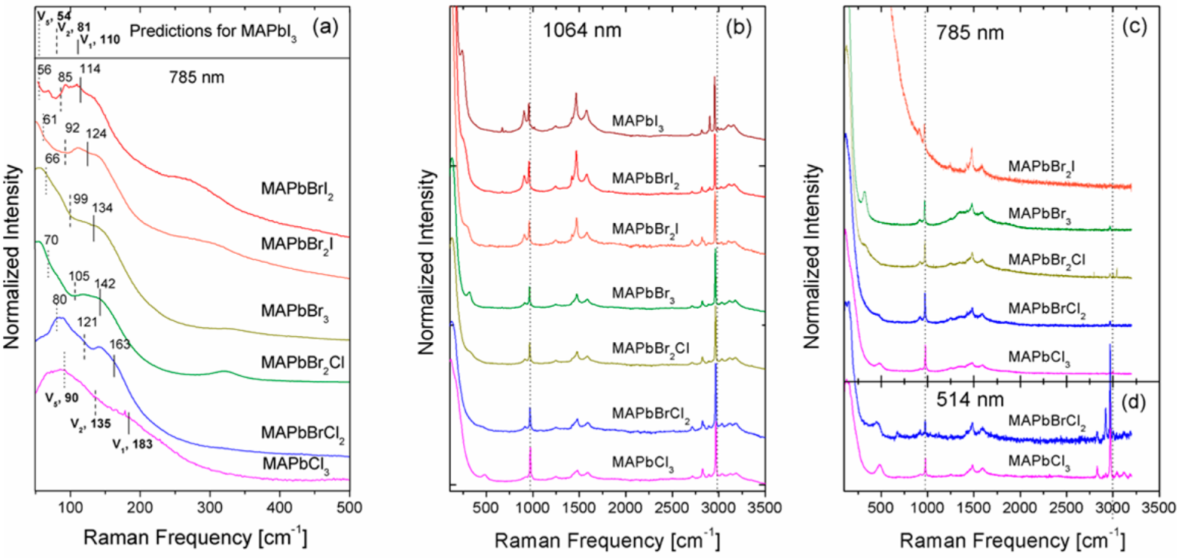

Figure 3. (a) Low-frequency Raman spectra obtained by excitation at 785 nm. Peak frequencies of ν_1 (solid line marks), ν_2 (dashed line marks), and ν_5 (dotted line marks) noted upon the graph are estimated from the experimentally recorded frequency of the ν_3 IR band and modes frequency ratios from the literature (for details see text). Raman spectra of the perovskite halide derivatives obtained by excitation at (b) 1064 nm, (c) 785 nm, and (d) 514 nm, at RT.

Table 1. Frequencies (in cm^{-1}) and Assignments of Vibrations Numbered in Series for MA Lead Derivatives MAPb[X], Where [X] Is the Halogen Composition[a],

mode/[X]	I3	I2Br	IBr2	Br3	Br2Cl	BrCl2	Cl3	assignment[b]
ν_1	(110)	114	124	134	142	163	183	ν_s (Pb–X)$^{\text{this work}}$
ν_2	(81)	85	92	99	105	121	135	ν_s (X–Pb–X)$^{\text{this work}}$
ν_3	103	107	116	125	133	152	171	ν_{as} (Pb–X)$^{\text{this work}}$
ν_4	65	69	72	76	82	91	114	δ_{as} (X–Pb–X)$^{\text{this work}}$
ν_5	(54)	56	61	66	70	80	90	δ_s (X–Pb–X)$^{\text{this work}}$
ν_6	249	264	286	323	334	460	488	τ (MA)[54,55]
ν_7	911	913	914	917	919	919	923	ρ (MA)[54,55]
ν_8	960	962	965	968	971	974	977	ν (C–N)[55]
ν_9	1247	1246	1247	1248	1249	1248	1249	ρ (MA)[30]
ν_{10}	1424	1423	1425	1428	1427	1426	1430	δ_s (CH_3)[55]
ν_{11}	1444	1444	1451	1450	1451	1453	1454	δ_{as} (CH_3)[55]
ν_{12}	1469	1472	1475	1478	1480	1483	1483	δ_s (NH_3^+)[30]
ν_{13}	1580	1581	1584	1587	1588	1593	1592	δ_{as} (NH_3^+)[30]
–	2706	2712	2716	2714	2715	2717	2719	combination modes[30]
–	2821	2823	2824	2827	2827	2829	2830	combination modes[30]
–	2906	2906	2845	2846	2845	2847	2848	combination modes[30]
ν_{14}	2959	2961	2963	2966	2968	2969	2972	ν_{as} (CH_3)[30]
ν_{15}	2993	3026	3030	3035	3036	3036	3040	ν_s (NH_3^+)[55]

[a] Modes from ν_6 and above were obtained from Raman spectra with 1064 nm excitation and are due to MA vibrations. Modes ν_3 and ν_4 were obtained from far-IR spectra. ν_1, ν_2 and ν_5 records are estimated frequencies and match well with experimental Raman spectra at low frequencies. Corresponding values for $MAPbI_3$ are shown in parentheses to indicate that Raman experimental data are not available in this work. [b] ν: stretching; δ: bending; ρ: rocking; τ: torsion; s:symmetric; as: asymmetric.

Raman bands due to the Pb–X vibrations of the octahedral structure are expected in the LF range. Among them the symmetric stretching mode ν_1 is expected to be the highest in frequency, followed with the asymmetric stretching mode ν_2 and the asymmetric deformation ν_5.[52] Since it is difficult to fit the spectra, we attempt an analysis based on the ratios of the frequencies between the various inorganic vibrational modes from the literature. Thus, according to data in ref 52., the ratios $\nu_1/\nu_3 = 1.07$, $\nu_2/\nu_1 = 0.74$, and $\nu_5/\nu_1 = 0.49$ are observed for $[PbCl_6]^{2-}$ whereas similar values are found for other systems, too, such as for $[SnX_6]^{2-}$ and $[SbX_6]^{3-}$. Thus, based on our ν_3 values from our far-IR analysis we have predicted the mean frequencies of the corresponding Raman bands. The respective calculated values of the three Raman modes are reported in Figure 3a and qualitatively describe the shifts observed as a function of the halide change. By extending the calculations for $MAPbI_3$, the mean frequencies for the three Raman active modes are predicted to be at $\nu_1 = 110$ cm^{-1}, $\nu_2 = 81$ cm^{-1}, and $\nu_5 = 54$ cm^{-1} (see also Figure 3a).

3.3. Variable Excitation Micro-Raman Spectra of All Perovskite Derivatives. Extensive Raman investigation with emphasis on MA vibrations was done by performing measurements in a broad frequency range (100−3500 cm^{-1}) using three different excitation lines at 514, 785, and 1064 nm. This allowed data acquisition both at resonance (res) as well as off-resonance conditions (off-res). An overview of materials and excitation wavelengths is shown in the Supporting Information (Table S2). In general, the majority of resonance Raman measurements obtained from the MAPbX_3 perovskites carries limited information on the vibrational properties of the materials. The main reason is that the strong absorption of the perovskites, when excited within the band gap, can induce decomposition or phase transformations in the materials. This is an issue especially for MAPbI_3 with a phase transition from tetragonal to pseudo-cubic near room temperature, at 330 K. Despite keeping the laser power density very low, by working under resonance or near resonance conditions the Raman signals are frequently masked by the presence of a strong PL background signal. Furthermore, temporary PL signals which change with illumination time were observed here in Br−I mixed halide perovskites and are attributed to phase segregation, as previously reported by Hoke et al.[12] (see Figure S3).

Figures 3b−d show an overview of the Raman spectra for all the perovskite films obtained under different excitation wavelengths, 1064 nm (Figure 3b), 785 nm (Figure 3c), and 514 nm (Figure 3d). In the case where the Raman features are masked by strong PL signals, the corresponding spectra are not presented. Thus, for MAPbI_3, we include only the spectrum obtained at 1064 nm excitation in Figure 3b, and no spectra in Figure 3c and Figure 3d, because, under near band gap or resonance excitation, the Raman signal is either covered by a strong PL background or is affected by the quick degradation of the sample showing spectroscopic changes during the measurement. MAPbCl_3 on the other hand shows no apparent change in its Raman spectrum, for all the excitation sources used. Hence, excitation at 1064 nm (Figure 3b) ensures off-resonance conditions in all cases allowing a clear and unambiguous overview of the full MA spectrum for all halide perovskite derivatives, and no spectral changes were observed that could be related to humidity or light exposure of the material. Furthermore, the quality of the spectra is excellent mainly due to the fast acquisition in the FT technique and the materials tolerating high laser power densities at 1064 nm excitation, which compensate well for the inherently weaker scattering efficiency vs the increase of the excitation wavelength (inverse fourth power law applies).

The Raman spectra reported in Figures 3b−d show a large number of MA bands which present significant changes in their characteristics (shifts, widths, intensities) with halogen composition. An overview of the frequencies of the measured Raman bands and their mode assignments can be found in Table 1. Almost all MA vibrational modes present a blue shift from MAPbI_3 toward MAPbCl_3 (see Figure S4) in accordance with the IR data in ref 30, which indicates strong NH_3−X interaction. In particular, the mode that is most sensitive to the halide content is the high-frequency ν_{15}−ν_s (NH_3^+) mode which positively shifts abruptly from MAPbI_3 to MAPbI_2Br by 33 cm^{-1} and then up to MAPbCl_3 by another 14 cm^{-1}. Significant positive shifts also occur in all other modes related to NH_3 vibrations. This is in line with recent NMR results,[53] which have shown that only the amine end of the MA group interacts strongly with the inorganic network. Nevertheless, the exact N−H bond lengths in MAPbX_3 cannot be accurately determined even with neutron diffraction methods due to the disorder in the MA group;[53] thus, the full understanding of the MA vibrational frequency shifts (e.g., the large ν_{15} shift for MAPbI_3 compared to the other perovskites) and the exact nature of the MA−halogen interaction is not possible.

Characteristic internal vibrational modes of MA appear at high frequencies, just below 1000 cm^{-1} (C−N stretching), at 1400−1600 cm^{-1} (CH_3 and NH_3 bending) and at around 3000 cm^{-1} (CH_3 and NH_3 stretching) and are well studied for methylammonium halides.[30,55] The most interesting vibrational modes are the rocking vibration, ν_7, and low-frequency torsion, ν_6, of MA around the C−N axis. The MA rocking mode, ν_7, appears in between 911 and 923 cm^{-1} and sharpens, increases in intensity, and red shifts when moving toward heavier halides Cl → Br → I (Figure 3b−d, Figure S4); the same trend was found for other modes (e.g., the ν_{12}, $\delta_s(\text{NH}_3^+)$ mode). This behavior can be attributed to orientational ordering of MA for which ν_7, having the E symmetry,[56] is a good indicator. The effect can be analyzed by the calculation of the correlation times (τ_c) from the peak Full Width at Half Maximum (FWHM),[29] which are shown in Figure 4a, according to eq 2

$$\tau_c = \frac{1}{2\pi c \text{FWHM}} \tag{2}$$

where c is the velocity of light.

The results show correlation times below 0.15 ps for the ν_7 rocking vibration for all perovskite derivatives. τ_c gradually

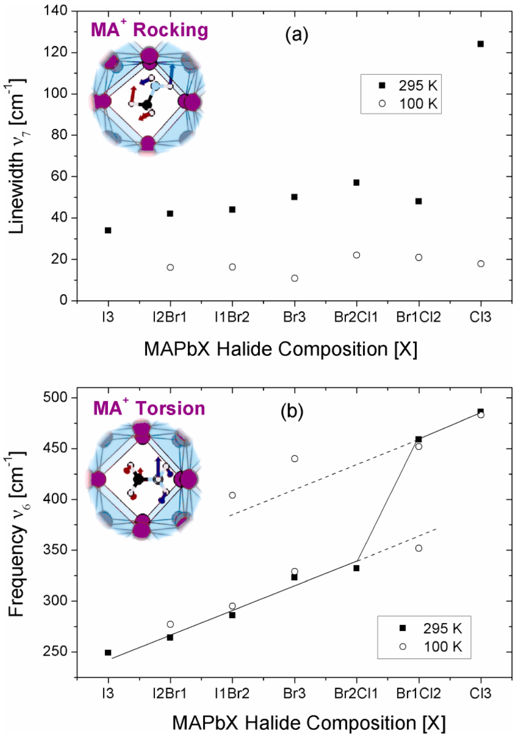

Figure 4. (a) FWHM of the ν_7 rocking mode averaged over measurements obtained at RT with different laser lines (solid squares—standard deviation <5 cm^{-1}) as well as at LT (100 K) obtained at 785 nm excitation (open circles). (b) Raman frequency of the torsional mode averaged over measurements obtained at RT with different laser lines (solid squares standard deviation <3 cm^{-1}) and corresponding results at LT (100 K) obtained at 785 nm (open circles). Solid line guides the eye for halogen dependence of the RT data and is extrapolated either sides with dashed lines.

decreases from 0.15 to 0.1 ps from $MAPbI_3$ up to $MAPbBrCl_2$ and drops to 0.05 ps for $MAPbCl_3$. Measurements of MA rocking vibration dynamics can be compared with early IR absorption data[29] obtained from large perovskite crystals, where the trend of correlation time decrease from heavy to light halides is also followed, as well as with recent results[34] on very high-quality thin films prepared with the dual source evaporation method. In both of these literature studies, the τ_c values for $MAPbI_3$ were substantially larger. Thus, the shorter correlation time in our samples is attributed to their polycrystalline character.

The ν_6 mode mainly consists of an NH_3 motion and has an A_2 symmetry which makes it forbidden in IR but permitted in Raman.[55] This mode is easily accessed in all Raman experiments and is analyzed in a straightforward way as it is not overlapping with other modes. For $MAPbCl_3$[54] the mode is observed at 488 cm^{-1} and presents an extremely large red frequency shift upon halide substitution, shifting down to 249 cm^{-1} for $MAPbI_3$ (see Figure 4b and Table 1). This large spread of resonance frequencies for MA is unusual for a torsional mode and indicates intense MA deformation and a strong interaction of MA with the inorganic cage. Fitting of ν_6 for different halide derivatives gives a continuous shift from $MAPbI_3$ to $MAPbBr_2Cl$, but jumps to higher wavenumbers for perovskites with large amounts of Cl, as shown in Figure 4b. According to recent theoretical studies,[23] different mechanisms like molecular deformation and dipolar orientational ordering of the MA as well as strength of the NH_3−X interaction are strongly affected by the nature of the halide in the perovskite and result in large shifts in the frequency of the MA torsion. Among them, changes in NH_3−X interaction upon halide substitution is the most prominent reason for the large frequency shift of the ν_6 mode, considering that it affects the frequencies of all other MA modes, too, in the same manner, even though to a much lesser extent. Preliminary calculations performed with the same methodology reported by Brivio at al.[38] confirm the observed increase of the torsional mode frequency for perovskites with Br and Cl with respect to iodine. This is due to a halogen specific NH_3−X interaction, and to a confinement effect. In fact, lighter halide results in a smaller cavity inside the inorganic cage that uplifts the frequencies of the molecular modes and reduces the distance between hydrogen and halide, amplifying the resulting shift. In Figure S5 we attempt a correlation of the torsional mode peak frequency at room temperature (RT) against the measured band gap for the various perovskite halides. Halide substitution results in vast changes of the materials optical properties, which can significantly affect their vibrational frequencies as also proposed before[30] by correlating the red shifts of MA vibrations in the Cl → Br → I order to the increase in the polarizability of the dielectric medium (Lorentz−Lorenz shift).

Interestingly, the signal intensity of ν_6 is much stronger for single halide perovskites (see Figure 3b−d), and its line width is not very broad, ranging from 40 to 60 cm^{-1}. In the mixed halide perovskites a big drop in the ν_6 intensity takes place which goes along with extensive line width broadening, reaching values up to 150 cm^{-1}. A general peak broadening can be caused in several ways. A decrease in long-range order and crystallinity typically yields broader peaks. Unresolved mode splitting also causes an increase of peak width and is connected to possible asymmetries of the mode. Such mode splitting can be enhanced by microstructural inhomogeneities due to an uneven distribution of a halide in the perovskite. This effect has been reported before for $MAPbI_{3-x}Br_x$, which forms microdomains upon crystallization that transform into a single phase within a few weeks[57] but also segregate again upon illumination.[12]

The informative torsional and rocking vibrations were further examined by comparative low-temperature Raman measurements in order to elucidate their behavior by lowering the symmetry of the perovskite structure.

3.4. Low-Temperature Raman Measurements. Another series of Raman experiments was performed for all perovskites at 100 K which is well below the phase transition of all materials into the orthorhombic phase.[46] Characteristic reduced spectra at low temperature are shown in Figure 5a obtained with excitation at 785 nm. The inset shows off-resonance spectra of $MAPbBrCl_2$ and $MAPbCl_3$ using 514 nm excitation. Peak frequencies of the strongest MA vibrations are given in Table S3. Mode splitting of the low-frequency modes was observed due to the lowering of the crystal symmetry. All materials transform from tetragonal to orthorhombic in the temperature range of 148.8−171.5 K.[58] Splitting was more evident for lighter halide derivatives, in accordance to early results for $MAPbCl_3$.[54] In the case of heavier derivatives, mode splitting was only partially observed due to the shifting of the majority of the modes below the experimentally accessed frequency range. Furthermore, apart from narrowing and blue shifting of the MA high-frequency bands above 950 cm^{-1}, no clear MA mode splitting was evidenced upon decrease of the temperature. A similar effect has been reported before for mid-IR data below the phase transition temperature[29] as well as for Raman in other perovskite systems[59] implying that the crystal deformation does not drastically affect the high-frequency vibrations of the MA units.

It is remarkable that at LT the rocking vibrations ν_7 and ν_9 at 920 and 1250 cm^{-1} present considerable line width narrowing. Thus, the ν_7 rocking mode width decreases to about 20 cm^{-1} for all perovskite derivatives (see Figure 4a) and the ν_7 correlation time increases from below 0.15 ps at RT to above 0.25 ps at 100 K, which implies MA dipolar ordering,[29] in accordance with quasi-elastic neutron-scattering results.[22]

Further insight into the behavior of the ν_6 torsion mode can be extracted from the low-temperature (LT) data. While the measurements at RT showed a jump to higher wavenumbers for the $MAPbBrCl_2$ and $MAPbCl_3$ perovskites, at LT pairs of peaks appeared (see spectra in Figure 5a and analysis in Figure 4b) that line up with modes on either side of the gap, suggesting that those peaks in fact represent two distinctive vibrational bands. The appearance of two torsional bands at low temperature is in line with early studies for $MAPCl_3$.[54] Doubling of the torsional modes for the low-symmetry orthorhombic phase and line width broadening might be due to different NH_3−X bonding schemes of the organic molecule within the hybrid.[60] On the other hand, the frequencies of the torsional modes at low temperature show small, mostly blue shifts relative to those at RT.

Another important aspect of the torsional mode is its significant broadening in the orthorhombic phase. The unit cell of this phase contains four different MA units and according to our preliminary calculations, the frequencies of respective modes are split in four due to slightly different local environments. This split is on the order of few cm^{-1} and therefore too small to be resolved but contributes to significant line width broadening. Moreover, as observed in molecules[61,62] or complex structures,[63] van der Waals forces that are enhanced at low temperature affect the stiffness of the bonds and

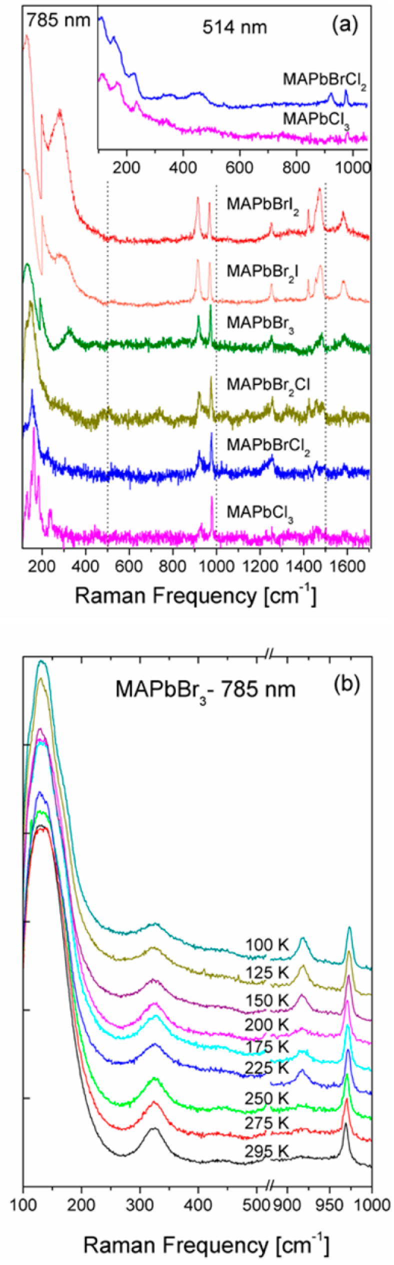

Figure 5. (a) Raman measurements of $MAPbX_{3-x}Y_x$ perovskites at 100 K obtained with 785 nm excitation. Intensity of the top three spectra below 200 cm^{-1} is scaled down by 3 for better vision of the spectra. Inset shows spectra obtained with 514 nm excitation. (b) Raman spectra of $MAPbBr_3$ (785 nm) vs temperature variation from 100 K (LT) to 295 K (RT).

influence the anharmonic terms of the vibration that lead to a larger broadening of the peak. This effect strongly depends and the geometry of the system and could justify the different behavior below the transition temperature. In previous work[64] an anomalous temperature behavior of a low-frequency Raman peak in NH_4Br around phase transition has been reported. This anomaly results in asymmetric peak shape and anomalous broadening of the signal. These effects are addressed and explained with a long-range order of the NH_4 cations. We can imagine that a similar mechanism, regarding the MA ordering, could influence the line widths at LT of the torsional mode in the hybrid MA perovskite halides, too.

In addition to fixed LT measurements at 100 K, variable temperature Raman measurements from 295 to 100 K have been carried out for $MAPbBr_3$. During this temperature ramp the material was transformed progressively from cubic to the tetragonal I phase (236.3 K), the tetragonal II phase at 154.0 K, and the orthorhombic phase at 148.8 K.[46] Recorded Raman spectra are shown in Figure 5b. $MAPbBr_3$ was chosen as the intermediate representative of our halide series and because of its high purity (see XRD in Figure S1), the fact that the full temperature dependence has not been reported before in the literature ($MAPbCl_3$ has been studied in ref 54 and $MAPbI_3$ Raman signal is covered by a strong PL background at 785 nm excitation), and its significance as light absorber for the preparation of very stable perovskite solar cells.[8−11,65]

All high-frequency MA modes above 950 cm^{-1} present a "normal" behavior with line narrowing and blue shift upon temperature decrease. Important observations are made by following the temperature dependence of the spectra below 950 cm^{-1} where peculiar behavior of the MA torsional and rocking modes at 320 and 925 cm^{-1} are observed upon moving from the cubic (295 K) to the orthorhombic phase (100 K).

Figure 6 plots the temperature dependence of the line widths for the "abnormal" torsional ν_6 and rocking ν_7 modes in comparison to the CN stretching ν_8 mode which shows a "normal" behavior. The slope of line width against temperature shows a change for ν_7, at about 175 K, slightly above the tetragonal I−II phase transition at 154 K. This transition temperature is close to the temperature of a discontinuous decrease of the real part of the dielectric permittivity[58] as well as of significant changes in the H^1−NMR spectra and relaxation time.[66] According to this early H^1−NMR result, the tetragonal I to tetragonal II phase transition affects the alignment of MA by "freezing" of the C−N axis.

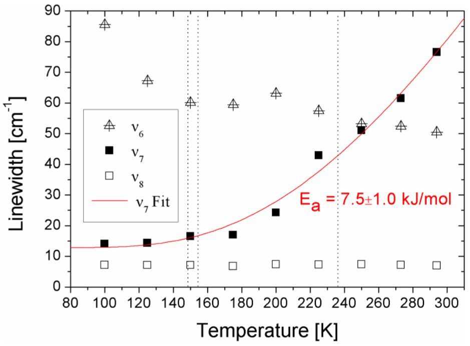

Figure 6. Temperature dependence of line widths for the torsional ν_6, rocking ν_7, and C−N stretching ν_8 vibrations of $MAPbBr_3$. Solid line represent fitting of ν_7 line widths by eq 3 with $b = 0$. Dotted lines mark the temperatures of phase transitions.

The temperature dependence of the line width of the ν_7 rocking mode in Figure 6 was used to calculate the activation energy (E_a) of the order−disorder process, according to eq 3[67−69]

$$\mathrm{FWHM}(T) = a + bT + c\exp(-E_a/RT) \tag{3}$$

where a, b, c are fitting parameters and R is the gas constant. The linear term describes the anharmonicity factor and the exponential term the increase of the line width due to the thermal reorientational motions. We fitted the FWHM(T) data of ν_7 in Figure 6 with eq 3, neglecting the linear term which has a small contribution, and ended up with an estimation of the activation energy of $E_a = 7.5 \pm 1.0$ kJ/mol which resembles the energy barrier in the disorder of the MA units. This value is very similar to that found for the rocking vibration of NH_3 in $[Mn(NH_3)_6](ClO_4)_2$.[69] As shown in Figure 6, the reorientational motions are not significantly disturbed near the phase transition temperature which is indicative that the order–disorder of the organic molecule does not contribute significantly to the phase transition mechanism.[69] Among different vibrational modes, the main torsional mode at about 320 cm^{-1} is the only one that shows line broadening instead of narrowing upon decreasing the temperature (see Figure 6). This broadening occurs progressively but shows a steep rise below the transition to the orthorhombic phase. This interesting behavior, which was also observed for other perovskite halides as discussed before, can be justified by the emergence of new unresolved torsional bands and long-range MA order in the low-symmetry phase.

4. CONCLUSIONS

In summary, our study gives a complete overview of the vibrational properties of single and mixed $MAPbX_3$ (X = Cl, Br, I) perovskites. Measurements in off-resonance conditions, at room- and low-temperatures, and a comparison of the Raman with far-IR spectra allow an unambiguous attribution of inorganic and organic modes and their shifts against halide constitution and temperature. Using three different excitation wavelengths for the Raman measurements, a significant influence of beam-induced degradation on the spectra of this material class can be ruled out for the first time in the literature. The low-frequency range is dominated by the modes of the inorganic anion, and the frequency shifts versus halide content is governed by the Pb–X reduced mass. Insight into structural dynamics of the MA cation has been given where specific vibrations such as the NH_3 rocking mode indicate ordering of MA at low temperatures. Among different modes, the MA torsion is particularly interesting since it spans a broad frequency range from 249 to 488 cm^{-1} by altering the halogen content. This behavior is attributed to changes in the interaction between the NH_3 head of MA and the halide. Furthermore, the MA torsional band shows broadening and splitting at 100 K in the orthorhombic phase, which indicates possible different MA–X bonding schemes. We hope that these findings encourage a broader usage of vibrational spectroscopy for inorganic–organic hybrid perovskites and aid a better understanding of their properties, which rank them among the most efficient solar cell active materials.

■ ASSOCIATED CONTENT

Ⓢ Supporting Information

The Supporting Information is available free of charge on the ACS Publications website at DOI: 10.1021/acs.jpcc.5b11256.

> Lattice parameters from XRD data for $MAPbX_3$ perovskites (Table S1); band gaps and laser excitation energies for the Raman and PL investigation of perovskite materials (Table S2); overview of main MA Raman frequency peaks above 900 cm^{-1}, measured at 100 K (Table S3); full powder XRD patterns of all halide perovkites (Figure S1); fitting analysis of the far-IR absorption spectra (Figure S2); spectra showing shifting of PL during measuring $MAPbI_2Br$ under resonance (514 nm) excitation, indicating phase segregation (Figure S3); Raman frequency shifts of strongest MA modes above 900 cm^{-1} for various halogen contents in $MAPbX_3$ (Figure S4); frequency of the ν_6 torsional mode at RT against the band gaps for all measured $MAPbX_3$ derivatives (Figure S5) (PDF)

■ AUTHOR INFORMATION

Corresponding Author

*Tel.: +30 210 6503668. Fax: +30 210 6511766. E-mail: a.kontos@inn.demokritos.gr.

Author Contributions

⊥These authors contributed equally.

The manuscript was written through contributions of all authors. All authors have given approval to the final version of the manuscript.

Notes

The authors declare no competing financial interest.

■ ACKNOWLEDGMENTS

We acknowledge Dr. George Kordas for providing the 50 cm^{-1} NIR filter for the low-frequency Raman measurements and Dr. Eirini Siranidi for her assistance in Raman spectra acquisition. For enlightening and amicable conversations we thank Dr. Jarvist Frost and Harry Georgiou. The research is funded from the European Union Seventh Framework Programme [FP7/2007-2013] ('DESTINY' project) under grant agreement 316494.

■ REFERENCES

(1) Kojima, A.; Teshima, K.; Shirai, Y.; Miyasaka, T. Organometal Halide Perovskites as Visible-Light Sensitizers for Photovoltaic Cells. *J. Am. Chem. Soc.* **2009**, *131*, 6050–6051.

(2) Im, J.-H.; Lee, C.-R.; Lee, J.-W.; Park, S.-W.; Park, N.-G. 6.5% Efficient Perovskite Quantum-Dot-Sensitized Solar Cell. *Nanoscale* **2011**, *3*, 4088–4093.

(3) Kim, H.-S.; Lee, C.-R.; Im, J.-H.; Lee, K.-B.; Moehl, T.; Marchioro, A.; Moon, S.-J.; Humphry-Baker, R.; Yum, J.-H.; Moser, J. E.; Grätzel, M.; Park, N.-G.; et al. Lead Iodide Perovskite Sensitized All-Solid-State Submicron Thin Film Mesoscopic Solar Cell with Efficiency Exceeding 9%. *Sci. Rep.* **2012**, *2*, 591.

(4) Lee, M. M.; Teuscher, J.; Miyasaka, T.; Murakami, T. N.; Snaith, H. J. Efficient Hybrid Solar Cells Based on Meso-Superstructured Organometal Halide Perovskites. *Science* **2012**, *338*, 643–647.

(5) Zhang, W.; Saliba, M.; Moore, D. T.; Pathak, S. K.; Hörantner, M. T.; Stergiopoulos, T.; Stranks, S. D.; Eperon, G. E.; Alexander-Webber, J. A.; Abate, A.; Sadhanala, A.; Yao, S.; Chen, Y.; Friend, R. H.; Estroff, L. A.; Wiesner, U.; Snaith, H. J.; et al. Ultrasmooth Organic–Inorganic Perovskite Thin-Film Formation and Crystallization for Efficient Planar Heterojunction Solar Cells. *Nat. Commun.* **2015**, *6*, 6142.

(6) Park, B.; Philippe, B.; Jain, S. M.; Zhang, X.; Edvinsson, T.; Rensmo, H.; Zietz, B.; Boschloo, G. Chemical Engineering of Methylammonium Lead Iodide/Bromide Perovskites: Tuning of Optoelectronic Properties and Photovoltaic Performance. *J. Mater. Chem. A* **2015**, *3*, 21760–21771.

(7) http://www.solarserver.com/solar-magazine/solar-news/current/2015/kw50/epfl-achieves-21-world-record-efficiency-for-perovskite-solar-pv-cells.html (accessed December, 21, 2015).

(8) Noh, J. H.; Im, S. H.; Heo, J. H.; Mandal, T. N.; Seok, S. Il. Chemical Management for Colorful, Efficient, and Stable Inorganic–Organic Hybrid Nanostructured Solar Cells. *Nano Lett.* **2013**, *13*, 1764–1769.

(9) Conings, B.; Drijkoningen, J.; Gauquelin, N.; Babayigit, A.; D'Haen, J.; D'Olieslaeger, L.; Ethirajan, A.; Verbeeck, J.; Manca, J.;

Mosconi, E.; Angelis, F. D.; Boyen, H.-G.; et al. Intrinsic Thermal Instability of Methylammonium Lead Trihalide Perovskite. *Adv. Energy Mater.* **2015**, *5*, 1500477.

(10) Zhang, Y.-Y.; Chen, S.; Xu, P.; Xiang, H.; Gong, X.-G.; Walsh, A.; Wei, S.-H. Intrinsic Instability of the Hybrid Halide Perovskite Semiconductor $CH_3NH_3PbI_3$. *arXiv Prepr.* **2015**, arXiv:1506.01301.

(11) Buin, A.; Comin, R.; Xu, J.; Ip, A. H.; Sargent, E. H. Halide-Dependent Electronic Structure of Organolead Perovskite Materials. *Chem. Mater.* **2015**, *27*, 4405−4412.

(12) Hoke, E. T.; Slotcavage, D. J.; Dohner, E. R.; Bowring, A. R.; Karunadasa, H. I.; McGehee, M. D. Reversible Photo-Induced Trap Formation in Mixed-Halide Hybrid Perovskites for Photovoltaics. *Chem. Sci.* **2015**, *6*, 613−617.

(13) Stranks, S. D.; Eperon, G. E.; Grancini, G.; Menelaou, C.; Alcocer, M. J. P.; Leijtens, T.; Herz, L. M.; Petrozza, A.; Snaith, H. J. Electron-Hole Diffusion Lengths Exceeding 1 Micrometer in an Organometal Trihalide Perovskite Absorber. *Science* **2013**, *342*, 341−344.

(14) Colella, S.; Mosconi, E.; Fedeli, P.; Listorti, A.; Gazza, F.; Orlandi, F.; Ferro, P.; Besagni, T.; Rizzo, A.; Calestani, G.; et al. $MAPbI_{3-x}Cl_x$ Mixed Halide Perovskite for Hybrid Solar Cells: The Role of Chloride as Dopant on the Transport and Structural Properties. *Chem. Mater.* **2013**, *25*, 4613−4618.

(15) Colella, S.; Mosconi, E.; Pellegrino, G.; Alberti, A.; Guerra, V. L. P.; Masi, S.; Listorti, A.; Rizzo, A.; Condorelli, G. G.; De Angelis, F.; et al. Elusive Presence of Chloride in Mixed Halide Perovskite Solar Cells. *J. Phys. Chem. Lett.* **2014**, *5*, 3532−3538.

(16) Starr, D. E.; Sadoughi, G.; Handick, E.; Wilks, R. G.; Alsmeier, J. H.; Köhler, L.; Gorgoi, M.; Snaith, H. J.; Bär, M. Direct Observation of an Inhomogeneous Chlorine Distribution in $CH_3NH_3PbI_{3-x}Cl_x$ Layers: Surface Depletion and Interface Enrichment. *Energy Environ. Sci.* **2015**, *8*, 1609−1615.

(17) Milot, R. L.; Eperon, G. E.; Snaith, H. J.; Johnston, M. B.; Herz, L. M. Temperature-Dependent Charge-Carrier Dynamics in $CH_3NH_3PbI_3$ Perovskite Thin Films. *Adv. Funct. Mater.* **2015**, *25*, 6218−6227.

(18) Weber, D. $CH_3NH_3PbX_3$, a Pb(II)-System with Cubic Perovskite Structure. *Z. Naturforsch., B: J. Chem. Sci.* **1978**, *33b*, 1443−1445.

(19) Poglitsch, A.; Weber, D. Dynamic Disorder in Methylammoniumtrihalogenoplumbates(II) Observed by Millimeter-Wave Spectroscopy. *J. Chem. Phys.* **1987**, *87*, 6373−6378.

(20) Wasylishen, R. E.; Knop, O.; Macdonald, J. B. Cation Rotation in Methylammonium Lead Halides. *Solid State Commun.* **1985**, *56*, 581−582.

(21) Weller, M. T.; Weber, O. J.; Henry, P. F.; Di Pumpo, A. M.; Hansen, T. C. Complete Structure and Cation Orientation in the Perovskite Photovoltaic Methylammonium Lead Iodide between 100 and 352 K. *Chem. Commun.* **2015**, *51*, 4180−4183.

(22) Leguy, A. M. A.; Frost, J. M.; McMahon, A. P.; Sakai, V. G.; Kochelmann, W.; Law, C.; Li, X.; Foglia, F.; Walsh, A.; O'Regan, B. C.; et al. The Dynamics of Methylammonium Ions in Hybrid Organic−Inorganic Perovskite Solar Cells. *Nat. Commun.* **2015**, *6*, 7124.

(23) Quarti, C.; Grancini, G.; Mosconi, E.; Bruno, P.; Ball, J. M.; Lee, M. M.; Snaith, H. J.; Petrozza, A.; Angelis, F. D. The Raman Spectrum of the CH3NH3PbI3 Hybrid Perovskite: Interplay of Theory and Experiment. *J. Phys. Chem. Lett.* **2014**, *5*, 279−284.

(24) Frost, J.; Butler, K.; Brivio, F.; Hendon, C. H.; van Schilfgaarde, M.; Walsh, A. Atomistic Origins of High-Performance in Hybrid Halide Perovskite Solar Cells. *Nano Lett.* **2014**, *14*, 2584−2590.

(25) Liu, S.; Zheng, F.; Koocher, N. Z.; Takenaka, H.; Wang, F.; Rappe, A. M. Ferroelectric Domain Wall Induced Band Gap Reduction and Charge Separation in Organometal Halide Perovskites. *J. Phys. Chem. Lett.* **2015**, *6*, 693−699.

(26) Leguy, A.; Azarhoosh, P.; Alonso, M. I.; Campoy-Quiles, M.; Weber, O. J.; Yao, J.; Bryant, D.; Weller, M. T.; Nelson, J.; Walsh, A.; van Schilfgaarde, M.; Barnes, P. R. F.; et al. Experimental and Theoretical Optical Properties of Methylammonium Lead Halide Perovskites. *Nanoscale* **2015**, DOI: 10.1039/C5NR05435D.

(27) Quarti, C.; Mosconi, E.; De Angelis, F. Interplay of Orientational Order and Electronic Structure in Methylammonium Lead Iodide: Implications for Solar Cells Operation. *Chem. Mater.* **2014**, *26*, 6557−6569.

(28) Wu, B.; Fu, K.; Yantara, N.; Xing, G.; Sun, S.; Sum, T. C.; Mathews, N. Charge Accumulation and Hysteresis in Perovskite-Based Solar Cells: An Electro-Optical Analysis. *Adv. Energy Mater.* **2015**, *5*, 1500829.

(29) Onoda-Yamamuro, N.; Matsuo, T.; Suga, H. Calorimetric and IR Spectroscopic Studies of Phase Transitions in Methylammonium Trihalogenoplumbates. *J. Phys. Chem. Solids* **1990**, *51*, 1383−1395.

(30) Glaser, T.; Muller, C.; Sendner, M.; Krekeler, C.; Semonin, O. E.; Hull, T. D.; Yaffe, O.; Owen, J. S.; Kowalsky, W.; Pucci, A.; et al. Infrared Spectroscopic Study of Vibrational Modes in Methylammonium Lead Halide Perovskites. *J. Phys. Chem. Lett.* **2015**, *6*, 2913−2918.

(31) Bakulin, A. A.; Selig, O.; Bakker, H. J.; Rezus, Y. L. A.; Müller, C.; Glaser, T.; Lovrincic, R.; Sun, Z.; Chen, Z.; Walsh, A.; et al. Real-Time Observation of Organic Cation Reorientation in Methylammonium Lead Iodide Perovskites. *J. Phys. Chem. Lett.* **2015**, *6*, 3663−3669.

(32) Müller, C.; Glaser, T.; Plogmeyer, M.; Sendner, M.; Döring, S.; Bakulin, A. A.; Brzuska, C.; Scheer, R.; Pshenichnikov, M. S.; Kowalsky, W.; et al. Water Infiltration in Methylammonium Lead Iodide Perovskite: Fast and Inconspicuous. *Chem. Mater.* **2015**, *27*, 7835−7841.

(33) Mosconi, E.; Quarti, C.; Ivanovska, T.; Ruani, G.; De Angelis, F. Structural and Electronic Properties of Organo-Halide Lead Perovskites: A Combined IR-Spectroscopy and Ab Initio Molecular Dynamics Investigation. *Phys. Chem. Chem. Phys.* **2014**, *16*, 16137−16144.

(34) Perez-Osorio, M. A.; Milot, R. L.; Filip, M. R.; Patel, J. B.; Herz, L. M.; Johnston, M. B.; Giustino, F. Vibrational Properties of the Organic−Inorganic Halide Perovskite $CH_3NH_3PbI_3$ from Theory and Experiment: Factor Group Analysis, First-Principles Calculations, and Low-Temperature Infrared Spectra. *J. Phys. Chem. C* **2015**, *119*, 25703−25718.

(35) Grancini, G.; Marras, S.; Prato, M.; Giannini, C.; Quarti, C.; De Angelis, F.; De Bastiani, M.; Eperon, G. E.; Snaith, H. J.; Manna, L.; Petrozza, A.; et al. The Impact of the Crystallization Processes on the Structural and Optical Properties of Hybrid Perovskite Films for Photovoltaics. *J. Phys. Chem. Lett.* **2014**, *5*, 3836−3842.

(36) Ledinsky, M.; Löper, P.; Niesen, B.; Holovsky, J.; Moon, S. J.; Yum, J. H.; De Wolf, S.; Fejfar, A.; Ballif, C. Raman Spectroscopy of Organic−Inorganic Halide Perovskites. *J. Phys. Chem. Lett.* **2015**, *6*, 401−406.

(37) Park, B.; Jain, S. M.; Zhang, X.; Hagfeldt, A.; Boschloo, G.; Edvinsson, T. Resonance Raman and Excitation Energy Dependent Charge Transfer Mechanism in Halide-Substituted Hybrid Perovskite Solar Cells. *ACS Nano* **2015**, *9*, 2088−2101.

(38) Brivio, F.; Frost, J. M.; Skelton, J. M.; Jackson, A. J.; Weber, O. J.; Weller, M. T.; Walsh, A.; Goni, A. R.; Leguy, A. M. A.; Barnes, P. R. F.; et al. Lattice Dynamics and Vibrational Spectra of the Orthorhombic, Tetragonal, and Cubic Phases of Methylammonium Lead Iodide. *Phys. Rev. B: Condens. Matter Mater. Phys.* **2015**, *92*, 144308.

(39) Gottesman, R.; Gouda, L.; Kalanoor, B. S.; Haltzi, E.; Tirosh, S.; Rosh-Hodesh, E.; Tischler, Y.; Zaban, A.; Quarti, C.; Mosconi, E.; et al. Photoinduced Reversible Structural Transformations in Free-Standing $CH_3NH_3PbI_3$ Perovskite Films. *J. Phys. Chem. Lett.* **2015**, *6*, 2332−2338.

(40) Leijtens, T.; Hoke, E. T.; Grancini, G.; Slotcavage, D. J.; Eperon, G. E.; Ball, J. M.; De Bastiani, M.; Bowring, A. R.; Martino, N.; Wojciechowski, K.; McGehee, M. D.; Snaith, H. J.; Petrozza, A.; et al. Mapping Electric Field-Induced Switchable Poling and Structural Degradation in Hybrid Lead Halide Perovskite Thin Films. *Adv. Energy Mater.* **2015**, *5*, 1500962.

(41) Antoniadou, M.; Siranidi, E.; Vaenas, N.; Kontos, A. G.; Stathatos, E.; Falaras, P. Photovoltaic Performance and Stability of

$CH_3NH_3PbI_{3-x}Cl_x$ Perovskites. *J. Surfaces Interfaces Mater.* **2014**, *2*, 323−327.

(42) Misra, R. K.; Aharon, S.; Li, B.; Mogilyansky, D.; Visoly-Fisher, I.; Etgar, L.; Katz, E. A. Temperature- and Component-Dependent Degradation of Perovskite Photovoltaic Materials under Concentrated Sunlight. *J. Phys. Chem. Lett.* **2015**, *6*, 326−330.

(43) Kedem, N.; Brenner, T. M.; Kulbak, M.; Schaefer, N.; Levcenko, S.; Levine, I.; Abou-Ras, D.; Hodes, G.; Cahen, D. Light-Induced Increase of Electron Diffusion Length in a P-N Junction Type $CH_3NH_3PbBr_3$ Perovskite Solar Cell. *J. Phys. Chem. Lett.* **2015**, *6*, 2469−2476.

(44) Larson, A. C.; von Dreele, R. B. General Structure Analysis System; Rep. LAUR 85-748; Los Alamos Lab., 1994.

(45) Kamitsos, E. I.; Kapoutsis, J. A.; Jain, H.; Hsieh, C. H. Vibrational Study of the Role of Trivalent Ions in Sodium Trisilicate Glass. *J. Non-Cryst. Solids* **1994**, *171*, 31−45.

(46) Onoda-Yamamuro, N.; Yamamuro, O.; Matsuo, T.; Suga, H. *P*−*T* Phase Relations of $CH_3NH_3PbX_3$ (X = Cl, Br, I) Crystals. *J. Phys. Chem. Solids* **1992**, *53*, 277−281.

(47) Stoumpos, C. C.; Malliakas, C. D.; Kanatzidis, M. G. Semiconducting Tin and Lead Iodide Perovskites with Organic Cations: Phase Transitions, High Mobilities, and Near-Infrared Photoluminescent Properties. *Inorg. Chem.* **2013**, *52*, 9019−9038.

(48) Choi, J. J.; Yang, X.; Norman, Z. M.; Billinge, S. J. L.; Owen, J. S. Structure of Methylammonium Lead Iodide within Mesoporous Titanium Dioxide: Active Material in High Performance Perovskite Solar Cells. *Nano Lett.* **2014**, *14*, 127−133.

(49) Wei, M.; Chung, Y.-H.; Xiao, Y.; Chen, Z. Color Tunable Halide Perovskite $CH_3NH_3PbBr_{3-x}Cl_x$ Emission via Annealing. *Org. Electron.* **2015**, *26*, 260−264.

(50) Wehrenfennig, C. Ultrafast Spectroscopy of Charge Separation, Transport, and Recombination Processes in Functional Materials for Thin-Film Photovoltaics, Ph.D. Thesis, Oxford University, 2014.

(51) Kitazawa, N.; Watanabe, Y.; Nakamura, Y. Optical Properties of $CH_3NH_3PbX_3$ (X = Halogen) and Their Mixed-Halide Crystals. *J. Mater. Sci.* **2002**, *37*, 3585−3587.

(52) Nakamoto, K. in *Infrared and Raman Spectra of Inorganic and Coordination Compounds, Part A, Theory and Applications in Inorganic Chemistry*, 6th ed.; Wiley: New York, 2009.

(53) Baikie, T.; Barrow, N. S.; Fang, Y.; Keenan, P. J.; Slater, P. R.; Piltz, R. O.; Gutmann, M.; Mhaisalkar, S. G.; White, T. J. A Combined Single Crystal Neutron/X-Ray Diffraction and Solid-State Nuclear Magnetic Resonance Study of the Hybrid Perovskites $CH_3NH_3PbX_3$ (X = I, Br and Cl). *J. Mater. Chem. A* **2015**, *3*, 9298−9307.

(54) Maalej, A.; Abid, A.; Kallel, A.; Daoud, A.; Lautie, A.; Romain, F. Phase Transitions and Crystal Dynamics in the Cubic Perovskite $CH_3NH_3PbCl_3$. *Solid State Commun.* **1997**, *103*, 279−284.

(55) Theoret, A.; Sandorfy, C. The Infrared Spectra of Solid Methylammonium Halides. II. *Spectrochim. Acta* **1967**, *23A*, 519−542.

(56) Matsuo, T.; Ueda, M.; Suga, H. Calorimetric and Spectroscopic Studies of the Critical Phase Transition in $(CH_3NH_3)_2[SnCl_6]$. *Chem. Phys. Lett.* **1981**, *82*, 577−580.

(57) Sadhanala, A.; Deschler, F.; Thomas, T. H.; Dutton, E.; Goedel, K. C.; Hanusch, F. C.; Lai, M. L.; Steiner, U.; Bein, T.; Docampo, P.; et al. Preparation of Single-Phase Films of $CH_3NH_3Pb(I_{1-x}Br_x)_3$ with Sharp Optical Band Edges. *J. Phys. Chem. Lett.* **2014**, *5*, 2501−2505.

(58) Onoda-Yamamuro, N.; Matsuo, T.; Duga, H. Dielectric Study of $CH_3NH_3PbX_3$ (X = Cl, Br, I). *J. Phys. Chem. Solids* **1992**, *53*, 935−939.

(59) Popović, Z. V.; Kontos, A. G.; Raptis, Y. S.; Isobe, M.; Ueda, Y. Raman Scattering Study of β-$Sr_{0.33}V_2O_5$ in Charge Disordered and Ordered Phase. *J. Phys.: Condens. Matter* **2006**, *18*, 7779−7787.

(60) Mitzi, D. B. Templating and Structural Engineering in Organic−Inorganic Perovskites. *J. Chem. Soc. Dalt. Trans.* **2001**, *1*, 1−12.

(61) Michels, J. P. J.; Schouten, J. A. Broadening of Vibrational Raman Spectra by Concentration Fluctuations: A Molecular Dynamics Survey. *Int. J. Thermophys.* **2001**, *22*, 339−355.

(62) Das, A.; Kumar, K. Raman Anisotropic Linewidth Dependence on the Van Der Waals Volume of the Interacting Systems. *J. Raman Spectrosc.* **1999**, *30*, 547−549.

(63) Rao, A. M.; Chen, J.; Richter, E.; Schlecht, U.; Eklund, P. C.; Haddon, R. C.; Venkateswaran, U. D.; Kwon, Y. K.; Tománek, D. Effect of van Der Waals Interactions on the Raman Modes in Single Walled Carbon Nanotubes. *Phys. Rev. Lett.* **2001**, *86*, 3895−3898.

(64) Wang, C. H.; Wright, R. B. Nature of the λ Transition and the 56 cm^{-1} Anomalous Raman Mode in Ammonium Bromide. *J. Chem. Phys.* **1972**, *57*, 4401.

(65) Jeon, N. J.; Noh, J. H.; Yang, W. S.; Kim, Y. C.; Ryu, S.; Seo, J.; Seok, S. Il. Compositional Engineering of Perovskite Materials for High-Performance Solar Cells. *Nature* **2015**, *517*, 476−480.

(66) Knop, O.; Wasylishen, R. E.; White, M. A.; Cameron, T. S.; Van Oort, M. J. M. Alkylammonium Lead Halides. Part 2. $CH_3NH_3PbX_3$ (X = Cl, Br, I) Perovskites: Cuboctahedral Halide Cages with Isotropic Cation Reorientation. *Can. J. Chem.* **1990**, *68*, 412−422.

(67) Carabatos-Nedelec, C.; Becker, P. Order−Disorder and Structural Phase Transitions in Solid-State Materials by Raman Scattering Analysis. *J. Raman Spectrosc.* **1997**, *28*, 663−671.

(68) Hagemann, H.; Gomes, S.; Renaudin, G.; Yvon, K. Raman Studies of Reorientation Motions of $[BH_4]^-$ Anions in Alkali Borohydrides. *J. Alloys Compd.* **2004**, *363*, 126−129.

(69) Hetmanczyk, J.; Hetmanczyk, L.; Migdal-Mikuli, A.; Mikuli, E. Vibrations and Reorientations of NH_3 Molecules in $[Mn(NH_3)_6]$-$(ClO_4)_2$ Studied by Infrared Spectroscopy and Theoretical (DFT) Calculations. *Spectrochim. Acta, Part A* **2015**, *136*, 1515−1522.

■ NOTE ADDED AFTER ASAP PUBLICATION

An error was found in the last paragraph of section 3.2 in the version published to the Web on January 26, 2016. This is corrected in the version published to the Web on January 27, 2016.

PCCP

COMMUNICATION

View Article Online
View Journal

Cite this: DOI: 10.1039/c6cp03474h

Received 20th May 2016,
Accepted 16th June 2016

DOI: 10.1039/c6cp03474h

www.rsc.org/pccp

Dynamic disorder, phonon lifetimes, and the assignment of modes to the vibrational spectra of methylammonium lead halide perovskites†

Aurélien M. A. Leguy,[a] Alejandro R. Goñi,*[bc] Jarvist M. Frost,*[d] Jonathan Skelton,[d] Federico Brivio,[d] Xabier Rodríguez-Martínez,[b] Oliver J. Weber,[d] Anuradha Pallipurath,[e] M. Isabel Alonso,[b] Mariano Campoy-Quiles,[b] Mark T. Weller,[d] Jenny Nelson,[af] Aron Walsh[d] and Piers R. F. Barnes*[c]

We present Raman and terahertz absorbance spectra of methylammonium lead halide single crystals (MAPbX$_3$, X = I, Br, Cl) at temperatures between 80 and 370 K. These results show good agreement with density-functional-theory phonon calculations. Comparison of experimental spectra and calculated vibrational modes enables confident assignment of most of the vibrational features between 50 and 3500 cm^{-1}. Reorientation of the methylammonium cations, unlocked in their cavities at the orthorhombic-to-tetragonal phase transition, plays a key role in shaping the vibrational spectra of the different compounds. Calculations show that these dynamic effects split Raman peaks and create more structure than predicted from the independent harmonic modes. This explains the presence of extra peaks in the experimental spectra that have been a source of confusion in earlier studies. We discuss singular features, in particular the torsional vibration of the C–N axis, which is the only molecular mode that is strongly influenced by the size of the lattice. From analysis of the spectral linewidths, we find that MAPbI$_3$ shows exceptionally short phonon lifetimes, which can be linked to low lattice thermal conductivity. We show that optical rather than acoustic phonon scattering is likely to prevail at room temperature in these materials.

Introduction

Raman spectroscopy can characterize the chemical environments in materials *in situ*, as well as revealing the nature of the lattice vibrations (phonons). Solar cells based on methylammonium lead halide (MAPbX$_3$, X = I, Br, Cl) have received considerable attention over the past few years, reaching power conversion efficiencies in excess of 20% in 2015.[2] A precise understanding of the phonon dispersion in these materials is crucial for developing quantitative models of ionic transport,[3] and recombination[4] and scattering[5] of (photo-generated) charges in devices. Reliable assignment of the optically accessible vibrational modes in MAPbX$_3$ (X = I, Br, Cl) will also enable the development of high throughput spectroscopic methods to assess the perovskite film quality during the manufacturing process.

As yet, it has been difficult to fully interpret the Raman spectra of MAPbI$_3$. The material is extremely sensitive to focused laser illumination, which can cause irreversible degradation; Ledinsky *et al.*[6] were the first to demonstrate the necessity of sub-bandgap illumination to achieve sufficient signal while avoiding chemical changes to the material.

Subsequent Raman studies of MAPbI$_3$ using bias white LED light in addition to above-bandgap excitation indicated that reversible changes in spectra occurred on prolonged exposure of the material to illumination. Specifically, at room temperature, peaks in the Raman spectrum appeared between 50 and 200 cm^{-1} after sustained illumination. These were attributed to a reversible change in the crystal structure.[7]

A first attempt at assigning the Raman spectra of MAPbI$_3$ to theoretical vibration modes at low wavenumbers was made by Quarti *et al.*;[8] however, the data acquired in this study are likely to contain contributions from degraded material induced by the optically-absorbed excitation source.[6] A tentative assignment of the Raman modes of MAPbCl$_3$ was proposed by Maaej and co-workers in ref. 9, while studies of the Raman spectrum of the vibrations of the CH$_3$NH$_3$$^+$ cation can be found in ref. 10 Together with various interpretations of the vibrational modes of related layered perovskite[11–14] and intercalation compounds,[15,16] these studies provide solid basis for unambiguous assignment of the spectra of MAPbX$_3$. Recently we have published a preliminary Raman spectrum of MAPbI$_3$ in the orthorhombic phase, compared

---

[a] Physics department, Imperial College London, SW7 2AZ, UK. E-mail: piers.barnes@imperial.ac.uk
[b] Institut de Ciència de Materials de Barcelona (ICMAB-CSIC), Campus UAB, 08193 Bellaterra, Spain. E-mail: goni@icmab.es
[c] ICREA, Passeig Lluís Companys 23, 08010 Barcelona, Spain
[d] Chemistry department, University of Bath, BA2 7AY, UK. E-mail: j.m.frost@bath.ac.uk
[e] School of chemistry, National University of Ireland Galway, Ireland
[f] SPECIFIC, College of Engineering, Swansea University, Baglan Bay Innovation and Knowledge Centre, SA12 7AX, UK

† Electronic supplementary information (ESI) available. See DOI: 10.1039/c6cp03474h

to first-principles lattice dynamics calculations on each of the three phases.[1] These calculations indicated that, at energies below 200 cm^{-1}, the spectrum can be attributed to a combination of the Pb/I cage modes and associated coupled motion of the $CH_3NH_3^+$ cations. In contrast, at wavenumbers greater than 200 cm^{-1} only molecular vibrations of the cations contribute to the spectral features. This is as would be expected by the large mismatch in mass between the organic and inorganic components.

Infrared absorption spectroscopy complements Raman: Raman inactive vibrations are often found to be infrared active, and *vice versa*. Infrared absorption spectroscopy is also not subject to the same degradation issues as Raman; however, care must be taken to ensure artefacts are not introduced during sample preparation and mounting using halide salts (*e.g.* pelleting with KBr), which may undergo ionic exchange with the sample. Fourier-transform infrared (FTIR) spectra were recently reported for $MAPbI_3$ thin films deposited by dual evaporation[17] in the 6–3500 cm^{-1} spectral range. The authors of ref. 18 noted the presence of extra peaks in their spectra that could not be explained by any of the predicted modes, which they tentatively assigned to second order harmonic effects. Similar data was reported between 800–3600 cm^{-1} for the three halide types at room temperature, noting few differences between them.[18] It is likely these features can be attributed primarily to vibrational modes of the CH_3NH_3 cation, as shown below and in ref. 17 and 18. Recent terahertz absorption spectra (overlapping the range of FTIR frequencies) have shown the existence of two vibrational bands around 1 and 2 THz (33 and 67 cm^{-1}, respectively), which were suggested to be coupled to the scattering (and thus mobility) of free carriers in the material.[5]

The three compounds of the $MAPbX_3$ family (X = I, Br, Cl) can exist in three different phases (or four in the case of $MAPbBr_3$) as summarized in Fig. 1 for temperatures up to 325 K. Here, building on our preliminary work on $MAPbI_3$,[1] we assign the features of Raman and terahertz absorption spectra measured at a wide range of temperatures to their respective vibrations on the basis of first principles calculations of the phonon spectra of each of the compounds. This allows us to confirm our previous predictions of the Raman and FTIR modes expected in the three halide types. Our measurements also reveal that peaks in the vibrational spectra are strongly broadened (with the appearance of new broad peaks) as reorientation of the methylammonium cation becomes unlocked at the transition from the orthorhombic to tetragonal phase. We propose an explanation of the peculiar dependence of the C–N torsion mode on the cavity size that is a marker of the degree of steric hindrance experienced by the cations. Our calculations also show that additional peaks are expected from dynamic disorder. We then discuss the effects of phonon–phonon coupling on materials properties such as charge carrier mobility, the rate of hot carrier relaxation, and the implications for thermal conductivity.

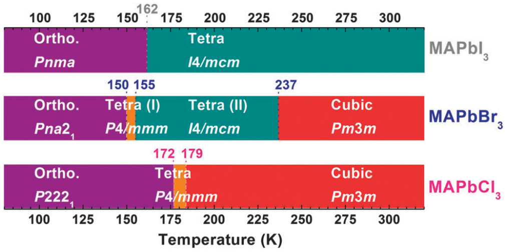

Fig. 1 Summary of the crystal systems and space groups adopted by $MAPbI_3$,[19–23] $MAPbBr_3$[20–23] and $MAPbCl_3$[9,20–23] over the temperature range measured. The orthorhombic phases of each compound are represented in purple, the tetragonal phases of the space group *I*4/*mmm* and *I*4/*mcm* are in orange and dark cyan, respectively. Red is for the *Pm*3*m* cubic phase. The colour code shown in this figure is consistently kept throughout the paper.

Conceptual advances

The hybrid perovskite family of compounds $CH_3NH_3PbX_3$ (where X = I, Br, Cl) can be used to make efficient solar cells and other semiconductor devices from low-cost ingredients deposited from solution. However, many fundamental properties of these materials have not been established, and, typically, devices made with them are not stable. We have compared the microscopic vibrations predicted in these crystals by *ab initio* calculations to peaks observed in Raman and terahertz spectra of $CH_3NH_3PbX_3$ over a wide range of temperatures. Theory was consistent with observation, enabling us to comprehensively assign the complicated vibrational modes to spectral features, many of which are common to all three materials. For $CH_3NH_3PbI_3$, these features are no longer well resolved at temperatures above ∼160 K, which can be explained because the organic moieties in the lattice cavities which are trapped in a given orientation in the low temperature phase are unlocked at temperatures above the phase transition. These insights into the types of active vibrations will help underpin our understanding both heat and electrical transport in these materials. Furthermore, the assignment of spectral peaks to particular vibrations which could be influenced by chemical changes will allow the stability of the materials exposed to different operating environments to be monitored using vibrational spectroscopy.

Methods

Sample preparation

Single crystals of $MAPbX_3$ (MA = CH_3NH_3; X = I, Br, Cl) were synthetized both from aqueous solution, based on the method described by Poglitsch and Weber,[20] and from inverse temperature crystallization in gamma-butyrolactone.[24] The detailed procedures are given in the ESI† Note S1.

Raman spectroscopy

Raman spectra were collected in backscattering geometry with a high resolution LabRam HR800 spectrometer using a grating with 600 lines per millimetre and equipped with a liquid-nitrogen cooled charge coupled device (CCD) detector. Raman measurements were carried out between 90 and 300 K using a gas flow cryostat with optical access that fits under the microscope of the Raman setup. Four optical sources are available for excitation: the 785 nm (infrared, IR) line of a diode-pumped solid-state laser, the 488 nm (blue) and 514.5 nm (green) lines from an Ar^+-ion gas laser, and the 632.5 nm (red) line from a He–Ne gas laser. The laser beam was focused onto the sample using a long working distance 20× microscope objective, yielding a spot size with a diameter of ~18 μm (area ~2.5×10^{-6} cm^2). Measurements of the cut-off energies of the different filters gives limits to the acquisition of spectra at low energies of ~20 cm^{-1} for the IR laser, 50 cm^{-1} for the red source, and 90 cm^{-1} for the blue one. The measured power densities at the sample position for IR, red and blue irradiation were 310 W cm^{-2}, 70 W cm^{-2} and 230 W cm^{-2}, respectively.

Heating by laser light directly absorbed by $MAPbI_3$ has been shown to lead to rapid degradation of the material, resulting in PbI_2 Raman signatures.[6] Since 785 nm light is only weakly absorbed, the heating effect of the laser was low enough to ensure the $MAPbI_3$ crystal structure was preserved. Samples were kept under vacuum inside the cryostat during the measurements. No degradation was observed for $MAPbBr_3$ and $MAPCl_3$ with any of the optical sources. Parasitic photoluminescence can also further limit the range of excitation energies, causing the Raman modes to disappear against a strong PL signal if they overlap. In practice, this was found only to be a significant issue for $MAPbBr_3$ at low Raman shift. The IR laser was therefore used as excitation source for $MAPbBr_3$ below 1800 cm^{-1}, while the red source gives better results above this energy. $MAPbI_3$ and $MAPbCl_3$ are studied in the non-resonant regime across the whole spectral range (20–3500 cm^{-1}).

Terahertz absorption spectroscopy

To complement the Raman measurements on $MAPbI_3$, terahertz time-domain transmission spectra were recorded on this material between 0.2 to 5 THz, using an Advantest TAS7500TS system at a resolution of 7.6 GHz and 8192 integrated scans. A description of the measurement setup can be found in ref. 25. Samples were prepared by geometrically mixing crushed single crystals of $MAPbI_3$ (40 mg) with polytetrafluoroethylene (PTFE; 600 mg) powder and making pellets using a two-ton tablet press. A cuvette containing the pellet was attached to the cold finger of a continuous-flow cryostat and cooled at a rate of approximately 25 K min^{-1} to 80 K. The system was placed under vacuum (2.8×10^{-1} mbar). The temperature was controlled using a 50 W heater and data was acquired at variable intervals up to 370 K. The temperature was stepped by 10 to 20 K away from the phase transitions, while smaller 5 K measurement steps were performed close to 160 and 330 K.

Computational methods

The vibrational frequencies for each phase of $MAPbI_3$ and for the cubic phase of $MAPbBr_3$ and $MAPbCl_3$ were calculated within the harmonic phonon approximation using second order force constants obtained from density functional theory (DFT). We used the PBEsol density functional in the vienna *ab initio* simulation package (VASP) code,[26–28] with rigorous convergence criteria to optimise the cell volume, shape and atomic positions, as described previously.[1] Spin–orbit coupling was not included as it does not influence the interatomic interactions at equilibrium; the conduction band formed by Pb 6p is unoccupied. The Phonopy package[29–31] was used to setup and post process supercell finite displacement calculations. The infrared (IR) activity was calculated using the mode eigenvectors and the Born effective-charge tensors. The Raman activity of each mode was obtained by following the eigenvector, and calculating the change in polarizability with an additional electronic structure calculation. Details are described in our earlier computational paper.[1]

Custom codes were written to provide eigenmode-resolved phonon partial densities of states; and to analyse the motion and energetic contribution of atoms at the gamma point.

Phonons are calculated around a local minimum on the potential energy surface of a material. The force constants, which define the change in force on a reference atom in response to the displacement of another, are used to construct a dynamical matrix, which is then diagonalised to give the eigenvalues (vibrational frequencies) and associated eigenvectors (normal modes of the motion). For a hybrid material, the potential energy surface has a complex structure, and there are multiple local potential energy minima. In hybrid halide perovskites, these minima are close in energy, such that thermal motion is sufficient to lead to continuous dynamic disorder. In order to sample the disorder in the phonon spectrum, we generated unit-cell structures with the methylammonium cation randomly orientated and displaced from its energy minimised location (see ESI† Note S2). These structures were then energy minimised by up to 101 optimisation steps with a conjugate gradient algorithm. The zone-centre phonon spectrum was subsequently recalculated using density functional perturbation theory. Some of these structures exhibited imaginary phonon modes, which is expected for dynamic structure snapshots away from the ground state configuration. However, most presented a full set of positive frequency modes, indicating that they were in a local potential energy minimum, at least with respect to the local structure within the unit cell.

Results and discussion

Characteristic features of the Raman spectra

The measured spectra of the three halide types, *viz.* $MAPbI_3$, $MAPbBr_3$ and $MAPbCl_3$, are shown in Fig. 2. The spectra can be understood as consisting of two parts: a low energy band of closely packed Raman peaks between the cut-off frequency of the optical filter at ~20 cm^{-1} (the cut-off frequency for the THz IR measurements corresponds to 7 cm^{-1}) and ~200 cm^{-1}, and the higher energy Raman-active modes forming bands spread between ~200 and 3300 cm^{-1}.

As detailed in the Methods section, particular care has to be taken when recording Raman spectra of $MAPbI_3$. The compound is extremely sensitive to focused laser light with above-bandgap frequency, as previously reported.[6] The use of above-bandgap lasers (488 nm, 514 nm or 633 nm) burns holes in the crystal, the result of which is a significant change in the collected spectra.

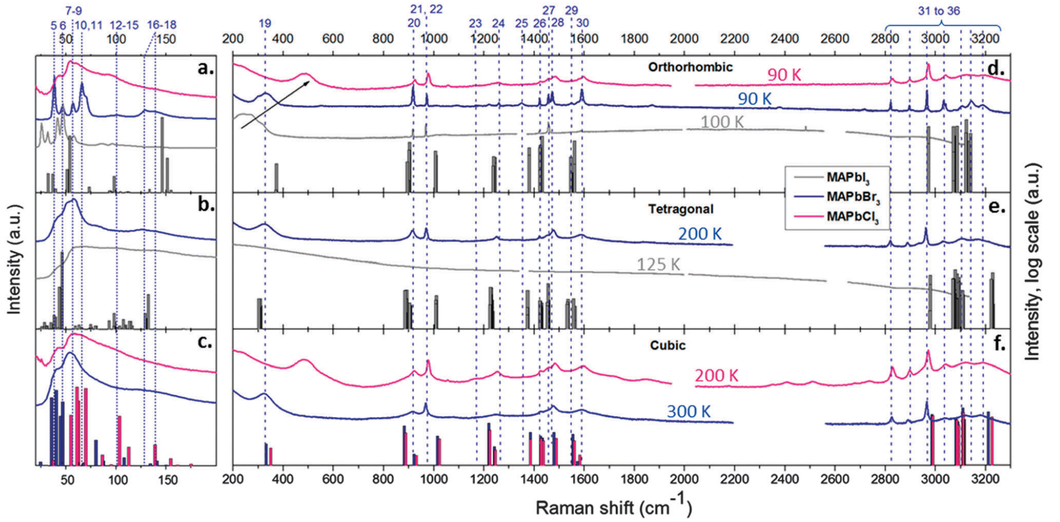

Fig. 2 Raman spectra of $MAPbI_3$ (solid grey line), $MAPbBr_3$ (solid blue line) and $MAPbCl_3$ (solid pink line) in their different phases: orthorhombic at low temperatures (top row, a and d), tetragonal at intermediate temperatures (middle row, b and e), and cubic at higher temperatures (bottom row, c and f). The temperatures are given above the spectra. The figure is split between the Raman shifts attributed to the cage modes (left hand side, a to c) and to the molecular modes (right hand side, logarithmic scale, d to f). The predicted eigenmodes of each phase are shown as bars in matching colours. The numbering of the eigenmode labels the main Raman peaks of $MAPbBr_3$ in the orthorhombic phase (defined in Table 1). Dotted lines show the positions of the labelled peaks and are intended as a guide to the eye. The arrow is used to emphasize the dramatic shift of mode number 19 for the different halides.

This problem was avoided by using only sub-bandgap irradiation (785 nm) to excite $MAPbI_3$.

Parasitic photoluminescence can dominate the signal for particular excitation wavelengths, thus further limiting the range of usable laser wavelengths, as explained in the Methods section. Moreover, different excitation wavelengths couple well with different vibrational modes. Short wavelength excitation allows the molecular modes at Raman shifts above ~200 cm^{-1} to be clearly resolved, but is less suitable for resolving the cage modes at lower energies. Conversely, it is not possible to resolve the high wavenumber molecular modes with IR laser excitation (as shown for $MAPbBr_3$ in Fig. S1 in the ESI†), yet this wavelength offers a clear picture of the inorganic sublattice (cage) modes. This is one of the reasons why it was not possible to obtain clearly resolved molecular peaks for $MAPbI_3$, since only IR irradiation could be used. The other reason for the lack of resolution of these molecular features is dynamic broadening, which is discussed in detail below. A better compromise can be found for $MAPbBr_3$ and $MAPbCl_3$, for which the cage modes could be investigated with IR light while the high-wavenumber molecular modes could be resolved with visible irradiation. An IR laser was used for $MAPbBr_3$ for the data collected between 200 and 1800 cm^{-1} to avoid parasitic photoluminescence.

Ab initio phonon calculations

First-principles lattice-dynamics calculations were performed to model the vibrational modes together with their corresponding spectroscopic intensities; see the Methods section and ref. 1. The energies and relative intensities of the dominant modes are plotted in Fig. 2. A clear separation in energy between the low frequency modes associated with the inorganic $(PbI_3^-)_n$ network and high-frequency modes of the organic $CH_3NH_3^+$ cations is evident. This separation is consistent with the two-part structure observed in the experimental spectra. The two-fold degeneracy of the E molecular modes is broken when the ions are caged in the cavity formed by the inorganic sub-lattice, forming separate bands with slightly red- or blue-shifted peaks. The torsional degree of freedom is formally of A_2 symmetry, which in the C_{3v} point group of the methylammonium molecule can be neither Raman nor IR active. As such, its presence in the experimental spectra shows a coupling of this mode into the motion of the inorganic cage.

Assignment of the brightest Raman peaks

Fig. 2 shows satisfactory agreement between the experimental spectra and the calculations, although shifts in energy are apparent in some cases. Qualitatively, the same number of bands can be observed at comparable energies. For all three compounds in the cubic phase, a low-energy band (between 0 and 200 cm^{-1}) is comprised of 18 eigenmodes. The first three are acoustic modes involving the translation of the entire lattice. The 15 remaining modes are cage-dominated optical modes, including 6 which are the overall translation and rotation of the organic cation coupled into the lattice motions (these would not be present in the molecular modes of an isolated MA in a vacuum) (see Tables 1 and 2). At higher energy (above ~200 cm^{-1}), 6 non-degenerate

Table 1 Assignment of the Raman peaks of $MAPbI_3$, $MAPbBr_3$ and $MAPbCl_3$ associated with the cage vibrations in the orthorhombic phase at frequency f_{MAPbX_3} (excitation wavelength 785 nm, samples at 100 K, "b" = broad, "sh" = shoulder, "LO" = longitudinal optic, and "TO" = transverse optic). The peak positions are compared to the brightest calculated Raman features of $MAPbI_3$ in the orthorhombic phase (see Table S1 in the ESI). A graphical illustration of the assignment can be found in the ESI, Fig. S2–S4. The peaks are tentatively related to those observed in the cubic phase (see also Fig. S5, ESI). A schematic representation of the vibrational mode eigenvectors can be found in Fig. 5

$f_{\text{theo, MAPbI}_3}$ orthorhombic (cm^{-1})	f_{MAPbI_3} exp. 100 K (cm^{-1})	f_{MAPbBr_3} exp. 100 K (cm^{-1})	f_{MAPbCl_3} exp. 100 K (cm^{-1})	Description	Corresponding mode number in the cubic phase (tentative)
0		—	—	Acoustic mode	1
0		—	—	Acoustic mode	2
0		—	—	Acoustic mode	3
15	—	—	42	Octahedra twist (TO)	4
27	26	39	54	Octahedra twist (TO)	5
32	32	47	61	Octahedra twist (TO)	6
37	42	58	75	Octahedra distortion (LO/TO)	7, 8
39	47	58	75	Octahedra distortion (LO/TO)	9
51	58	66	94	Nodding donkey around N	10
54	58	66	94	Nodding donkey around N	11
73	sh	71	94	Lurching MA (LO-like)	12
93	86	99	124b	Lurching MA (LO-like)	13
94	86	99	124b	Lurching MA (LO-like)	13
98	97b	129	168b	Lurching MA (LO-like)	14
104	97b	129	168b	Lurching MA (LO-like)	14
112	97b	138	168b	Lurching MA (LO-like)	14
133	sh	—	184	Lurching MA (LO-like)	15
146	143b	148	238b	Nodding donkey around C	16
151	143b	148	238b	Attempt roll around C–N	17
155	143b	148	238b	Nodding donkey around C	18

A modes and 6 doubly-degenerate E modes are predicted for the methylammonium cation $CH_3NH_3^+$ (see Table 3), which correspond to 18 predicted modes in the cubic phase once the symmetry-breaking effect of the surrounding lattice is taken into account (we number these modes 19 to 36). The tetragonal and orthorhombic configurations correspond to lower-symmetry arrangements, causing further splitting of most of the bands. This increases the number of predicted modes from 36 to 144. However, the energies of the split bands remain close together, such that once effects of disorder are accounted for (discussed below), they cannot be separately resolved experimentally. For this reason most of our discussion will refer to assignments of the modes of the cubic phases. Fig. 3 shows the phonon dispersion, and the density of phonon states for each of the three compounds at room temperature (see caption for details). Negative frequencies (or 'soft modes') are seen for the acoustic modes at the *R* and *M* points in the Brillouin zone, suggesting the possibility of anti-ferroelectric tilting behaviour in all three compounds. It is interesting to note the spread of energies for the groups of modes (sets of modes with the same colour hue but varying tones) that would be degenerate in

Table 2 Assignment of the THz peaks of $MAPbI_3$ associated with the cage vibrations in the orthorhombic (80 K), tetragonal (220 K) and cubic phases at frequency f_{MAPbX_3} (350 K) (see also Fig. S6–S8 in the ESI). In the table, "exp" = experimental, "w" = weak, "b" = broad, "sh" = shoulder, "s" = strong, "LO" = longitudinal optic, and "TO" = transverse optic. Features which are partially distinguishable, but not reliably so, are marked with a question mark. A schematic representation of the vibrational mode eigenvectors can be found in Fig. 5

Mode #	$f_{\text{theo, MAPbI}_3}$ cubic (cm^{-1})	f_{MAPbI_3} exp. 80 K (cm^{-1})	f_{MAPbI_3} exp. 220 K (cm^{-1})	f_{MAPbI_3} exp. 350 K (cm^{-1})	Description
1	0	—	—	—	Acoustic mode
2	0	—	—	—	Acoustic mode
3	0	—	—	—	Acoustic mode
4	19	21sh	22sh	19sh, w	Octahedra twist (TO)
5	27	27sh	26sh, w	28sh, w	Octahedra twist (TO)
6	29	33	29sh, w	31sh, w	Octahedra twist (TO)
7	33	35s	32sh	35s	Octahedra distortion (LO/TO)
8	33	35s	32sh	35s	Octahedra distortion (LO/TO)
9	35	38s	35s	35s	Octahedra distortion (LO/TO)
10	58	57sh, b	51sh, b	56sh, b	Nodding donkey around N
11	66	63?	64sh	56sh, b	Nodding donkey around N
12	69	69s	72s	73s	Lurching MA (LO-like)
13	75	71s	76s	78s	Lurching MA (LO-like)
14	81	80sh, w	81sh, b	81s	Lurching MA (LO-like)
		82sh, w	83sh, b		
15	92	93sh	93sh, w	95?	Lurching MA (LO-like)
16	117	106b	106?sh, b	102?	Nodding donkey around C
17	128	—	—	—	Attempt roll around C–N
18	133	147sh	141?	138?	Nodding donkey around C

Table 3 Assignment of the molecular Raman peaks of $MAPbI_3$, $MAPbBr_3$ and $MAPbCl_3$ in the orthorhombic phase at frequency f_{MAPbX_3} (see Fig. S12–S14 in the ESI). The excitation wavelength was 785 nm for $MAPbI_3$, 785 nm for $MAPbBr_3$ between 200–1700 cm^{-1} and 633 nm above, and 488 nm for $MAPbCl_3$. The samples were measured at 100 K. In the table, "w" = weak, "b" = broad, "sh" = shoulder, "s" = strong, "LO" = longitudinal optic, "TO" = transverse optic and features marked "?" are those which are difficult to reliably detect. Since little temperature evolution is expected for the molecular Raman peaks, the comparison given with the theoretical modes of $MAPbI_3$ is to the cubic phase (see Table S1 in the ESI for an extensive list of the 72 undegenerate molecular modes of $MAPbI_3$ in the orthorhombic phase). See Fig. 5 for a graphical representation of the eigenvectors of the 18 molecular modes

Mode #	Sym. group	$f_{\text{theo, MAPbI}_3}$ cubic (cm^{-1})	f_{MAPbI_3} (cm^{-1})	f_{MAPbBr_3} (cm^{-1})	f_{MAPbCl_3} (cm^{-1})	Description
19	A_2	315	199/223/243/272/312	297/326	483	C–N torsion
20	E	876	889	915	925	?
21	E	909	916	970	978	C–N asymmetric bend
22	A_1	1007	968	994	1002	C–N stretch
				1017	1058	
				1059		
23	E	1215	1008?	1115	1164	C–N symmetric bend
				1143		
				1178		
24	E	1234	1043?	1236	1255	C–N symmetric bend
25	A_1	1378	—	1352	—	CH_3 asymmetric breathing
26	E	1418	1420	1421		CH_3 symmetric breathing
27	E	1425	1420	1458	1425	CH_3 symmetric breathing
28	A_1	1464	1457	1471	1457	NH_3 asymmetric breathing
29	E	1542	sh	1573	1485	NH_3 symmetric breathing
30	E	1558	1586	1590	1596	NH_3 symmetric breathing
31	A_1	2971	2949b	2821	2830	C–H asymmetric stretch
32	E	3067	2949b	2896	2899	C–H symmetric stretch
33	E	3074	2949b	2965	2972	C–H symmetric stretch
34	A_1	3087	2949b	3033	3040	N–H asymmetric stretch
35	E	3096	2949b	3106	3117	N–H symmetric stretch
36	E	3199	2949b	3144	3190	N–H symmetric stretch
				3179		

an inorganic cubic perovskite. This spread is indicative of the disorder introduced in the material by the anisotropic nature of the MA ion. The gradient in the modes (dE/dq) becomes steeper with smaller halide ions, indicating an increase in the crystal 'stiffness' (bulk modulus).

Assignment of the cage modes

Our assignment of the experimental cage modes identified at 100 K for the three compounds (*i.e.* in their orthorhombic phases) is given in Table 1 (see also Fig. S2–S4 in the ESI†). The assignment is performed in the orthorhombic phase since the data is better resolved at low temperature, below the order–disorder phase transition, as will be discussed in detail below. Among the 144 modes expected in the orthorhombic phase, most have a small associated activity. Thus, only the brightest calculated peaks were considered for the assignment of the experimental features in the low symmetry phase. The assignment is interpreted by matching the predicted bright Raman modes in the orthorhombic phase to the nearest predicted band in the cubic phase (see Fig. S5, ESI†).

Fig. 4 shows the breakdown of the calculated eigenvectors in the cubic phase in terms of the relative energetic contribution of each element. For each of the three compounds, modes 1 to 18 show substantial involvement of the inorganic sublattice (cage) *via* both lead and halide-atom displacements. The effects of statistical order on these modes will be discussed following section. Modes 1, 2 and 3 are the acoustic modes, characterized by rigid translation of the lattice along the three Cartesian directions. These necessarily have zero frequency at the gamma point and, by their translational symmetry, no associated spectroscopic activity. Modes 4, 5 and 6 correspond to twists of the octahedra (see Fig. 5 for a graphical representation) that occur through the flexing of Pb–I–Pb bonds. These vibrational modes can be categorized as transverse-optic modes (TO), the eigenvector is symmetric with respect to inversion, and would be of Γ_{25} symmetry in a fully inorganic cubic perovskite. The next three modes (7, 8 and 9) are the distortions of the octahedra by a change in angle of the I–Pb–I bonds, of Γ_{15} symmetry. They exhibit a mixed nature of transverse- and longitudinal-optic phonons (TO and LO, respectively), the nature of which was inferred from the calculation of infrared activity. Modes 12 to 15 are truly coupled vibrations between cages and MA cations. They correspond to collisions of MA ions with the inorganic sub-lattice, correlated with changes in the Pb–I bond lengths. These modes are infrared active and LO-like.

The remaining cage modes stand out in Fig. 4, since they show more balanced relative contributions from the inorganic and organic moieties. In particular, the 'nodding donkey' modes (10, 11, 16 and 18 in Fig. 5) show moderate coupling between the cage and cation, with a smaller contribution from Pb atoms than for modes 12–15. They correspond to rotational vibration of the cation around the nitrogen (10 and 11) or the carbon atom (16 and 18). These motions are coupled with reorganizations of the surrounding octahedra, and would not be present in full inorganic perovskite. Similarly, mode 17 is the roll of the MA ions around their C–N axes, which is coupled to iodide displacements. It should be borne in mind that Fig. 4

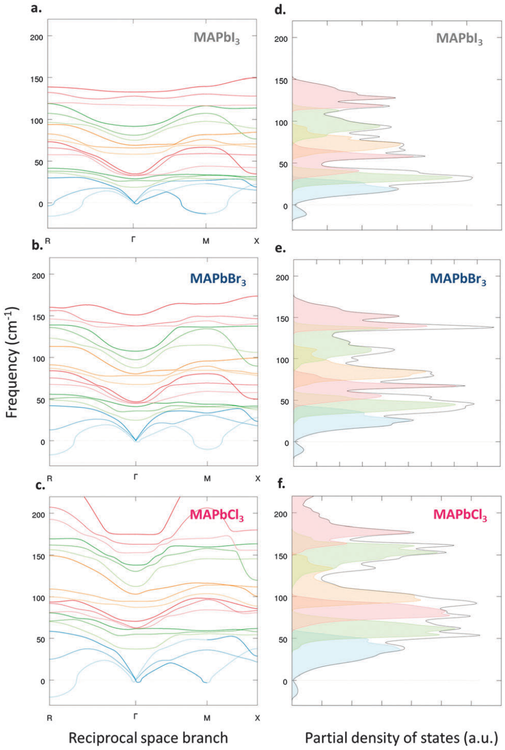

Fig. 3 Phonon dispersions of the 18 low frequency (inorganic cage) modes within the harmonic approximation using a pseudo cubic lattice for (a) MAPbI$_3$, (b) MAPbBr$_3$ and (c) MAPbCl$_3$ at room temperature. In all cases negative frequency, 'soft' modes are located around the Brillouin-zone boundary points $M[2\pi/a(1/2,1/2,0)]$ and $R[2\pi/a(1/2,1/2,1/2)]$. The band structures are plotted considering band crossings. The colour refers to the nature of the phonon eigenmode, which can change according to its proximity to other modes to avoid crossings (indicated by changes in shades). The three orthogonal acoustic modes (modes 1–3 in Table 2) are plotted in blue shades. The remaining modes (4–18 in Table 2) are optical, plotted in groups of three with a similar shade for each orthogonal mode (these would be degenerate if the MA ions were replaced by a spherical atom). Modes 4–6 are in green, 7–9 in red, 10–12 in orange, 13–15 in green and 16–18 in red. Density of phonon states decomposed by sets of three orthogonal phonon eigenmodes for MAPbI$_3$ (d), MAPbBr$_3$ (e) and MAPbCl$_3$ (f) integrated over the full Brillouin zone, but not considering band crossings.

is an energy breakdown of the modes, and so significant energetic contributions from the Pb and I atoms correspond to very small-amplitude displacements from equilibrium because of the high atomic mass relative to those of N, C and H.

For the iodide perovskite, complementary terahertz absorption-spectra measurements were carried out to investigate vibrational modes below the cut-off frequency of the Raman setup. Fig. 6 shows the spectra measured for MAPbI$_3$ at temperatures ranging from 80 to 370 K. To help identify the absorption features against the broad background, the second derivative of the terahertz absorbance is given in the ESI,† Fig. S6–S8, and compared with expected infrared-active vibrational modes obtained from the calculations. The experimental data are in good agreement with the predicted infrared activity and clearly shows two bands, centred around 1 and 2 THz, which is in agreement with previous observations.[5] The 1 THz band can be attributed to the octahedral twists and distortions, while the 2 THz band occurs where the nodding donkey around N and the ''lurching'' modes are observed. A complete assignment of the distinguishable features is given in Table 2.

Our observation of low energy modes is consistent with these materials behaving as soft semiconductors. This would imply that the material is potentially susceptible to ferro-elastic phase changes[32] in the presence of electrostatic forces induced by accumulations of separated charges in the material, which might explains recent observations of crystal photo-/electro-striction.[33] The strong variation in the width of the Raman modes observed with temperature (discussed further in the section on temperature evolution) implies that similar changes in Raman activity could be expected with variation in crystal structure induced by other mechanisms (such as those induced by changes in the electric field in the material resulting from an accumulation of photogenerated or ionic charges). A process such as this might be consistent with the Raman properties varying with illumination time observed by Gottesman *et al.*[34]

We note that formation and accumulation of iodide vacancies in the crystal lattice MAPbI$_3$ at room temperature might add structure to its Raman spectrum. Changes in the mass of the average oscillators involving iodine is expected to result in a blue-shift of the associated peaks. Modes become localised by the increased defect density, which disrupts the selection rules that prevent the observation of modes in perfect lattices, and therefore might reveal previously suppressed modes.

Assignment of the isolated mode

While the majority of the molecular modes show no significant change in wavenumber between the different halides, the feature labelled eigenmode 19 in the spectra in Fig. 2 is atypical in that it exhibits a blue shift as the average lattice constant shrinks from ~6.3 to ~5.9 to ~5.7 Å for X = I, Br and Cl, respectively[19,20,35] (corresponding to lattice volumes of 254, 206 and 183 Å^3).[20,35] We attribute this 'isolated' band around 240 cm^{-1} for MAPbI$_3$, 310 cm^{-1} for MAPbBr$_3$ and 480 cm^{-1} for MAPbCl$_3$ (see Table 2) to the torsional vibration of $CH_3NH_3^+$, which is consistent with previous reports.[9,17,36,37] It is striking that this mode shows such high sensitivity to the halide atom in the compound, orders of magnitude more acute than in the other molecular modes. It is important to note that this mode is spectroscopically inactive outside the lattice – to be observed at all, the motion has to be coupled with the cage. Fig. 4 reveals that hydrogen atoms store more than 95% of the energy in this C–N torsion mode. The sensitivity of the MA torsional movements to steric hindrance by the surrounding lattice cages suggests that the spectral peak corresponding to this vibration could be used to probe variation of lattice structure in spatially-resolved studies, or in mixed-halide systems.

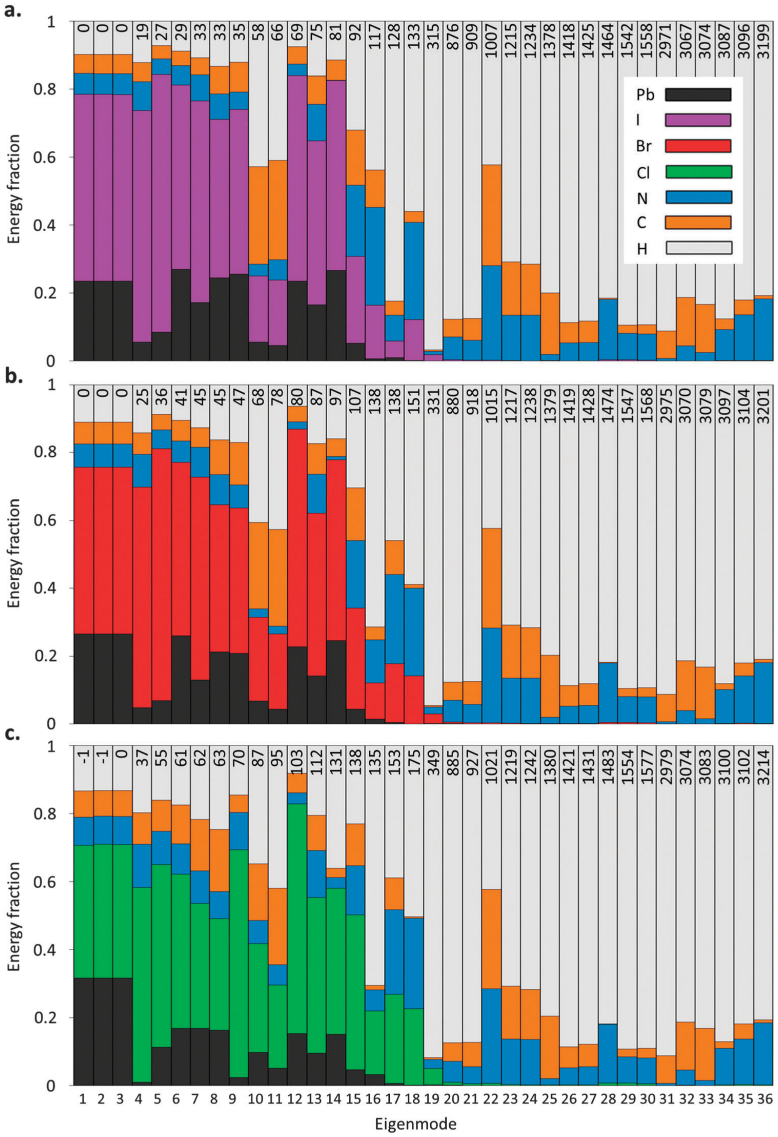

Fig. 4 Decomposition of the 36 gamma-point eigenmodes of cubic $MAPbI_3$ (a), $MAPbBr_3$ (b) and $MAPbCl_3$ (c) into relative energetic contribution of each atom. The contribution of Pb is shown in dark grey, C in orange, N in blue, H in white, I in purple, Br in red and Cl in green. The number of each mode is given at the bottom of the plot, and the corresponding frequency (in cm^{-1}) at the top.

Similar behaviour is observed with mode 17, which corresponds to the rotation of the whole MA cation around the C–N axis. This mode is strongly populated in MD simulations[1] and corresponds to a large-amplitude movement upon which steric hindrance has a strong influence.

The interpretation of the 'isolated band' could be complicated by the possibility that the MA ions may have a disordered arrangement within the lattice. We have recently used quasi-elastic neutron scattering measurements to show that the MA ions jump between different orientations within the lattice; simulations of this process suggested increasingly disordered orientations with increasing temperature.[38]

The measured 'isolated' feature assigned to C–N torsional vibrations is broader and shows more structure than expected,

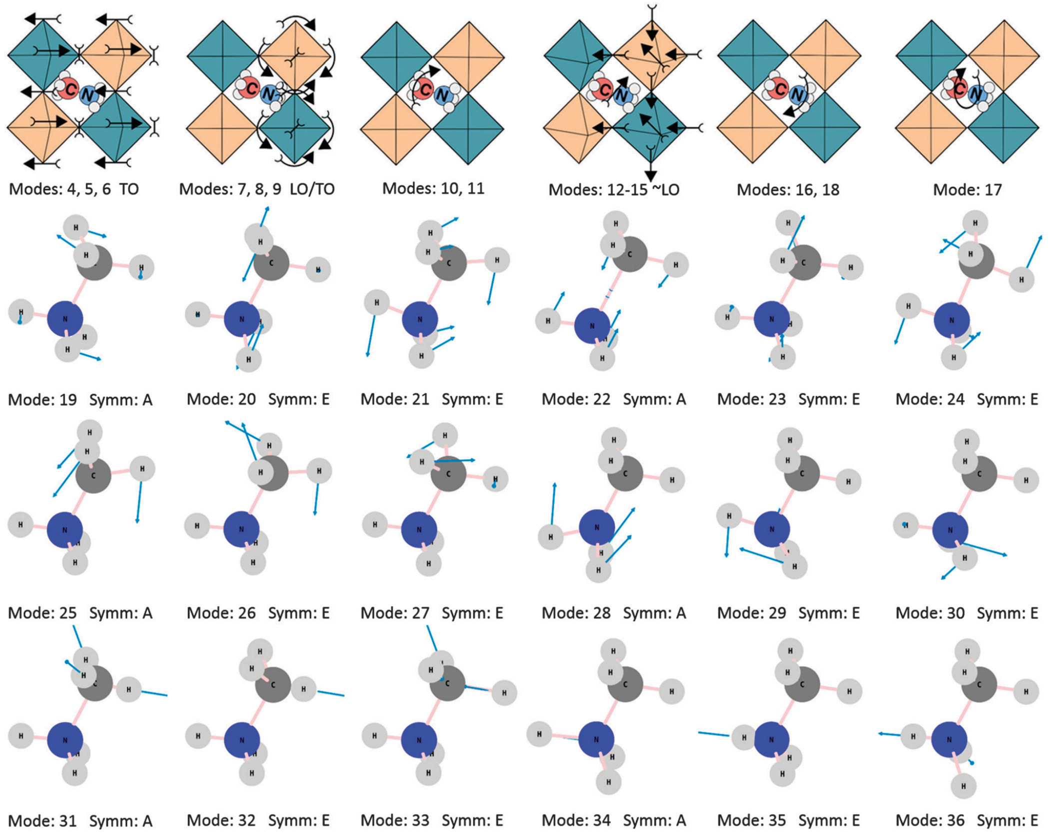

Fig. 5 Schematic representations of the vibrational modes geometries of the 36 zone-centre (Γ-point) phonon modes of the methylammonium lead halides in the cubic phase. The first row shows the 6 cage-vibration types (the acoustic modes are omitted, since they correspond to translations of the whole lattice and are therefore spectroscopically inactive). The last three rows show the molecular modes (numbered 19 to 36).

but no other phonon mode is anticipated in the region. To further investigate this interesting feature, we performed additional calculations to take statistical disorder into account. A hundred snapshots were considered in which the organic cation was randomly oriented and displaced, and only allowed partial relaxation before calculating the vibrational features of the crystal. The effect of disorder on mode 19 in $MAPbI_3$ is shown in Fig. 7 (see Fig. S9–S11, ESI,† for the complete set of calculated spectra of the three halide systems with dynamic disorder taken into account). The feature is changed in two major ways: (i) the resulting spectral feature, as a convolution of the 100 individual snapshots, is noticeably broadened compared to the ordered system. Full widths at half maxima (FWHMs) exceeding 150 cm^{-1} are expected, which match well with the measured linewidths for this mode; (ii) a second peak is created at lower Raman shift energies (a shoulder in the case of $MAPbI_3$), illustrating that additional spectral features can result from disorder only. We believe that these extra peaks may have been misinterpreted in former studies as being harmonic overtones or combination bands, which would be much less intense and thus barely detectable. Statistical orientational disorder is likely to be intermixed with dynamic disorder. The effect of dynamic disorder on the peak widths is detailed in the section below discussing the temperature dependence of the Raman spectra.

Assignment of the molecular modes

Assigning the predicted molecular modes to the nearest Raman feature seems justified (see Fig. S12–S14 in the ESI† for annotated spectra) and is consistent with previous reports on $MAPbCl_3$.[9,10] The internal modes of $CH_3NH_3^+$ show little change upon halide substitution or across the phase changes. In fact, the peak positions are close to what is obtained for bare methylammonium ions.[10] This observation corroborates the FTIR investigation of Glaser *et al.*[18] and Raman measurements from Mattoni *et al.*[39] Our tentative assignment is given in Table 3. Since little temperature evolution can be seen, the corresponding theoretical peaks are given for the cubic phase. Fig. 5 shows the eigenvectors associated with

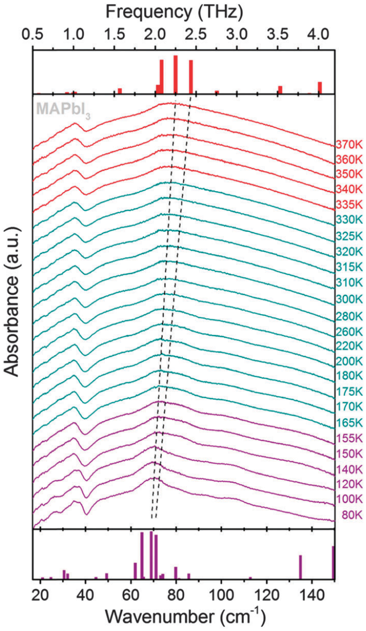

Fig. 6 Terahertz absorption spectra of $MAPbI_3$ measured at temperatures between 80 and 370 K. Spectra were recorded in the 0.5 to 4.5 THz energy range with 10 to 20 K steps away from the phase transitions, and 5 K steps around 160 and 330 K. The top and bottom bar charts give the predicted infrared activity of the low-frequency modes in the cubic and orthorhombic phases, respectively. The dotted lines join infrared-active modes in the orthorhombic and cubic phases, and are intended as guides for the eye in order to visualise the shift and broadening of the band around 2 THz.

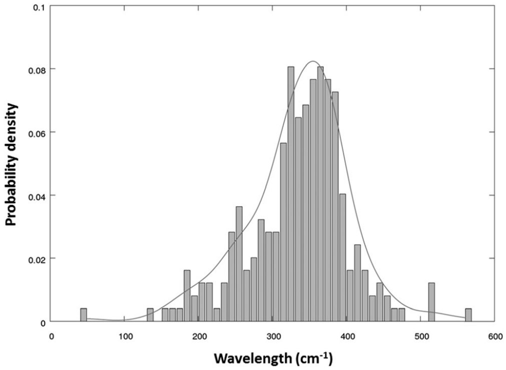

Fig. 7 Effect of disorder on the frequency of the MA torsional mode (19 in Fig. 3 and Table 3) of $MAPbI_3$. The histograms show the distribution of frequencies of mode 19, extracted from 248 individual calculations in which the MA cation was randomly orientated and partially relaxed (see ESI†). The solid line is the kernel density estimation of these sampled data.

each vibrational mode. Fig. 4 shows that modes 20 to 36 are similar for the three halide types, and are composed almost entirely (*i.e.* >99%) of displacements of the atoms in the cations. A collection of weak unidentified features can be observed between 1000 and 1200 cm^{-1} as well as extra peaks above 2500 cm^{-1} (see Fig. 2). These features might be a consequence of stochastic disorder in the material. For the features above 2500 cm^{-1}, hydrogen atoms are likely to be significantly involved in the vibrations, and so these features might therefore correspond to different hydrogen-bonding configurations. We note however that even if the samples were kept in deep vacuum, we cannot exclude the possibility that the unidentified features are parasitic peaks from trapped solvent[38,40] or due to water ingress into the material.[41,42]

Temperature evolution of the modes

In the case of $MAPbI_3$, Fig. 8a–e show that most of Raman peaks weaken in intensity and broaden at the orthorhombic-to-tetragonal phase change (around 160 K, see Fig. S15 and S16 in the ESI†). Fig. S17a in the ESI,† further illustrates this phenomenon by revealing a clear and sharp step-like increase of the peak linewidths when the temperature is increased across the low-temperature phase transition. The broadening is so strong in the case of $MAPbI_3$ that some Raman features almost disappear above ~150 K. For example, the sharp molecular doublet with peaks at 925 and 980 cm^{-1} in Fig. 8d, which we assigned to the C–N bending and stretching, respectively, disappears altogether across the phase change. We attribute this extreme broadening to the change of dynamics which occurs when the full reorientation of the methylammonium ions inside the cavity is unlocked.

The rapid realignment of the C–N axis of $CH_3NH_3^+$ was predicted in MD studies[43,44] and observed by nuclear magnetic resonance (NMR),[45,46] adiabatic calorimetric measurements,[46] quasi-elastic neutron scattering (QENS)[38,47] and optical 2D vibrational spectroscopy.[48] However, there is no Raman peak directly ascribed to this motion, since it is correlated with cage vibrations. In other words, since the MA cations are very light compared to the surrounding lattice, we expect that they can be 'pushed around' by the cage vibrations. This creates a continuum of different environments for the cations, thus causing a strong broadening of most of the vibrational features. The unlocking of what is effectively a new dynamical degree of freedom creates a statistical distribution of vibrational modes corresponding to the resultant different local crystal configurations.

Further insight is obtained from the functional form that yields the best description of the spectral features. All the Raman peaks of the three compounds are best described by sharp Lorentzian functions in the low temperature orthorhombic phase. An increase of temperature in this phase leads to an increase in the peak width although the peak retains its Lorentzian shape (known as homogenous broadening). The homogeneous broadening occurs because the activation of constrained MA reorientations produces dynamic disorder which, on average, is distributed evenly through the lattice, this results in an increased spread in scattering energies. However, the nature of the temperature-induced broadening changes abruptly in the tetragonal phase.

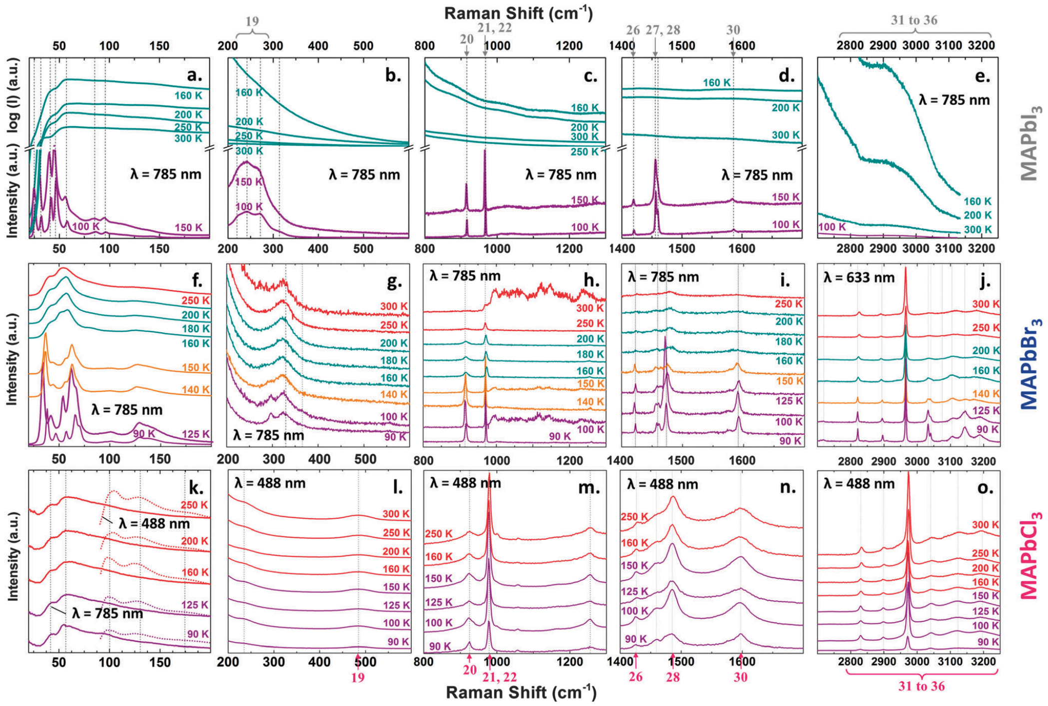

Fig. 8 Temperature dependence of the Raman spectra of $MAPbI_3$ (top row a to e), $MAPbBr_3$ (middle row f to j) and $MAPbCl_3$ (bottom row k to o). Each graph on a row has a different y-axis to best show the temperature evolution of the peaks. In the case of $MAPbI_3$, a logarithmic scale is used above the axis break to facilitate reading. The colour code is the same as in Fig. 1. The data is reported for the excitation wavelength λ yielding the clearest data (specified on each graph).

Some of the cage modes of $MAPbI_3$ become better fitted by Gaussians functions in this phase (see Table S2 in the ESI†). This is known as inhomogeneous broadening and is likely to be due to the appearance of a distribution of bond lengths resulting from spatial disorder in the orientation and/or position of the MA molecules within the perovskite cages. Inhomogeneous broadening is expected to be temperature-independent if the structure and dynamics of the material is conserved.

Inhomogeneous broadening of Raman peaks is a recurrent feature in disordered materials. It has been reported in manganese perovskites such as $LaMnO_3$ near the displacive orthorhombic-to-cubic phase change, and has been attributed to an increase in lattice disorder.[49] A comparable effect can occur with organic (*e.g. trans*-stilbene[50]) or inorganic (*e.g.* SF_6 and WF_6, ref. 51) molecules, and is often interpreted as statistical broadening due to environmental fluctuation. Temperature-independent inhomogeneous broadening has been reported for III–V semiconductors (*e.g.* GaAs, InAs, GaSb and InP, ref. 52), and is considered to be a surface effect caused by the microscopic disorder generated during the polishing process.

Fig. 8a–e, shows the temperature evolution of the FWHM in $MAPbI_3$. The Raman features associated with cage vibrations merge across the phase change around 160 K, and the corresponding abrupt broadening of the peaks can be seen in Fig. S17a in the ESI.† Similarly, the terahertz absorption spectra given in Fig. 6 show significant broadening over the 80 to 370 K temperature range. In particular, the structure in the broad feature around 2 THz gradually disappears, presumably as the individual peaks broaden. The typical increase of FWHM of a cage mode in $MAPbI_3$ at the orthorhombic-tetragonal transition is from about $W_L \sim 10$ to $W_G \sim 50$ cm^{-1} yielding the ratio $W_L/W_G \sim 5$ (W_L and W_G are the FWHMs of Lorentzian and Gaussian peaks, respectively). Furthermore, Fig. S17a in the ESI† shows that W_G in the tetragonal phase is temperature independent. At room temperature, broadening of the Raman peaks is dominated by inhomogeneous effects ($W_G \gg W_L$) that we attribute to a wide spread of bond-length distribution correlated with the variety of allowed MA orientations.

A broadening of the cage peaks is also apparent across $MAPbBr_3$ the Tetragonal I to Tetragonal II phase change, although this is less extreme than in the case of $MAPbI_3$. In particular, the individual modes can still be traced across the phase change, as can be seen in Fig. 8f–j. For $MAPbBr_3$, the typical broadening of a cage mode is $W_G/W_L \sim 2$. Despite the fact that the broadening in $MAPbBr_3$ is stronger for the cage modes, the molecular peaks exhibit a non-negligible broadening.

Once in the tetragonal phase, there is still an increase in linewidth with increasing temperature, but this is by far less pronounced than at the phase transition. Similar abrupt broadening as in $MAPbI_3$ can be seen from Fig. S17b in the ESI,† coinciding with a change in the nature of the first five cage modes from Lorentzian to Gaussian (see Tables S2–S4 in the ESI†).

Evidence of the reorientation of the cation in $MAPbBr_3$ being unlocked between 150 and 155 K can be found in the dielectric and calorimetric measurements reported by Onoda-Yamamuro.[21,22] More recently, Swainson *et al.*[53] studied the relaxation dynamics of $MAPbBr_3$ by QENS, and confirmed the melting of orientation order at this temperature.

In the case of $MAPbBr_3$, W_G and W_L are similar in the disordered phase. Due to the structural similarities between $MAPbI_3$ and $MAPbBr_3$, we believe that the homogeneous component of the broadening W_L in $MAPbBr_3$ remains of the same order as for $MAPbI_3$. The inhomogeneous contribution W_G is reduced in $MAPbBr_3$, presumably due to the smaller size of the cage voids, which leads to a reduction of the reorientation possibilities for the MA molecules which, in turn, limits the spread of the bond-length distribution.

Interestingly, little temperature evolution of the Raman peaks is observed for $MAPbCl_3$ over the 90 to 300 K range, although similar broadening behaviour might be expected (see Fig. 8k–o and Fig. S17c, ESI†). Only a few of the cage modes seem to be linearly broadened across the investigated temperature range and the Lorentzian nature of the Raman peaks is preserved across the phase changes. At low temperatures, the FWHM of the Raman peaks in $MAPbCl_3$ is large compared to the other compounds (at 90 K the FWHM of a typical cage mode is ~ 10 cm^{-1} for $MAPbI_3$, ~ 15 cm^{-1} for $MAPbBr_3$ and ~ 40 cm^{-1} in $MAPbCl_3$).

The same aforementioned studies[21,22,46] demonstrate that, for $MAPbCl_3$, the head-to-tail ordering of the cation in the orthorhombic phase is completely removed in the cubic phase. The limited temperature-evolution of the broadening in $MAPbCl_3$ can thus have two origins: (i) there is no reorientation of the MA cations in the cavity (coupled with a cage deformation mode), or (ii) these rearrangements do occur, but the initial and final surroundings of the cations are the same. NMR studies[45,46] seem to rule out the first hypothesis. The chloride already adopts a cubic perovskite structure by 180 K. Of the three halides, the chloride structure tolerance factor is closest to the ideal value of 1.[54] We therefore propose that the unhindered rotations in the more cubic cavity might preserve the width of the Raman peaks, even at room temperature.

The conservation of Lorentzian shape of the Raman peaks on the investigated temperature range means that at all temperatures: $W_G \ll W_L$. This behaviour can again be rationalized by considerations on the size of the cage voids. On the one hand, the voids are sufficiently small that even though the reorientation of the MA molecules is unlocked in the cubic phase, inhomogeneous effects (*i.e.* W_G) are reduced because their emergence is limited by the highly symmetrical environment. On the other hand, the small size of the voids enhances a lot steric hindrance and consequently the dynamic coupling is enhanced as well. This leads to a strong increase in homogeneous linewidth which now dominates the Raman FWHM at any temperature.

For all three compounds, the coupling between both organic and inorganic sub-lattices leads to an increase in the existing Raman peak widths rather than creating a distribution of new mode frequencies. The resulting homogeneous dynamic broadening of Raman peaks is inversely proportional to the associated phonon lifetime, τ ($\tau = \hbar/\mathrm{FWHM}$).[55] Thus the abrupt increase of most of the peak widths displayed in Fig. S17a–c in the ESI,† corresponds to a drastic decrease of the phonon lifetime associated with the mode. The estimated typical phonon lifetimes of a cage mode (the 'nodding donkey' around N, mode 10 in the cubic phase), the C–N torsion mode (number 19 in the cubic phase), and a molecular vibration (the C–N symmetric stretch) are given for the three methylammonium lead halide compounds in Fig. 9a–c. The data points plotted with open circles in Fig. 9 correspond to the estimated phonon lifetimes for homogeneously broadened peaks (*i.e.* peaks that are best fitted with Lorentzian functions). In that case, the Lorentzian contribution to the broadening can be deconvolved from the Gaussian contribution induced by the experimental setup, using the approach detailed in ref. 56 and summarized in ESI† Note S3. However, in the case when inhomogeneous broadening dominates, the former method can only yield a lower limit on the phonon lifetime (shown as filled square markers in Fig. 9).

Effect of vibrational modes on heat and electrical transport

Introducing a weakly coupled mass inside a host lattice is a strategy to reduce its thermal conductivity. Efficient thermoelectric materials (*i.e.* with large values of *ZT*, the thermoelectric figure-of-merit) like skutterudites are designed with so called 'rattler' atoms.[57–59] Rattlers have been shown to be responsible for significant broadening of the Raman peaks compared with the "unfilled" structure, due to a drastic reduction of the phonon lifetimes.[60] Unlocking the reorientation of the MA ion in $CH_3NH_3PbX_3$ appears to act like the activation of a rattler. This is consistent with the recent observations showing that thermal conductivity is heavily suppressed in $MAPbI_3$ compared with model systems,[61] and can decrease abruptly as the temperature is increased across the orthorhombic-to-tetragonal transition in films on some substrates.[62] The estimation of the thermal conductivity of $MAPbI_3$ in that study corroborates a previous experimental study[63] yielding a value between 0.3 and 0.5 W K^{-1} m^{-1} at room temperature. To put this value into perspective, it can be compared to the thermal conductivity of PbI_2 (~ 2.7 W K^{-1} m^{-1}),[64] single layer graphene (~ 5000 W K^{-1} m^{-1}),[65] Aluminium (~ 222 W K^{-1} m^{-1}),[66] quartz glass (~ 1.4 W K^{-1} m^{-1}),[67] the record thermoelectric materials CdTe and SnSe (~ 2 and 0.6 W K^{-1} m^{-1}, respectively),[68,69] the polymer P3HT (~ 0.2 W K^{-1} m^{-1})[70] or air (~ 0.025 W K^{-1} m^{-1}).[71] It has been suggested that $CH_3NH_3AI_3$ (A = Pb and Sn) might be of interest for thermoelectric application, with *ZT* values that could reach values between 1 and 2 (values above 2 are required to compete with conventional power generators).[72]

The phonon lifetimes seen in Fig. 9 (around 0.1 ps for $MAPbI_3$ or below) are generally short relative to other semiconductors at room temperature: for optical phonons at 300 K, values of ~ 2 ps and ~ 4 ps were reported in bulk silicon[73] and natural germanium crystals,[74] respectively. Lower values (between 0.1 and ~3 ps for optical phonons between 0.5 and 4 THz)[75] are expected at 300 K for the good thermoelectric materials PbSe and PbTe. In these materials, optical phonons contribute considerably to the lattice thermal conductivity and serve as important scattering channels for acoustic phonons.[75]

As discussed above, the short phonon lifetimes in $MAPbX_3$ imply a high degree of anharmonic phonon–phonon coupling. The phonon lifetimes observed, particularly at room temperature, where the Raman peaks can no longer be resolved for many modes, might also be expected to contribute to a reduction of the charge-carrier mobility through electron–phonon interactions.

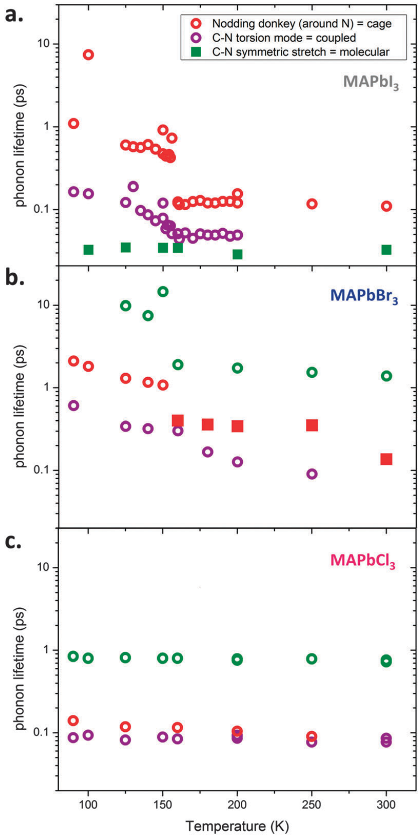

Fig. 9 Temperature dependence of the estimated phonon lifetimes for $MAPbI_3$ (a), $MAPbBr_3$ (b) and $MAPbCl_3$ (c). Three representative phonons were selected: the green markers show a typical molecular mode for each compound (here the C–H symmetric stretch, see Table 3), the red markers stand for a typical cage mode (mode number 10, the 'nodding donkey' around N, see Tables 1 and 2), and the purple triangles represent the C–N torsion mode (*i.e.* the isolated mode, see Table 3). Open circle markers have been used to plot the lifetimes of homogeneously broadened peaks while filled square markers show the lower limit of the phonon lifetime in the case of inhomogeneous broadening, as detailed in ESI† Note S3.

Two independent studies[76,77] have reported that the temperature dependence of the mobility for $MAPbI_3$ is proportional to $T^{-1.4}$ or $T^{-1.6}$, which is close to the $T^{-1.5}$ behaviour expected for band-like transport limited by phonon scattering, as observed in germanium.[78] The mobility values reported for $CH_3NH_3PbX_3$ at room temperature – in excess of 100 cm^2 V^{-1} s^{-1} for $MAPbI_3$ (ref. 64 and 65) appear to be remarkably high for a solution processed material, particularly when combined with the observation that these materials display behaviour consistent with a high concentration of ionic defects.[3,79,80] However, mobilities up to 1000 cm^2 V^{-1} s^{-1} could be expected from the calculated electron band dispersion reported in several studies[81] that yield a charge carrier effective mass as small as $m_0^* \sim 0.12$ for electrons and 0.15 for holes.[82] At room temperature, two scattering processes may limit charge carrier mean free path in $CH_3NH_3PbX_3$: impurity scattering (independent of phonons) and electron–phonon scattering. Short phonon lifetimes indicate that inelastic electron–phonon scattering is likely, and energy transferred can dissipate quickly.

The optical phonon modes we have identified have much lower energies than conventional semiconductors, where the lowest optical modes are typically around 40 meV (9 THz).[55,83] In these conventional materials the optical modes will not be significantly populated at room temperature, and since electrons will not have this energy either, these phonons will not contribute to electron scattering processes. This point is illustrated

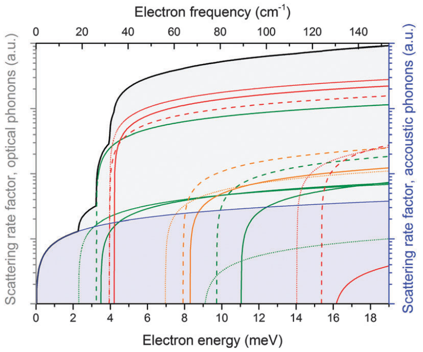

Fig. 10 Electron–phonon scattering rate factor for optical and acoustic phonons as a function of electron energy. This approximate quantity is synthesised from a superposition of estimated contributions from each phonon. These are derived from the energy of each mode at the Γ point, scaled by its relative IR activity (considered a proxy for its piezoelectric coupling), convolved with a parabolic density of electronic states at finite temperature. The contribution of acoustic modes is obtained assuming equipartition holds.[84] Optical modes are assumed dispersion-less, acoustic modes with linear dispersion. Only optical phonon emission by electrons is accounted for in this figure, the contribution of phonon absorption processes by charge carriers can be found in ref. 84 and would increase the scattering contribution of optical modes at lower energies. The sets of green, red and orange curves correspond to the optical eigenmodes in Fig. 3. The black curve gives the sum of the optical phonon contribution to the scattering rate factor. The scattering rate per electron of a given energy at a temperature T can be obtained by convolution of the scattering factor with a Bose–Einstein distribution function.

in Fig. 10, this shows a factor proportional to electron–phonon (emission) scattering rate as a function of electron energy including a decomposition into the relative contributions to this rate from different modes. The figure indicates the sharp turn-on from the contribution of optical phonons to the electron–phonon scattering rate as electron energies increase. For $MAPbI_3$, we observe the lowest optical mode is activated from $\sim$4 meV (1 THz), well below the thermal energy at room temperature (26 meV). This suggests that optical, rather than acoustic, phonon scattering may dominate loss of mobility at room temperature in these materials.

Conclusion

In conclusion we have performed a complete assignment of the main features observed in Raman and terahertz absorption spectra of the three methylammonium lead halide perovskites to their respective vibrational modes. From the temperature dependence of the spectra, we have shown the key role of two types of disorder in the $CH_3NH_3PbX_3$ material family, *viz.* (i) dynamic disorder caused by the unlocking of the rotation of the methylammonium ions in their cavities, causing homogeneous peak broadening, and (ii) statistical disorder caused by the various possible cation orientations, which leads to inhomogeneous peak broadening. In particular, we have demonstrated that statistical broadening can give rise to extra peaks in the spectra. The peak broadening occurring at the orthorhombic-to-tetragonal phase change in $MAPbI_3$ is the most pronounced and corresponds to a step-like decrease of the lifetimes of most of the low frequency modes. This change results in the observed decrease in the thermal conductivity of $MAPbI_3$ at room temperature. The observation of short phonon lifetimes combined with our assignment of low-energy optical phonons suggests that optical phonon scattering is likely to dominate at room temperature in these materials.

Data access

The structures used for the phonon calculations are available from https://github.com/WMD-group/hybrid-perovskites, while the raw data from the phonon calculations, including simulated spectra and mode eigenvectors, are available from https://github.com/WMD-group/Phonons. Custom codes written to analyse gamma point motion are available at https://github.com/jarvist/Julia-Phonons, the customised version of Phonopy to provide eigenmode-resolved partial densities of states is available at https://github.com/jarvist/phonopy.

Acknowledgements

The authors thank Juraj Sibik and Axel Zeitler for their contribution in the measurement and interpretation of the terahertz absorption spectra, and Philip Calado and Davide Moia for their helpful discussions regarding the TOC graphic. PB and AL are grateful to the EPSRC (EP/J002305/1, EP/M014797/1 and EP/M023532/1) for financial support. The work at Bath was supported by the EPSRC (EP/K016288/1, EP/K004956/1, EP/L000202, and EP/M009580/1) and the ERC (Grant 277757). ARG, MIA and MCQ thank the Spanish Ministry of Economy and Competitiveness (MINECO) for its support through Grant No. CSD2010-00044 (Consolider NANOTHERM) and MAT2015-70850-P (HIBRI2). The work at ICMAB was carried out under the auspices of the Spanish Severo Ochoa Centre of Excellence program (grant SEV-2015-0496). F. B. is funded through the EU DESTINY Network (Grant No. 316494). JN acknowledges the EPSRC for founding (EP/J017361). AP would like to thank the Royal Irish Academy for the Charlemont grant for funding the research visit that made the terahertz work possible.

References

1 F. Brivio, J. M. Frost, J. M. Skelton, A. J. Jackson, O. J. Weber, M. T. Weller, A. R. Goni, A. M. A. Leguy, P. R. F. Barnes and A. Walsh, *Phys. Rev. B: Condens. Matter Mater. Phys.*, 2015, **92**, 144308.
2 M. A. Green, K. Emery, Y. Hishikawa, W. Warta and E. D. Dunlop, *Prog. Photovoltaics.*, 2015, **23**, 1–9.
3 C. Eames, J. M. Frost, P. R. F. Barnes, B. C. O'Regan, A. Walsh and M. S. Islam, *Nat. Commun.*, 2015, **6**, 7497.
4 S. D. Stranks, V. M. Burlakov, T. Leijtens, J. M. Ball, A. Goriely and H. J. Snaith, *Phys. Rev. Appl.*, 2014, **2**, 034007.
5 C. La-o-vorakiat, H. Xia, J. Kadro, T. Salim, D. Zhao, T. Ahmed, Y. M. Lam, J.-X. Zhu, R. A. Marcus, M.-E. Michel-Beyerle and E. E. M. Chia, *J. Phys. Chem. Lett.*, 2015, **7**, 1–6.
6 M. Ledinsky, P. Loper, B. Niesen, J. Holovsky, S.-J. Moon, J.-H. Yum, S. D. Wolf, A. Fejfar and C. Ballif, *J. Phys. Chem. Lett.*, 2015, **6**, 401–406.
7 R. Gottesman, E. Haltzi, L. Gouda, S. Tirosh, Y. Bouhadana, A. Zaban, E. Mosconi and F. De Angelis, *J. Phys. Chem. Lett.*, 2014, **5**, 2662–2669.
8 C. Quarti, G. Grancini, E. Mosconi, P. Bruno, J. M. Ball, M. Lee, H. J. Snaith, E. Petrozza and F. De Angelis, *J. Phys. Chem. Lett.*, 2013, **5**, 279–284.
9 A. Maaej, M. Bahri, Y. Abid, N. Jaidane, Z. B. Lakhdar and A. Lautie, *Phase Transitions*, 1998, **64**, 179–190.
10 J. T. Edsall and H. Scheinberg, *J. Chem. Phys.*, 1940, **8**, 520–525.
11 P. S. R. Prasad, S. Sathaiah and H. D. Bist, *Chem. Phys. Lett.*, 1987, **142**, 341–344.
12 C. Carabatos-Nedelec, M. Oussaid and K. Nitsch, *J. Raman Spectrosc.*, 2003, **34**, 388–393.
13 M. Couzi, A. Daoud and R. Perret, *Phys. Status Solidi A*, 1977, **41**, 271–282.
14 Y. Abid, *J. Phys.: Condens. Matter*, 1994, **6**, 6447–6454.
15 N. Preda, L. Mihut, M. Baibarac, I. Baltog and S. Lefrant, *J. Phys.: Condens. Matter*, 2006, **18**, 8899.
16 R. F. Warren and W. Y. Liang, *J. Phys.: Condens. Matter*, 1993, **5**, 6407.
17 M. A. Pérez-Osorio, R. L. Milot, M. R. Filip, J. B. Patel, L. M. Herz, M. B. Johnston and F. Giustino, *J. Phys. Chem. C*, 2015, **119**, 25703–25718.
18 T. Glaser, C. Mueller, M. Sendner, C. Krekeler, O. E. Semonin, T. D. Hull, O. Yaffe, J. S. Owen, W. Kowalsky, A. Pucci and R. Lovrincic, *J. Phys. Chem. Lett.*, 2015, **6**, 2913–2918.

19 M. T. Weller, O. J. Weber, P. F. Henry, A. M. Di Pumpo and T. C. Hansen, *Chem. Commun.*, 2015, **51**, 4180–4183.

20 A. Poglitsch and D. Weber, *J. Chem. Phys.*, 1987, **87**, 6373–6378.

21 N. Onoda-Yamamuro, T. Matsuo and H. Suga, *J. Phys. Chem. Solids*, 1992, **53**, 935–939.

22 N. Onoda-Yamamuro, T. Matsuo and H. Suga, *J. Phys. Chem. Solids*, 1990, **51**, 1383–1395.

23 N. Onoda-Yamamuro, O. Yamamuro, T. Matsuo and H. Suga, *J. Phys. Chem. Solids*, 1992, **53**, 277–281.

24 M. I. Saidaminov, A. L. Abdelhady, B. Murali, E. Alarousu, V. M. Burlakov, W. Peng, I. Dursun, L. Wang, Y. He, G. Maculan, A. Goriely, T. Wu, O. F. Mohammed and O. M. Bakr, *Nat. Commun.*, 2015, **6**, 7586.

25 K. Lien Nguyen, T. Friscic, G. M. Day, L. F. Gladden and W. Jones, *Nat. Mater.*, 2007, **6**, 206–209.

26 G. Kresse and J. Furthmüller, *Comput. Mater. Sci.*, 1996, **6**, 15–50.

27 G. Kresse and D. Joubert, *Phys. Rev. B: Condens. Matter Mater. Phys.*, 1999, **59**, 1758–1775.

28 J. P. Perdew, A. Ruzsinszky, G. a. I. Csonka, O. A. Vydrov, G. E. Scuseria, L. A. Constantin, X. Zhou and K. Burke, *Phys. Rev. Lett.*, 2008, **100**, 136406.

29 A. Togo, L. Chaput, I. Tanaka and G. Hug, *Phys. Rev. B: Condens. Matter Mater. Phys.*, 2010, **81**, 174301.

30 J. M. Skelton, S. C. Parker, A. Togo, I. Tanaka and A. Walsh, *Phys. Rev. B: Condens. Matter Mater. Phys.*, 2014, **89**, 205203.

31 A. Togo, L. Chaput and I. Tanaka, *Phys. Rev. B: Condens. Matter Mater. Phys.*, 2015, **91**, 094306.

32 I. M. Hermes, S. A. Bretschneider, V. W. Bergmann, D. Li, A. Klasen, J. Mars, W. Tremel, F. Laquai, H.-J. Butt, M. Mezger, R. Berger, B. J. Rodriguez and S. A. L. Weber, *J. Phys. Chem. C*, 2016, **120**, 5724–5731.

33 Y. Zhou, L. You, S. Wang, Z. Ku, H. Fan, D. Schmidt, A. Rusydi, L. Chang, L. Wang, P. Ren, L. Chen, G. Yuan, L. Chen and J. Wang, *Nat. Commun.*, 2015, **6**, 11193.

34 R. Gottesman, L. Gouda, B. S. Kalanoor, E. Haltzi, S. Tirosh, E. Rosh-Hodesh, Y. Tischler, A. Zaban, C. Quarti, E. Mosconi and F. De Angelis, *J. Phys. Chem. Lett.*, 2015, **6**, 2332–2338.

35 K. P. Ong, T. Wee Goh and A. Huan, *J. Phys. Chem. A*, 2015, 11033–11038.

36 C. J. Ludman, C. I. Ratcliffe and T. C. Waddington, *J. Chem. Soc., Faraday Trans. 2*, 1975, 1759–1780.

37 R. G. Niemann, A. G. Kontos, D. Palles, E. I. Kamitsos, A. Kaltzoglou, F. Brivio, P. Falaras and P. J. Cameron, *J. Phys. Chem. C*, 2016, **120**, 2509–2519.

38 A. M. A. Leguy, J. M. Frost, A. P. McMahon, V. G. Sakai, W. Kochelmann, C. Law, X. Li, F. Foglia, A. Walsh, B. C. O'Regan, J. Nelson, J. T. Cabral and P. R. F. Barnes, *Nat. Commun.*, 2015, **6**, 7124.

39 A. Mattoni, A. Filippetti, M. I. Saba, C. Caddeo and P. Delugas, *J. Phys. Chem. Lett.*, 2016, **7**, 529–535.

40 A. E. Williams, P. J. Holliman, M. J. Carnie, M. L. Davies, D. A. Worsley and T. M. Watson, *J. Mater. Chem. A*, 2014, **2**, 19338–19346.

41 A. M. A. Leguy, Y. Hu, M. Campoy-Quiles, M. I. Alonso, O. J. Weber, P. Azarhoosh, M. van Schilfgaarde, M. T. Weller, T. Bein, J. Nelson, P. Docampo and P. R. F. Barnes, *Chem. Mater.*, 2015, **27**, 3397–3407.

42 J. S. Manser, M. I. Saidaminov, J. A. Christians, O. M. Bakr and P. V. Kamat, *Acc. Chem. Res.*, 2016, **49**, 330–338.

43 J. M. Frost, K. T. Butler and A. Walsh, *APL Mater.*, 2014, **2**, 081506.

44 J. Even, L. Pedesseau and C. Katan, *J. Phys. Chem. C*, 2014, **118**, 11566–11572.

45 R. E. Wasylishen, O. Knop and J. B. Macdonald, *Solid State Commun.*, 1985, **56**, 581–582.

46 O. Knop, R. E. Wasylishen, M. A. White, T. S. Cameron and M. J. M. Van Oort, *Can. J. Chem.*, 1990, **68**, 412.

47 T. Chen, B. J. Foley, B. Ipek, M. Tyagi, J. R. D. Copley, C. M. Brown, J. J. Choi and S.-H. Lee, *Phys. Chem. Chem. Phys.*, 2015, **17**, 31278–31286.

48 A. A. Bakulin, O. Selig, H. J. Bakker, Y. L. A. Rezus, C. Mueller, T. Glaser, R. Lovrincic, Z. Sun, Z. Chen, A. Walsh, J. M. Frost and T. L. C. Jansen, *J. Phys. Chem. Lett.*, 2015, **6**, 3663–3669.

49 E. Granado, J. A. Sanjurjo, C. Rettori, J. J. Neumeier and S. B. Oseroff, *Phys. Rev. B: Condens. Matter Mater. Phys.*, 2000, **62**, 11304–11307.

50 A. B. Myers, M. O. Trulson and R. A. Mathies, *J. Chem. Phys.*, 1985, **83**, 5000–5006.

51 A. A. Makarov, I. Y. Petrova, E. A. Ryabov and V. S. Letokhov, *J. Phys. Chem. A*, 1998, **102**, 1438–1449.

52 D. J. Evans and S. Ushioda, *Phys. Rev. B: Condens. Matter Mater. Phys.*, 1974, **9**, 1638–1645.

53 I. P. Swainson, C. Stock, S. F. Parker, L. Van Eijck, M. Russina and J. W. Taylor, *Phys. Rev. B: Condens. Matter Mater. Phys.*, 2015, **92**, 100303.

54 G. Kieslich, S. Sun and A. K. Cheetham, *Chem. Sci.*, 2015, **6**, 3430–3433.

55 P. Y. Yu and M. Cardona, *Fundamentals of Semiconductors*, Springer-Verlag, 3rd edn, 2001.

56 J. J. Olivero and R. L. Longbothum, *J. Quant. Spectrosc. Radiat. Transfer*, 1977, **17**, 233–236.

57 B. C. Sales, D. Mandrus and R. K. Williams, *Science*, 1996, **272**, 1325–1328.

58 M. S. Dresselhaus, G. Chen, M. Y. Tang, R. G. Yang, H. Lee, D. Z. Wang, Z. F. Ren, J. P. Fleurial and P. Gogna, *Adv. Mater.*, 2007, **19**, 1043–1053.

59 G. J. Snyder and E. S. Toberer, *Nat. Mater.*, 2008, **7**, 105–114.

60 G. S. Nolas and C. A. Kendziora, *Phys. Rev. B: Condens. Matter Mater. Phys.*, 1999, **59**, 6189–6192.

61 T. Hata, G. Giorgi and K. Yamashita, *Nano Lett.*, 2016, **16**, 2749–2753.

62 Z. Guo, S. J. Yoon, J. S. Manser, P. V. Kamat and T. Luo, *J. Phys. Chem. C*, 2016, **120**, 6394–6401.

63 A. Pisoni, J. Jaćimović, O. S. Barišić, M. Spina, R. Gaál, L. Forró and E. Horváth, *J. Phys. Chem. Lett.*, 2014, **5**, 2488–2492.

64 T. S. Silva, A. S. Alves, I. Pepe, H. Tsuzuki, O. Nakamura, M. M. F. d'Aguiar Neto, A. F. da Silva, N. Veissid and C. Y. An, *J. Appl. Phys.*, 1998, **83**, 6193–6195.

65 A. A. Balandin, S. Ghosh, W. Bao, I. Calizo, D. Teweldebrhan, F. Miao and C. N. Lau, *Nano Lett.*, 2008, **8**, 902–907.

66 W. J. Parker, R. J. Jenkins, C. P. Butler and G. L. Abbott, *J. Appl. Phys.*, 1961, **32**, 1679–1684.

67 C. Kittel, *Phys. Rev.*, 1949, **75**, 972–974.

68 J. P. Heremans, V. Jovovic, E. S. Toberer, A. Saramat, K. Kurosaki, A. Charoenphakdee, S. Yamanaka and G. J. Snyder, *Science*, 2008, **321**, 554–557.

69 L.-D. Zhao, S.-H. Lo, Y. Zhang, H. Sun, G. Tan, C. Uher, C. Wolverton, V. P. Dravid and M. G. Kanatzidis, *Nature*, 2014, **508**, 373–377.

70 J. A. Malen, K. Baheti, T. Tong, Y. Zhao, J. A. Hudgings and A. Majumdar, *J. Heat Transfer*, 2011, **133**, 081601.

71 *CRC Handbook of Chemistry and Physics*, ed. R. C. Weast, The Cemical Rubber Co., 50th edn, 1969.

72 Y. He and G. Galli, *Chem. Mater.*, 2014, **26**, 5394–5400.

73 B. C. Daly, K. Kang, Y. Wang and D. G. Cahill, *Phys. Rev. B: Condens. Matter Mater. Phys.*, 2009, **80**, 174112.

74 H. D. Fuchs, C. H. Grein, R. I. Devlen, J. Kuhl and M. Cardona, *Phys. Rev. B: Condens. Matter Mater. Phys.*, 1991, **44**, 8633–8642.

75 Z. Tian, J. Garg, K. Esfarjani, T. Shiga, J. Shiomi and G. Chen, *Phys. Rev. B: Condens. Matter Mater. Phys.*, 2012, **85**, 184303.

76 T. J. Savenije, C. S. Ponseca, L. Kunneman, M. Abdellah, K. Zheng, Y. Tian, Q. Zhu, S. E. Canton, I. G. Scheblykin, T. Pullerits, A. Yartsev and V. Sundström, *J. Phys. Chem. Lett.*, 2014, **5**, 2189–2194.

77 H. Oga, A. Saeki, Y. Ogomi, S. Hayase and S. Seki, *J. Am. Chem. Soc.*, 2014, **136**, 13818–13825.

78 F. J. Morin, *Phys. Rev.*, 1954, **93**, 62–63.

79 J. Beilsten-Edmands, G. E. Eperon, R. D. Johnson, H. J. Snaith and P. G. Radaelli, *Appl. Phys. Lett.*, 2015, **106**, 173502.

80 W. Tress, N. Marinova, S. M. Zakeeruddin, M. K. Nazeeruddin and M. Graetzel, *Energy Environ. Sci.*, 2015, **8**, 995–1004.

81 T. Zhao, W. Shi, J. Xi, D. Wang and Z. Shuai, *Sci. Rep.*, 2016, **7**, 19968.

82 F. Brivio, K. T. Butler, A. Walsh and M. van Schilfgaarde, *Phys. Rev. B: Condens. Matter Mater. Phys.*, 2014, **89**, 155204.

83 H. Richter, Z. P. Wang and L. Ley, *Solid State Commun.*, 1981, **39**, 625–629.

84 B. K. Ridley, *Quantum Processes in Semiconductors*, Oxford University Press, 5th edn, 2013.

Chapter 5

Mixed halide alloys

5.1 Introduction

One of the reasons for hybrid perovskite success is the ease of their preparation. A thin-film of perovskite is usually prepared spin coating the precursors on the proper substrate. This type of procedure is far from an ideal thermodynamic equilibrium and results in a defect rich material. At the same time, it allows to easily intermix differents precursor and control the composition of the film in order to tune the optoelectronic properties of the materials.

Most of the first produced cells had a small percentage (about 4%) of chlorine in the final film. The presence of this impurity was difficult to avoid or control, but improved the efficiency and the stability of devices[197] improving the crystallinity of MAPI. The presence of chlorine was mostly a by-product of the synthesis, but other attempts have been done to study the intentional presence of different ions in the material.[198–201]

Changing the amount of halide in the structure can impact significantly the nanostructure of thin-films as shown in Figure 5.1. The surface roughness, for example, increase with the addiction of bromine to $\mathrm{MAPbI_3}$. At the same time, this also affects also the electro-optical properties changing the material response to illumination.

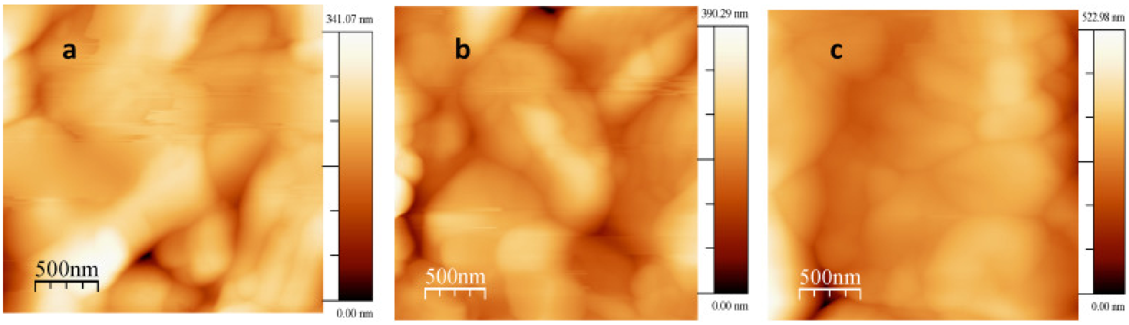

FIGURE 5.1: The picture shows the surface roughness for perovskite with composition $MAPbI_{2.8}Br0.2$ (a), $MAPbI_{2.4}Br0.6$ (b) and $\mathrm{MAPbI_2Br}$. The surface roughness increases from 41.24 nm to 42.73 nm with a small introduction of Br and reach 56.99 nm for the compound (c). Figure taken from reference.[199]

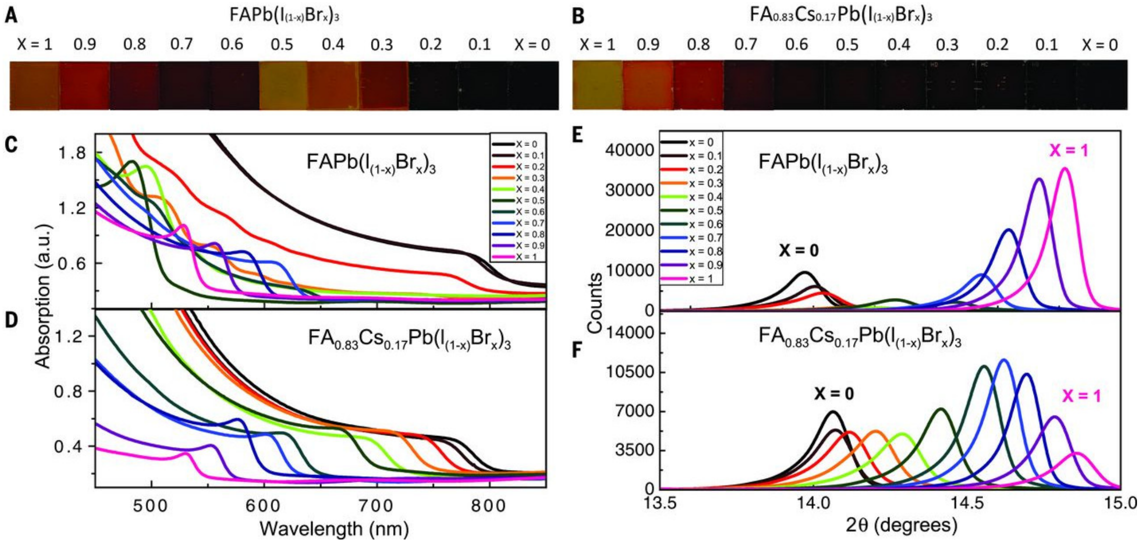

FIGURE 5.2: The figure reports perovskites thin films with different content of halide. In panel A is clear that for intermediate composition of Iodine and Bromine the system undergoes a bleaching, while the same effect is not observed in the material reported in panel B. The figure has been adapted from reference.[202]

Recently McMeekin *et al.*[202] observed that perovskites with mixed composition are unstable and undergo spontaneous degradation. This effect is well pictured in Figure 5.2 where different perovskites film are compared.

To better understand the thermodynamic related to the stability of mixed perovskites, we considered the solid solutions of compound with general formula $\mathrm{MAPb(X_{(1\text{-}x)}Y_x)_3}$ with X,Y =Cl, Br, I and particularly on the Br−I system.

5.2 Computational setup

To simulate the solid solutions of $\mathrm{MAPb(X_{(1\text{-}x)}Y_x)_3}$ we considered seven possible compositions: $x = 0, \frac{\{1..5\}}{6}, 1$. This choice was determined by the pick of a 2×1×1 supercell expansion where six halides are present. The size was limited by the calculation cost of the system, and we considered only the cubic phase described in Chapter 3. The number of different possible structures for a binary alloy with n is given by a binomial coefficient $\binom{m}{n}$ where m is the number of substituted species. The total number of configuration for each possible compositions is hence 2^n.

Perovskites have three halide sites per unit formula leading to 2^{3n} possible compositions for a supercell with n unit formula. This results in an unapproachable number of calculations even for the smallest isotropic 2×2×2 supercell expansion. If we consider the inorganic perovskite case, the presence of a symmetry group (space group $Pm\bar{3}m$) permits to reduce the number of structures. We used the code SOD[203] to identify the unique symmetry independent structures for the archetype $\mathrm{CsPbI_3}$ perovskite. Even applying this simplification, the number of unique structure is too high for both the 2×2×2 and the 2×2×1 supercells. This leave us with the choice of a 2×1×1 where the 64 possible structures are reduced to 21 unique configurations.

In principle the same procedure can not be applied to the hybrid pervoskites, because the molecule breaks the symmetry. Nonetheless to reduce the computational costs for this systems we decided to partially explore the configuration space and consider only the inequivalent structures of the inorganic case, substituting the central cation with the molecule aligned to the direction of cell expansion. Once built the cell have been completely optimised.

The calculations have been performed with the VASP code as described in the previous chapters. We considered a smaller plane waves cut-off of 500 eV and a k-mesh of $3\times6\times6$. The optimisation threshold was set to converge the forces below 1.0 $\frac{meV}{\text{Å}}$.

5.3 Related publications

The results for $MAPb(Br_{(1-x)}I_x)_3$ have been collected in one primary publication that appeared in Journal of Physical Chemistry Letters (2016). The work was performed in close collaboration with Dr. Clovis Caetano who provide expertise and guidance on the alloys thermodynamics.

We also performed calculation on Br/Cl and I/Cl combinations whose results are reported in the following sections.

The publication is included under Creative Commons license.

The Journal of Physical Chemistry Letters

Letter

pubs.acs.org/JPCL

Thermodynamic Origin of Photoinstability in the $CH_3NH_3Pb(I_{1-x}Br_x)_3$ Hybrid Halide Perovskite Alloy

Federico Brivio,[†] Clovis Caetano,[‡] and Aron Walsh*[,†,§]

[†]Centre for Sustainable Chemical Technologies and Department of Chemistry, University of Bath, Claverton Down, Bath BA2 7AY, United Kingdom

[‡]Universidade Federal da Fronteira Sul, Realeza Paraná 85770-000, Brazil

[§]Global E^3 Institute and Department of Materials Science and Engineering, Yonsei University, Seoul 120-749, Korea

ABSTRACT: The formation of solid-solutions of iodide, bromide, and chloride provides the means to control the structure, band gap, and stability of hybrid halide perovskite semiconductors for photovoltaic applications. We report a computational investigation of the $CH_3NH_3PbI_3/CH_3NH_3PbBr_3$ alloy from density functional theory with a thermodynamic analysis performed within the generalized quasi-chemical approximation. We construct the phase diagram and identify a large miscibility gap, with a critical temperature of 343 K. The observed photoinstability in some mixed-halide solar cells is explained by the thermodynamics of alloy formation, where an initially homogeneous solution is subject to spinodal decomposition with I and Br-rich phases, which is further complicated by a wide metastable region defined by the binodal line.

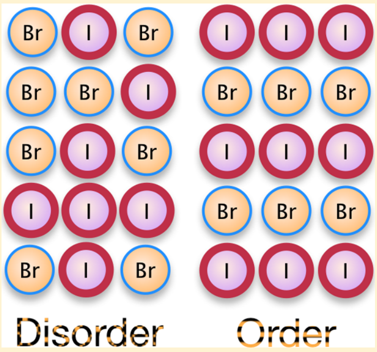

The last four years have seen the emergence of photovoltaic devices based on methylammonium lead iodide ($MAPbI_3$, MA = $CH_3NH_3^+$) and related hybrid organic−inorganic perovskites. The excitement in the field has led to a large research effort and a rapid development of high-efficiency devices.[1−3] The physical properties of $MAPbI_3$, in particular the band gap, can be tuned in several ways: (i) changing the central organic molecule MA, for example substituting it by the formamidinium (FA);[4] (ii) replacing Pb by another cation, for example Sn or Ge;[5] (iii) substituting iodine by bromine or chlorine.

The first hybrid perovskite photovoltaic devices included small amounts of chlorine, which were believed to be randomly interchanged with iodine forming the $MAPb(I_{1-x}Cl_x)_3$ pseudobinary alloy. Mixed $MAPb(I_{1-x}Br_x)_3$ has been recently successfully produced by different groups.[1,6−11] The motivating factors for the I/Br mixture are increased chemical stability and control of the band gap toward tandem solar cell applications. However, it is still not completely understood whether the alloy is stable against phase segregation in the entire range of composition. There has been some evidence for photoinduced phase separation,[12−14] which can affect measurements and performance when the material is photoexcited.[15,16] This effect is unusual, as typically electron and ion transport are decoupled (electrons move quickly with short lifetimes compared to slower ion diffusion processes). There have been some initial theoretical studies of the stability of this alloy, but they either focus on a single composition[17] or are based on the inorganic $CsPb(I_{1-x}Br_x)_3$ system.[18]

In this Letter we combine first-principles total energy calculations with a statistical mechanical treatment of the configurational space of the solid-solution formed between $MAPbI_3$ and $MAPbBr_3$. From this model, we determine how the thermodynamic potentials of the alloy vary with respect to composition and temperature. From this analysis, we construct the first phase diagram of the system. The qualitative picture that emerges is that the I/Br mixture has a miscibility gap *above* room temperature and that heavily mixed systems ($0.3 < x < 0.6$) will be subject to spinodal decomposition and phase separation at 300 K. The main two approximations in our model are the supercell expansion, which limits the configurational space of the alloy that is sampled, and the use of a pseudocubic building block, as the end member compounds and alloys show temperature-dependent structures.[6,9,19]

The calculated energy of mixing as a function of the alloy composition is shown in Figure 1. The variation is unusual, as had been already pointed out by Yin et al. for the $CsPb(I_{1-x}Br_x)_3$ alloy.[18] The $MAPb(I_{1-x}Br_x)_3$ alloy presents a large spread in the energy of mixing in the Br-rich region, which may suggest a tendency for spontaneous ordering in this region at low temperatures. Indeed, there are two configurations that have negative energies of mixing and should be stable against phase separation into the pure end-member compounds, as indicated by the convex hull in Figure 1. These configurations correspond to ordered structures of $MAPbIBr_2$ and $MAPbI_{1/2}Br_{5/2}$, as shown in Figure 2. Both structures are formed when the iodine ions are located at the apical positions, forming superlattices along the [001] direction. From the

Received: February 2, 2016
Accepted: March 7, 2016
Published: March 7, 2016

DOI: 10.1021/acs.jpclett.6b00226
J. Phys. Chem. Lett. 2016, 7, 1083−1087

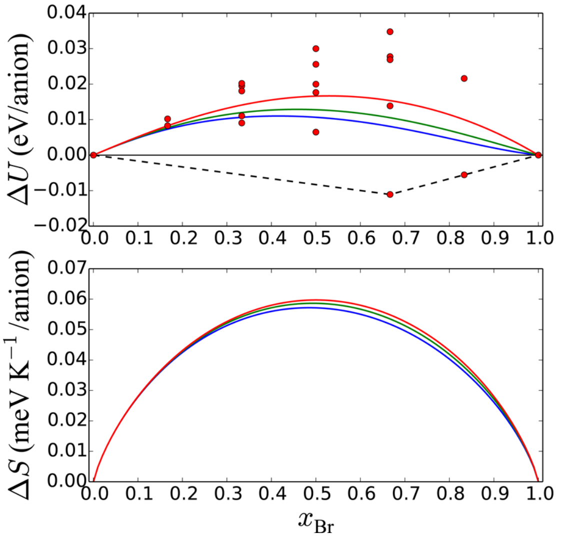

Figure 1. Energy of mixing (top) and entropy of mixing (bottom) as functions of the $CH_3NH_3Pb(I_{1-x}Br_x)_3$ alloy composition. The symbols are the values calculated for each configuration (eq 1). The solid lines show the behavior for the alloy at 200 K (blue), 300 K (green) and for a completely random alloy in the high T limit (red) within the generalized quasi-chemical approximation. The dashed line represents the convex hull.

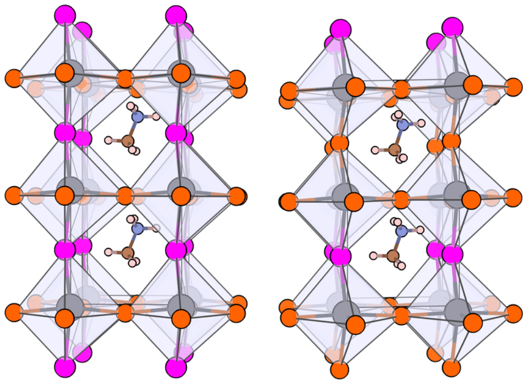

Figure 2. Stable ordered structures identified for $MAPbIBr_2$ and $MAPbI_{1/2}Br_{5/2}$, which minimize internal strain arising from the size mismatch between I and Br. The atoms at the corners of the octahedra are the halides Br (orange) and I (pink). The most stable structures are layered with iodine at the apical positions.

Shannon ionic radii,[20] the mismatch between the two halides is 0.24 Å (r_{I} = 2.20 Å, r_{Br} = 1.96 Å). These two ordered structures provide the structural freedom to separate the Pb−I (longer) and Pb−Br (shorter) interatomic separations along distinct directions, so that internal strain is minimized.

The variation in the energy of mixing of the alloy calculated within the generalized quasi-chemical approximation (GQCA)[21] is also shown in Figure 1. The shape of the curve changes considerably with temperature, becoming more symmetric for high temperatures. At room temperature, the energy of mixing of the solid solution can be well represented by the expression $\Omega x(1-x)$, with $\Omega = 0.06{-}0.02x$ (in eV/anion), i.e., with a small deviation from the regular solution behavior. As can also be seen in Figure 1, the variation in the entropy of mixing of the alloy with temperature is close to the ideal solution expression $-k_B[x \ln x + (1-x)\ln(1-x)]$, which is expected for a random alloy at high temperatures. The variation of the free energy for $MAPb(I_{1-x}Br_x)_3$ is shown in Figure 3. For low temperatures the curve is asymmetric around $x = 1/2$ and is considerably lower in the Br-rich region, a consequence of the existence of the two ordered structures with negative energies of mixing described above. Also for low temperatures the free energy presents points with the same tangent, which indicates the existence of a miscibility gap. As the temperature increases, the shape of the curve becomes more symmetric as the probability of sampling all possible configurations increases.

Based on the Helmholtz free energy variation, we built the phase diagram of $MAPb(I_{1-x}Br_x)_3$, which is shown in Figure 4. The phase diagram reflects the asymmetry of the free energy, showing that the solid solution is more stable in the Br-rich region for typical growth temperatures. The phase diagram also shows that, at 300 K, the alloy is not stable against phase separation in the range of compositions between $x_1 = 0.19$ and $x_2 = 0.68$, the miscibility gap. Under equilibrium conditions, the pure compounds $MAPbI_3$ and $MAPbBr_3$ are not miscible inside this region, and two phases of compositions x_1 and x_2 must be formed. Also at room temperature, the alloy has spinodal points at the compositions $x_1' = 0.28$ and $x_2' = 0.58$, so in the intervals $x_1 < x < x_1'$ and $x_2' < x < x_2$ the alloy can present metastable phases, i.e., resistant to small fluctuations in composition. The existence of a miscibility gap at low temperatures is not a surprise, since there is a difference of 6% between the equilibrium lattice constants of $MAPbI_3$ and $MAPbBr_3$. The mismatch of the lattice constants is generally associated with the instability of isovalent solid solutions.[22] The critical temperature—the temperature above which the solid solution is stable for any composition—is 343 K, a value considerably higher than the temperature of 223 K estimated by Yin et al. for the $CsPb(I_{1-x}Br_x)_3$ perovskite.

Our model provides a simple thermodynamic explanation for the photoinduced phase separation observed in mixed halide solar cells. In an initial state, a uniform mixture can be fabricated either through control of the deposition kinetics or by annealing above the miscibility temperature. At room temperature, the uniform mixture becomes unstable, but phase separation will be a slow process. Illumination at high light intensities has the effect of overcoming these kinetic barriers and changing the local temperature. Another possible

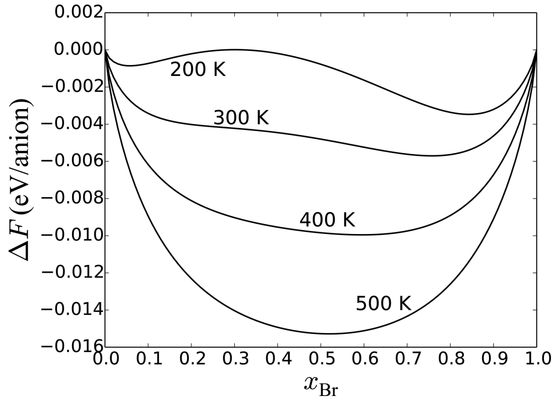

Figure 3. Calculated Helmholtz free energy as a function of the alloy composition and temperature as calculated within the generalized quasi-chemical approximation.

contribution associated with the photocurrent in an active solar cell is electromigration, which will affect Br more than I due to the lower atomic mass.

Direct comparison with experiment is made difficult by the fact that most studies have reported the stoichiometry of the precursor solutions, but not the final materials. Hoke et al. investigated a range of compositions from $x = 0$ to 1, which were annealed at 373 K.[13] A blue-shift in optical absorption was found from I-rich to Br-rich compositions except for around $x = 0.5$, which showed a behavior that indicated phase separation into I-rich domains of $x \sim 0.2$ from analysis of the spectral shift in photoluminescence. Note that as Br-rich domains will have larger band gaps, they can be spectrally "invisible". The observed behavior fits very well with our predicted phase diagram (Figure 4). Upon light soaking, compositions of $x > 0.2$ were all found to exhibit decomposition to the $x \sim 0.2$ phase, which from our calculations can be interpreted as the spinodal line at 300 K. A recent investigation by Gil-Escrig of solar cells made from the Br/I mixture show a similar behavior with a marked decrease in performance for Br-rich compositions. The kinetics of these reorganization processes are consistent with the rapid anion exchange observed for these perovskites.[23,24] Low activation energies for solid-state diffusion have been predicted from simulation studies,[25−27] and there is increasing evidence for mass transport in real devices.[28,29] While it is unlikely that there is a mechanism to stabilize Br-rich mixtures toward practical devices, compositional engineering—in the three-dimensional $Cs_{1-x}MA_xPb_{1-y}Sn_yI_{3-z}Br_z$ system for example—may provide a solution to thermodynamically robust wider band gap materials.

To summarize, we have reported a statistical mechanical study of the solid-solution formed by two halide hybrid perovskites informed by quantum mechanical total energy calculations. The resulting phase diagram for $MAPb(I_{1-x}Br_x)_3$ reveals several important features: (i) a critical temperature for mixing of 343 K; (ii) a window between $0.3 < x < 0.6$ that is unstable with respect to spinodal decomposition at 300 K; (iii) a binodal (coexistence) point at $x = 0.2$ and $x = 0.7$ at 300 K. The thermodynamic metastability of this alloy for intermediate Br/I compositions explains the sensitivity of the mixture to preparatory conditions, temperature, and the operation conditions of a solar cell.

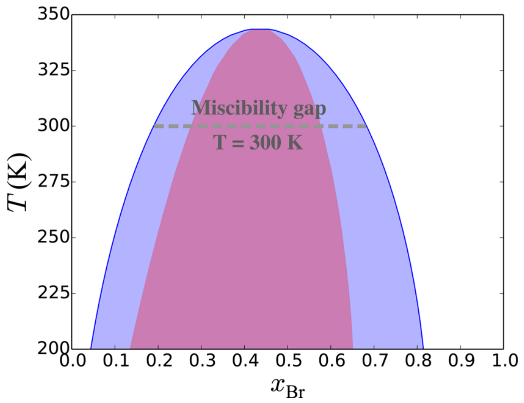

Figure 4. Predicted phase diagram of the $MAPb(I_{1-x}Br_x)_3$ alloy. The purple and pink lines are the binodal and spinodal lines, respectively. The dashed horizontal line shows the miscibility gap at room temperature. A thermodynamically stable solid-solution can be formed in the white region only.

COMPUTATIONAL METHODS

Disordered materials are challenging to accurately describe using atomistic simulations. We model the halide alloy as a statistical ensemble of independent configurations for seven compositions: $x = 0, \frac{1}{6}, \frac{1}{3}, \frac{1}{2}, \frac{2}{3}, \frac{5}{6}, 1$. The mixing energy of each configuration with energy E_j is defined as

$$\Delta U_j = E_j - (1 - x)E_{MAPbI_3} - xE_{MAPbBr_3} \tag{1}$$

where the last two terms represent fractions of the total energy of the pure compounds. The thermodynamic properties of the alloy were determined using the generalized quasi-chemical approximation.[21] This method has been successfully employed in the thermodynamic analysis of semiconductor alloys.[30,31] By taking into account the total energy and the degeneracy of each configuration, the method provides simple expressions for the mixing contribution to the alloy internal energy ΔU and the configurational entropy ΔS as functions of the composition x and temperature T accordingly to a Boltzmann distribution. With these thermodynamic potentials, the Helmholtz free energy of the alloy can be directly evaluated:

$$\Delta F(x, T) = \Delta U(x, T) - T\Delta S(x, T) \tag{2}$$

The phase diagram of the alloy can be built by calculating the free energy at different temperatures. For each temperature, the binodal points are determined by collecting the compositions for which ΔF has a common tangent. The spinodal points are those in which the second derivative of ΔF vanishes. The model has been implemented in a set of Python codes.

The configuration energies E_j were each computed within the framework of Kohn−Sham density functional theory (DFT).[32] We considered a tetragonal supercell with 2 × 1 × 1 expansion of a pseudocubic perovskite building block, which corresponds to six anions.[33,34] The total number of configurations for this system is $2^6 = 64$. For a perfect inorganic cubic perovskite (O_h symmetry), the three halide sites are equivalent, which reduces the total number of configurations to 21 in total (using the SOD code[35]). Due to the presence of $CH_3NH_3^+$ cation, the symmetry is formally lowered. As a compromise between computational cost and accuracy, we take the symmetry-reduced inequivalent configurations and perform a full structural relaxation for each case. The initial cells were constructed using a linear combination of the end member lattice constants (a = 6.28 and 5.91 Å for $MAPbI_3$ and $MAPbBr_3$, respectively), i.e. Vegard's law. As the molecules are known to be rotationally active at room temperature,[36,37] a range of orientations may be accessible, but this effect is not included in our current model. Contributions from rotational and vibrational entropy are not taken into account in the free energy expansion.

For the DFT total energy calculations, we used the VASP[38] code with the Perdew−Burke−Ernzerhof exchange-correlation functional revised for solids (PBEsol)[39] and the projector augmented-wave formalism[40] including scalar-relativistic corrections. A plane-wave cutoff energy of 500 eV and a 3 × 6 × 6 k-point mesh were used for all the configurations. The lattice volume and shape, and the atomic positions of each configuration were fully optimized to minimize atomic forces below 1.0 meV/Å.

Data Access Statement. The GQCA alloy code is available from https://github.com/WMD-group/GQCA_alloys and the crystal structures from https://github.com/WMD-group/hybrid-perovskites.

AUTHOR INFORMATION

Corresponding Author

*E-mail: E-mail: a.walsh@bath.ac.uk.

Notes

The authors declare no competing financial interest.

ACKNOWLEDGMENTS

The simulations performed in this work benefited from membership of the UK's HPC Materials Chemistry Consortium, which is funded by EPSRC grant EP/L000202. A.W. is funded by ERC Starting Grant No. 277757, F.B. is supported by EU-FP7 Grant No. 316494, and C.C. acknowledges support from the Brazilian Research Agency CNPq Grant No. 249280/2013-2 PDE.

REFERENCES

(1) Jeon, N. J.; Noh, J. H.; Kim, Y. C.; Yang, W. S.; Ryu, S.; Seok, S. I. Solvent Engineering for High-performance Inorganic-organic Hybrid Perovskite Solar Cells. *Nat. Mater.* **2014**, *13*, 897.

(2) Zhou, H.; Chen, Q.; Li, G.; Luo, S.; Song, T.-b.; Duan, H.-S.; Hong, Z.; You, J.; Liu, Y.; Yang, Y. Interface Engineering of Highly Efficient Perovskite Solar Cells. *Science* **2014**, *345*, 542.

(3) Ahn, N.; Son, D.-Y.; Jang, I.-H.; Kang, S. M.; Choi, M.; Park, N.-G. Highly Reproducible Perovskite Solar Cells with Average Efficiency of 18.3% and Best Efficiency of 19.7% Fabricated via Lewis Base Adduct of Lead(II) Iodide. *J. Am. Chem. Soc.* **2015**, *137*, 8696.

(4) Jeon, N. J.; Noh, J. H.; Yang, W. S.; Kim, Y. C.; Ryu, S.; Seo, J.; Seok, S. I. Compositional Engineering of Perovskite Materials for High-performance Solar Cells. *Nature* **2015**, *517*, 476.

(5) Hao, F.; Stoumpos, C. C.; Chang, R. P. H.; Kanatzidis, M. G. Anomalous Band Gap Behavior in Mixed Sn and Pb Perovskites Enables Broadening of Absorption Spectrum in Solar Cells. *J. Am. Chem. Soc.* **2014**, *136*, 8094.

(6) Noh, J. H.; Im, S. H.; Heo, J. H.; Mandal, T. N.; Seok, S. I. Chemical Management for Colorful, Efficient, and Stable Inorganic-organic Hybrid Nanostructured Solar Cells. *Nano Lett.* **2013**, *13*, 1764.

(7) Sadhanala, A.; Deschler, F.; Thomas, T. H.; Dutton, S. E.; Goedel, K. C.; Hanusch, F. C.; Lai, M. L.; Steiner, U.; Bein, T.; Docampo, P.; et al. Preparation of Single Phase Films of $CH_3NH_3Pb(I_{1-x}Br_x)_3$ with Sharp Optical Band Edges. *J. Phys. Chem. Lett.* **2014**, *5*, 2501.

(8) Kulkarni, S. A.; Baikie, T.; Boix, P. P.; Yantara, N.; Mathews, N.; Mhaisalkar, S. Band-gap Tuning of Lead Halide Perovskites Using a Sequential Deposition Process. *J. Mater. Chem. A* **2014**, *2*, 9221.

(9) Fedeli, P.; Gazza, F.; Calestani, D.; Ferro, P.; Besagni, T.; Zappettini, A.; Calestani, G.; Marchi, E.; Ceroni, P.; Mosca, R. Influence of the Synthetic Procedures on the Structural and Optical Properties of Mixed-Halide (Br,I) Perovskite Films. *J. Phys. Chem. C* **2015**, *119*, 21304.

(10) Ledinský, M.; Löper, P.; Niesen, B.; Holovský, J.; Moon, S.-J.; Yum, J.-H.; De Wolf, S.; Fejfar, A.; Ballif, C. Raman Spectroscopy of Organic Inorganic Halide Perovskites. *J. Phys. Chem. Lett.* **2015**, *6*, 401.

(11) Gil-Escrig, L.; Miquel-Sempere, A.; Sessolo, M.; Bolink, H. J. Mixed Iodide-bromide Methylammonium Lead Perovskite-based Diodes for Light Emission and Photovoltaics. *J. Phys. Chem. Lett.* **2015**, *6*, 3743.

(12) Egger, D. A.; Edri, E.; Cahen, D.; Hodes, G. Perovskite Solar Cells: Do We Know What We Do Not Know? *J. Phys. Chem. Lett.* **2015**, *6*, 279.

(13) Hoke, E. T.; Slotcavage, D. J.; Dohner, E. R.; Bowring, A. R.; Karunadasa, H. I.; McGehee, M. D. Reversible Photo-induced Trap Formation in Mixed-halide Hybrid Perovskites for Photovoltaics. *Chem. Sci.* **2015**, *6*, 613.

(14) Niemann, R. G.; Kontos, A. G.; Palles, D.; Kamitsos, E. I.; Kaltzoglou, A.; Brivio, F.; Falaras, P.; Cameron, P. J. Halogen Effects on Ordering and Bonding of $CH_3NH_3^+$ in $CH_3NH_3PbX_3$ (X= Cl, Br, I) Hybrid Perovskites: A Vibrational Spectroscopic Study. *J. Phys. Chem. C* **2016**, *120*, 2509.

(15) Xiao, Z.; Yuan, Y.; Shao, Y.; Wang, Q.; Dong, Q.; Bi, C.; Sharma, P.; Gruverman, A.; Huang, J. Giant Switchable Photovoltaic Effect in Organometal Trihalide Perovskite Devices. *Nat. Mater.* **2015**, *14*, 193.

(16) Yuan, Y.; Huang, J. Ion Migration in Organometal Trihalide Perovskite and Its Impact on Photovoltaic Efficiency and Stability. *Acc. Chem. Res.* **2016**, *49*, 286.

(17) Mosconi, E.; Amat, A.; Nazeeruddin, M. K.; Grätzel, M.; De Angelis, F. First Principles Modeling of Mixed Halde Organometal Perovskites for Photovoltaic Applications. *J. Phys. Chem. C* **2013**, *117*, 13902.

(18) Yin, W.-J.; Yan, Y.; Wei, S.-H. Anomalous Alloy Properties in Mixed Halide Perovskites. *J. Phys. Chem. Lett.* **2014**, *5*, 3625.

(19) Onoda-Yamamuro, N.; Matsuo, T.; Suga, H. Calorimetric and IR Spectroscopic Studies of Phase Transitions in Methylammonium Trihalogenoplumbates (II). *J. Phys. Chem. Solids* **1990**, *51*, 1383.

(20) Shannon, R. D. Revised Effective Ionic Radii and Systematic Studies of Interatomic Distances in Halides and Chalcogenides. *Acta Crystallogr., Sect. A: Cryst. Phys., Diffr., Theor. Gen. Crystallogr.* **1976**, *32*, 751.

(21) Sher, A.; van Schilfgaarde, M.; Chen, A.-B.; Chen, W. Quasichemical Approximation in Binary Alloys. *Phys. Rev. B: Condens. Matter Mater. Phys.* **1987**, *36*, 4279.

(22) Stringfellow, G. Calculation of Ternary and Quaternary III-V Phase Diagrams. *J. Cryst. Growth* **1974**, *27*, 21.

(23) Yang, T.-Y.; Gregori, G.; Pellet, N.; Grätzel, M.; Maier, J. The Significance of Ion Conduction in a Hybrid Organic-Inorganic Lead-Iodide-Based Perovskite Photosensitizer. *Angew. Chem., Int. Ed.* **2015**, *54*, 7905.

(24) Zhang, Y.; Liu, M.; Eperon, G. E.; Leijtens, T. C.; McMeekin, D.; Saliba, M.; Zhang, W.; De Bastiani, M.; Petrozza, A.; Herz, L. M.; et al. Charge Selective Contacts, Mobile Ions and Anomalous Hysteresis in Organic-Inorganic Perovskite Solar Cells. *Mater. Horiz.* **2015**, *2*, 315.

(25) Eames, C.; Frost, J. M.; Barnes, P. R. F.; O'Regan, B. C.; Walsh, A.; Islam, M. S. Ionic Transport in Hybrid Lead Iodide Perovskite Solar Cells. *Nat. Commun.* **2015**, *6*, 7497.

(26) Haruyama, J.; Sodeyama, K.; Han, L.; Tateyama, Y. First-Principles Study of Ion Diffusion in Perovskite Solar Cell Sensitizers. *J. Am. Chem. Soc.* **2015**, *137*, 10048.

(27) Azpiroz, J. M.; Mosconi, E.; Bisquert, J.; De Angelis, F. Defects Migration in Methylammonium Lead Iodide and their Role in Perovskite Solar Cells Operation. *Energy Environ. Sci.* **2015**, *8*, 2118.

(28) Hentz, O.; Zhao, Z.; Gradecak, S. Impacts of Ion Segregation on Local Optical Properties in Mixed Halide Perovskite Films. *Nano Lett.* **2016**, *16*, 1485.

(29) Shi, J.; Xu, X.; Zhang, H.; Luo, Y.; Li, D.; Meng, Q. Intrinsic Slow Charge Response in the Perovskite Solar Cells: Electron and Ion Transport. *Appl. Phys. Lett.* **2015**, *107*, 163901.

(30) Teles, L. K.; Furthmüller, J.; Scolfaro, L. M. R.; Leite, J. R.; Bechstedt, F. First-principles Calculations of the Thermodynamic and Structural Properties of Strained $In_xGa_{1-x}N$ and $Al_xGa_{1-x}N$ Alloys. *Phys. Rev. B: Condens. Matter Mater. Phys.* **2000**, *62*, 2475.

(31) Schleife, A.; Eisenacher, M.; Rödl, C.; Fuchs, F.; Furthmüller, J.; Bechstedt, F. Ab initio Description of Heterostructural Alloys: Thermodynamic and Structural Properties of $Mg_xZn_{1-x}O$ and $Cd_xZn_{1-x}O$. *Phys. Rev. B: Condens. Matter Mater. Phys.* **2010**, *81*, 245210.

(32) Kohn, W.; Sham, L. J. Self-consistent Equations Including Exchange and Correlation Effects. *Phys. Rev.* **1965**, *140*, A1133.

(33) Frost, J. M.; Butler, K. T.; Brivio, F.; Hendon, C. H.; van Schilfgaarde, M.; Walsh, A. Atomistic Origins of High-Performance in Hybrid Halide Perovskite Solar Cells. *Nano Lett.* **2014**, *14*, 2584.

(34) Brivio, F.; Frost, J. M.; Skelton, J. M.; Jackson, A. J.; Weber, O. J.; Weller, M. T.; Goni, A. R.; Leguy, A. M. A.; Barnes, P. R. F.; Walsh, A. Lattice Dynamics and Vibrational Spectra of the Orthorhombic,

Tetragonal, and Cubic Phases of Methylammonium Lead Iodide. *Phys. Rev. B: Condens. Matter Mater. Phys.* **2015**, *92*, 144308.

(35) Grau-Crespo, R.; Hamad, S.; Catlow, C. R. A.; de Leeuw, N. H. Symmetry-adapted Configurational Modelling of Fractional Site Occupancy in Solids. *J. Phys.: Condens. Matter* **2007**, *19*, 256201.

(36) Leguy, A.; Hu, Y.; Campoy-Quiles, M.; Alonso, M. I.; Weber, O. J.; Azarhoosh, P.; van Schilfgaarde, M.; Weller, M. T.; Bein, T.; Nelson, J.; et al. The Reversible Hydration of $CH_3NH_3PbI_3$ in Films, Single Crystals and Solar Cells. *Chem. Mater.* **2015**, *27*, 3397.

(37) Bakulin, A. A.; Selig, O.; Bakker, H. J.; Rezus, Y. L. A.; Müller, C.; Glaser, T.; Lovrincic, R.; Sun, Z.; Chen, Z.; Walsh, A.; et al. Real-Time Observation of Organic Cation Reorientation in Methylammonium Lead Iodide Perovskites. *J. Phys. Chem. Lett.* **2015**, *6*, 3663.

(38) Kresse, G.; Furthmüller, J. Efficient Iterative Schemes for Ab initio Total-energy Calculations Using a Plane-wave Basis Set. *Phys. Rev. B: Condens. Matter Mater. Phys.* **1996**, *54*, 11169.

(39) Perdew, J. P.; Ruzsinszky, A.; Csonka, G. I.; Vydrov, O. A.; Scuseria, G. E.; Constantin, L. A.; Zhou, X.; Burke, K. Restoring the Density-Gradient Expansion for Exchange in Solids and Surfaces. *Phys. Rev. Lett.* **2008**, *100*, 136406.

(40) Blöchl, P. E. Projector Augmented-wave Method. *Phys. Rev. B: Condens. Matter Mater. Phys.* **1994**, *50*, 17953.

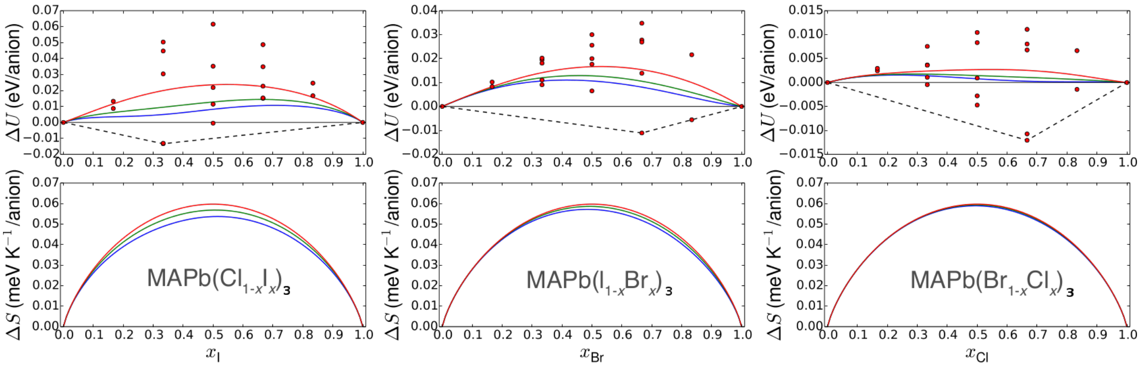

FIGURE 5.3: The diagram reports the energy of mixing (top row) and the entropy of mixing (bottom row) for the three studied cases in function of the composition. The solid lines report the behavior at 200 K (blue), 300 K (green) and for the high temperature limit (red). The dashed line represent the convex hull and the circle spots are the value for each configuration considered.

5.4 Further study

5.4.1 Other halide solid solutions

We employed the same model to study the other two possible binary halide perovskites: $MAPb(Cl_{(1\text{-}x)}I_x)_3$, $MAPb(Br_{(1\text{-}x)}Cl_x)_3$. We used the same type of crystallographic cells and computational setup.

The results for the energy of mixing and the entropy are reported in Figure 5.3. The energy of mixing is larger for the $MAPb(Cl_{(1\text{-}x)}I_x)_3$ case, due to the larger mismatch between the ionic radii. This correlation is particularly clear for $MAPb(Br_{(1\text{-}x)}Cl_x)_3$, the halide have similar size and the energies of the different structures fall within a smaller interval. All the structure present a convex hull and in the case of $MAPb(I_{(1\text{-}x)}Br_x)_3$, this is formed by the presence of two stable structures.

In all cases lowering the temperature results in a more asymmetric curve, which is due to the presence of the convex hull.

The structures correlated to the presence of the convex hull are reported in Figure 5.4. We can notice that the size of the cell is affected by the presence of the halides. It is minimum for the Cl-Br case, and maximum to for the $MAPbICl_2$ and $MAPbIBr_2$. The structure are similar, but there are two main difference. The octahedra are mostly distorted in the Cl−I case and the molecule is rotated of 90° with respect to the others in the Cl−Br system.

The stability of these structure is due to their capability to minimise the stress that originate from the radii mismatch of the ions. The presence of such ordered structure is particularly interesting because could explain the formation of different micro-crystalline domains or phase segregation.

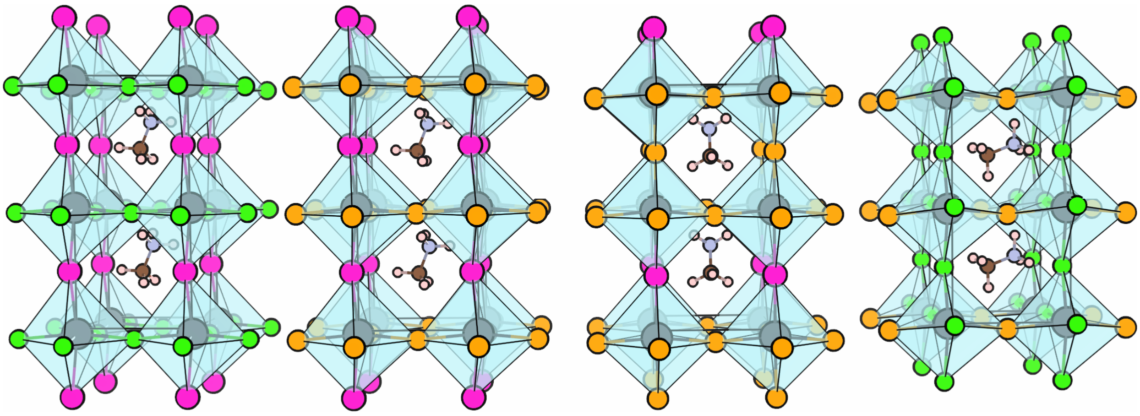

FIGURE 5.4: The figure reports the structure responsible for the presence of the convex hull. The first structure refers to $\mathrm{MAPbCl_2I}$, the second and the third to $\mathrm{MAPbBr_2I}$ and $MAPbBr_{\frac{5}{2}}I_{\frac{1}{2}}$ and the fourth to $\mathrm{MAPbBrCl_2}$. All the structures presents a layered motif with the larger halide occupying the apical positions with respect to the plane perpendicular to the C−N bond. The only exception is the third structure where the lower stoichiometry of I where the same motif is alternated with Br layers.

Using the total energy and the entropy of the system it is possible to calculate the Helmholtz free energy of the system according to:

$$F(x,T) = U(x,T) - TS(x,T) \tag{5.1}$$

From the free energy it is possible to calculate the phase diagram for the different alloys, that are reported in Figure 5.5.

We reported the phase diagram only above 200 K. This was necessary because calculation below that value suffered of numerical noise in the calculation of the free energy because of the restricted sampling we considered.

We can observe that the critical temperature decrease as the radii difference decreases, and in the case of the Cl-Br it falls below 200 K. The critical temperatures are similar to the one calculated for the analogous inorganic perovskites with Cs instead of MA reported by Yin *et al.*[204]. Because the entropy behaviour is similar in all three cases, the phase separation is due to the presence of particularly stable structures.

5.4.2 Larger supercell

We performed some initial calculations using a larger supercell with expansion 2×2×1. Within this expansion there are 12 halide sites. If we consider a binary alloys this lead to $\sum_{k=1}^{12}\binom{n}{k} = 2^{12} = 4096$ structures. To reduce this number we considered the equivalent ideal inorganic perovskites and we reduced the number of the configurations to 270. This number and the size of the supercell makes the calculation of all the structures almost 2 orders of magnitude larger than the analogous calculation on the 2×1×1 system. Even if we were not able

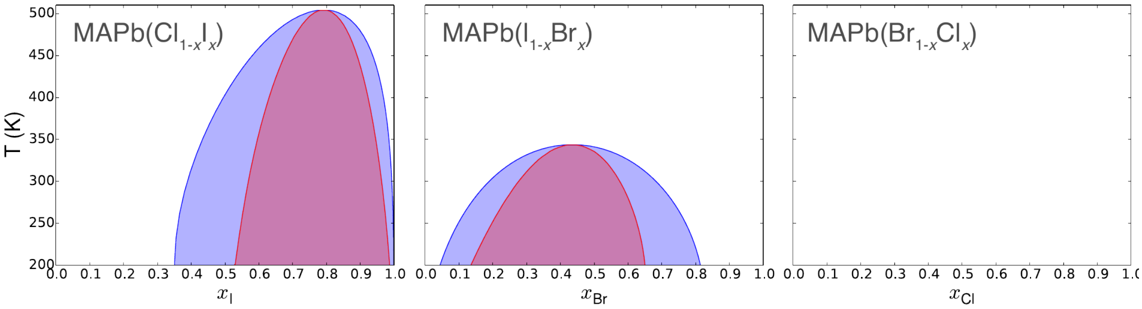

FIGURE 5.5: The graph reports the three phase diagrams for the different alloys. The red and blue regions together form the miscibility gap, while the white area is the portion of the configurational space where the random solid solution is stable. Within the miscibility gap the red region is the unstable portion of the diagram, while the system is metastable in the blue area. The third compound is completely miscible above 200 K and the phase diagram is empty. The critical temperature decrease if the radii mismatch is smaller.

to perform all the possible structures, we performed the calculation for the 50% composition for the three possible pairs and for the alloys where halides are in ratio 1:5. The expansion has been performed along the a and b direction and keeping the molecule laying in the ab plane.

For the MAPb($I_{(1-x)}Br_x)_3$ we calculated the enthalpy of mixing and we identified two structures with negative energy of mixing. Both of the structures found are similar to the one observed in the small supercell case. The first structure, left panel of Figure 5.6, occurs for an equal stoichiometry of the two halides. They form octahedra with the two apical positions occupied by different species, while the plane is formed by opposite similar halides. This supercell is larger and this allows extra degrees of freedom on apical halides. They are occupied by the same type of halide along one crystallographic direction, while they alternate in the direction along the which the molecule lies. This induces a different tilting in the structure that form distortion in that direction.

The other structure occurs for the bromine rich case $MAPbBr_{\frac{5}{2}}I_{\frac{1}{2}}$. This structure is similar to the case observed in Br-poor case of the Cl-I alloy. The larger I cation form layers perpendicular to the molecule. In this case, due to the larger cell and a reduced stoichiometry, the plane are alternated with Br ions.

5.4.3 Conclusion

We built a simple thermodynamic model to study the behaviour of hybrid perovskites with mixed halide composition. This class of compound has a complex structure that lacks symmetry that could reduce the configurational space.

To solve these problems we considered only a small 2×1×1 supercell expansion and perform a partial sampling of the configuration considering the inequivalent configuration for an inorganic perovksite.

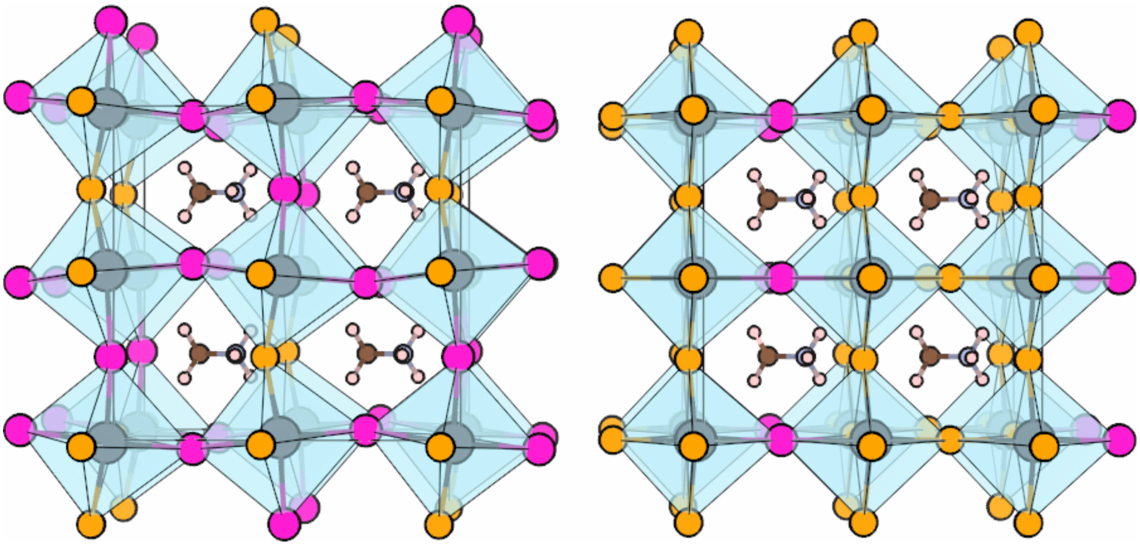

FIGURE 5.6: The figure reports stable structure for the $2 \times 2 \times 1$ supercell expansion calculations. The left figure reports the case of $MAPbBr_{\frac{3}{2}}I_{\frac{3}{2}}$, while the latter the case of $MAPbBr_{\frac{5}{2}}I_{\frac{1}{2}}$. The left structure is give by octahedra where the planar positions are occupied by alternating halides, so as the apical ones. The right one is similar to the one previously reported with the Iodine ions laying on alternating planes perpendicular to the molecules orientation.

Using the GQCA we calculated the phase diagram of the compound. We identified the presence of a miscibility gap, and the existence of a critical temperature that depends on the halide radii mismatch. Our results are consistent with previous work on inorganic perovskites. The miscibility gap is due to the presence of particularly stable ordered structures. The stability is related to the orientation of the molecule, and particular structures that minimise the stress due to the halide mismatch.

The emergence of the miscibility gap with metastable regions can explain the reported photoinstability of the materials that can undergo phase separation.

Chapter 6

Conclusions

In this thesis we focused on the materials for solar energy conversion, following the argument that the Sun provides a *free* amount of energy that dwarfs human needs. The photovoltaic effect has been discovered at the end of the XIX century, but it has intensely developed after the second world war. Since then, the photovoltaic technology has been divided in technology generations. The first included bulk semiconductors, such as silicon cells, and it is now a mature technology. The second generation was based on the use of thin film of similar materials. Technology based on the third and last generation exploit molecular materials properties to achieve the photovoltaic effect with cheaper and environmentally friendly techniques.

In the last two decades the third generation has been mostly dominated by the Dye Sensitises Solar Cells. The development of such technology did not lead to the expected commercial success, but originated a prosperous research community. Within this community the research lead to the rediscovery of a new class of materials, the hybrid perovskites that proved to be great light harvesters enabling the creation of solar cells with high performances. The behaviour and the properties of these materials are complex and seems to combine the properties of traditional semiconductor and nanostructures.

Hybrid perovskites employed in solar cells with reasonably high photovoltaic conversion has been reported in 2009 and, after some topical studies in 2012, they became one of the hottest topic in the field. The number of peer review publications exceeded a thousand, as showed in Figure 6.1.

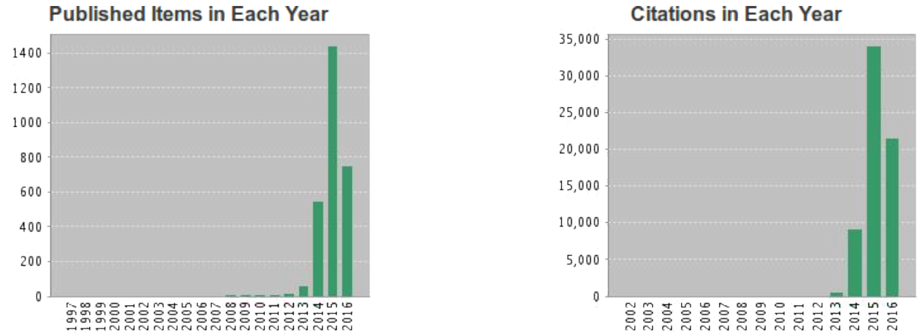

FIGURE 6.1: Citation report for the keyword "perovskite solar cells" accordingly to Thomson-Reuters Web of Knowledge. Updated to June 2016.

This permitted a huge progress from the experimental point of view and the initial gap with the most mature technologies had been closed. In the Chapters of this thesis we presented our contributions to rationalise the behaviour of the hybrid perovskites.

In Chapter 1 we started considered the simpler inorganic perovskites and calculated different properties with DFT techniques. We move on from these results and extended the study to hybrid perovskites considering their geometry optimization and the electronic structure. We found that the molecule is able to rotate inside the inorganic cage, and it does not affect significantly the electronic properties in terms of band gap, but it is crucial to define the structure.

The band gap we found using the GGA exchange-correlation potential PBEsol reproduces well the experimental results, but this agreement is due to an error compensation. DFT calculations does not take in account many-body effects, that would open the band gap, and the spin-orbit coupling, that reduces the band gap. To solve this problem we performed GW calculations to better describe the electronic properties. This permitted us to properly address the behaviour of hybrid perovskite more similarly to canonical semiconductors. It also emerged a particular effect that lead to a split of the minimum of the valence band: the Rashba splitting that we described. The displacement of the electronic minima could lead to longer life time of the carriers, which would explain the high efficiency of hybrid perovskite solar cells.

The structure of the perovskite is critical to control the properties of the materials. Chapter two focuses on how the vibration of the structure can affect those properties. Initially we used a simple harmonic approximation and we observed a coupling between the molecular and cage modes. This permitted us to simulate with good agreement experimental Raman and IR spectra. The reproduction of experimental data is particularly useful because it allows us to interpret the nature of the signal, allowing a better comprehension of the phenomena observed.

The harmonic approximation has some limitations, so we extended the study performing quasi-harmonic approximation simulations. This consists of a set of harmonic calculations with fixed out-of-equilibrium volumes and allows to recover some anharmonic effects. In particular we obtained the Grüneisen parameter and the thermal conductibility for MAPI. Although we used different approximations, even in this case our results matched accurately the experimental data.

An important aspect that contributed to the success of hybrid perovskite is their facile synthesis, and the possibility to tune their behaviour changing their composition. On the other hand their use in real device resulted in poor stability, due to the tendency of decompose and degrade under intense illumination. We used a thermodynamic approach to investigate the behaviour of different perovskites when mixed halide compositions were considered. The complexity of the hybrid perovskites does not allow simplification of the configurational space, and in theory all the possibilities should be considered. To approach the problem we needed to arbitrary restrict the configuration to take in account assuming the symmetry of the system after substituting the organic cation with an inorganic one.

The large mismatch between the radii of the halides induce a significant stress in the system. This stress favours some ordered configurations that minimize the strain in the structure. Due to this there is a miscibility gap with the presence of a metastable region. This can explain how measurements of perovskite can often degrade the materials inducing phase transitions due to light irradiation or heating of the sample. Rationalising the thermodynamic behaviour can improve the composition of new cell, and explain experimental evidence.

This work has provided some fundamental understanding of the electronic, and vibrational properties of hybrid perovskites. Looking forward the main area of development of the field regards the study of dynamical properties of such systems, with particular attention to ion diffusion, and extended defects.

The description of such effects can enable a more complete study of hybrid perovskite for applications beyond photovoltaics. This could be achieved partly by applying more extensively the techniques we presented in this work, but a complete description of large-scale effects is not within the capability of current *ab-initio* techniques. To increase the size of studied systems other approaches are needed. For example, force fields to describe hybrid perovskites are still lacking. Such achievement could be useful not only for itself, but as a resource to be implemented in more sophisticated quantum mechanics/molecular mechanics (QM/MM) simulations.

In an era of increasing calculation power, the use of multi-scale methods in addition to new computational algorithms based on large-scale "big-data" undertakings such as the Materials Project, are expanding the capability of simulations. In the near future, we will likely see a prominent shift toward these exciting new paradigms.

Bibliography

(1) Kittel, C.; Kroemer, H., *Thermal physics*; Macmillan: 1980.
(2) International Energy Agency, *Key world energy statistics*; International Energy Agency: 2007.
(3) Teichmüller, M. *International Journal of Coal Geology* **1989**, *12*, 1–87.
(4) Halbouty, M. T., *Giant Oil and Gas Fields of the Decade, 1990-1999*; AAPG memoir v. 78; American Association of Petroleum Geologists: 2003.
(5) Gold, T.; Soter, S. *Scientific American* **1980**, *242*.
(6) Shafiee, S.; Topal, E. *Energy policy* **2009**, *37*, 181–189.
(7) Baglione, M.; Duty, M.; Pannone, G. *Vehicle system energy analysis methodology and tool for determining vehicle subsystem energy supply and demand*; tech. rep.; SAE Technical Paper, 2007.
(8) Thomas, J. *SAE International Journal of Passenger Cars-Mechanical Systems* **2014**, *7*, 1374–1384.
(9) Spliethoff, H. In *Power Generation from Solid Fuels*; Springer: 2010, pp 73–219.
(10) Bezdek, R. H. In *2010 IEEE Conference on Innovative Technologies for an Efficient and Reliable Electricity Supply (CITRES)*, 2010, pp 121–126.
(11) Kost, C.; Mayer, J. N.; Thomsen, J; Hartmann, N; Senkpiel, C; Philipps, S; Nold, S; Lude, S; Saad, N; Schlegl, T *Fraunhofer Institute for Solar Energy Systems ISE* **2013**.
(12) Sorrell, S.; Speirs, J.; Bentley, R.; Brandt, A.; Miller, R. *Energy Policy* **2010**, *38*, 5290–5295.
(13) Slade, R.; Gross, R.; Bauen, A. *Energy & Environmental Science* **2011**, *4*, 2645–2657.
(14) De Almeida, P.; Silva, P. D. *Energy Policy* **2009**, *37*, 1267–1276.
(15) Würfel, P.; Würfel, U., *Physics of solar cells: from basic principles to advanced concepts*; John Wiley & Sons: 2009.
(16) Miller, S. L.; Orgel, L. E., *The origins of life on the earth*; Prentice-Hall Englewood Cliffs - NJ: 1974.
(17) Höök, M.; Tang, X. *Energy Policy* **2013**, *52*, 797–809.
(18) Peterson, T. C.; Connolley, W. M.; Fleck, J. *Bulletin of the American Meteorological Society* **2008**, *89*, 1325–1337.
(19) King, D. A. *Science* **2004**, *303*, 176–177.
(20) King, D. A. *Philosophical Transactions of the Royal Society A: Mathematical, Physical & Engineering Sciences* **2007**, *365*, 883–895.
(21) International Energy Agency *World energy outlook Special Report* **2013**.
(22) Novakov, T; Ramanathan, V; Hansen, J. E.; Kirchstetter, T. W.; Sato, M; Sinton, J. E.; Sathaye, J. A. *Geophysical Research Letters* **2003**, *30*, DOI: 10.1029/2002GL016345.

(23) Etheridge, D. M.; Steele, L. P.; Langenfelds, R. L.; Francey, R. J.; Barnola, J. M.; Morgan, V. I. *Trends: a compendium of data on global change* **1998**, 351–364.

(24) Ångström, A. *Geografiska Annaler* **1930**, *12*, 130–159.

(25) Schneider, S. H. *Science* **1989**, *243*, 771–781.

(26) Nordhaus, W. D. *The Economic Journal* **1991**, *101*, 920–937.

(27) Lashof, D. A.; Tirpak, D. A., *Policy options for stabilizing global climate: Report to Congress*; United States Environmental Protection Agency, Office of Policy, Planning, and Evaluation: 1990; Vol. 2.

(28) Risbey, J. *Nature* **2015**, *517*, 562–563.

(29) Dai, A.; Fyfe, J. C.; Xie, S.-P.; Dai, X. *Nature Climate Change* **2015**, *5*, 555–559.

(30) Karl, T. R.; Arguez, A.; Huang, B.; Lawrimore, J. H.; McMahon, J. R.; Menne, M. J.; Peterson, T. C.; Vose, R. S.; Zhang, H.-M. *Science* **2015**, *348*, 1469–1472.

(31) Oppenheimer, M. *Nature* **1998**, *393*, 325–332.

(32) Mercer, J. H. *Nature* **1978**, *271*, 321–325.

(33) Raval, A; Ramanathan, V *Nature* **1989**, *342*, 758–761.

(34) What is Ocean Acidification?, http://www.pmel.noaa.gov/co2/story/What+is+Ocean+Acidification%3F (accessed 02/08/2016).

(35) Raven, J.; Caldeira, K.; Elderfield, H.; Hoegh-Guldberg, O.; Liss, P.; Riebesell, U.; Shepherd, J.; Turley, C.; Watson, A., *Ocean acidification due to increasing atmospheric carbon dioxide*; The Royal Society: 2005.

(36) Doney, S. C.; Fabry, V. J.; Feely, R. A.; Kleypas, J. A. *Marine Science* **2009**, *1*.

(37) Querol, X.; Fernández-Turiel, J.; López-Soler, A. *Fuel* **1995**, *74*, 331–343.

(38) Färe, R.; Grosskopf, S.; Tyteca, D. *Ecological Economics* **1996**, *18*, 161–175.

(39) Jacobson, M. Z. *Journal of Geophysical Research: Atmospheres* **2010**, *115*.

(40) Jacobson, M. Z.; Colella, W. G.; Golden, D. M. *Science* **2005**, *308*, 1901–1905.

(41) Cifuentes, L.; Borja-Aburto, V. H.; Gouveia, N.; Thurston, G.; Davis, D. L. *Science* **2001**, *293*.

(42) Houghton, J. T.; Callander, B. A., *Climate change 1992: the supplementary report to the IPCC scientific assessment*; Cambridge University Press: 1992.

(43) Oreskes, N. *Science* **2004**, *306*, 1686.

(44) Doran, P. T.; Zimmerman, M. K. *Eos, Transactions American Geophysical Union* **2009**, *90*, 22–23.

(45) Cook, J.; Nuccitelli, D.; Green, S. A.; Richardson, M.; Winkler, B.; Painting, R.; Way, R.; Jacobs, P.; Skuce, A. *Environmental Research Letters* **2013**, *8*, 24024.

(46) Lazard Lazard's levelized cost of energy analysis — version 8.0., https://www.lazard.com/media/1777/levelized_cost_of_energy_-_version_80.pdf (accessed 08/02/2016).

(47) Administration, U. E. I. Annual Energy Outlook 2014., http://www.eia.gov/forecasts/aeo/pdf/electricity_generation.pdf (accessed 08/02/2016).

(48) Tobin, M. Components of levelized cost of energy., http://public.tableau.

com/profile/mitchtobin#!/vizhome/LazardLCOE/Dashboard7 (accessed 08/02/2016).

(49) International Energy Agency **2015**.

(50) Froggatt, A.; Schneider, M. *Proceedings of the IEEE* **2015**, *103*, 487–490.

(51) Wittneben, B. B. F. *Environmental Science & Policy* **2012**, *15*, 1–3.

(52) Mansur, L. K.; Rowcliffe, A. F.; Nanstad, R. K.; Zinkle, S. J.; Corwin, W. R.; Stoller, R. E. *Journal of Nuclear Materials* **2004**, *329*, 166–172.

(53) Glasstone, S.; Sesonske, A., *Nuclear reactor engineering: reactor systems engineering*; Springer Science & Business Media: 2012.

(54) Ashley, S. F.; Parks, G. T.; Nuttall, W. J.; Boxall, C.; Grimes, R. W. *Nature* **2012**, *492*, 31–33.

(55) Armaroli, N.; Balzani, V. *Energy for a sustainable world* **2010**.

(56) Piancastelli, L; Frizziero, L; Rocchi, I *Far East Journal of Electronics and Communications* **2014**, *12*, 19.

(57) EurObservER Wind power barometer., www.eurobserv-er.org (accessed 02/08/2016).

(58) Dixon, P. *Renewable Energy Focus* **2015**, *16*, 78–80.

(59) McCully, P.; Others, *Rivers no more: the environmental effects of dams.* Zed Books: 1996.

(60) Robbins, P. *Encyclopedia of Environment and Society* **2007**, *3*.

(61) Of concerned scientists, U. Environmental Impacts of Wind Power., http://www.ucsusa.org/clean_energy/our-energy-choices/renewable-energy/environmental-impacts-wind-power.html (accessed 02/08/2016).

(62) Smil, V., *Energy at the crossroads: global perspectives and uncertainties*; MIT press: 2005.

(63) Global Horizontal Irradiation., http://www.nature.com/news/paradox-at-the-heart-of-mathematics-makes-physics-problem-unanswerable-1.18983 (accessed 02/08/2016).

(64) Killinger, S.; Kreifels, N.; Burger, B.; Müller, B.; Stiff, G.; Wittwer, C. *Energy Technology* **2015**.

(65) Feldman, D.; Barbose, G.; Margolis, R.; James, T.; Weaver, S.; Darghouth, N.; Fu, R.; Davidson, C.; Booth, S.; Wiser, R. Photovoltaic System Pricing Trends., http://www.nrel.gov/docs/fy14osti/62558.pdf (accessed 08/02/2016).

(66) National Renewable Energy Laboratory Best Research-Cell Efficiencies., http://www.nrel.gov/ncpv/images/efficiency_chart.jpg (accessed 08/02/2016).

(67) Green, M. A. *Progress in Photovoltaics: Research and Applications* **2001**, *9*, 123–135.

(68) Green, M. A., *Third generation photovoltaics*; Springer: 2006.

(69) Conibeer, G. *Materials today* **2007**, *10*, 42–50.

(70) Shah, A.; Torres, P; Tscharner, R.; Wyrsch, N; Keppner, H *Science* **1999**, *285*, 692–698.

(71) Chopra, K. L.; Paulson, P. D.; Dutta, V; Others *Progress in Photovoltaics* **2004**, *12*, 69–92.

(72) Heeger, A. J. *Advanced Materials* **2014**, *26*, 10–28.

(73) O'Regan, B.; Grätzel, M. *Nature* **1991**, *353*, 737–740.
(74) Kamins, T., *Polycrystalline silicon for integrated circuit applications*; Springer Science & Business Media: 2012; Vol. 45.
(75) Fujishima, A. *Nature* **1972**, *238*, 37–38.
(76) Merck DSSC scheme., http://www.merck-performance-materials.jp/en/solar_and_energy/photovoltaics/dssc/dssc_technology/dssc_technology.html (accessed 02/08/2016).
(77) Reijnders, L. *Journal of Cleaner Production* **2010**, *18*, 307–312.
(78) Li, B.; Wang, L.; Kang, B.; Wang, P.; Qiu, Y. *Solar Energy Materials and Solar Cells* **2006**, *90*, 549–573.
(79) Grätzel, M. *Journal of Photochemistry and Photobiology C: Photochemistry Reviews* **2003**, *4*, 145–153.
(80) Sigma Aldrich Price of dye., http://www.sigmaaldrich.com/catalog/product/aldrich/703206?lang=en&region=GB (accessed 02/08/2016).
(81) Rose, G. *Annalen der Physik* **1839**, *124*, 551–573.
(82) Navrotsky, A; Weidner, D. *Washington DC American Geophysical Union Geophysical Monograph Series* **1989**, *45*, DOI: 10.1029/GM045.
(83) Watanabe, S.; Fujii, T. *Review of scientific instruments* **1996**, *67*, 3898–3903.
(84) Strauss, K. F.; Daud, T. In *Aerospace Conference Proceedings, 2000 IEEE*, 2000; Vol. 5, pp 399–408.
(85) Ghasdi, M.; Alamdari, H. *Sensors and Actuators B: Chemical* **2010**, *148*, 478–485.
(86) Cerdà, J; Arbiol, J; Dezanneau, G; Diaz, R; Morante, J. R. *Sensors and Actuators B: Chemical* **2002**, *84*, 21–25.
(87) Holc, J.; Slunčko, J.; Hrovat, M. *Sensors and Actuators B: Chemical* **1995**, *26*, 99–102.
(88) Arakawa, T.; Kurachi, H.; Shiokawa, J. *Journal of Materials Science* **1985**, *20*, 1207–1210.
(89) El-Batanouny, M.; Wooten, F., *Symmetry and condensed matter physics: a computational approach*; Cambridge University Press: 2008.
(90) Glazer, M.; Burns, G.; Glazer, A. N., *Space groups for solid state scientists*; Elsevier: 2012.
(91) Megaw, H. D. *Proceedings of the Physical Society* **1946**, *58*, 133.
(92) Li, C.; Lu, X.; Ding, W.; Feng, L.; Gao, Y.; Guo, Z. *Acta Crystallographica Section B: Structural Science* **2008**, *64*, 702–707.
(93) Li, Y. Y.; Lin, C. K.; Zheng, G. L.; Cheng, Z. Y.; You, H; Wang, W. D.; Lin, J **2006**, 3463–3469.
(94) Glazer, A. M. *Acta Crystallographica Section B: Structural Science* **1972**, *28*, 3384 3392.
(95) Glazer, A. M. *Acta Crystallographica Section A: Crystal Physics, Diffraction, Theoretical and General Crystallography* **1975**, *31*, 756–762.
(96) Gingla, F; Vogt, T; Akiba, E; Yvon, K *Journal of alloys and compounds* **1999**, *282*, 125–129.
(97) He, T; Huang, Q; Ramirez, A. P.; Wang, Y; Regan, K. A.; Rogado, N; Hayward, M. A.; Haas, M. K.; Slusky, J. S.; Inumara, K; Others *Nature* **2001**, *411*, 54–56.

(98) Eibenstein, U; Jung, W *Journal of Solid State Chemistry* **1997**, *133*, 21–24.

(99) Schaak, R. E.; Avdeev, M; Lee, W.-L.; Lawes, G; Zandbergen, H. W.; Jorgensen, J. D.; Ong, N. P.; Ramirez, A. P.; Cava, R. J. *Journal of Solid State Chemistry* **2004**, *177*, 1244–1251.

(100) Shannon, R. D. *Acta Crystallographica Section A: Crystal Physics, Diffraction, Theoretical and General Crystallography* **1976**, *32*, 751–767.

(101) Kieslich, G.; Sun, S.; Cheetham, T. *Chemical Science* **2014**, *5*, 4712–4715.

(102) Wyckoff, R. W. G. *American Journal of Science* **1928**, *s5-16*, 349–359.

(103) Couzi, M.; Daoud, A.; Perret, R. *Physica Status Solidi (a)* **1977**, *41*, 271–282.

(104) Weber, D. *Zeitschrift für Naturforsch. B* **1978**, *33b*, 862–865.

(105) Weber, D. *Zeitschrift für Naturforsch. B* **1978**, *33b*, 1443–1445.

(106) Raaen, A.; Svare, I; Fibich, M *Physica Scripta* **1982**, *25*, 957.

(107) Fuess, H; Körfer, M; Arend, H; Kind, R *Solid State Communications* **1985**, *56*, 137–139.

(108) Onoda-Yamamuro, N.; Matsuo, T.; Suga, H. *Journal of Physics and Chemistry of Solids* **1990**, *51*, 1383–1395.

(109) Onoda-yamamuro, N. Physico-chemical Study of Some Perovskite-type Methyl- ammonium Trihalogenometallates., Doctoral Thesis, Osaka University, 1992.

(110) Kojima, A.; Teshima, K.; Shirai, Y.; Miyasaka, T. *Journal of the American Chemical Society* **2009**, *131*, 6050–6051.

(111) Cheng, Z.; Lin, J. *CrystEngComm* **2010**, *12*, 2646.

(112) Wang, H.; Liu, Y.; Li, M.; Huang, H.; Xu, H. M.; Hong, R. J.; Shen, H. *Optoelectronics and Advanced Materials, Rapid Communications* **2010**, *4*, 1166–1169.

(113) Yamada, K.; Nakada, K.; Takeuchi, Y.; Nawa, K.; Yamane, Y. *Bulletin of the Chemical Society of Japan* **2011**, *84*, 926–932.

(114) Im, J.-H.; Lee, C.-R.; Lee, J.-W.; Park, S.-W.; Park, N.-G. *Nanoscale* **2011**, *3*, 4088–93.

(115) Chung, I.; Lee, B.; He, J.; Chang, R. P. H.; Kanatzidis, M. G. *Nature* **2012**, *485*, 486–489.

(116) Chung, I.; Song, J.-H.; Im, J.; Androulakis, J.; Malliakas, C. D.; Li, H.; Freeman, A. J.; Kenney, J. T.; Kanatzidis, M. G. *Journal of the American Chemical Society* **2012**, *134*, 8579–8587.

(117) Bach, U.; Daeneke, T. *Angewandte Chemie - International Edition* **2012**, *51*, 10451–10452.

(118) Etgar, L.; Gao, P.; Xue, Z.; Peng, Q.; Chandiran, A. K.; Liu, B.; Nazeeruddin, M. K.; Grätzel, M. *Journal of the American Chemical Society* **2012**, *134*, 17396–17399.

(119) Lee, M. M.; Teuscher, J.; Miyasaka, T.; Murakami, T. N.; Snaith, H. J. *Science* **2012**, *338*, 643–647.

(120) Im, J.-H.; Chung, J.; Kim, S.-J.; Park, N.-G. *Nanoscale research letters* **2012**, *7*, 353.

(121) Kim, H.-S.; Lee, C.-R.; Im, J.-H.; Lee, K.-B.; Moehl, T.; Marchioro, A.; Moon, S.-J.; Humphry-Baker, R.; Yum, J.-H.; Moser, J. E.; Grätzel, M.; Park, N.-G. *Scientific Reports* **2012**, *2*, 591.

(122) Stoumpos, C. C.; Malliakas, C. D.; Kanatzidis, M. G. *Inorganic chemistry* **2013**, *52*, 9019–38.

(123) Snaith, H. J. *The Journal of Physical Chemistry Letters* **2013**, *4*, 3623–3630.

(124) Tegmark, M.; Wheeler, J. A. *arXiv preprint quant-ph/0101077* **2001**.

(125) Top500.org November 2013., http://top500.org/lists/2015/11/ (accessed 02/08/2016).

(126) is the official web site of the Nobel Prize, N. Nobel Prizes 2013., http://www.nobelprize.org/nobel_prizes/lists/year/ (accessed 02/08/2016).

(127) Gill, P. M. W. *Journal of Chemical Physics* **1994**.

(128) Jensen, F., *Introduction to computational chemistry*; John Wiley & Sons: 2007.

(129) Hohenberg, P; Kohn, W *Physical Review B* **1964**, *136*, 864.

(130) Kohn, W; Sham, L. J. *Physical Review* **1965**, *140*, A1133.

(131) Hanninen, V. Introduction to Computational Chemistry - Lecture 7., http://www.helsinki.fi/kemia/fysikaalinen/opetus/jlk/luennot/Lecture7.pdf (accessed 02/08/2016).

(132) Sahni, V., *Quantal density functional theory*; Springer: 2004.

(133) Hellmann, H. *The Journal of Chemical Physics* **1935**, *3*, 61.

(134) Quester, W. Sketch Pseudopotentials., https://commons.wikimedia.org/wiki/File:Sketch_Pseudopotentials.png (accessed 02/08/2016).

(135) Marsman, M. VASP: Plane waves, the PAW method, and the Selfconsistency cycle., http://th.fhi-berlin.mpg.de/th/Meetings/DFT-workshop-Berlin2011/presentations/2011-07-14_Marsman_Martijn.pdf (accessed 02/08/2016).

(136) Hamann, D. R.; Schlüter, M; Chiang, C *Physical Review Letters* **1979**, *43*, 1494.

(137) Vanderbilt, D. *Physical Review B* **1990**, *41*, 7892.

(138) Blochl, P. E. *Physical Review B* **1994**, *50*, 17953.

(139) Kresse, G.; Joubert, D *Physical Review B* **1999**, *59*, 1758.

(140) Yates, J. An Introduction to Pseudopotentials., http://www.tcm.phy.cam.ac.uk/~jry20/gipaw/tutorial_pp.pdf (accessed 02/08/2016).

(141) Perdew, J. P. *International Journal of Quantum Chemistry* **1985**, *28*, 497–523.

(142) Haynes, P., *PhD Thesis: Linear-scaling methods in ab initio quantum-mechanical calculations*, 1998.

(143) Cramer, C. J., *Essentials of computational chemistry: theories and models*; John Wiley & Sons: 2013.

(144) Perdew, J. P.; Ernzerhof, M.; Burke, K. *The Journal of Chemical Physics* **1996**, *105*, 9982–9985.

(145) Perdew, J. P.; Ruzsinszky, A.; Csonka, G. I.; Vydrov, O. A.; Scuseria, G. E.; Constantin, L. A.; Zhou, X.; Burke, K. *Physical Review Letters* **2008**, *100*, 136406.

(146) Burke, K. Group Page., http://dft.uci.edu/research.php (accessed 02/08/2016).

(147) Becke, A. D. *The Journal of chemical physics* **1997**, *107*, 8554–8560.

(148) Schmider, H. L.; Becke, A. D. *The Journal of chemical physics* **1998**, *108*, 9624–9631.
(149) Adamo, C.; Barone, V. *The Journal of chemical physics* **1999**, *110*, 6158–6170.
(150) Adamo, C.; Scuseria, G. E.; Barone, V. *The Journal of chemical physics* **1999**, *111*, 2889–2899.
(151) Heyd, J.; Scuseria, G. E.; Ernzerhof, M. *The Journal of Chemical Physics* **2003**, *118*, 8207–8215.
(152) Paolo, U. Introduction to the GW method., http://www.quantum-espresso.org/wp-content/uploads/2013/06/talk_school_shanghai13.pdf (accessed 02/08/2016).
(153) Matteo, G. The one-particle Green's function and the GW approximation., http://benasque.org/2012tddft/talks_contr/049_12benasque_gw.pdf (accessed 02/08/2016).
(154) Fabien, B. The GW approximation in 90 minutes or so., http://www.tddft.org/bmg/files/seminarios/127407.pdf (accessed 02/08/2016).
(155) Van Hove, L. *Physical Review* **1953**, *89*, 1189.
(156) Placzek, G.; Van Hove, L *Physical Review* **1954**, *93*, 1207.
(157) Guyer, R. A.; Krumhansl, J. A. *Physical Review* **1966**, *148*, 766.
(158) Porezag, D.; Pederson, M. R. *Physical Review B* **1996**, *54*, 7830.
(159) Vasp Manual:static dielectric matrix, ion-clamped piezoelectric tensor and the Born effective charges using density functional perturbation theory., http://cms.mpi.univie.ac.at/vasp/vasp/LEPSILON_static_dielectric_matrix_ion_clamped_piezoelectric_tensor_Born_effective_charges.html (accessed 02/08/2016).
(160) Ackland, G. J.; Warren, M. C.; Clark, S. J. *Journal of Physics: Condensed Matter* **1997**, *9*, 7861.
(161) Togo, A.; Tanaka, I. *Scripta Materialia* **2015**, *108*, 1–5.
(162) Togo, A. Phonopy manual., 2011.
(163) Togo, A Phonopy v. 1.8. 5., http://phonopy.sourceforge.net (accessed 08/02/2016).
(164) Vinet, P.; Rose, J. H.; Ferrante, J.; Smith, J. R. *Journal of Physics: Condensed Matter* **1989**, *1*, 1941.
(165) Murnaghan, F. D. *Proceedings of the National Academy of Sciences* **1944**, *30*, 244–247.
(166) Birch, F. *Physical Review* **1947**, *71*, 809–824.
(167) Guggenheim, E. A.; McGlashan, M. L. In *Proceedings of the Royal Society of London A: Mathematical, Physical and Engineering Sciences*, 1951; Vol. 206, pp 335–353.
(168) Sher, A; van Schilfgaarde, M.; Chen, A.-B.; Chen, W. *Physical Review B* **1987**, *36*, 4279.
(169) Hirotsu, S. *Journal of the Physical Society of Japan* **1971**, *31*, 552–560.
(170) Trots, D. M.; Myagkota, S. V. *Journal of Physics and Chemistry of Solids* **2008**, *69*, 2520–2526.
(171) Shanno, D. F. *Journal of Optimization Theory and Applications* **1985**, *46*, 87–94.

(172) Harada, J.; Sakata, M.; Hoshino, S.; Hirotsu, S. *Journal of the Physical Society of Japan* **1976**, *40*, 212–218.
(173) Bulanova, G. G.; B, P. A.; V, S. L.; I, S. A., 1930.
(174) Donaldson, J. D.; Silver, J.; Hadjiminolis, S.; Ross, S. D. *Dalton Transactions* **1975**, 1500–1506.
(175) Yamada, K.; Funabiki, S.; Horimoto, H.; Matsui, T.; Okuda, T.; Ichiba, S. *Chemistry Letters* **1991**, *20*, 801–804.
(176) Van Lenthe, E.; Baerends, E.-J.; Snijders, J. G. *The Journal of chemical physics* **1994**, *101*, 9783–9792.
(177) Kresse, G *Physical Review B* **1996**, *54*.
(178) Monkhorst, H. J.; Pack, J. D. *Physical Review B* **1976**, *13*, 5188.
(179) Verma, A. S.; Kumar, A *Journal of Alloys and Compounds* **2012**, *541*, 210 214.
(180) Murtaza, G; Ahmad, I. *Physica B: Condensed Matter* **2011**, *406*, 3222–3229.
(181) Brik, M. G. *Solid State Communications* **2011**, *151*, 1733–1738.
(182) Aroyo, M. I.; Orobengoa, D.; de la Flor, G.; Tasci, E. S.; Perez-Mato, J. M.; Wondratschek, H. *Acta Crystallographica Section A: Crystal Physics, Diffraction, Theoretical and General Crystallography* **2014**, *70*, 126–137.
(183) Wei, S.-H.; Zunger, A. *Physical Review B* **1999**, *60*, 5404–5411.
(184) Fan, L.-Q.; Wu, J.-H. *Acta Crystallographica Section E Crystallographic Communications* **2007**, *63*, i189.
(185) Brivio, F.; Walker, A. B.; Walsh, A. *Applied Physics Letters* **2013**, *1*, 042111.
(186) Yamada, Y.; Nakamura, T. *Applied Physics Express* **2014**, *032302*.
(187) Blakemore, J. S. *Journal of Applied Physics* **1982**, *53*, R123–R181.
(188) Watson, G. W.; Kelsey, E. T.; de Leeuw, N. H.; Harris, D. J.; Parker, S. C. *Journal of the Chemical Society, Faraday Transactions* **1996**, *92*, 433–438.
(189) Peng, B.; Peter, K.; Wietasch, H.; Thelakkat, M. **2004**, *5215*, 60–70.
(190) Etgar, L.; Gao, P.; Xue, Z.; Peng, Q.; Chandiran, A. K.; Liu, B.; Nazeeruddin, M. K.; Grätzel, M. *Journal of the American Chemical Society* **2012**, *134*, 17396–17399.
(191) Malinkiewicz, O.; Yella, A.; Lee, Y. H.; Espallargas, G. M.; Graetzel, M.; Nazeeruddin, M. K.; Bolink, H. J. *Nature Photonics* **2013**, *8*, DOI: 10.1038/nphoton.2013.341.
(192) Frost, J. M.; Butler, K. T.; Brivio, F.; Hendon, C. H.; Van Schilfgaarde, M.; Walsh, A. *Nano Letters* **2014**, *14*, 2584–2590.
(193) Niemann, R. G.; Kontos, A. G.; Palles, D.; Kamitsos, E. I.; Kaltzoglou, A.; Brivio, F.; Falaras, P.; Cameron, P. J. *The Journal of Physical Chemistry C* **2016**.
(194) Ledinsky, M.; L0per, P.; Niesen, B.; Holovsky, J.; Moon, S.-J.; Yum, J.-H.; De Wolf, S.; Fejfar, A.; Ballif, C. *The journal of physical chemistry letters* **2015**, *6*, 401–406.
(195) Karhanek, D. Calculation of vibrational (IR) intensities in VASP 5.*., http://homepage.univie.ac.at/david.karhanek/downloads.html (accessed 02/08/2016).
(196) Fonari, A. Raman off-resonant activity calculator using VASP as a back-end., https://github.com/raman-sc/VASP (accessed 02/08/2016).
(197) Chen, Q.; Zhou, H.; Fang, Y.; Stieg, A. Z.; Song, T.-B.; Wang, H.-H.; Xu, X.; Liu, Y.; Lu, S.; You, J.; Sun, P.; McKay, J.; Goorsky, M. S.; Yang, Y. en

Nature Communications **2015**, *6*.
(198) Ye, S.; Sun, W.; Li, Y.; Yan, W.; Peng, H.; Bian, Z.; Liu, Z.; Huang, C. *Nano Letters* **2015**, *15*, 3723–3728.
(199) Atourki, L.; Vega, E.; Mar\'\i, B.; Mollar, M.; Ahsaine, H. A.; Bouabid, K.; Ihlal, A. *Applied Surface Science* **2016**, *371*, 112–117.
(200) Jacobsson, T. J.; Schwan, L. J.; Ottosson, M.; Hagfeldt, A.; Edvinsson, T. *Inorganic Chemistry* **2015**.
(201) Lanty, G.; Jemli, K.; Wei, Y.; Leymarie, J.; Even, J.; Lauret, J.-S.; Deleporte, E. *Journal of Physical Chemistry Letters* **2014**, *5*, 3958–63.
(202) McMeekin, D. P.; Sadoughi, G.; Rehman, W.; Eperon, G. E.; Saliba, M.; Hörantner, M. T.; Haghighirad, A.; Sakai, N.; Korte, L.; Rech, B.; Johnston, M. B.; Herz, L. M.; Snaith, H. J. *Science* **2016**, *351*, 151–155.
(203) Grau-Crespo, R; Hamad, S; Catlow, C. R. A.; de Leeuw, N. H. *Journal of Physics: Condensed Matter* **2007**, *19*, 256201.
(204) Yin, W.-J.; Yan, Y.; Wei, S.-H. *The Journal of Physical Chemistry Letters* **2014**, *5*, 3625–3631.